New methods for the speciated detection of peroxy radicals

Alexander David Brennan

Submitted in accordance with the requirements for the degree of Doctor of Philosophy

The University of Leeds

School of Chemistry

September 2019

The candidate confirms that the work submitted is his own, except where work which has formed part of jointly authored publications has been included. The contribution of the candidate and the other authors to this work has been explicitly indicated below. The candidate confirms that appropriate credit has been given within the thesis where reference has been made to the work of others

Chapters 4 and 5 are based on work from jointly authored publications, these are:

Chapter 4:

Title: A new method for atmospheric detection of the CH_3O_2 radical

Authors: Onel, L., Brennan, A., Seakins, P. W., Whalley, L. and Heard, D. E.

Published in Atmospheric Measurement Techniques, 10, 3985-4000, 2017.

All data acquired and analysed by both the candidate and Onel, L.

Chapter 5:

Title: An intercomparison of HO_2 measurements by fluorescence assay by gas expansion and cavity ring-down spectroscopy within HIRAC (Highly Instrumented Reactor for Atmospheric Chemistry)

Authors: Onel, L., Brennan, A., Gianella, M., Ronnie, G., Aguilla, A. L., Hancock, G., Whalley, L., Seakins, P. W., Ritchie, G. A. D., Heard, D. E.

Published in Atmospheric Measurement Techniques, 10, 4877-4894, 2017.

All data acquired and analysed by both the candidate and Onel, L.

Gianella, M designed the Cavity Ringdown Spectrometer and helped the candidate install and use it. Gianella, M also developed software to model the pressure broadening of the HO_2 absorption cross section, and to calculate and produce Allan deviation plots.

Acknowledgements

So…after a lot of procrastination and a little bit of writing, it's finally finished.

The first and foremost person to thank is Lavinia Onel, with whom I worked closely for most of this PhD. Thank you for showing me the ropes at the start and thank you for keeping everything so well organised over the years.

The second person to thank is Freja Østerstrøm, with whom I also worked closely with for the second half of this PhD. Thank you for your help with the very intensive cross-reaction experiments, and with the mountains of data analysis.

Dwayne, Paul and Lisa, thank you for having me as your student for four years and offering continued support and advice. I have greatly enjoyed my time here, except for the part where I wrote this document.

Trev, thanks for the help when it came to troubleshooting equipment. I learned a lot about electronics and programming from you.

Mark, similar thanks are in order, particularly when working on pumps, lasers and that damned FTIR.

To our collaborators from Oxford, thanks for helping get the funding together for this project. Thank you to Michele Gianella, who regularly made the long trip to Leeds to install and help us run the cavity ringdown spectrometer. There were a few long days getting that thing working…

Tom and Diogo, thanks for your help on getting the global fitting for data analysis working, and for your advice on various topics along the way.

Graham, thanks for your help with any problems I had, even though you had more than your fair share of your own.

Abstract

Organic peroxy radicals, RO_2, are a key component of the reaction cycles that control the chemical composition of the troposphere and how efficiently pollutants like greenhouse gases are removed. They are formed through the oxidation of any biogenic or anthropogenic volatile organic compound (VOC) in the troposphere and lead to the production of ozone, secondary organic aerosols, organic nitrates and more. Despite the significance of RO_2 radicals in tropospheric chemistry, there are currently no methods in regular use that can perform speciated measurements of the radicals in the field, instead only the sum of all RO_2 can be measured routinely.

In this thesis a new method is developed to specifically detect the methyl-peroxy radical, CH_3O_2, which is the simplest and most abundant RO_2 radical in the troposphere. The method is based on Fluorescence Assay by Gas Expansion (FAGE) and detects CH_3O_2 by converting it to CH_3O by titration with NO, which is then detected by Laser Induced Fluorescence (LIF) using ~298 nm light to excite the A^2A_1 ($\nu'_3 = 3$) $\leftarrow$ X^2E ($\nu''_3 = 0$) electronic transition. With a limit of detection of ~2×10^8 molecule cm^{-3} for a 5-minute averaging time the method could be a viable technique in low NO_x environments where CH_3O_2 levels are estimated to be ~$2 - 6 \times 10^8$ molecule cm^{-3}.

The method was tested using the Highly Instrumented Reaction for Atmospheric Chemistry (HIRAC), an atmospheric simulation chamber that can operate at temperatures between ~250 – 350 K. Using the new FAGE method in conjunction with HIRAC, the temperature dependent kinetics of the CH_3O_2 self-reaction were measured between 268 – 344 K, giving a temperature dependent rate coefficient of $k_{6.1} = (4.2 \pm 3.8) \times 10^{-14} \exp[(516 \pm 284)/T]$ cm^3 $molecule^{-1}$ s^{-1} and a value at 298 K of $k_{6.1} = (2.37 \pm 1.09) \times 10^{-13}$ cm^3 $molecule^{-1}$ s^{-1}. No significant temperature dependence was found, but the rate coefficients are approximately 30 % lower than current literature. A RO_xLIF instrument, newly developed for HIRAC, was also used to make preliminary measurements of the CH_3O_2 self-reaction at 295 K, finding a value that was similarly ~30 % lower than literature.

The temperature dependence of the CH_3O_2 + HO_2 reaction was also measured using the new FAGE method, giving a temperature dependent rate coefficient of $k_{6.3}$ = (1.26 ± 0.38) × 10^{-13} exp[(1119 ± 89)/T] cm^3 $molecule^{-1}$ s^{-1} and a value at 298 K of $k_{6.3}$ = (5.38 ± 0.18) × 10^{-12} cm^3 $molecule^{-1}$ s^{-1}, agreeing well with literature values.

Table of Contents

List of Figures

List of Abbreviations

AOM:	Acousto-optic modulator
BBO:	Barium borate
CFCs:	Chlorofluorocarbons
CIMS:	Chemical ionisation - Mass spectrometry
CPM:	Channel photomultiplier
CRDS:	Cavity ringdown spectrometer
DAQ:	Data acquisition
DOAS:	Differential optical absorption spectroscopy
ECHAMP:	Ethane chemical amplifier
ELVOCs:	Extremely low volatility organic compounds
ESR:	Electron spin resonance
FAGE:	Fluorescence assay by gas expansion
FTIR:	Fourier transform infra-red
HIRAC:	Highly instrumented reactor for atmospheric chemistry
HOMs:	Highly oxidised molecules
HPALDs:	Hydro-peroxy aldehydes
IUPAC:	International Union of Pure and Applied Chemistry
JPL:	Jet Propulsion Laboratory

LIF:	Laser induced fluorescence
LIM:	Leuven isoprene mechanism
LOD:	Limit of detection
MCM:	Master chemical mechanism
MCP:	Microchannel plate
MCS:	Multichannel scaler
MIESR:	Matrix isolation and electron spin resonance
NIST:	National Institute for Standards and Technology
PERCA:	Peroxy radical chemical amplification
SAPHIR chamber:	Simulation of atmospheric photochemistry in a large reaction chamber
SOA:	Secondary organic aerosol
VOC:	Volatile organic compound

Chapter 1. Understanding oxidation chemistry in the troposphere

The composition of the atmosphere is of vital importance to the quality of life on the planet Earth and is directly influenced by anthropogenic and biogenic emissions. Molecules emitted into the atmosphere may persist for mere tenths of seconds or hundreds of years, and during their lifetime they interact to form new gases or aerosols, each of which may warm or cool the planet, or affect the health of the life at the surface. The chemistry of the atmosphere is very complex, but by identifying and studying key species an understanding of the atmosphere can be developed, which will allow for informed decisions on policy changes that may help to counteract pollution and climate change. Radical species are ideal targets to help understand the chemical processes occurring in the atmosphere as they have short lifetimes, meaning their concentrations in any given area are governed primarily by the chemical environment rather than transportation.

The study of atmospheric oxidation chemistry consists of three main parts; laboratory-based measurements, computer modelling and field-based measurements. The laboratory-based measurements provide data that describe the behaviour of atmospheric species, such as rate coefficients, branching ratios, absorption cross-sections and photodissociation quantum yields. These data are used in computer modelling to generate chemical simulations of the atmosphere which can be used to predict the effect of policy changes on the chemistry of the atmosphere, and how it might affect health or climate. Comparison of the models with real-world data gathered through field measurements are a good way to test the quality of the models, and by extension assess current understanding of atmospheric chemistry.

An example of the impact these studies can have is the discovery of the Ozone hole over the Antarctic in 1985 through UV absorption field measurements (Farman et al., 1985). This prompted great deal of research, which identified heterogeneous chemistry on the surface of polar stratospheric clouds involving chlorine chemistry catalysing the destruction of ozone (Anderson et al., 1989). The presence of anthropogenically emitted chlorofluorocarbons (CFCs) were identified as the source of chlorine, which led to the adoption of the Montreal

Protocol in 1987, stipulating the phasing out of CFCs and other substances that deplete ozone. As a result, the size of the Ozone hole has stabilised and modelling predicts a return to normal levels in the mid-21st century (WMO, 2014, Solomon et al., 2016)

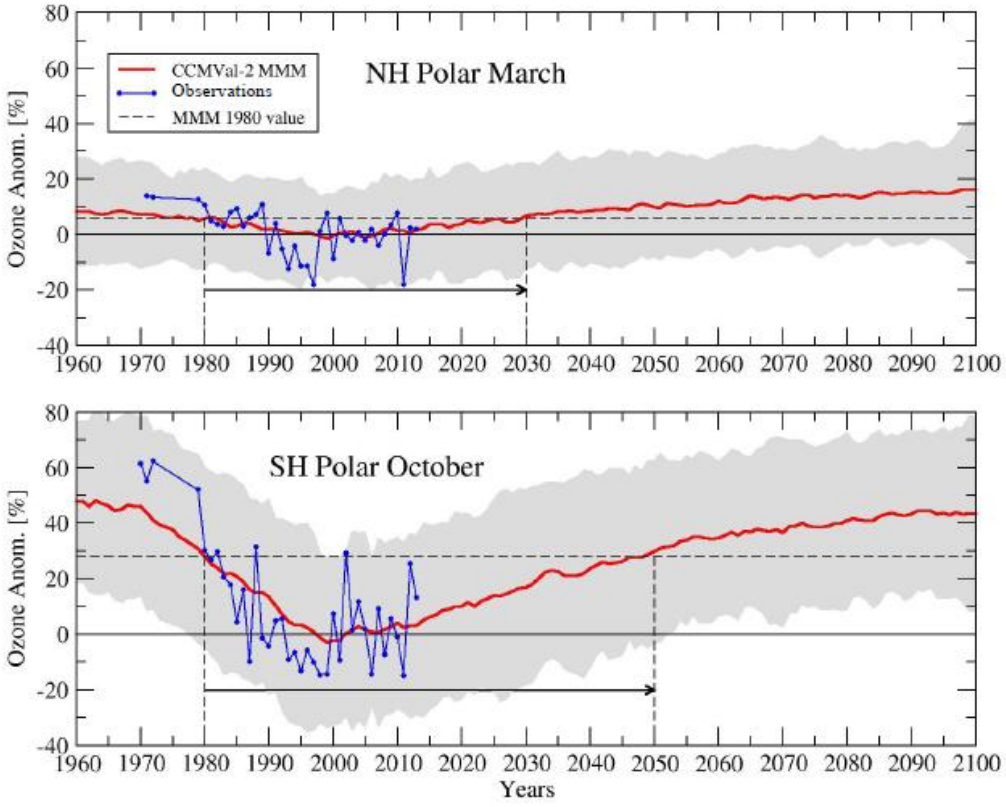

Figure 1.1 Measured (blue) and modelled (red) ozone anomaly (% of ozone relative to 1998-2008). Modelling reproduces measured data well and predicts return to 1980s ozone levels in the northern (upper panel) and southern (lower panel) polar hemisphere by 2050. Image taken from (WMO, 2014).

The now well-established link between rising global temperatures and human activity, the effects of greenhouse gases and their chemical properties and proposed mitigation methods (IPCC, 2013) is another example, perhaps the most notable. Closely linked to this is air quality, particularly in urban environments, where Public Health England has attributed between 28000 and 36000 deaths annually in the United Kingdom to human related polluted in cities (PHE, 2019). This is another important area where understanding the chemical processes that occur in the atmosphere is vital to human health.

1.1 Tropospheric oxidation chemistry

The troposphere extends a relatively short distance, ~10 km on average, from the surface of the Earth yet contains approximately 80 % of the total mass of the atmosphere, making it the most critical and changeable portion of the atmosphere to study. The chemistry of the troposphere changes depending on the type of environment being examined, such as polluted air over cities where anthropogenic emissions are high compared to clean air in remote areas, or highly forested areas where biogenic emissions are high, or the marine boundary layer and polar regions where halogen and heterogenous chemistry become important. Under most conditions the highly reactive hydroxyl radical, OH, is the dominant oxidant during daylight hours (Levy, 1971), destroying trace species such as CO, CH_4 and other volatile organic compounds (VOCs), making it key to the removal of pollutants and some greenhouse gases, and to the production of a range of secondary atmospheric species, such as ozone, aldehydes and aerosols, which contribute to acid rain and the formation of photochemical smog. Peroxy radicals (RO_2), mainly CH_3O_2 and HO_2, are almost always produced in the process and form a route to re-generate OH and form the HO_x cycle (HO_x = OH + HO_2), which is shown in Figure 1.2. This cycle controls the oxidative capacity of the troposphere during daylight hours and therefore governs its composition, making the radicals that make up the HO_x cycle valuable targets for study.

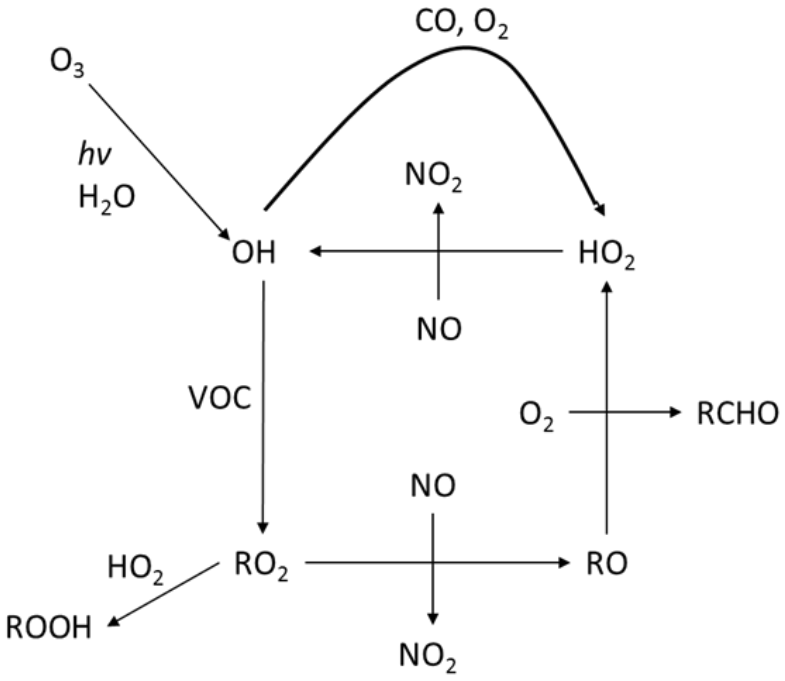

Figure 1.2 A simplified HO_x cycle showing the general reaction scheme that follows OH reacting with VOC. The cycle is initiated by the photolysis of O_3 in the presence of H_2O and shows how each OH radical produced can react numerous times to destroy pollutants. Also important are the NO reaction steps that produce NO_2, a precursor to tropospheric O_3 and photochemical smog.

The cycle is initiated by OH, and the main daytime source of OH in the clean troposphere is the photolysis of ozone at λ <340 nm, giving $O(^1D)$, which subsequently reacts with water vapour to produce OH (R 1.1-R 1.2). Another source of OH that is more prevalent in urban areas is the photolysis of HONO at λ <400 nm (R 1.3).

$$O_3 + h\nu(< 340\ \text{nm}) \rightarrow O(^1D) + O_2 \qquad \textbf{R 1.1}$$

$$O(^1D) + H_2O \rightarrow 2OH \qquad \textbf{R 1.2}$$

$$HONO + h\nu(< 400\ \text{nm}) \rightarrow NO + OH \qquad \textbf{R 1.3}$$

This dependence on sunlight causes a diurnal profile in OH levels, and subsequently the other constituents of the HO_x cycle, where concentrations usually peak at solar noon, although cloud cover can shift the timing of this peak. The maximum radical concentration varies depending on the environment and

how efficiently the HO_x cycle is completed, OH is typically in the range of ~10^6 – 10^7 molecule cm^{-3} (Heard, 2006, Stone et al., 2012) whereas the longer lived HO_2 and RO_2 radicals tend to exist in concentrations up to 10^8 molecule cm^{-3}. With such low concentrations, highly sensitive measurement equipment is required to detect these radical species. One of the most common methods to detect OH and HO_2 is Fluorescence Assay by Gas Expansion, first developed in 1984 (Hard et al., 1984), which draws gas through a pinhole into a low-pressure cell and detects OH through Laser Induced Fluorescence (LIF) at 308 nm. HO_2 is detected by first converting it to OH by reaction with NO. The FAGE method will be discussed in detail in Chapter 3 and is central to this thesis. Measurement techniques of RO_2 radicals are discussed in more detail in section 1.2.

Figure 1.3 shows a time series of OH, HO_2 and RO_2 measured in Wangdu, a rural site in the North China Plain (Tan et al., 2017). On most days in the time series the radicals follow a typical diurnal profile, reaching maximum levels around midday. A few exceptions, such as the 25th July, featured low radical concentrations due to attenuated solar radiation – i.e. cloud cover. The measurements are shown in black and are accompanied by modelled concentrations in blue that are in good agreement.

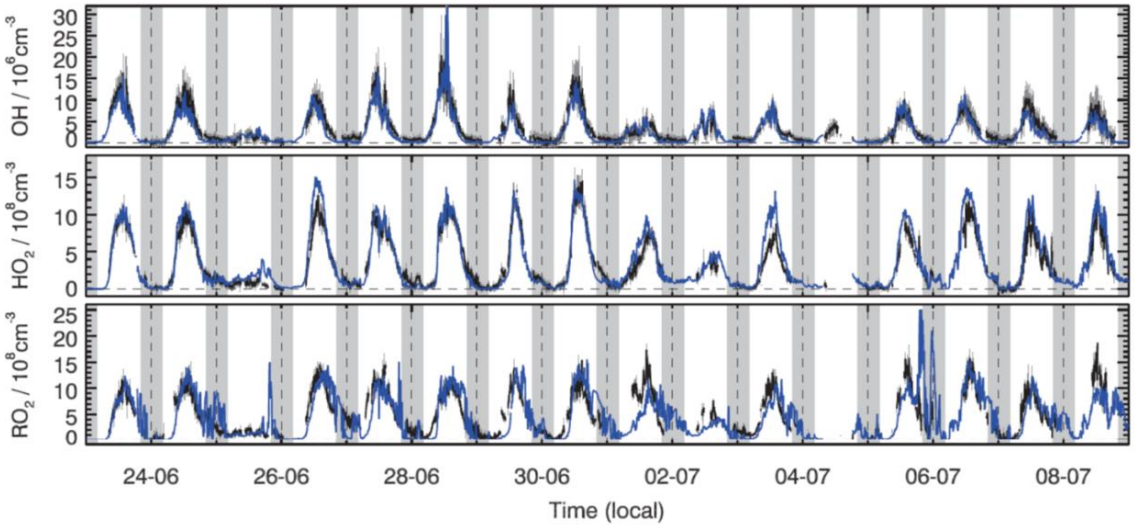

Figure 1.3 Time series of measured (black) and modelled (blue) OH, HO_2 and total RO_2 concentrations. The vertical dashed lines denote midnight. Measurements were made at a rural site in the North China Plain. The radical concentrations follow the typical diurnal profile with maximum concentrations reached around midday. Figure modified from Tan *et al.*, 2017.

1.1.1 Peroxy-Radical chemistry in the Troposphere

Peroxy radicals (RO_2) are a key component of the HO_x cycle, and together with HO_2 their reaction with NO provides the only route to net O_3 production in the troposphere. Reaction with NO_2 produces peroxy nitrates which act as long-lived NO_x reservoirs, allowing pollutants to be transported to new environments (Browne and Cohen, 2012). In urban environments where NO_x is high (~10 ppb) these reactions are very fast, however in cleaner rural environments (NO_x < 500 ppt) competition from other reactions such as RO_2 + RO_2 self and cross-reactions begin to compete. These other reactions are particularly important in pristine forested environments, such as tropical rainforests, where vast quantities of biogenic VOCs are emitted. With such high VOC loading and therefore a large sink for OH radicals, it was assumed that oxidative capacity of the troposphere would be low in these regions. However, measurements over the areas like the Amazon rainforest and the Pearl River Delta revealed this was not the case and, as Figure 1.4 shows, OH concentrations were much higher than chemical modelling predicted (Hofzumahaus et al., 2009, Lelieveld et al., 2008, Whalley et al., 2011).

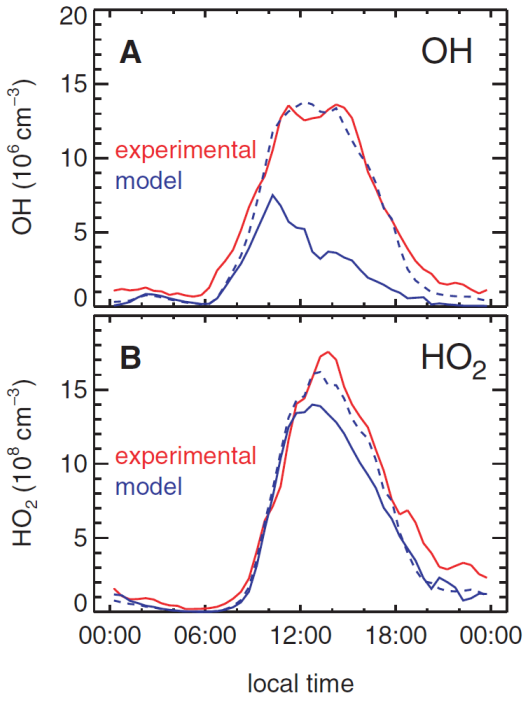

Figure 1.4 Mean diurnal profiles of (A) OH and (B) HO_2 comparing measured values (red) to modelled data (blue). Modelling was performed using the Regional Atmospheric Chemistry Mechanism (RACM), the solid blue line is the result with no modifications, and underpredicts OH by a factor of ~3-5 after 10 am, when NO levels decrease below 1 ppb. The dotted line is the same model but with artificially enhanced recycling of $RO_2 \rightarrow OH$. Figure taken from Hofzumahaus *et al.,* 2009

The discrepancy was caused by insufficient understanding of the peroxy-radical chemistry in these areas. Isoprene is the most abundant non-methane VOC, with natural emissions in excess of 500 Tg per year, or about 50 % of all biogenic VOCs (Guenther et al., 2006). Reaction of Isoprene with OH generates Isoprene-RO_2, as per the HO_x cycle, but in these pristine environments the peroxy radical is able re-generate OH radicals. The mechanism through which this happens has become a focal point of scientific research. Unimolecular chemistry, which was unaccounted for until this point as it involved high energy barriers unlikely to be exceeded under atmospheric conditions, has emerged as the most likely mechanism of OH regeneration, as RO_2 radical lifetimes are long in these pristine environments (Orlando and Tyndall, 2012). The Leuven Isoprene Mechanism (LIM, Figure 1.5), proposed and developed through theoretical *ab initio* calculations by Peeters *et al.* (Peeters et al., 2009, Peeters and Müller, 2010, Peeters et al., 2014) is a focus of current research into isoprene OH recycling.

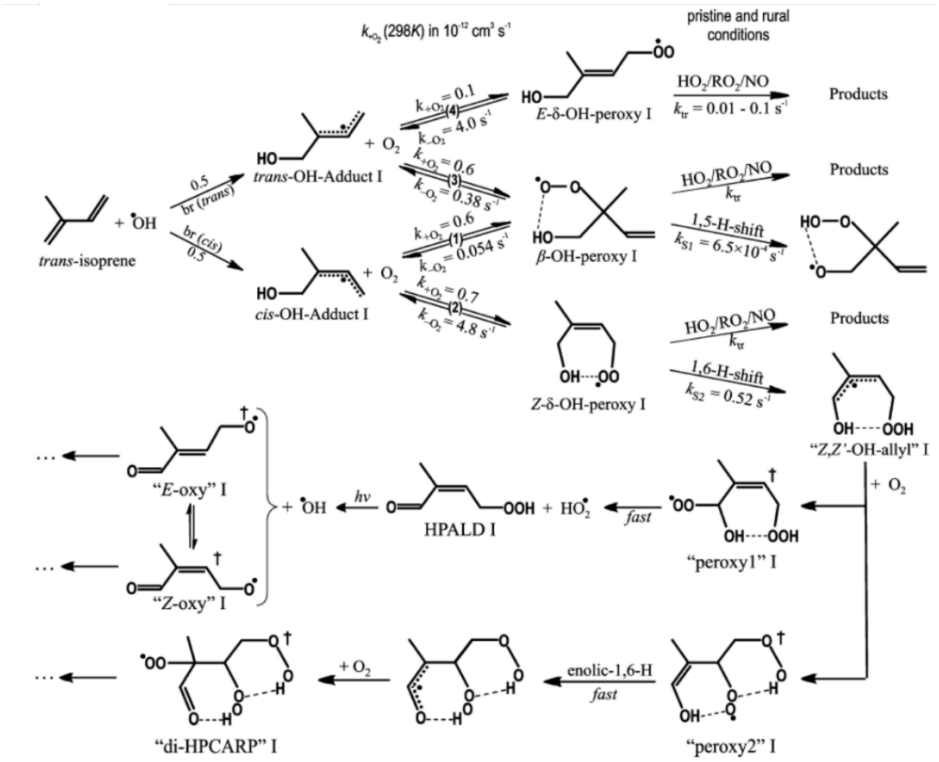

Figure 1.5 The Leuven Isoprene Mechanism (LIM1), derived through theoretical modelling by Peeters *et al.,* 2014. The mechanism shows that the OH initiated oxidation of isoprene can lead to the recycling of OH radicals through the formation of photolabile hydroperoxyl aldehydes (HPALDs). The formation of di-hidroperoxyl-carbonyl peroxy radicals (di-HPCARP) may also lead to the formation of OH through isomerisation and further reactions with HO_2 or NO. Image taken from Peeters *et al.,* 2014.

According to LIM, isoprene-RO_2 undergoes unimolecular isomerisation and eventually forms hydro-peroxy aldehydes (HPALDs), which rapidly photolyses to produce OH, and di-hydroperoxyl-carbonyl peroxy radicals (di-HPCARP) which can also lead to OH regeneration after further isomerisation and reaction with HO_2 or NO (Peeters et al., 2014), potentially allowing one isoprene-RO_2 to produce multiple OH radicals. The mechanism does not completely close the missing OH source and can in fact lead to overprediction of HO_2 (Whalley et al., 2011, Archibald et al., 2011, Lu et al., 2012). The mechanism is still being tested and refined, with new possible pathways to produce OH being discovered, (Peeters and Müller, 2010, Fuchs et al., 2013, Teng et al., 2017, Wennberg et al., 2018, Bates and Jacob, 2019, Muller et al., 2019), such as those shown in Figure 1.6, and components of it have since been incorporated into chemical models (Jenkin et al., 2015, Jenkin et al., 2019a).

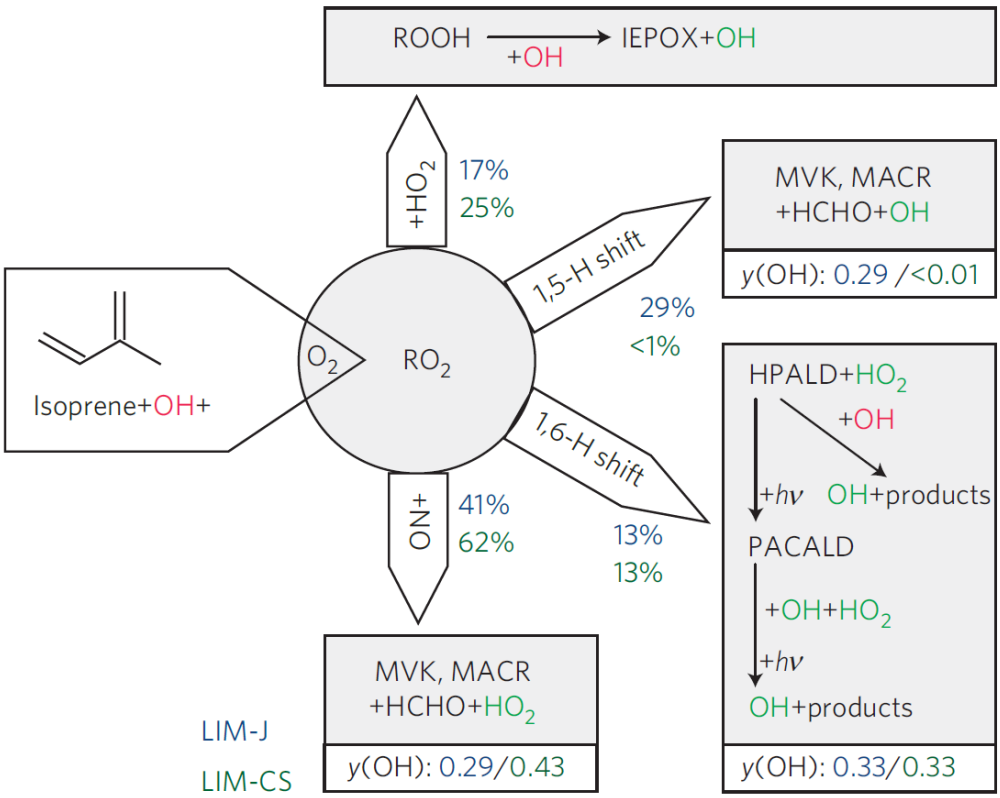

Figure 1.6 Schematic of the atmospheric oxidation of isoprene by OH. Consumed OH is marked in red, whereas the formation of OH and HO_2 is marked in green. The percentage values represent the branching ratio of each channel using two variations of the LIM mechanism (see reference for details). *y*(OH) is the yield of OH from each branch. Figure taken from Fuchs *et al.*, 2013.

Currently, the inclusion of isoprene OH recycling mechanisms into chemical models does not fully reconcile the difference between high measured OH and low modelled OH in forested environments. As all the measurements were made using the FAGE method, another factor that needs considering is instrumental interference, which could contribute to over-measurement of OH (Stone et al., 2012). FAGE interference effects were tested in a forested environment in California by mixing high concentrations of hexafluoro propene (C_3F_6) into the gas just prior to sampling into the instrument. This quickly reacts with any OH present, removing it from the sample before it can be detected, yet large OH signals were still observed. This meant OH was being generated inside the FAGE instrument, possibly by the degradation of RO_2 species (Mao et al., 2012). Figure 1.7 is a measurement of OH in a forested region before and after this interference was accounted for.

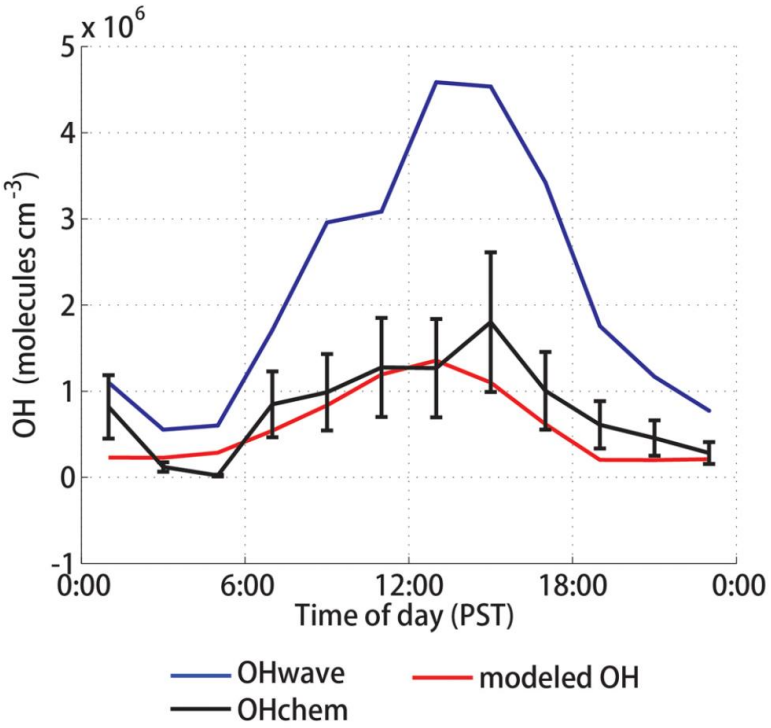

Figure 1.7 Diurnal profile of measured and modelled OH measured by FAGE in 2009 in a forested region. OHwave (blue) is the signal without the C_3F_6 scavenger, and greatly overpredicts the modelled OH (red). Injecting the C_3F_6 to consume ambient OH revealed that the degradation of RO_2 inside the instrument was causing approximately a factor of 4 overestimation. Subtraction of this interference gave OHchem, which agrees with the modelled profile. Mao *et al.*, 2012.

Interferences in FAGE HO_2 measurements also need to be considered, as the required conversion of HO_2 to OH by reaction with NO can also convert RO_2 species, particularly isoprene oxidation products, into OH as well, which are subsequently detected as an interference (Fuchs et al., 2011, Whalley et al., 2013, Lew et al., 2018).

With the importance of the unimolecular chemistry of RO_2 radicals now realised, the formation of highly oxidised molecules (HOMs, or extremely low volatility organic compounds - ELVOCs) through repeated isomerisation and auto-oxidation of RO_2 derived species (Crounse et al., 2013), as shown in Figure 1.8. HOMs have become another large area of research (Burkholder et al., 2017), as they are of low volatility and condense to form secondary organic aerosols (SOA). These reactions are not limited to isoprene, as other important biogenic VOCs, primarily the monoterpenes α-pinene and limonene, also take part (Ehn et al., 2014, Ehn et al., 2017). It is important to understand SOA formation as they

provide surfaces for multiphase chemistry to occur, promote the formation of clouds and particulate matter (Tröstl et al., 2016), scatter and absorb solar radiation and are harmful to health (Hallquist et al., 2009).

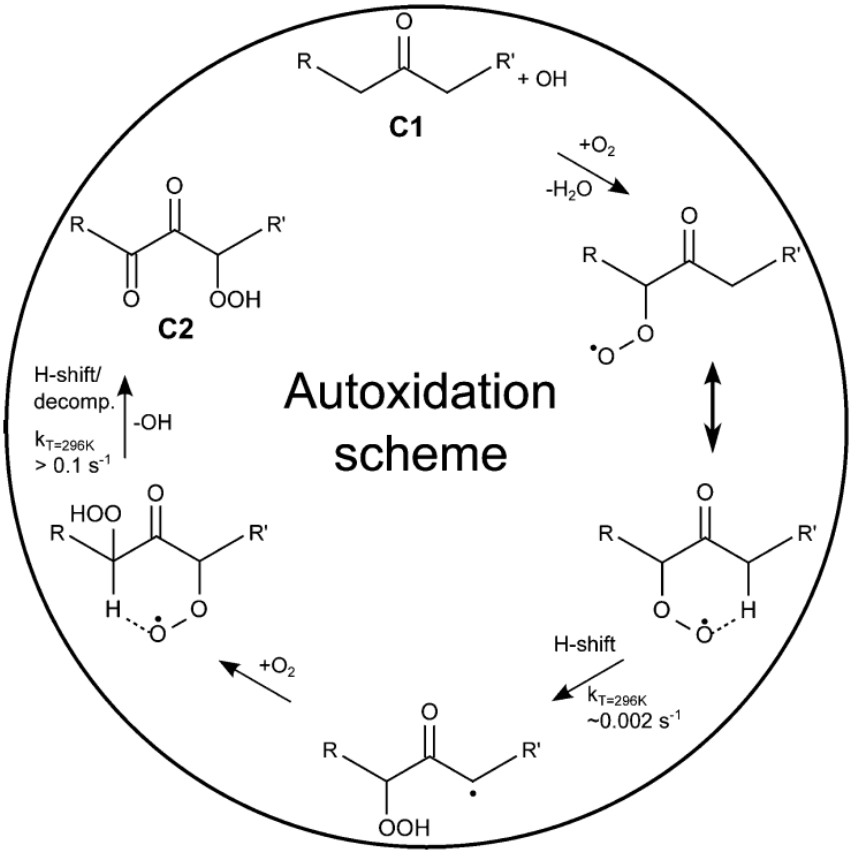

Figure 1.8 General auto-oxidation reaction pathway, where a simple carbonyl compound, C1, is converted to the highly functionalised dicarbonyl hydroperoxide, C2. Further oxidation may occur, and as the Oxygen:Carbon ratio gets higher the molecule becomes less volatile and will eventually condense. Image taken from Crounse *et al.,* 2013.

There is another emerging area of interest in the reaction of RO_2 radicals with OH, which were ignored until relatively recently when it was postulated through theoretical chemical modelling that the reaction may be significant in the marine boundary layer (Archibald et al., 2009). Laboratory experiments later showed that the CH_3O_2 + OH rate coefficient was fast enough to corroborate those predictions (Bossolasco et al., 2014), and that the reaction may be important in very low NO_x environments (Fittschen et al., 2014, Peng et al., 2019). Further study into these RO_2 + OH reactions has begun, including the longer chain RO_2 radicals, $C_2H_5O_2$, $C_3H_7O_2$ and $C_4H_9O_2$ (Faragó et al., 2015, Assaf et al., 2017).

Very recently this RO_2 + OH chemistry has been proposed as an interference source in FAGE instruments to account for a portion of the discrepancies in high biogenic environments discussed above (Fittschen et al., 2019), where longer chain RO_2 radicals (>C_4, such as isoprene-RO_2) form tri-oxide species, ROOOH, which decompose inside FAGE instruments to produce OH and generate spurious signal. The mechanism by which this happens is unknown, and more research is required into this (Fittschen, 2019).

The complex RO_2 chemistry discussed here is not limited to forested areas, as recent measurements in London revealed poor agreement between modelled and measured OH, HO_2 and RO_2 radicals under relatively low NO_x conditions (<1 ppb), particularly when VOC loading increased during warm weather. The discrepancy was attributed to insufficient understanding of RO_2 chemistry and may have been related to unaccounted for auto-oxidation of monoterpenes (Whalley et al., 2018).

The chemical processes discussed in this section show that the chemistry of the troposphere is very complex, and relies on atmospheric measurements, chemical modelling and laboratory studies to elucidate the mechanisms of the various processes occurring. The Master Chemical Mechanism (MCM, version 3.3.1 at the time of writing) is a database of tropospheric chemical reactions, including their mechanisms and rate coefficients, with the aim of being able to explicitly describe the gas phase chemistry of the troposphere, and it is continually updated with new laboratory findings (Jenkin et al., 2015). The International Union of Pure and Applied Chemistry (IUPAC), the National Institute for Standards and Technology (NIST) and the NASA Jet Propulsion Laboratory (JPL) operate databases containing kinetic information on a vast array of chemical processes, and routinely perform reviews to provide recommendations of the most reliable kinetic data to the scientific community. There is now a large body of knowledge surrounding the chemistry of RO_2 radicals, yet the highly complex chemistry and sheer number of different species present in the atmosphere means uncertainties remain in RO_2 kinetics, and in the ability of field measurements to accurately detect and quantify these species (Jenkin et al., 2019b).

1.1.2 The methyl-peroxy radical

Methane (CH_4) tends to be the most abundant VOC in the troposphere with global concentration of approximately 1800 ppb (IPCC, 2013). It is a major greenhouse gas and has a long tropospheric lifetime of 9 – 10 years (Prather et al., 2012, Naik et al., 2013). The large abundance and long lifetime of CH_4 means a large fraction of RO_2 in the troposphere will be the methyl-peroxy radical (CH_3O_2) (Tyndall et al., 2001) formed through the reactions:

$$OH + CH_4 \rightarrow H_2O + CH_3 \quad \textbf{R 1.4}$$

$$CH_3 + O_2 + M \rightarrow CH_3O_2 + M \quad \textbf{R 1.5}$$

$$CH_3O_2 + NO \rightarrow NO_2 + CH_3O \quad \textbf{R 1.6}$$

$$NO_2 + h\nu(< 434\ \text{nm}) \rightarrow NO + O(^3P) \quad \textbf{R 1.7}$$

$$O(^3P) + O_2 + M \rightarrow O_3 + M \quad \textbf{R 1.8}$$

where M is a third body, such as O_2 or N_2. Oxidation of NO to NO_2 by CH_3O_2 provides the route to forming tropospheric O_3 by photolysis of NO_2 at λ<434 nm. Alternatively, in low NO_x environments the CH_3O_2 radical lifetime increases, allowing other reactions to take place. An important reaction is the CH_3O_2 self-reaction which can take place through either of the channels (Orlando and Tyndall, 2012):

$$CH_3O_2 + CH_3O_2 \rightarrow CH_3OH + HCHO + O_2 \quad \textbf{R 1.9a}$$

$$CH_3O_2 + CH_3O_2 \rightarrow 2CH_3O + O_2 \quad \textbf{R 1.9b}$$

The self-reaction has been studied exclusively by time resolved UV absorption measurements of CH_3O_2, using either flash or modulated photolysis of Cl_2 in the presence of CH_4 and O_2 to generate radicals *via* the following scheme:

$$Cl_2 + h\nu \rightarrow 2Cl$$ **R 1.10**

$$CH_4 + Cl_2 \rightarrow CH_3 + HCl$$ **R 1.11**

$$CH_3 + O_2 + M \rightarrow CH_3O_2 + M$$ **R 1.12**

where M is a bath gas. The absorption of UV light, typically 250 nm, was used to monitor the CH_3O_2 concentration with the rate of change of the absorption signal being proportional to the rate of the self-reaction (Cox and Tyndall, 1980, Sander and Watson, 1980, Sander and Watson, 1981, Kurylo and Wallington, 1987, McAdam et al., 1987, Jenkin et al., 1988, Lightfoot et al., 1990, Simon et al., 1990). The absorption signal is related to the CH_3O_2 concentration through its absorption cross section at 250 nm, σ_{250nm}, which is a relatively uncertain, with values between 2.8 and 4.5 × 10^{-18} cm^2 $molecule^{-1}$ used (Atkinson et al., 2006). The UV absorption spectra of RO_2 radicals are broad and featureless, making the UV absorption method unselective and possibly allowing interferences to go unaccounted for during experiments to determine the cross section. The high CH_3O_2 concentrations (10^{13}-10^{15} molecule cm^{-3}) used during measurements of the self-reaction could have caused secondary chemical processes to occur and affect the measured rates, especially considering the self-reaction rate is relatively slow (Tyndall et al., 2001).

Another important process is the cross-reaction with HO_2 which may also proceed through two channels:

$$CH_3O_2 + HO_2 \rightarrow CH_3OOH + O_2$$ **R 1.13**

$$CH_3O_2 + HO_2 \rightarrow HCHO + H_2O + O_2$$ **R 1.14**

The measurement techniques used to study this reaction is more diverse than the self-reaction, incorporating IR absorption techniques and chemical ionisation mass spectrometry (Raventos-Duran et al., 2007) as well as UV absorption. The reported values are overall in good agreement, but the same systematic uncertainty exists in the methods employing UV-absorption (Atkinson et al., 2006).

1.2 Peroxy-radical measurement techniques

The detection of radical species in the atmosphere is difficult owing to their high reactivity, low lifetime and very low concentration. This requires highly sensitive instruments with detection limits in the range 10^5-10^7 molecule cm^{-3} depending in the target radical and environment. The atmospheric measurement of HO_x radicals is well documented, with field campaigns in aircraft (Commane et al., 2010, Ren et al., 2012, Brune et al., 2018) and on the ground (Williams et al., 2011, Edwards et al., 2013, Wolfe et al., 2014, Griffith et al., 2016, Whalley et al., 2018, Kundu et al., 2019) and is dominated by three main methods. Two of them, Fluorescence Assay by Gas Expansion (FAGE) and Differential Optical Absorption Spectroscopy (DOAS), are optical spectroscopic techniques that use lasers to probe air samples (Heard and Pilling, 2003, Hoffmann et al., 2011, Stone et al., 2012). The FAGE method was introduced briefly in section 1.1, and will be discussed in more detail in Chapter 3. The third method, Chemical Ionisation – Mass Spectrometry (CIMS), uses mass spectrometry to indirectly measure OH after chemical conversion to isotopically labelled H_2SO_4 (Tanner et al., 1997, Heard and Pilling, 2003, Stone et al., 2012, Muller et al., 2018, Sanchez et al., 2018). This thesis focuses on the CH_3O_2 radical, the current methods to detect it are indirect methods that require numerous chemical conversion steps, and most are incapable of specific measurements of CH_3O_2, instead they measure the sum of all RO_2 species. These methods are discussed briefly below.

1.2.1 PERCA

The PEroxy Radical Chemical Amplification (PERCA) method is an indirect RO_x ($OH + HO_2 + RO + RO_2$) detection method that titrates RO_x with NO and CO to create a chain reaction cycle that produces NO_2:

$$RO_2 + NO \rightarrow RO + NO_2 \qquad \textbf{R 1.15}$$

$$RO + O_2 \rightarrow R'CHO + HO_2 \qquad \textbf{R 1.16}$$

$$HO_2 + NO \rightarrow OH + NO_2 \qquad \textbf{R 1.17}$$

$$OH + CO + \rightarrow CO_2 + H \qquad \textbf{R 1.18}$$

where M is N_2 or O_2. Reactions R 1.15 - R 1.18 typically cycle 100-150 times, meaning each RO_2 radical can produce hundreds of NO_2 molecules, amplifying its concentration to detectable levels (Cantrell and Stedman, 1982). Originally NO_2 was often detected by luminol chemiluminescence (Cantrell and Stedman, 1982, Clemitshaw et al., 1997) although detection by LIF (Sadanaga et al., 2004, Miyazaki et al., 2010) and cavity enhanced methods have been developed (Kebabian et al., 2008, Liu et al., 2009). The detected NO_2 concentration is then divided by the chain length to calculate RO_2, meaning accurate knowledge of the reaction cycle and conditions are required. Cavity enhanced PERCA offers very good RO_2 detection limits in the range of 1.5×10^7 for 1-minute averaging (Wood and Charest, 2014, Chen et al., 2016).

A modification to the PERCA method has allowed for differentiation between HO_2 and RO_2 radicals through the attachment of a denuder to remove HO_2 radicals from the sampled gas. This method takes advantage of the higher heterogeneous loss rate of HO_2 onto glass beads compared to RO_2 radicals to destroy ~90 % of HO_2 radicals before they reach the PERCA instrument, compared to only 15 % of RO_2 (Miyazaki et al., 2010). Subtraction of the signal with the denuder from the total RO_2 measurement without it allows for speciated quantification of HO_2 and RO_2 radicals. Currently this technique has not seen deployment to the field.

A drawback to PERCA is that its sensitivity is heavily dependent on the relative humidity as water molecules attenuate the reaction chain length, limiting NO_2 production and therefore sensitivity. Water molecules on the walls of the instrument also enhance radical losses and cause the instrument sensitivity to vary (Mihele and Hastie, 1998, Mihele et al., 1999). Additionally, ambient NO_2 is detected in the background, and any O_3 present will react with the NO titrant to produce NO_2, meaning any variations in these molecules will cause the background signal to vary as well (Clemitshaw et al., 1997). In a very recent development, the attachment of a commercially available Nafion (Teflon/perfluoro-3,6-dioxa-4-methyl-7-octene-sulfonic acid copolymer) dryer removes water vapour from sampled gas and supresses the effects of changes in humidity (Yang et al., 2019).

1.2.2 ECHAMP

A variant of the PERCA method has been recently developed where the CO used in the amplifier has been replaced by ethane, christened the Ethane Chemical AMPlifier (ECHAMP) (Wood et al., 2017). This reduces the overall sensitivity of the instrument, but it is far more stable to changes in humidity. An added benefit is that CO is no longer required, making the instrument safer to deploy and transport (although NO is still required). The chemiluminescence detection method of NO_2 has been replaced by a cavity enhanced NO_2 detector, and the instrument achieved detection limits of 4×10^7 molecule cm^{-3} for 15-minute averaging times during a campaign in a forest in Indiana (Kundu et al., 2019). The ECHAMP instrument was recently deployed to three locations in San Antonio, Texas, to measure total RO_2 (Anderson et al., 2019), the resulting diurnal profiles are shown in Figure 1.9 where each data point is a 2-minute average

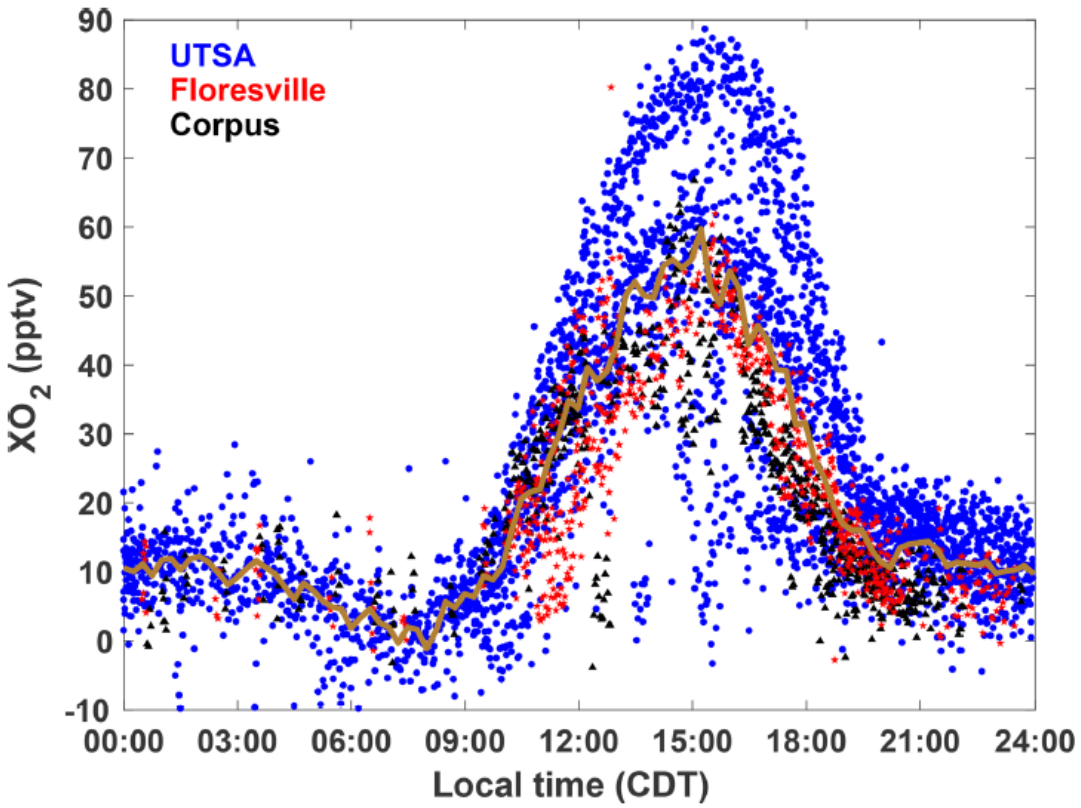

Figure 1.9 The diurnal profile of the total peroxy radical concentration, [XO_2] = [RO_2] + [HO_2], measured using the ECHAMP instrument at three locations in San Antonio, Texas. Maximum concentrations were reached around 3 pm, with the highest recorded values of approximately 80 ppb (10^9 molecule cm^{-3}). The gold line represents the median value of all data for 15-minute time bins. Figure taken from Anderson *et al.*, 2019.

1.2.3 PerCIMS (aka ROXMAS)

PerCIMS is an amplification technique, like PERCA, that converts RO_2 and HO_2 into OH via the same reaction scheme, R 1.15 - R 1.17, but then uses SO_2 to convert the OH to into H_2SO_4 *via*:

$$OH + SO_2 + M \rightarrow HSO_3 + M \qquad \textbf{R 1.19}$$

$$HSO_3 + O_2 \rightarrow HO_2 + SO_3 \qquad \textbf{R 1.20}$$

$$SO_3 + H_2O \rightarrow H_2SO_4 \qquad \textbf{R 1.21}$$

where M is N_2 or O_2. The H_2SO_4 is then detected by CIMS to give the total concentration of HO_2 + RO_2 (Hanke et al., 2002, Edwards et al., 2003, Ren et al., 2003). The high sensitivity offered by CIMS detection and the comparatively low

atmospheric background of H_2SO_4 means that less amplification is required to generate signal. This allows short reaction chain lengths of 10-15 cycles to be used, which limits the impact of interferences and loss processes (Hanke et al., 2002). Differentiation between sampled HO_2 and RO_2 can be made by diluting the sampled gas with either O_2 or N_2 to favour or disfavour R1.16. A low O_2 concentration will disfavour R1.16, meaning the H_2SO_4 that is produced will mostly originate from atmospheric HO_2. At higher O_2 concentration, HO_2 and RO_2 are measured together. PerCIMS can reach detection limits around 2.5×10^7 molecule cm^{-3} with 15 second averaging (Ren et al., 2012) and does not suffer the same water vapour dependency that PERCA does.

1.2.4 RO_xLIF

RO_xLIF is a more recent development (Fuchs et al., 2008, Whalley et al., 2013) that converts RO_x into OH through the same reactions as PERCA but uses Laser Induced Fluorescence (LIF) to detect the OH produced. The high sensitivity offered by OH LIF detection means that no chemical amplification is required. It operates by drawing gas into a low-pressure pre-reactor and injecting high concentrations of NO and CO (0.7 ppm and 0.17 % respectively). The NO converts all RO_2 and HO_2 into OH through reactions R 1.15 - R 1.17, which is then rapidly converted back to HO_2 by the added CO in R 1.18 to prevent loss of OH to the instrument walls, creating an $[HO_2]/[OH]$ equilibrium ratio of approximately 50. The reaction mixture is then drawn into another cell at lower pressure, converted back into OH by reaction with NO, and then detected by LIF at ~308 nm. The instrument can distinguish between HO_2 and RO_2 by switching off the NO injection into the pre-reactor, stopping the conversion reactions R 1.15 and R 1.16, allowing the instrument to measure only HO_2.

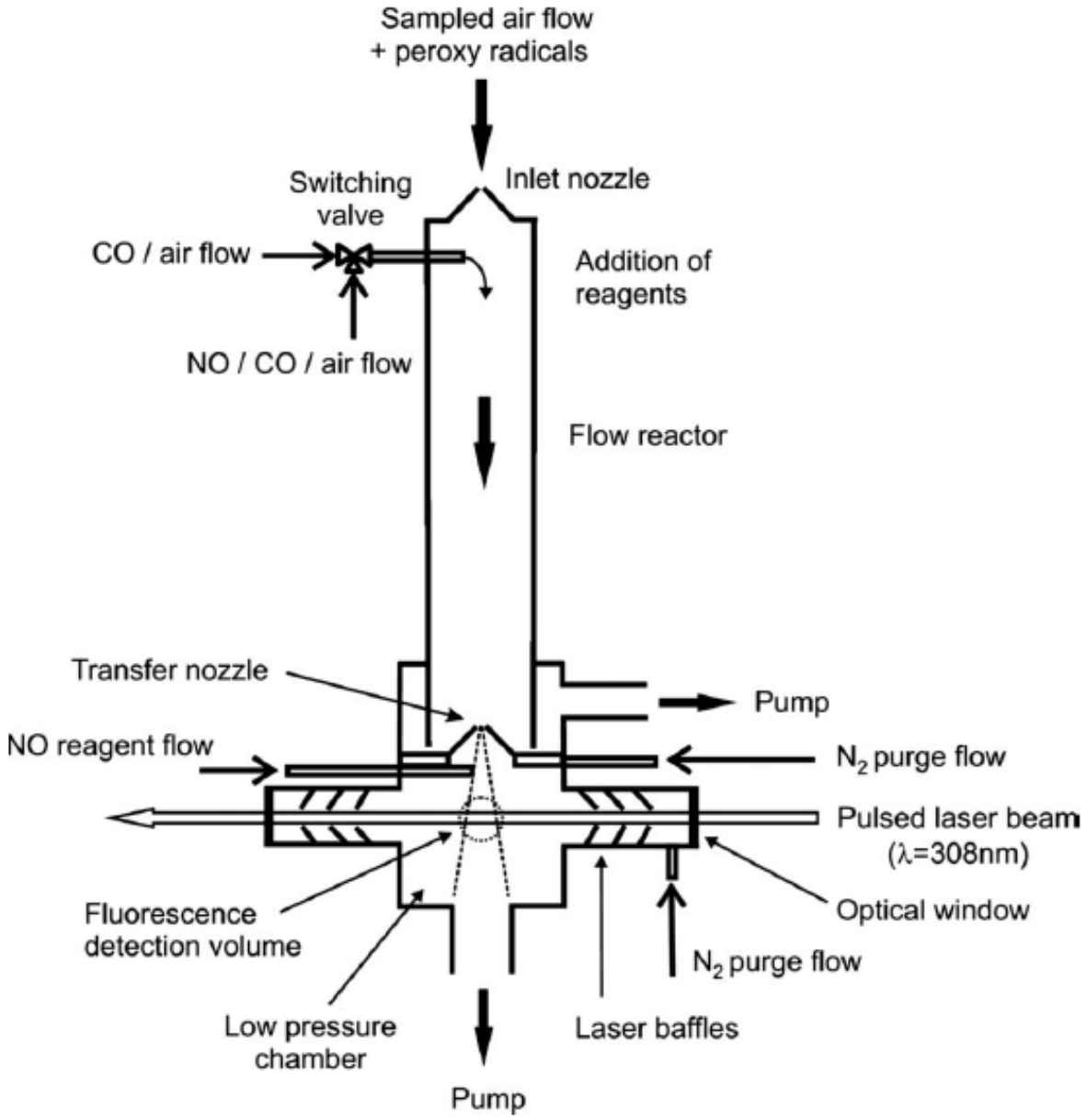

Figure 1.10 Schematic of the RO_xLIF instrument at Forschungszentrum Jülich. Air is drawn into the flow reactor at ~20 Torr where RO_x radicals are converted into HO_2 by the added NO and CO. A portion of the gas is then transferred to the LIF cell at 2.6 Torr, where the HO_2 is converted into OH and detected by LIF at 308 nm. Figure taken from Fuchs et al., 2008

The RO_xLIF method is not susceptible to the same water vapour dependency that hinders PERCA measurements as it does not rely on chemical amplification, and a water layer is unlikely to form on the instrument walls as the pressure is ~40 times lower (Fuchs et al., 2008). Very good detection limits in the region of 10^6 molecule cm^{-3} for 1-minute averaging have been reported (Fuchs et al., 2009).

RO_xLIF has been used in conjunction with a FAGE HO_x instrument to perform semi-specific measurements of RO_2 radicals. To do this $[RO_2]_{total}$ was measured by RO_xLIF, while simultaneous measurements of $[HO_2]$ were made using FAGE, which converts HO_2 to OH by reaction with NO. By injecting higher than usual concentrations of NO into the FAGE cell, this conversion step may also convert alkene, aromatic and long-chain RO_2 radicals, but there is insufficient time to convert the shorter chain (< C_3) RO_2 radicals which have much slower rate coefficients, giving an estimation of $[RO_2]_{long\text{-}chain}$. This is shown in Figure 1.11.

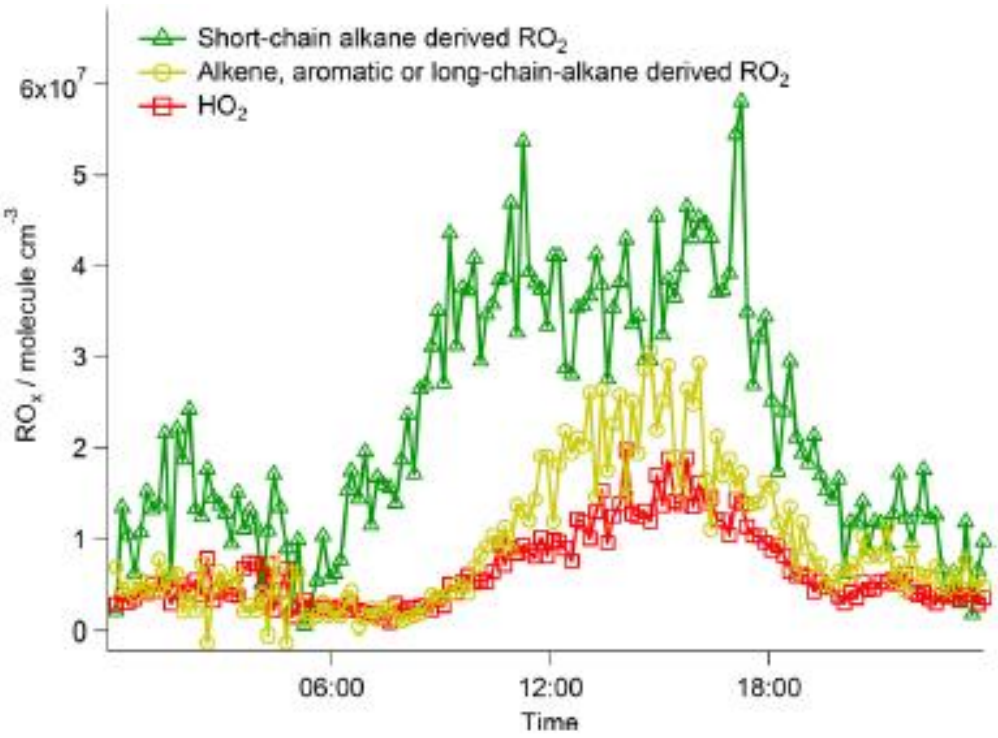

Figure 1.11 Average diurnal profile of HO_2 (measured by FAGE), alkene, aromatic or long chain RO_2 (measured as interference in FAGE) and short chain RO_2 (calculated by subtracting the FAGE interference from the total RO_2 measured by RO_xLIF. Image taken from Whalley *at al.,* 2013.

1.2.5 MIESR

Matrix Isolation and Electron Spin Resonance (MIESR) spectroscopy is the only method that can simultaneously detect HO_2 and CH_3O_2 radicals directly. This is highly advantageous as it almost eliminates interferences. In principle the measurement is absolute, but losses inside the instrument need to be accounted for by calibration (Mihelcic et al., 2003). These advantages come at the cost of convenience and time resolution, as it takes 30 minutes of sampling time to build up a reliable signal and analysis must be performed off-site. The method operates by drawing gas into a vacuum chamber and around a copper cold finger that is cooled to 77 K by liquid nitrogen. Deuterated water is injected into the gas stream and upon freezing onto the cold finger traps radicals in the crystal matrix. The cold finger is then removed off-site for analysis by electron spin resonance (ESR), with the trapped radicals remaining stable for up to two weeks when stored under vacuum at 77 K. ESR analysis can specifically measure HO_2, NO_2, NO_3 and $CH_3C(O)O_2$. With exception of $CH_3C(O)O_2$, which has a prominent ESR feature, the spectra of other RO_2 molecules overlap too much and only the sum of all RO_2 species can be measured (Mihelcic et al., 1985).

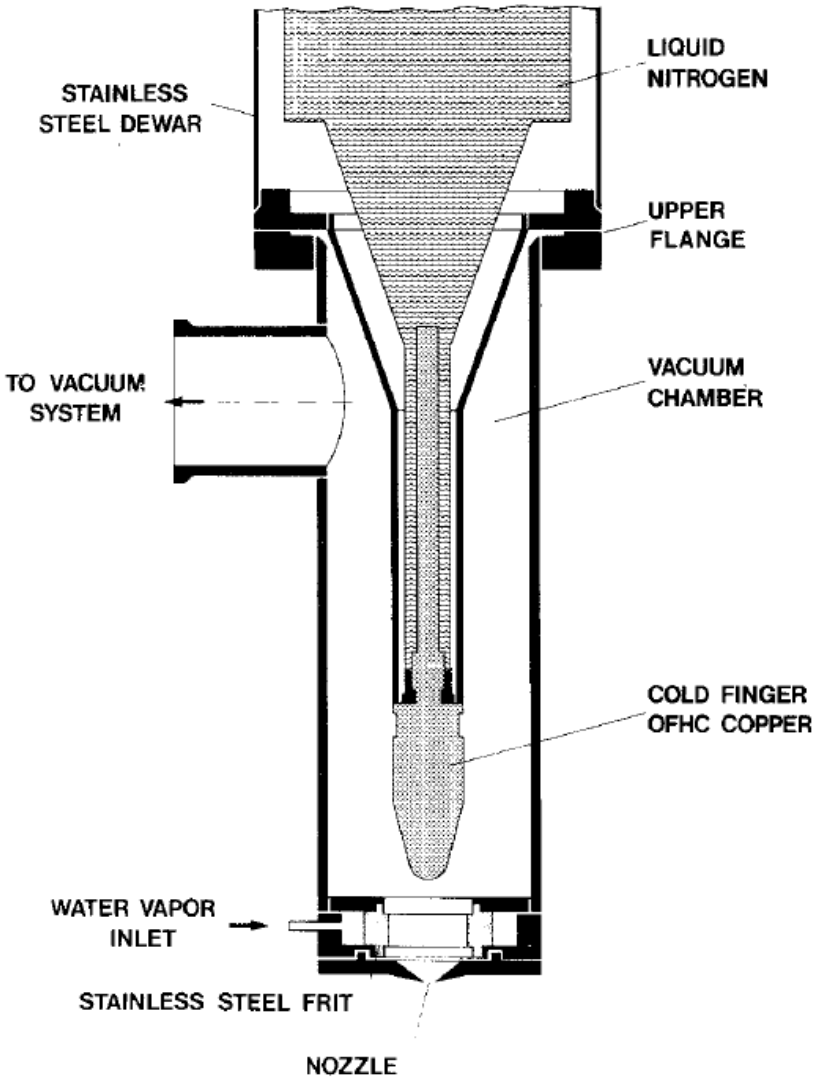

Figure 1.12 Diagram of the MIESR gas sampling apparatus and cold finger. Gas is drawn into the 0.1 mbar vacuum chamber through a 0.2-0.3 mm pinhole. Water vapour, later changed to D_2O, is injected into the gas stream and freezes onto the copper cold finger, trapping radicals in the ice matrix. The cold finger is then removed for offsite ESR analysis. Image taken from Mihelcic *et al.,* 1985.

MIESR has not been used for tropospheric measurements recently, the last use was reported in 2003 with detection limits for RO_2 in the range of 5×10^7 molecule cm^{-3} (Mihelcic et al., 2003). The direct measurements offered by MIESR make it a good benchmark against which other instruments can be tested. An inter-comparison experiment with a RO_xLIF instrument inside the SAPHIR atmospheric simulation chamber is shown in Figure 1.13 (Fuchs et al., 2009).

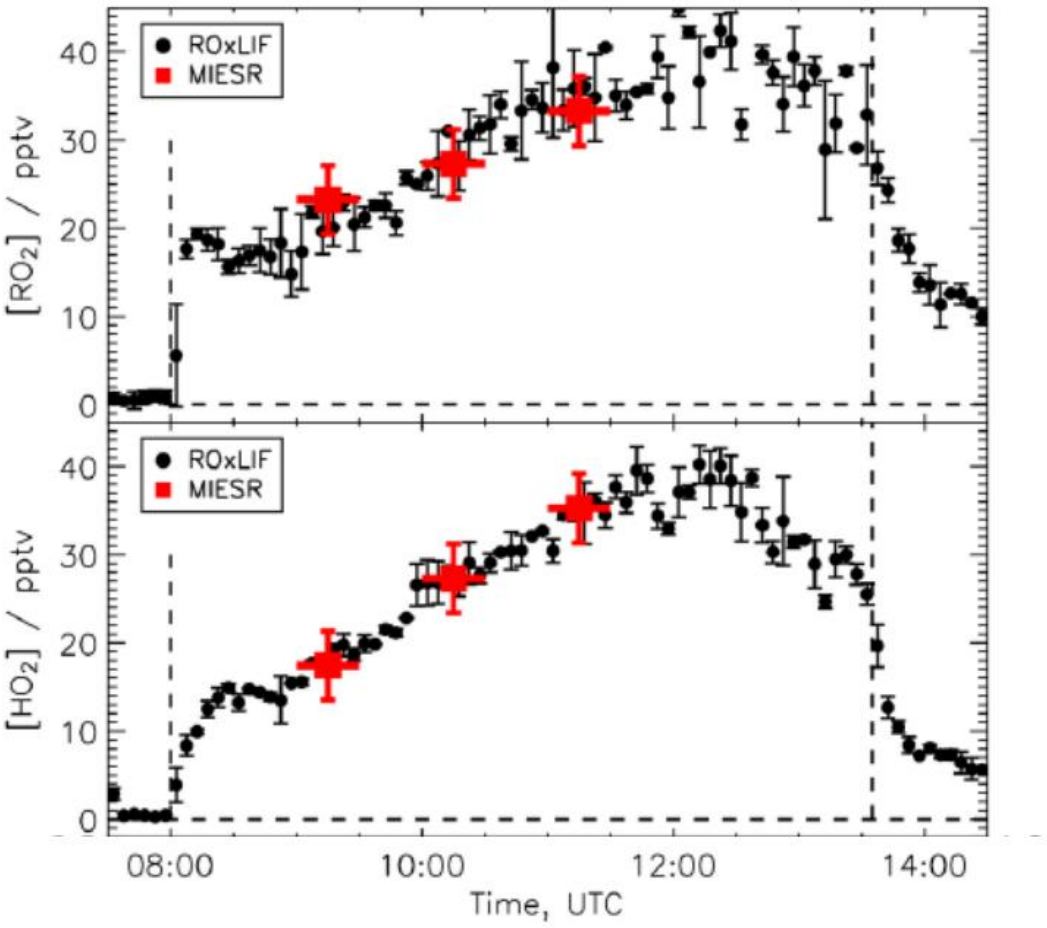

Figure 1.13 Comparison of HO_2 and RO_2 measured by simultaneously by RO_xLIF and MIESR in an atmospheric simulation chamber, SAPHIR. There is very good agreement between the two methods, although the relatively poor time resolution MIESR is evident. Image modified from Fuchs *et al.*, 2009.

1.3 Aims of this thesis

Despite being a key factor in tropospheric chemistry CH_3O_2 radicals are not measured routinely, unlike OH and HO_2. When CH_3O_2 is measured, it is through the techniques highlighted above, most of which are non-specific and may be prone to interference. The MIESR technique, while it was a direct measurement, suffered poor time resolution and is no longer used. Additionally, all the current recommendations for the kinetics of the CH_3O_2 self-reaction employ UV absorption methods which are relatively insensitive, and the typically broad, featureless UV spectra of peroxy radicals make it unselective and could introduce errors into the measurements. Accurate modelling of the troposphere in these environments relies on knowing the kinetic properties of RO_2 radicals, and the ability to detect, identify and quantify them in the troposphere.

Given the complexity of tropospheric chemistry, outlined in section 1.1, there is clearly a need for measurement techniques that can perform speciated measurements of RO_2 radicals with enough sensitivity to be employed in the atmosphere, improving how well radical behaviour can be defined and help constrain highly complex chemical models. The ability to measure a specific RO_2 species in a kinetics experiment would also be highly advantageous, reducing the probability of interference from other species. With a high sensitivity it would be possible to perform kinetic experiments at lower concentrations, thus reducing the effects of secondary chemistry.

As CH_3O_2 is the most abundant organic peroxy radical, this thesis aims to develop a new measurement technique that can perform speciated detection of CH_3O_2 radicals in a field-measurement scenario and use it to measure the kinetic behaviour of CH_3O_2 in an atmospheric simulation chamber, the Highly Instrumented Reactor for Atmospheric Chemistry (HIRAC). The new technique is based upon FAGE method. There is also scope use the instrument to detect higher RO_2 radicals at different LIF excitation wavelengths, such as $C_2H_5O_2$ at 323 nm.

1.3.1 Outline of thesis

HIRAC plays a central role in the development and testing of the new FAGE technique, therefore the details of HIRAC and its instrumentation are described in Chapter 2, including a newly installed Cavity RingDown Spectrometer (CRDS). An already existing FAGE instrument for detecting OH and HO_2 radicals is outlined in Chapter 3, and in Chapter 4 this FAGE instrument is modified to detect CH_3O and CH_3O_2 radicals. Once developed, the new instrument was tested in the HIRAC chamber by comparison against the newly installed CRDS instrument Chapter 5. Finally, the FAGE method was used to study the kinetics of the CH_3O_2 self-reaction and the CH_3O_2 + HO_2 cross-reaction at various temperatures in the HIRAC chamber in Chapter 6.

1.4 References

Anderson, D. C., Payelec, J., Daube, C., Herndon, S. C., Knighton, W. B., Lerner, B. M., Roscioli, J. R., Yacovitch, T. I. & Wood, E. C. 2019. Characterization of ozone production in San Antonio, Texas, using measurements of total peroxy radicals. *Atmospheric Chemistry and Physics,* 19**,** 2845-2860.

Anderson, J. G., Brune, W. H., Lloyd, S. A., Toohey, D. W., Sander, S. P., Starr, W. L., Loewenstein, M. & Podolske, J. R. 1989. Kinetics of O_3 destruction by ClO and BrO within the antarctic vortex - an analysis based on in situ ER-2 data. *Journal of Geophysical Research-Atmospheres,* 94**,** 11480-11520.

Archibald, A. T., Levine, J. G., Abraham, N. L., Cooke, M. C., Edwards, P. M., Heard, D. E., Jenkin, M. E., Karunaharan, A., Pike, R. C., Monks, P. S., Shallcross, D. E., Telford, P. J., Whalley, L. K. & Pyle, J. A. 2011. Impacts of HO_x regeneration and recycling in the oxidation of isoprene: Consequences for the composition of past, present and future atmospheres. *Geophysical Research Letters,* 38**,** Issue 5.

Archibald, A. T., Petit, A. S., Percival, C. J., Harvey, J. N. & Shallcross, D. E. 2009. On the importance of the reaction between OH and RO_2 radicals. *Atmospheric Science Letters,* 10**,** 102-108.

Assaf, E., Tanaka, S., Kajii, Y., Schoemaecker, C. & Fittschen, C. 2017. Rate constants of the reaction of C-2-C-4 peroxy radicals with OH radicals. *Chemical Physics Letters,* 684**,** 245-249.

Atkinson, R., Baulch, D. L., Cox, R. A., Crowley, J. N., Hampson, R. F., Hynes, R. G., Jenkin, M. E., Rossi, M. J. & Troe, J. 2006. Evaluated kinetic and photochemical data for atmospheric chemistry: Volume II - gas phase reactions of organic species. *Atmospheric Chemistry and Physics,* 6**,** 3625-4055.

Bates, K. H. & Jacob, D. J. 2019. A new model mechanism for atmospheric oxidation of isoprene: global effects on oxidants, nitrogen oxides, organic products, and secondary organic aerosol. *Atmospheric Chemistry and Physics,* 19**,** 9613-9640.

Bossolasco, A., Farago, E. P., Schoemaecker, C. & Fittschen, C. 2014. Rate constant of the reaction between CH_3O_2 and OH radicals. *Chemical Physics Letters,* 593**,** 7-13.

Browne, E. C. & Cohen, R. C. 2012. Effects of biogenic nitrate chemistry on the NO_x lifetime in remote continental regions. *Atmospheric Chemistry and Physics,* 12**,** 11917-11932.

Brune, W. H., Ren, X. R., Zhang, L., Mao, J. Q., Miller, D. O., Anderson, B. E., Blake, D. R., Cohen, R. C., Diskin, G. S., Hall, S. R., Hanisco, T. F., Huey, L. G., Nault, B. A., Peisch, J., Pollack, I., Ryerson, T. B., Shingler, T., Sorooshian, A., Ullmann, K., Wisthaler, A. & Wooldridge, P. J. 2018. Atmospheric oxidation in the presence of clouds during the Deep Convective Clouds and Chemistry (DC3) study. *Atmospheric Chemistry and Physics,* 18**,** 14493-14510.

Burkholder, J. B., Abbatt, J. P. D., Barnes, I., Roberts, J. M., Melamed, M. L., Ammann, M., Bertram, A. K., Cappa, C. D., Carlton, A. G., Carpenter, L. J., Crowley, J. N., Dubowski, Y., Georges, C., Heard, D. E., Herrmann, H., Keutsch, F. N., Kroll, J. H., Mcneill, V. F., Ng, N. L., Nizkorodov, S. A., Orlando, J. J., Percival, C. J., Picquet-Varrault, B., Rudich, Y., Seakins, P.

W., Surratt, J. D., Tanimoto, H., Thornton, J. A., Tong, Z., Tyndall, G. S., Wahner, A., Weschler, C. J., Wilson, K. R. & Ziemann, P. J. 2017. The Essential Role for Laboratory Studies in Atmospheric Chemistry. *Environmental Science & Technology,* 51**,** 2519-2528.

Cantrell, C. A. & Stedman, D. H. 1982. A posssible technique for the measurement of atmospheric peroxy-radicals. *Geophysical Research Letters,* 9**,** 846-849.

Chen, Y., Yang, C. Q., Zhao, W. X., Fang, B., Xu, X. Z., Gai, Y. B., Lin, X. X., Chen, W. D. & Zhang, W. J. 2016. Ultra-sensitive measurement of peroxy radicals by chemical amplification broadband cavity-enhanced spectroscopy. *Analyst,* 141**,** 5870-5878.

Clemitshaw, K. C., Carpenter, L. J., Penkett, S. A. & Jenkin, M. E. 1997. A calibrated peroxy radical chemical amplifier for ground-based tropospheric measurements. *Journal of Geophysical Research-Atmospheres,* 102**,** 25405-25416.

Commane, R., Floquet, C. F. A., Ingham, T., Stone, D., Evans, M. J. & Heard, D. E. 2010. Observations of OH and HO_2 radicals over West Africa. *Atmospheric Chemistry and Physics,* 10**,** 8783-8801.

Cox, R. A. & Tyndall, G. S. 1980. Rate constants for the reactions of CH_3O_2 with HO_2, NO and NO_2 using molecular modulation spectrometry. *Journal of the Chemical Society-Faraday Transactions II,* 76**,** 153-163.

Crounse, J. D., Nielsen, L. B., Jorgensen, S., Kjaergaard, H. G. & Wennberg, P. O. 2013. Autoxidation of Organic Compounds in the Atmosphere. *Journal of Physical Chemistry Letters,* 4**,** 3513-3520.

Edwards, G. D., Cantrell, C. A., Stephens, S., Hill, B., Goyea, O., Shetter, R. E., Mauldin, R. L., Kosciuch, E., Tanner, D. J. & Eisele, F. L. 2003. Chemical ionization mass spectrometer instrument for the measurement of tropospheric HO_2 and RO_2. *Analytical Chemistry,* 75**,** 5317-5327.

Edwards, P. M., Evans, M. J., Furneaux, K. L., Hopkins, J., Ingham, T., Jones, C., Lee, J. D., Lewis, A. C., Moller, S. J., Stone, D., Whalley, L. K. & Heard, D. E. 2013. OH reactivity in a South East Asian tropical rainforest during the Oxidant and Particle Photochemical Processes (OP3) project. *Atmospheric Chemistry and Physics,* 13**,** 9497-9514.

Ehn, M., Berndt, T., Wildt, J. & Mentel, T. 2017. Highly Oxygenated Molecules from Atmospheric Autoxidation of Hydrocarbons: A Prominent Challenge for Chemical Kinetics Studies. *International Journal of Chemical Kinetics,* 49**,** 821-831.

Ehn, M., Thornton, J. A., Kleist, E., Sipila, M., Junninen, H., Pullinen, I., Springer, M., Rubach, F., Tillmann, R., Lee, B., Lopez-Hilfiker, F., Andres, S., Acir, I. H., Rissanen, M., Jokinen, T., Schobesberger, S., Kangasluoma, J., Kontkanen, J., Nieminen, T., Kurten, T., Nielsen, L. B., Jorgensen, S., Kjaergaard, H. G., Canagaratna, M., Dal Maso, M., Berndt, T., Petaja, T., Wahner, A., Kerminen, V. M., Kulmala, M., Worsnop, D. R., Wildt, J. & Mentel, T. F. 2014. A large source of low-volatility secondary organic aerosol. *Nature,* 506**,** 476-496.

Faragó, E. P., Schoemaecker, C., Viskolcz, B. & Fittschen, C. 2015. Experimental determination of the rate constant of the reaction between $C_2H_5O_2$ and OH radicals. *Chemical Physics Letters,* 619**,** 196-200.

Farman, J. C., Gardiner, B. G. & Shanklin, J. D. 1985. Large losses of total ozone in Antarctica reveal seasonal ClO_x/NO_x interaction. *Nature,* 315**,** 207-210.

Fittschen, C. 2019. The reaction of peroxy radicals with OH radicals. *Chemical Physics Letters,* 725**,** 102-108.

Fittschen, C., Al Ajami, M., Batut, S., Ferracci, V., Archer-Nicholls, S., Archibald, A. T. & Schoemaecker, C. 2019. ROOOH: a missing piece of the puzzle for OH measurements in low-NO environments? *Atmospheric Chemistry and Physics,* 19**,** 349-362.

Fittschen, C., Whalley, L. K. & Heard, D. E. 2014. The Reaction of CH_3O_2 Radicals with OH Radicals: A Neglected Sink for CH_3O_2 in the Remote Atmosphere. *Environmental Science & Technology,* 48**,** 7700-7701.

Fuchs, H., Bohn, B., Hofzumahaus, A., Holland, F., Lu, K. D., Nehr, S., Rohrer, F. & Wahner, A. 2011. Detection of HO_2 by laser-induced fluorescence: calibration and interferences from RO_2 radicals. *Atmospheric Measurement Techniques,* 4**,** 1209-1225.

Fuchs, H., Brauers, T., Haseler, R., Holland, F., Mihelcic, D., Musgen, P., Rohrer, F., Wegener, R. & Hofzumahaus, A. 2009. Intercomparison of peroxy radical measurements obtained at atmospheric conditions by laser-induced fluorescence and electron spin resonance spectroscopy. *Atmospheric Measurement Techniques,* 2**,** 55-64.

Fuchs, H., Hofzumahaus, A., Rohrer, F., Bohn, B., Brauers, T., Dorn, H. P., Haseler, R., Holland, F., Kaminski, M., Li, X., Lu, K., Nehr, S., Tillmann, R., Wegener, R. & Wahner, A. 2013. Experimental evidence for efficient hydroxyl radical regeneration in isoprene oxidation. *Nature Geoscience,* 6**,** 1023-1026.

Fuchs, H., Holland, F. & Hofzumahaus, A. 2008. Measurement of tropospheric RO_2 and HO_2 radicals by a laser-induced fluorescence instrument. *Review of Scientific Instruments,* 79**,** 12.

Griffith, S. M., Hansen, R. F., Dusanter, S., Michoud, V., Gilman, J. B., Kuster, W. C., Veres, P. R., Graus, M., De Gouw, J. A., Roberts, J., Young, C., Washenfelder, R., Brown, S. S., Thalman, R., Waxman, E., Volkamer, R., Tsai, C., Stutz, J., Flynn, J. H., Grossberg, N., Lefer, B., Alvarez, S. L., Rappenglueck, B., Mielke, L. H., Osthoff, H. D. & Stevens, P. S. 2016. Measurements of hydroxyl and hydroperoxy radicals during CalNex-LA: Model comparisons and radical budgets. *Journal of Geophysical Research-Atmospheres,* 121**,** 4211-4232.

Guenther, A., Karl, T., Harley, P., Wiedinmyer, C., Palmer, P. I. & Geron, C. 2006. Estimates of global terrestrial isoprene emissions using MEGAN (Model of Emissions of Gases and Aerosols from Nature). *Atmospheric Chemistry and Physics,* 6**,** 3181-3210.

Hallquist, M., Wenger, J. C., Baltensperger, U., Rudich, Y., Simpson, D., Claeys, M., Dommen, J., Donahue, N. M., George, C., Goldstein, A. H., Hamilton, J. F., Herrmann, H., Hoffmann, T., Iinuma, Y., Jang, M., Jenkin, M. E., Jimenez, J. L., Kiendler-Scharr, A., Maenhaut, W., Mcfiggans, G., Mentel, T. F., Monod, A., Prevot, A. S. H., Seinfeld, J. H., Surratt, J. D., Szmigielski, R. & Wildt, J. 2009. The formation, properties and impact of secondary organic aerosol: current and emerging issues. *Atmospheric Chemistry and Physics,* 9**,** 5155-5236.

Hanke, M., Uecker, J., Reiner, T. & Arnold, F. 2002. Atmospheric peroxy radicals: ROXMAS, a new mass-spectrometric methodology for speciated measurements of HO_2 and Sigma RO_2 and first results. *International Journal of Mass Spectrometry,* 213**,** 91-99.

Hard, T. M., Obrien, R. J., Chan, C. Y. & Mehrabzadeh, A. A. 1984. Tropospheric free-radical determination by FAGE. *Environmental Science & Technology,* 18**,** 768-777.

Heard, D. E. 2006. Atmospheric field measurements of the hydroxylradical using laser-induced fluorescence spectroscopy. *Annual Review of Physical Chemistry.* Palo Alto: Annual Reviews.

Heard, D. E. & Pilling, M. J. 2003. Measurement of OH and HO_2 in the troposphere. *Chemical Reviews,* 103**,** 5163-5198.

Hoffmann, T., Huang, R. J. & Kalberer, M. 2011. Atmospheric Analytical Chemistry. *Analytical Chemistry,* 83**,** 4649-4664.

Hofzumahaus, A., Rohrer, F., Lu, K. D., Bohn, B., Brauers, T., Chang, C. C., Fuchs, H., Holland, F., Kita, K., Kondo, Y., Li, X., Lou, S. R., Shao, M., Zeng, L. M., Wahner, A. & Zhang, Y. H. 2009. Amplified Trace Gas Removal in the Troposphere. *Science,* 324**,** 1702-1704.

IPCC. 2013. *Climate Change 2013: The Physical Science Basis, Contribution of Working Group 1 to the Fifth Assessment Report of the Intergovernmental Panel on Climate Change* [Online]. Cambridge, UK: Cambridge University Press. [Accessed 25th September 2019].

Jenkin, M. E., Cox, R. A., Hayman, G. D. & Whyte, L. J. 1988. Kinetic study of the reactions CH_3O_2 + CH_3O_2 and CH_3O_2 + HO_2 using molecular modulation spectroscopy. *Journal of the Chemical Society-Faraday Transactions Ii,* 84**,** 913-930.

Jenkin, M. E., Khan, M. A. H., Shallcross, D. E., Bergstrom, R., Simpson, D., Murphy, K. L. C. & Rickard, A. R. 2019a. The CRI v2.2 reduced degradation scheme for isoprene. *Atmospheric Environment,* 212**,** 172-182.

Jenkin, M. E., Valorso, R., Aumont, B. & Rickard, A. R. 2019b. Estimation of rate coefficients and branching ratios for reactions of organic peroxy radicals for use in automated mechanism construction. *Atmospheric Chemistry and Physics,* 19**,** 7691-7717.

Jenkin, M. E., Young, J. C. & Rickard, A. R. 2015. The MCM v3.3.1 degradation scheme for isoprene. *Atmospheric Chemistry and Physics,* 15**,** 11433-11459.

Kebabian, P. L., Wood, E. C., Herndon, S. C. & Freedman, A. 2008. A practical alternative to chemiluminescence-based detection of nitrogen dioxide: Cavity attenuated phase shift spectroscopy. *Environmental Science & Technology,* 42**,** 6040-6045.

Kundu, S., Deming, B. L., Lew, M. M., Bottorff, B. P., Rickly, P., Stevens, P. S., Dusanter, S., Sklaveniti, S., Leonardis, T., Locoge, N. & Wood, E. C. 2019. Peroxy radical measurements by ethane - nitric oxide chemical amplification and laser-induced fluorescence during the IRRONIC field campaign in a forest in Indiana. *Atmospheric Chemistry and Physics,* 19**,** 9563-9579.

Kurylo, M. J. & Wallington, T. J. 1987. The temperature dependence of the rate constant for the gas-phase disproportionation reaction of CH_3O_2 radicals. *Chemical Physics Letters,* 138**,** 543-547.

Lelieveld, J., Butler, T. M., Crowley, J. N., Dillon, T. J., Fischer, H., Ganzeveld, L., Harder, H., Lawrence, M. G., Martinez, M., Taraborrelli, D. & Williams, J. 2008. Atmospheric oxidation capacity sustained by a tropical forest. *Nature,* 452**,** 737-740.

Levy, H. 1971. Normal Atmosphere - Large radical and formaldehyde concentrations predicted. *Science,* 173**,** 141-&.

Lew, M. M., Dusanter, S. & Stevens, P. S. 2018. Measurement of interferences associated with the detection of the hydroperoxy radical in the atmosphere using laser-induced fluorescence. *Atmospheric Measurement Techniques,* 11**,** 95-109.

Lightfoot, P. D., Lesclaux, R. & Veyret, B. 1990. Flash photolysis study of the CH_3O_2 + CH_3O_2 reaction - rate constants and branching ratios from 248 to 573 K. *Journal of Physical Chemistry,* 94**,** 700-707.

Liu, Y. D., Morales-Cueto, R., Hargrove, J., Medina, D. & Zhang, J. S. 2009. Measurements of Peroxy Radicals Using Chemical Amplification-Cavity Ringdown Spectroscopy. *Environmental Science & Technology,* 43**,** 7791-7796.

Lu, K. D., Rohrer, F., Holland, F., Fuchs, H., Bohn, B., Brauers, T., Chang, C. C., Haseler, R., Hu, M., Kita, K., Kondo, Y., Li, X., Lou, S. R., Nehr, S., Shao, M., Zeng, L. M., Wahner, A., Zhang, Y. H. & Hofzumahaus, A. 2012. Observation and modelling of OH and HO_2 concentrations in the Pearl River Delta 2006: a missing OH source in a VOC rich atmosphere. *Atmospheric Chemistry and Physics,* 12**,** 1541-1569.

Mao, J., Ren, X., Zhang, L., Van Duin, D. M., Cohen, R. C., Park, J. H., Goldstein, A. H., Paulot, F., Beaver, M. R., Crounse, J. D., Wennberg, P. O., Digangi, J. P., Henry, S. B., Keutsch, F. N., Park, C., Schade, G. W., Wolfe, G. M., Thornton, J. A. & Brune, W. H. 2012. Insights into hydroxyl measurements and atmospheric oxidation in a California forest. *Atmospheric Chemistry and Physics,* 12**,** 8009-8020.

Mcadam, K., Veyret, B. & Lesclaux, R. 1987. UV absorption spectra of HO_2 and CH_3O_2 radicals, and the kinetics of their mutual reactions at 298 K. *Chemical Physics Letters,* 133**,** 39-44.

Mihelcic, D., Holland, F., Hofzumahaus, A., Hoppe, L., Konrad, S., Musgen, P., Patz, H. W., Schafer, H. J., Schmitz, T., Volz-Thomas, A., Bachmann, K., Schlomski, S., Platt, U., Geyer, A., Alicke, B. & Moortgat, G. K. 2003. Peroxy radicals during BERLIOZ at Pabstthum: Measurements, radical budgets and ozone production. *Journal of Geophysical Research-Atmospheres,* 108**,** 17.

Mihelcic, D., Musgen, P. & Ehhalt, D. H. 1985. An improved method of measuring tropspheric NO_2 and RO_2 by matrix-isolation and electron-spin-resonance. *Journal of Atmospheric Chemistry,* 3**,** 341-361.

Mihele, C. M. & Hastie, D. R. 1998. The sensitivity of the radical amplifier to ambient water vapour. *Geophysical Research Letters,* 25**,** 1911-1913.

Mihele, C. M., Mozurkewich, M. & Hastie, D. R. 1999. Radical loss in a chain reaction of CO and NO in the presence of water: Implications for the radical amplifier and atmospheric chemistry. *International Journal of Chemical Kinetics,* 31**,** 145-152.

Miyazaki, K., Parker, A. E., Fittschen, C., Monks, P. S. & Kajii, Y. 2010. A new technique for the selective measurement of atmospheric peroxy radical concentrations of HO_2 and RO_2 using a denuding method. *Atmospheric Measurement Techniques,* 3**,** 1547-1554.

Muller, J. B. A., Elste, T., Plass-Dulmer, C., Stange, G., Holla, R., Claude, A., Englert, J., Gilge, S. & Kubistin, D. 2018. A novel semi-direct method to

measure OH reactivity by chemical ionization mass spectrometry (CIMS). *Atmospheric Measurement Techniques,* 11**,** 4413-4433.

Muller, J. F., Stavrakou, T. & Peeters, J. 2019. Chemistry and deposition in the Model of Atmospheric composition at Global and Regional scales using Inversion Techniques for Trace gas Emissions (MAGRITTE v1.1) - Part 1: Chemical mechanism. *Geoscientific Model Development,* 12**,** 2307-2356.

Naik, V., Voulgarakis, A., Fiore, A. M., Horowitz, L. W., Lamarque, J. F., Lin, M., Prather, M. J., Young, P. J., Bergmann, D., Cameron-Smith, P. J., Cionni, I., Collins, W. J., Dalsoren, S. B., Doherty, R., Eyring, V., Faluvegi, G., Folberth, G. A., Josse, B., Lee, Y. H., Mackenzie, I. A., Nagashima, T., Van Noije, T. P. C., Plummer, D. A., Righi, M., Rumbold, S. T., Skeie, R., Shindell, D. T., Stevenson, D. S., Strode, S., Sudo, K., Szopa, S. & Zeng, G. 2013. Preindustrial to present-day changes in tropospheric hydroxyl radical and methane lifetime from the Atmospheric Chemistry and Climate Model Intercomparison Project (ACCMIP). *Atmospheric Chemistry and Physics,* 13**,** 5277-5298.

Orlando, J. J. & Tyndall, G. S. 2012. Laboratory studies of organic peroxy radical chemistry: an overview with emphasis on recent issues of atmospheric significance. *Chemical Society Reviews,* 41**,** 6294-6317.

Peeters, J. & Müller, J. F. 2010. HO_x radical regeneration in isoprene oxidation via peroxy radical isomerisations. II: experimental evidence and global impact. *Physical Chemistry Chemical Physics,* 12**,** 14227-14235.

Peeters, J., Müller, J. F., Stavrakou, T. & Nguyen, V. S. 2014. Hydroxyl Radical Recycling in Isoprene Oxidation Driven by Hydrogen Bonding and Hydrogen Tunneling: The Upgraded LIM1 Mechanism. *Journal of Physical Chemistry A,* 118**,** 8625-8643.

Peeters, J., Nguyen, T. L. & Vereecken, L. 2009. HO_x radical regeneration in the oxidation of isoprene. *Physical Chemistry Chemical Physics,* 11**,** 5935-5939.

Peng, Z., Lee-Taylor, J., Orlando, J. J., Tyndall, G. S. & Jimenez, J. L. 2019. Organic peroxy radical chemistry in oxidation flow reactors and environmental chambers and their atmospheric relevance. *Atmospheric Chemistry and Physics,* 19**,** 813-834.

PHE. 2019. *Review of interventions to improve outdoor air quality and public health* [Online]. PHE publications. [Accessed 25th September 2019]

Prather, M. J., Holmes, C. D. & Hsu, J. 2012. Reactive greenhouse gas scenarios: Systematic exploration of uncertainties and the role of atmospheric chemistry. *Geophysical Research Letters,* 39**,** 5.

Raventos-Duran, M. T., Mcgillen, M., Percival, C. J., Hamer, P. D. & Shallcross, D. E. 2007. Kinetics of the CH_3O_2 + HO_2 reaction: A temperature and pressure dependence study using chemical ionization mass spectrometry. *International Journal of Chemical Kinetics,* 39**,** 571-579.

Ren, X., Mao, J., Brune, W. H., Cantrell, C. A., Mauldin, R. L., Hornbrook, R. S., Kosciuch, E., Olson, J. R., Crawford, J. H., Chen, G. & Singh, H. B. 2012. Airborne intercomparison of HO_x measurements using laser-induced fluorescence and chemical ionization mass spectrometry during ARCTAS. *Atmospheric Measurement Techniques,* 5**,** 2025-2037.

Ren, X. R., Edwards, G. D., Cantrell, C. A., Lesher, R. L., Metcalf, A. R., Shirley, T. & Brune, W. H. 2003. Intercomparison of peroxy radical measurements at a rural site using laser-induced fluorescence and Peroxy Radical

Chemical Ionization Mass Spectrometer (PerCIMS) techniques. *Journal of Geophysical Research-Atmospheres,* 108**,** 9.

Sadanaga, Y., Matsumoto, J., Sakurai, K., Isozaki, R., Kato, S., Nomaguchi, T., Bandow, H. & Kajii, Y. 2004. Development of a measurement system of peroxy radicals using a chemical amplification/laser-induced fluorescence technique. *Review of Scientific Instruments,* 75**,** 864-872.

Sanchez, D., Jeong, D., Seco, R., Wrangham, I., Park, J. H., Brune, W. H., Koss, A., Gilman, J., De Gouw, J., Misztal, P., Goldstein, A., Baumann, K., Wennberg, P. O., Keutsch, F. N., Guenther, A. & Kim, S. 2018. Intercomparison of OH and OH reactivity measurements in a high isoprene and low NO environment during the Southern Oxidant and Aerosol Study (SOAS). *Atmospheric Environment,* 174**,** 227-236.

Sander, S. P. & Watson, R. T. 1980. Kinetics studies of the reactions of CH_3O_2 with NO, NO_2 and CH_3O_2 at 298 K. *Journal of Physical Chemistry,* 84**,** 1664-1674.

Sander, S. P. & Watson, R. T. 1981. Temperature dependence of the self-reaction of CH_3O_2 radicals. *Journal of Physical Chemistry,* 85**,** 2960-2964.

Simon, F. G., Schneider, W. & Moortgat, G. K. 1990. UV absorption spectrum of the methylperoxy radical and the kinetics of its disproportionation reaction at 300 K. *International Journal of Chemical Kinetics,* 22**,** 791-812.

Solomon, S., Ivy, D. J., Kinnison, D., Mills, M. J., Neely, R. R. & Schmidt, A. 2016. Emergence of healing in the Antarctic ozone layer. *Science,* 353**,** 269-274.

Stone, D., Whalley, L. K. & Heard, D. E. 2012. Tropospheric OH and HO_2 radicals: field measurements and model comparisons. *Chemical Society Reviews,* 41**,** 6348-6404.

Tan, Z. F., Fuchs, H., Lu, K. D., Hofzumahaus, A., Bohn, B., Broch, S., Dong, H. B., Gomm, S., Haseler, R., He, L. Y., Holland, F., Li, X., Liu, Y., Lu, S. H., Rohrer, F., Shao, M., Wang, B. L., Wang, M., Wu, Y. S., Zeng, L. M., Zhang, Y. S., Wahner, A. & Zhang, Y. H. 2017. Radical chemistry at a rural site (Wangdu) in the North China Plain: observation and model calculations of OH, HO_2 and RO_2 radicals. *Atmospheric Chemistry and Physics,* 17**,** 663-690.

Tanner, D. J., Jefferson, A. & Eisele, F. L. 1997. Selected ion chemical ionization mass spectrometric measurement of OH. *Journal of Geophysical Research-Atmospheres,* 102**,** 6415-6425.

Teng, A. P., Crounse, J. D. & Wennberg, P. O. 2017. Isoprene Peroxy Radical Dynamics. *Journal of the American Chemical Society,* 139**,** 5367-5377.

Tröstl, J., Chuang, W. K., Gordon, H., Heinritzi, M., Yan, C., Molteni, U., Ahlm, L., Frege, C., Bianchi, F., Wagner, R., Simon, M., Lehtipalo, K., Williamson, C., Craven, J. S., Duplissy, J., Adamov, A., Almeida, J., Bernhammer, A. K., Breitenlechner, M., Brilke, S., Dias, A., Ehrhart, S., Flagan, R. C., Franchin, A., Fuchs, C., Guida, R., Gysel, M., Hansel, A., Hoyle, C. R., Jokinen, T., Junninen, H., Kangasluoma, J., Keskinen, H., Kim, J., Krapf, M., Kurten, A., Laaksonen, A., Lawler, M., Leiminger, M., Mathot, S., Mohler, O., Nieminen, T., Onnela, A., Petaja, T., Piel, F. M., Miettinen, P., Rissanen, M. P., Rondo, L., Sarnela, N., Schobesberger, S., Sengupta, K., Sipila, M., Smith, J. N., Steiner, G., Tome, A., Virtanen, A., Wagner, A. C., Weingartner, E., Wimmer, D., Winkler, P. M., Ye, P. L., Carslaw, K. S., Curtius, J., Dommen, J., Kirkby, J., Kulmala, M., Riipinen, I., Worsnop, D. R., Donahue, N. M. & Baltensperger, U. 2016. The role of low-volatility

organic compounds in initial particle growth in the atmosphere. *Nature,* 533**,** 527-547.

Tyndall, G. S., Cox, R. A., Granier, C., Lesclaux, R., Moortgat, G. K., Pilling, M. J., Ravishankara, A. R. & Wallington, T. J. 2001. Atmospheric chemistry of small organic peroxy radicals. *Journal of Geophysical Research-Atmospheres,* 106**,** 12157-12182.

Wennberg, P. O., Bates, K. H., Crounse, J. D., Dodson, L. G., Mcvay, R. C., Mertens, L. A., Nguyen, T. B., Praske, E., Schwantes, R. H., Smarte, M. D., St Clair, J. M., Teng, A. P., Zhang, X. & Seinfeld, J. H. 2018. Gas-Phase Reactions of Isoprene and Its Major Oxidation Products. *Chemical Reviews,* 118**,** 3337-3390.

Whalley, L. K., Blitz, M. A., Desservettaz, M., Seakins, P. W. & Heard, D. E. 2013. Reporting the sensitivity of laser-induced fluorescence instruments used for HO_2 detection to an interference from RO_2 radicals and introducing a novel approach that enables HO_2 and certain RO_2 types to be selectively measured. *Atmospheric Measurement Techniques,* 6**,** 3425-3440.

Whalley, L. K., Edwards, P. M., Furneaux, K. L., Goddard, A., Ingham, T., Evans, M. J., Stone, D., Hopkins, J. R., Jones, C. E., Karunaharan, A., Lee, J. D., Lewis, A. C., Monks, P. S., Moller, S. J. & Heard, D. E. 2011. Quantifying the magnitude of a missing hydroxyl radical source in a tropical rainforest. *Atmospheric Chemistry and Physics,* 11**,** 7223-7233.

Whalley, L. K., Stone, D., Dunmore, R., Hamilton, J., Hopkins, J. R., Lee, J. D., Lewis, A. C., Williams, P., Kleffmann, J., Laufs, S., Woodward-Massey, R. & Heard, D. E. 2018. Understanding in situ ozone production in the summertime through radical observations and modelling studies during the Clean air for London project (ClearfLo). *Atmospheric Chemistry and Physics,* 18**,** 2547-2571.

Williams, J., Crowley, J., Fischer, H., Harder, H., Martinez, M., Petaja, T., Rinne, J., Back, J., Boy, M., Dal Maso, M., Hakala, J., Kajos, M., Keronen, P., Rantala, P., Aalto, J., Aaltonen, H., Paatero, J., Vesala, T., Hakola, H., Levula, J., Pohja, T., Herrmann, F., Auld, J., Mesarchaki, E., Song, W., Yassaa, N., Nolscher, A., Johnson, A. M., Custer, T., Sinha, V., Thieser, J., Pouvesle, N., Taraborrelli, D., Tang, M. J., Bozem, H., Hosaynali-Beygi, Z., Axinte, R., Oswald, R., Novelli, A., Kubistin, D., Hens, K., Javed, U., Trawny, K., Breitenberger, C., Hidalgo, P. J., Ebben, C. J., Geiger, F. M., Corrigan, A. L., Russell, L. M., Ouwersloot, H. G., De Arellano, J. V. G., Ganzeveld, L., Vogel, A., Beck, M., Bayerle, A., Kampf, C. J., Bertelmann, M., Kollner, F., Hoffmann, T., Valverde, J., Gonzalez, D., Riekkola, M. L., Kulmala, M. & Lelieveld, J. 2011. The summertime Boreal forest field measurement intensive (HUMPPA-COPEC-2010): an overview of meteorological and chemical influences. *Atmospheric Chemistry and Physics,* 11**,** 10599-10618.

WMO. 2014. *World Meteorological Organisation: Scientific assessment of ozone depletion: 2014* [Online]. Geneva, Switzerland. [Accessed 25th September 2019].

Wolfe, G. M., Cantrell, C., Kim, S., Mauldin, R. L., Karl, T., Harley, P., Turnipseed, A., Zheng, W., Flocke, F., Apel, E. C., Hornbrook, R. S., Hall, S. R., Ullmann, K., Henry, S. B., Digangi, J. P., Boyle, E. S., Kaser, L., Schnitzhofer, R., Hansel, A., Graus, M., Nakashima, Y., Kajii, Y., Guenther, A. & Keutsch, F. N. 2014. Missing peroxy radical sources within

a summertime ponderosa pine forest. *Atmospheric Chemistry and Physics,* 14**,** 4715-4732.

Wood, E. C. & Charest, J. R. 2014. Chemical Amplification - Cavity Attenuated Phase Shift Spectroscopy Measurements of Atmospheric Peroxy Radicals. *Analytical Chemistry,* 86**,** 10266-10273.

Wood, E. C., Deming, B. L. & Kundu, S. 2017. Ethane-Based Chemical Amplification Measurement Technique for Atmospheric Peroxy Radicals. *Environmental Science & Technology Letters,* 4**,** 15-19.

Yang, C. Q., Zhao, W. X., Fang, B., Yu, H., Xu, X. Z., Zhang, Y., Gai, Y. B., Zhang, W. J., Chen, W. D. & Fittschen, C. 2019. Improved Chemical Amplification Instrument by Using a Nafion Dryer as an Amplification Reactor for Quantifying Atmospheric Peroxy Radicals under Ambient Conditions. *Analytical Chemistry,* 91**,** 776-779.

Chapter 2. HIRAC – Atmospheric simulation chamber, design and instrumentation

In this chapter the Highly Instrumented Reactor for Atmospheric Chemistry (HIRAC) is introduced. It is an atmospheric simulation chamber that is useful for studying chemical reactions and earns its name from the multitude of measurement instruments connected to it, and it plays a central role in the experiments performed as part of this thesis. A newly constructed Cavity RingDown Spectrometer (CRDS) for the detection of HO_2 and CH_3O_2 radicals is also described here, as it is integral to the HIRAC chamber and is used extensively in Chapter 5.

Chambers like HIRAC enable the complex chemistry of the atmosphere to be broken down and simplified by isolating key species and reactions for individual study. While useful, simulation chambers are imperfect as the chamber walls inevitably interfere with the chemical system they contain, whether by heterogeneous loss or by harbouring contaminants from previous work. These effects can be mitigated through careful selection of construction materials and making the chamber as large as possible to achieve small surface area / volume ratios, but there is always a compromise. The SAPHIR chamber (Simulation of Atmospheric PHotochemistry In a large Reaction chamber) at Forschungszentrum Jülich is a notable example; it is a very large double-walled Teflon bag, ~270 m^3 in volume with a surface/volume ratio of ~1 m^{-1} (Karl et al., 2004). The Teflon construction allows actinic solar radiation to pass into the chamber and initiate photochemistry, closely simulating real-world processes. The SAPHIR chamber sees regular use for both chemical experiments and instrument intercomparisons (Fuchs et al., 2017, Novelli et al., 2018, Albrecht et al., 2019), however it is restricted to ambient temperature and pressures, and is at the mercy of the weather.

The HIRAC chamber is much smaller, with a larger surface area to volume ratio and is constructed from stainless steel rather than relatively inert Teflon. However, HIRAC is faster and easier to use, can operate over a wide temperature and pressure range and is well suited for the development and testing of new instruments. It is also capable of making accurate kinetic measurements when

wall losses are accounted for (Glowacki et al., 2007a, Winiberg et al., 2015, Winiberg et al., 2016, Bejan et al., 2018).

2.1 Construction

The HIRAC chamber is a 2 m long cylinder with an internal diameter of 1.2 m, giving a volume of ~2.25 m^3 and a surface/volume ratio of ~5.8 m^{-1} when internal components are considered (Glowacki et al., 2007a). The chamber is constructed from stainless steel which allows the chamber to be evacuated to a typical minimum pressure of ~0.5 mbar by a rotary backed roots blower pump (Leybold Trivac D40B and Ruvac WAU251) with a charcoal catchpot (BOC Edwards ITC300) mounted on the inlet to prevent back-diffusion of pump oil into the chamber. The metal walls also facilitate temperature control through a series of pipes that are welded onto the outer skin of the chamber. A thermostat unit (Huber Unistat 390W) pumps a thermofluid (Huber DW-Therm) through the pipes and allows the chamber to be heated or cooled between -20 and +80 ˚C (253 – 353 K). The chamber is wrapped in neoprene insulation to aid temperature control and to prevent excessive condensation/ice formation on the outer surfaces. This temperature and pressure control allow simulation of atmospheres from the troposphere to the stratosphere, and from tropical forests to polar regions. For this work detailed in this thesis the chamber was operated at pressures ranging from ~100 mbar up to 1000 mbar, and temperatures from 263 to 343 K.

Gas inside the chamber is mixed by four aluminium fans, two mounted at each end, driven by variable speed DC motors mounted on the outside of the chamber. Torque is transmitted to the fans *via* a ferro-fluidic feedthrough (Ferrotec SS-250-SLBD) and flexible driveshaft to minimise vibrations transferred to the chamber. The mixing efficiency of these fans has been determined in previous work by measuring dilute NO from several combinations of injection and sampling points on the chamber and found mixing times of approximately 1 minute (Glowacki et al., 2007a).

2.2 Photolysis lamps

A key feature of the HIRAC chamber is eight UV lamps, which are used in nearly all experiments detailed in this thesis to initiate chemical reactions and to generate radicals. The UV tube lamps are placed in eight 2300 x 50 mm quartz tubes that are mounted radially in the chamber approximately ~400 mm from the centre. The ends of the tubes protrude through the end plates of chamber and are flushed with nitrogen to prevent ozone production and help cool the lamps during operation. Each tube houses a single UV tube lamp, which can be swapped depending on the wavelength required, with lamps centred around 254, 300 and 360 nm available (Phillips: G55T8/OH 7G, TL 40W/12 RS SLV and TL-D 36W/BLB respectively). The spectral output of these lamps has been measured by Dr. F. A. F. Winiberg (Winiberg, 2015), whose results are shown in Figure 2.1. For most of the work shown in this thesis, the ~360 nm lamps are used to photolyse Cl_2 and initiate chemistry, however the 254 nm lamps are used briefly in Chapter 5 to photolyse acetone and produce CH_3O_2.

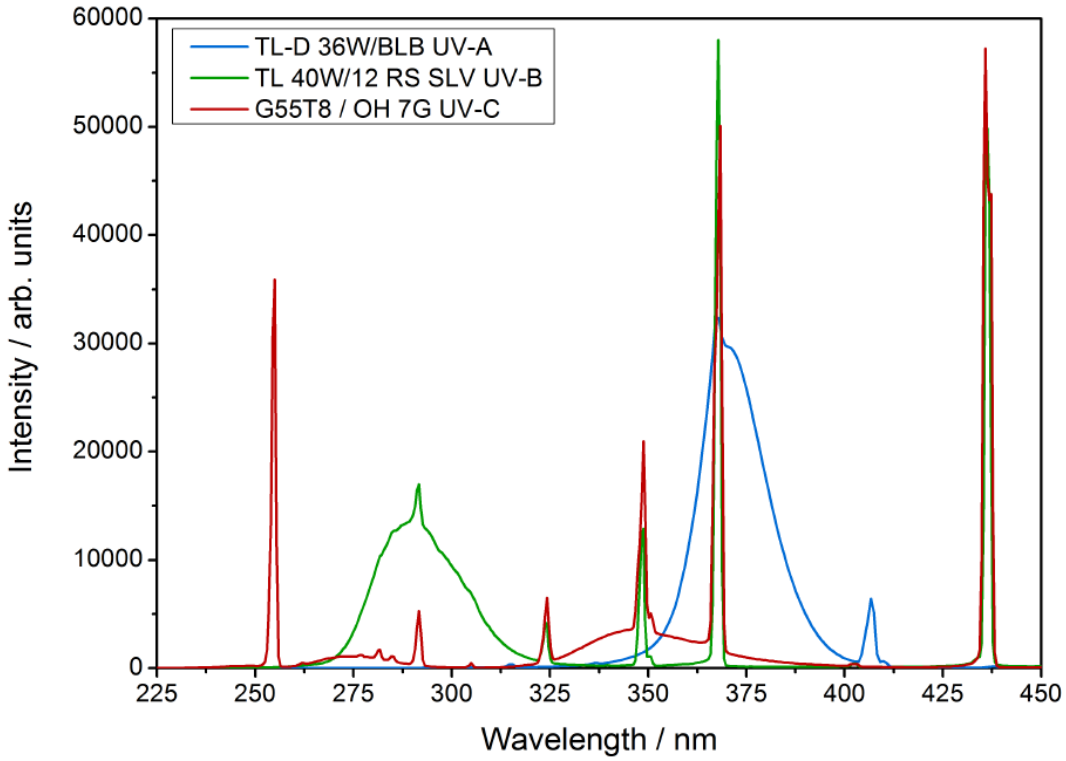

Figure 2.1 The spectral output of the 254 nm (red), 300 nm (green) and 360 nm (blue) lamps, measured in HIRAC using a spectral radiometer. The 360 nm lamps were used predominantly in this thesis. Figure produced by Dr. F. A. F. Winiberg (Winiberg, 2015).

The lamps are not large enough to extend the full length of the chamber, so each lamp is placed alternately closer to one end of the chamber or the other to achieve as homogeneous a radiation field as possible, and a computational study has shown that reflections off the steel walls help to smooth out any radiation hotspots (Glowacki et al., 2007a).

The lamps generate heat during use and have an optimum operating temperature, approximately 40-50 ˚C. The change in intensity of the lamps during use was measured by Dr. F. A. F. Winiberg (Winiberg, 2015), the results at various chamber temperatures are shown in Figure 2.2. When switched on under normal temperatures, i.e. ~295 K, the lamp intensity rises over the course of around 1-2 minutes as they warm up, and radical production rises with it before reaching a plateau. The lamps continue to warm up and reach around 50 ˚C, but their intensity remains relatively constant. The hot lamps have very little effect on the overall chamber temperature as the tubes they reside in are constantly flushed with nitrogen and prevent significant heat transfer to the chamber gas. Under cold chamber conditions the warm up period is extended significantly, up to 5-10 minutes in some cases, and the spike at ~50 s was likely caused by a delayed lamp ignition due to the low temperature. These effects could cause repeatability difficulties in some experiments at low temperatures (Chapter 6). Note that the plots in Figure 2.2 are not relative to each other, and the overall output intensity does not change significantly with temperature.

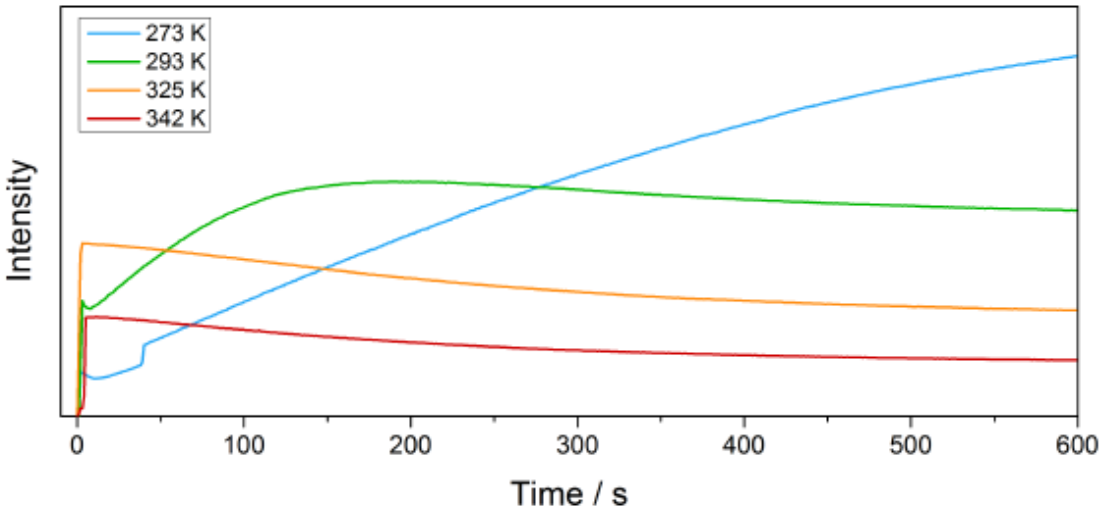

Figure 2.2 Time series of the intensity of the HIRAC lamps at 343. 325, 293 and 273 K (red, orange, green and blue, respectively). The lamps have an optimum operating temperature of ~320 K, at which point the intensity plateaus. Under cold chamber conditions (blue) the lamps have a long warm-up period that can cause problems during experiments. Figure produced by Dr. F. A. F. Winiberg (Winiberg, 2015).

Leaving the lamps switched on generates a near steady state radical concentration inside the chamber if enough reagents are present, and only switching on a portion of the eight lamps allows a small range of radical concentrations to be generated. Switching off the lamps ends radical production and causes the radical concentration to decay, allowing kinetic measurements to be made. A recurring experimental technique in this thesis will be the process of switching the lamps on and off at approximately 1 to 2-minute intervals to generate a series of kinetic decays, which will be monitored using either FAGE, RO_xLIF or CRDS.

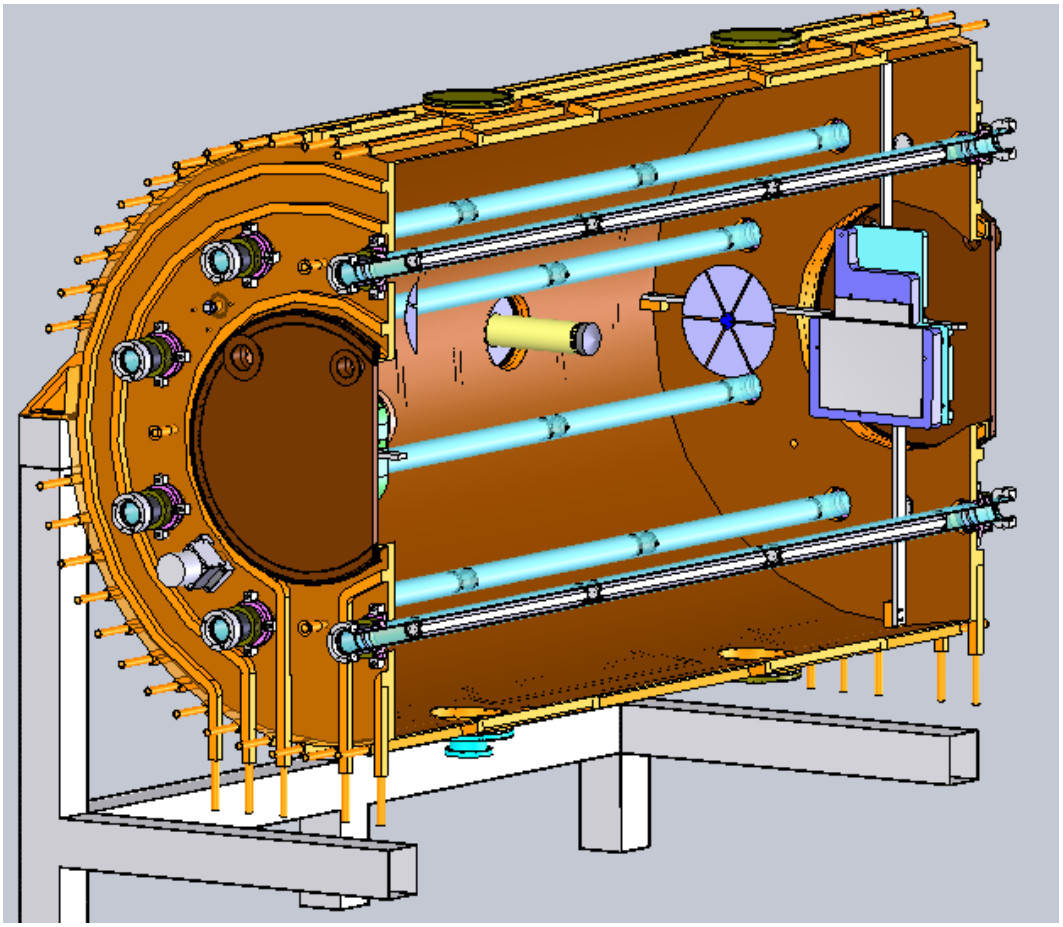

Figure 2.3 A cutaway view of the HIRAC chamber. Six of the eight quartz tubes are depicted in pale blue, and one of the four mixing fans can be seen in grey at the back of the image. The FAGE inlet is shown in yellow protruding into the chamber through one of the ISO K-160 flanges with the inlet far from the walls. The large FTIR field mirror is mounted on an aluminium cross at the back of the chamber, whilst the accompanying object mirrors are obscured by the front K-500 flange.

2.3 Chamber operation and reagent delivery

Gaseous or volatile reagents are delivered to the chamber through a 1 litre stainless steel cylinder connected to a vacuum line. The cylinder is evacuated to pressures around 10^{-3} mbar by a rotary vane vacuum pump (Edwards RV5), with the pressure monitored by two capacitance manometers, one for low range (0-10 Torr) and another for high range (0-1000 Torr) (Leybold CTR-90). Reagents can be admitted to the vacuum line from glass fingers, lecture bottles or gas cylinders through any of four cajon fittings. By measuring the pressure of reagents in the vacuum line and the volume of the steel cylinder the ideal gas law can be used calculate the concentration of reagents added to the chamber. Pure nitrogen is used to push reagents from the steel cylinder into the chamber. Liquid

reagents are delivered by syringe through a rubber septum mounted in one of the K-500 flanges. The number of instruments sampling from the chamber, particularly the FAGE instrument, mean the pressure inside HIRAC constantly drops during experiments. To correct for this, a pair of mass flow controllers (Brooks 5850E) meter oxygen and nitrogen into the chamber to maintain the set pressure, typically 1000 mbar.

2.4 Instrumentation

The pressure in the chamber is monitored by a 0 – 1000 Torr capacitance manometer (Leybold CTR-90 1000 Torr), and six thermocouples are distributed around the inside of the chamber to monitor the temperature, typically reporting values within approximately 1 K of each other indicating no significant temperature gradients exist.

An FTIR spectrometer (IFS 66/S, Bruker) is coupled to a modified Chernin cell inside HIRAC, the beam path is shown in Figure 2.4 and full details of the instrument and optical setup can be found in (Glowacki et al., 2007b). The IR light enters the chamber through a KBr window mounted in the end of HIRAC, and a set of mirrors inside each end of the chamber pass the light back and forth 72 times to give a total path length of 144 m. Instead of mounting to the walls of the chamber, the mirrors are mounted on aluminium crosses so to prevent misalignment as the walls flex with temperature or pressure. The light exits the chamber through another KBr window on the same flange and is directed onto a mercury cadmium telluride (MCT) detector that is cooled with liquid nitrogen. The FTIR instrument was used to measure the branching ratio of the CH_3O_2 self-reaction in section 6.2.1.

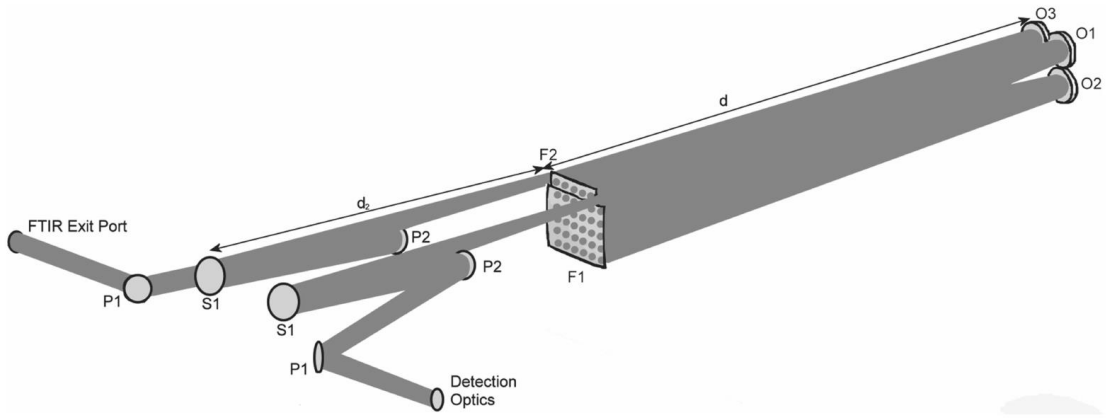

Figure 2.4 Diagram of the FTIR beam path. Field mirrors F1 and F2, and Object mirrors O1, O2 and O3 are located inside the chamber, mounted on aluminium crosses ~10 mm inset from the ends if the chamber. This keeps them off the chamber end flanges, which will distort as the internal pressure changes. The IR beam passes longitudinally through the centre of the chamber 72 times before exiting the chamber and impinges upon an MCT detector, which is cooled to 77 K with liquid nitrogen. Figure taken from Glowacki *et al.,* 2007a.

Six ISO-K160 flanges are used to interface thermocouples and the pump line to the chamber, as well as the sample lines for a NO_x analyser (Thermo Electron Corporation, Model 42 C), O_3 analyser (Thermo Electron Environmental instruments, Model 49 C) and two gas chromatography analysers (Trace Analytical, Model RGA3). One of these ISO-K60 flanges is a feedthrough to allow either the FAGE instrument or RO_xLIF instrument to sample from the chamber. The FAGE inlet is depicted as the yellow tube in Figure 2.3, and this is the position that all FAGE and RO_xLIF measurements are made in this thesis. Currently the FAGE and RO_xLIF instruments cannot both be attached to the chamber at the same time, but work is under way to install a second feedthrough to allow simultaneous measurements.

Four ISO – K500 flanges provide mounting points for more complex instrumentation like the CRDS system (section 2.5 below) or the FTIR system, as well as access to the chamber interior for maintenance.

2.5 Cavity Ringdown Spectrometer

Cavity Ringdown Spectroscopy (CRDS) is not a new measurement technique (Scherer et al., 1997, Faragó et al., 2015, Assaf et al., 2017, Gianella et al., 2018), but the system described here is newly developed for the HIRAC chamber and plays an important role in the development and validation of the CH_3O_2 FAGE technique. As an absorption-based measurement it has the potential to provide an absolute measurement of radicals, measurements without the need for calibration. This makes it a powerful benchmark to test the FAGE instrument, both for HO_2 measurements and its newly developed CH_3O_2 detection capabilities and is another tool to further enhance the HIRAC chamber's capabilities. To measure these two radicals the CRDS was set up with different optical components to suit the wavelengths required; 1506 nm for HO_2 and 1333 nm for CH_3O_2.

2.5.1 Principle of operation

CRDS uses two highly reflective mirrors to trap photons between them and create an optical resonator, a schematic is shown in Figure 2.5. Injecting laser light with a frequency that matches the cavity resonant frequencies allows for constructive interference and causes light intensity to build up inside the cavity. A small fraction of the oscillating photons leaks out of the cavity through the mirrors and is detected, the intensity of these leaking photons is proportional to the power circulating inside the cavity.

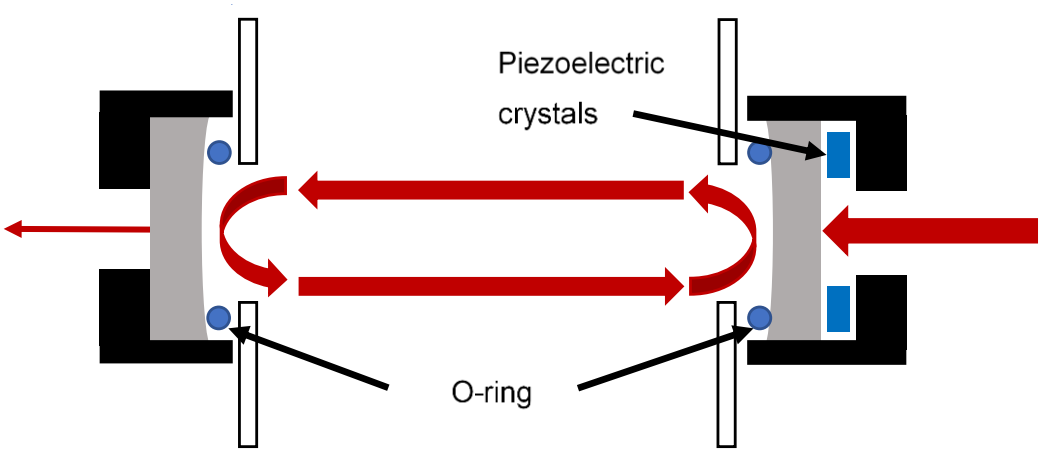

Figure 2.5 Schematic cross-sectional diagram of the CRDS mirror assembly, where the infra-red light (red arrows) enters from the right hand side, circulates between the mirrors (grey) and leaks out of the left hand mirror towards the detector. The mirrors are sealed against the walls of HIRAC (white boxes) by an O-ring and held in place by the mirror mounts (black). The pliable O-ring allows the mounts to tilt the mirrors and align the cavity. Piezoelectric crystals placed between the inlet mirror and its mount are used to modulate the cavity length.

Switching off the laser causes the light intensity to exponentially decay, or 'ringdown', with a characteristic time that describes the various light losses, such as scattering and transmission/attenuation through the mirrors. Introducing an absorbing species to the cavity will add an extra intensity drain to the system, and the ringdown time will decrease. This effect is shown in Figure 2.6 where a ringdown event at ~1506 nm is shown before and after the addition of and absorbing species, methanol.

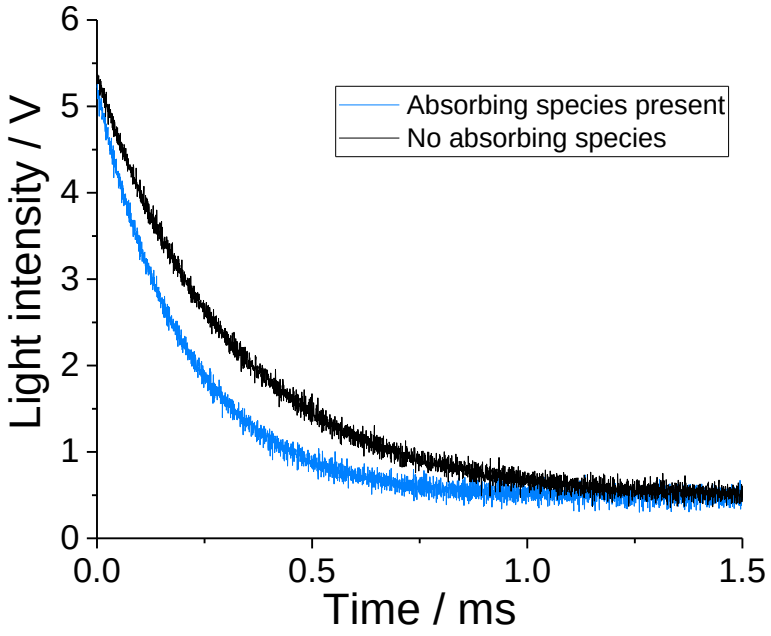

Figure 2.6 A pair of ringdown decays measured using the CRDS system in HIRAC at ~1506 nm. The light intensity is measured as a voltage on a photodiode. The black decay is a ringdown in air, whilst the blue decay is a ringdown in the same air with methanol present at ~10^{14} molecule cm^{-3}. This second decay is much faster due to the additional absorption loss, and the difference between the two decays is directly proportional to the methanol concentration.

This change in ringdown time can be related to the concentration of the absorbing species by:

$$[\mathrm{A}] = \frac{1}{\sigma \times c}\left(\frac{1}{\tau} - \frac{1}{\tau_0}\right) \qquad \textbf{Eq. 2.1}$$

where $[\mathrm{A}]$ is the concentration of the absorber, c is the speed of light, τ_0 is the ringdown time in the absence of A, and τ is the ringdown time with A present. The absorption cross section, σ, describes the probability of species A absorbing a photon, and depends upon the wavelength of light used and the conditions that species A is under, such as temperature, pressure and the other species present around them. It can be thought of as the area that the molecule presents to the photons, with higher areas corresponding to a higher absorption chance and stronger signal. Long path lengths are desirable for CRDS, and indeed all absorption-based measurements, as they enhance the observed signal too. The

Beer-Lambert law shows the relationship between the absorption cross section, path length, concentration and absorbance:

$$A = \sigma c l \qquad \textbf{Eq. 2.2}$$

where A is the absorbance, c is the concentration of the absorber and l is the path length, a longer path length offers more opportunity for photons to be absorbed.

The optical cavity relies on constructive interference to amplify the light intensity between the mirrors and generate a standing wave, and for this to happen the distance between the mirror faces must fit an integer number of half-wavelengths between them. A fixed width cavity would be unable to support a standing wave as vibrations and thermal changes would constantly move the cavity length out of range, making reliable measurements impossible. Instead, the cavity length is constantly modulated by mounting the input mirror on three piezoelectric crystals driven by a triangle wave generator at around 20 Hz. This ensures that the cavity reaches resonance regularly, even as the chamber vibrates or thermally distorts. It also makes it possible for the cavity to support different wavelengths easily, so HO_2 and CH_3O_2 can be measured using the same hardware and it is possible to tune the laser wavelength over each transition. The large 1.4 m cavity in HIRAC was able to reach long ringdown times of up to 350 µs, from which the total path length of the light can be approximated at >100 km or >70,000 passes. The laser used is a distributed feedback (DFB) laser with ~10 mW output power, and with so many passes it can lead to hundreds of watts of circulating power in the cavity. The output wavelength can be tuned over a small range by controlling the temperature of the laser, and enabled scanning of the HO_2 and CH_3O_2 transitions with their respective laser.

2.5.2 CRDS design and operation

The CRDS instrument was set up across the HIRAC chamber as shown in Figure 2.7, and is almost identical when measuring HO_2 or CH_3O_2. The only difference is the wavelength specification of each component – i.e the HO_2 components are rated for ~1506 nm and the CH_3O_2 components for ~1333 nm. The cavity is formed by two highly reflective 1 in. diameter mirrors (99.999 %, Layertec, curvature radius = 1 m) housed in custom built mounts that allow the mirrors to

be tilted slightly in three dimensions against an o-ring whilst maintaining a gas tight seal. The position of the mirror on the laser injection side is modulated along the cavity axis using a piezoelectric transducer at ~20 Hz, with the overall distance between the two mirrors being ~1.4 m. Laser light of ~1.3 μm is generated by a distributed feedback (DFB) fibre pig-tailed diode laser (NTT Electronics, NLK1B5EAAA) held in a butterfly laser diode mount (Thorlabs LM14S2). The electrical current that drives the laser diode and thermoelectric cooler is generated by a Thorlabs ITC502 driver. The DFB fibre is connected to an inline optical isolator (Thorlabs IO-H-1335APC) that prevents light reflected from the cavity from entering back into the laser, which would seed the laser and lock it to a very narrow frequency output. This process is called mode-locking and can be a useful tool but in this application prevents the laser from scanning effectively. After the optical isolator the light passes through an acousto-optic modulator (AOM, Gooch & Housego Fibre-Q M040-0.5C8H-3-F2S) which acts a switch to turn the laser off and trigger a ringdown event. Finally, the light passes through a fibre collimator (Thorlabs CFC-8X-C) and is then guided into the cavity by two silver mirrors (Thorlabs PF10-03-P01). On the detection side of the cavity, light leaking out of the mirror is directed onto another silver mirror that guides the light through a f = 30 mm focusing lens (Thorlabs LA1805-C) onto an InGaAs photodiode (Thorlabs DET10C/M). As the light leakage is very low intensity the photodiode signal is amplified (FEMTO DLPCA-200) before being sent to a data acquisition unit (DAQ, National Instruments USB-6361) and to a custom-built comparator that acts as a trigger unit. The comparator compares the amplified photodiode signal with a manually adjustable threshold voltage, and upon reaching the threshold the AOM is switched off to block the laser and trigger a ringdown event. The DAQ is simultaneously triggered and acquires the signal ringdown. The system resets after a set time (typically 5 ms) ready for the next event. The acquired data are processed using a custom made LabView program that fits the ringdown events with an exponential function to extract the ringdown time, τ. Eq. 2.1 is then used to convert the absorbance to the radical concentration. The analysis of CRDS data will be discussed in more detail in section 5.2, where the instrument is used to measure both HO_2 and CH_3O_2 radicals.

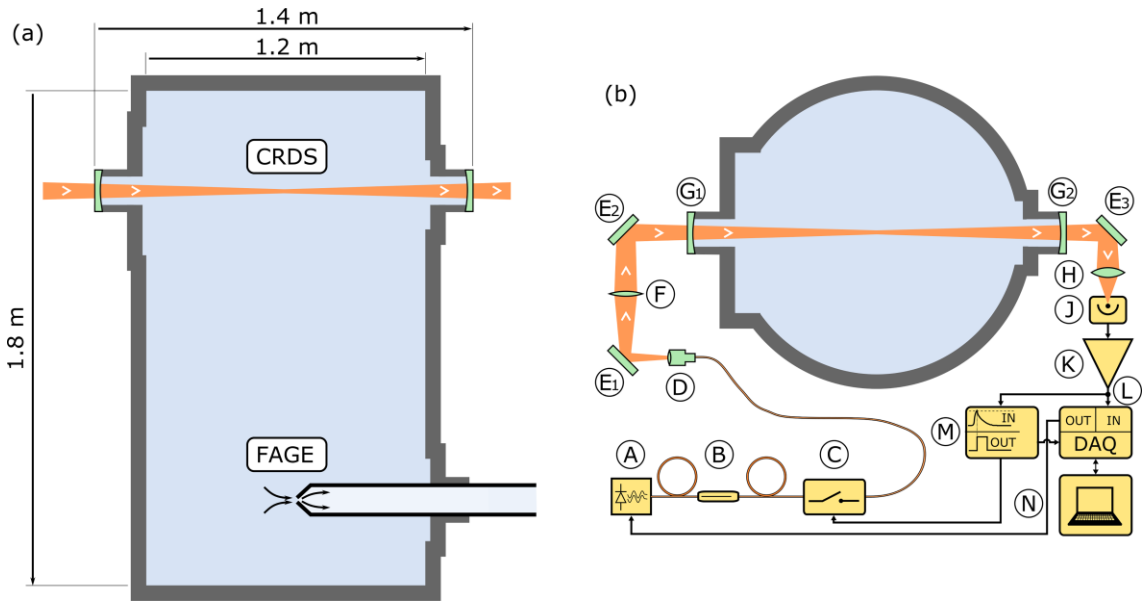

Figure 2.7 Schematic diagram of a) the position of the CRDS system in HIRAC, and to show its position relative to the FAGE instrument. b) The CRDS setup and components: A) Diode laser, B) Optical Isolator, C) Acousto-optic modulator, D) Collimator lens, E) Silver mirrors, F) Focusing lens, G) Cavity mirrors, H) Focusing lens, J) Photodiode, K) Amplifier, L) LabView DAQ, M) Trigger comparator, N) Control computer. Figure constructed by Dr. Michele Gianella of the University of Oxford.

2.6 References

Albrecht, S. R., Novelli, A., Hofzumahaus, A., Kang, S., Baker, Y., Mentel, T., Wahner, A. & Fuchs, H. 2019. Measurements of hydroperoxy radicals (HO_2) at atmospheric concentrations using bromide chemical ionisation mass spectrometry. *Atmospheric Measurement Techniques,* 12**,** 891-902.

Assaf, E., Sheps, L., Whalley, L., Heard, D., Tomas, A., Schoemaecker, C. & Fittschen, C. 2017. The Reaction between CH_3O_2 and OH Radicals: Product Yields and Atmospheric Implications. *Environmental Science & Technology,* 51**,** 2170-2177.

Bejan, I. G., Winiberg, F. A. F., Mortimer, N., Medeiros, D. J., Brumby, C. A., Orr, S. C., Kelly, J. & Seakins, P. W. 2018. Gas-phase rate coefficients for a series of alkyl cyclohexanes with OH radicals and Cl atoms. *International Journal of Chemical Kinetics,* 50**,** 544-555.

Faragó, E. P., Schoemaecker, C., Viskolcz, B. & Fittschen, C. 2015. Experimental determination of the rate constant of the reaction between $C_2H_5O_2$ and OH radicals. *Chemical Physics Letters,* 619**,** 196-200.

Fuchs, H., Novelli, A., Rolletter, M., Hofzumahaus, A., Pfannerstill, E. Y., Kessel, S., Edtbauer, A., Williams, J., Michoud, V., Dusanter, S., Locoge, N., Zannoni, N., Gros, V., Truong, F., Sarda-Esteve, R., Cryer, D. R., Brumby, C. A., Whalley, L. K., Stone, D., Seakins, P. W., Heard, D. E., Schoemaecker, C., Blocquet, M., Coudert, S., Batut, S., Fittschen, C., Thames, A. B., Brune, W. H., Ernest, C., Harder, H., Muller, J. B. A., Elste, T., Kubistin, D., Andres, S., Bohn, B., Hohaus, T., Holland, F., Li, X., Rohrer, F., Kiendler-Scharr, A., Tillmann, R., Wegener, R., Yu, Z. J., Zou, Q. & Wahner, A. 2017. Comparison of OH reactivity measurements in the atmospheric simulation chamber SAPHIR. *Atmospheric Measurement Techniques,* 10**,** 4023-4053.

Gianella, M., Reuter, S., Press, S. A., Schmidt-Bleker, A., Van Helden, J. H. & Ritchie, G. A. D. 2018. HO_2 reaction kinetics in an atmospheric pressure plasma jet determined by cavity ring-down spectroscopy. *Plasma Sources Science & Technology,* 27**,** 12.

Glowacki, D. R., Goddard, A., Hemavibool, K., Malkin, T. L., Commane, R., Anderson, F., Bloss, W. J., Heard, D. E., Ingham, T., Pilling, M. J. & Seakins, P. W. 2007a. Design of and initial results from a Highly Instrumented Reactor for Atmospheric Chemistry (HIRAC). *Atmospheric Chemistry and Physics,* 7**,** 5371-5390.

Glowacki, D. R., Goddard, A. & Seakins, P. W. 2007b. Design and performance of a throughput-matched, zero-geometric-loss, modified three objective multipass matrix system for FTIR spectrometry. *Applied Optics,* 46**,** 7872-7883.

Karl, M., Brauers, T., Dorn, H. P., Holland, F., Komenda, M., Poppe, D., Rohrer, F., Rupp, L., Schaub, A. & Wahner, A. 2004. Kinetic Study of the OH-isoprene and O_3-isoprene reaction in the atmosphere simulation chamber, SAPHIR. *Geophysical Research Letters,* 31**,** 4.

Novelli, A., Kaminski, M., Rolletter, M., Acir, I. H., Bohn, B., Dorn, H. P., Li, X., Lutz, A., Nehr, S., Rohrer, F., Tillmann, R., Wegener, R., Holland, F., Hofzumahaus, A., Kiendler-Scharr, A., Wahner, A. & Fuchs, H. 2018. Evaluation of OH and HO_2 concentrations and their budgets during photooxidation of 2-methyl-3-butene-2-ol (MBO) in the atmospheric

simulation chamber SAPHIR. *Atmospheric Chemistry and Physics,* 18**,** 11409-11422.

Scherer, J. J., Paul, J. B., Okeefe, A. & Saykally, R. J. 1997. Cavity ringdown laser absorption spectroscopy: History, development, and application to pulsed molecular beams. *Chemical Reviews,* 97**,** 25-51.

Winiberg, F. A. F. 2015. Characterisation of FAGE apparatus for HOx detection and application in an environmental chamber*. PhD Thesis, University of Leeds*.

Winiberg, F. A. F., Dillon, T. J., Orr, S. C., Gross, C. B. M., Bejan, I., Brumby, C. A., Evans, M. J., Smith, S. C., Heard, D. E. & Seakins, P. W. 2016. Direct measurements of OH and other product yields from the HO_2 + $CH_3C(O)O_2$ reaction. *Atmospheric Chemistry and Physics,* 16**,** 4023-4042.

Winiberg, F. A. F., Smith, S. C., Bejan, I., Brumby, C. A., Ingham, T., Malkin, T. L., Orr, S. C., Heard, D. E. & Seakins, P. W. 2015. Pressure-dependent calibration of the OH and HO_2 channels of a FAGE HOx instrument using the Highly Instrumented Reactor for Atmospheric Chemistry (HIRAC). *Atmospheric Measurement Techniques,* 8**,** 523-540.

Chapter 3. FAGE instrument for detection of HO_x radicals – design and principle of operation

In this chapter the design and operating principles of a Fluorescence Assay by Gas Expansion (FAGE) instrument for the detection of OH and HO_2 radicals by Laser Induced Fluorescence (LIF) in a laboratory setting is described. This instrument is the starting point for the development of a novel CH_3O_2 FAGE instrument, which is described in Chapter 4, where most of the principles and components discussed here are relevant.

The hydroxyl radical, OH, is a common target of atmospheric measurements, as it is considered the most important radical in atmospheric processes (section 1.1). Early methods of measuring OH in the atmosphere used off-resonant LIF, where the $A^2\Sigma^+(v'=1)\leftarrow X^2\Pi_i(v''=0)$ OH transition was excited at 282 nm and the resulting fluorescence between 308-315 nm was detected. The fluorescence signal was very weak as at atmospheric pressure the excited OH radical is rapidly quenched by collisions with other molecules, but the off-resonant nature of the experiment meant the weak fluorescence at 308 could be distinguished from the much stronger 282 nm laser scatter by use of a spectrometer (Wang et al., 1975). However, the 282 nm excitation light also photolysed ambient ozone and formed OH in the instrument at much higher levels than the ambient OH itself (Wang et al., 1976) through the reactions:

$$O_3 + h\nu\,(282\ \text{nm}) \rightarrow O(^1D) + O_2 \qquad \textbf{R 3.1}$$

$$O(^1D) + H_2O \rightarrow OH + OH \qquad \textbf{R 3.2}$$

This interference made the method non-viable for tropospheric measurements, however it is still a viable method to detect stratospheric OH (Wennberg et al., 1994) as H_2O concentrations are much lower, OH concentrations are much higher and the reduced pressure increases the OH fluorescence quantum yield (Heard, 2006).

All tropospheric measurements of OH now use on-resonance fluorescence, where the $A^2\Sigma^+(v'=0)\leftarrow X^2\Pi_i(v''=0)$ OH is excited at 308 nm, note v' = 0, and fluoresces at the same wavelength. Both the off and on-resonance transitions

are shown in Figure 3.1. This eliminates the ozone interference problem but introduces a new one - distinguishing between the already weak fluorescence and the strong laser light of the same wavelength. This problem is mitigated by performing LIF at reduced pressure, reducing the collisional quenching of the excited OH radical and extending its fluorescence lifetime, potentially up to ~700 ns (German, 1975), well past that of the laser scatter. This allows the laser scattered light to be temporally differentiated from the fluorescence. Additionally, the reduced number density inside the instrument at low pressure reduces the scattering of the laser light (Stevens et al., 1994). This is the basis of the FAGE technique, first developed in 1984 (Hard et al., 1984), where gas is sampled into a low pressure cell and OH is detected by LIF at 308 nm. The FAGE method is now widely used to measure OH and HO_2 radicals in the troposphere (Hofzumahaus et al., 1996, Faloona et al., 2004, Dusanter et al., 2009, Novelli et al., 2014, Whalley et al., 2011, Commane et al., 2010).

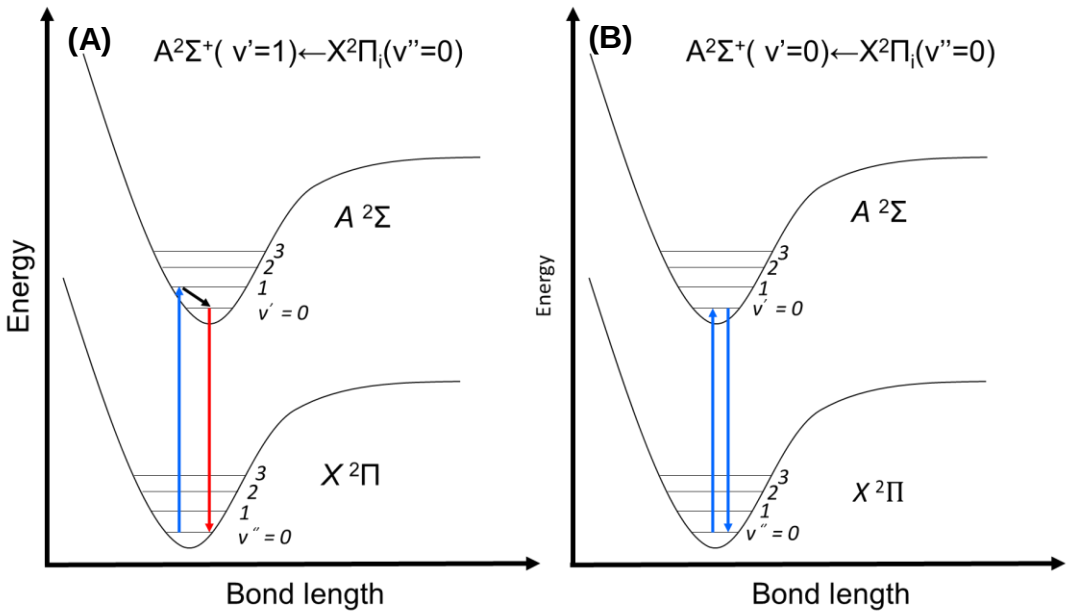

Figure 3.1 (A) Off-resonance LIF - electronic transition of OH when excited by ~282 nm light to the v'=1 vibrational energy level in the $A^2\Sigma$ electronic state (blue arrow), followed by vibrational relaxation to v'=0 (black arrow) and radiative decay (~308 nm fluorescence) to the ground state (red arrow). (B) On-resonance LIF – excitation of OH by 308 nm to the v'=0 vibronic energy level

Direct FAGE measurements of HO_2 are not possible, either because the weak HO-O bond is easily broken by laser light, or the excited HO_2 molecule is able to undergo internal conversion (distribute the excitation energy into vibrations of its bonds) so the energy is lost rather than re-emitted as fluorescence. HO_2 must therefore be converted into OH prior to excitation by injecting NO:

$$HO_2 + NO \rightarrow NO_2 + OH \qquad \textbf{R 3.3}$$

which is then detected by LIF as OH.

3.1 FAGE Design and operation

The FAGE instrument is an amalgamation of five distinct elements, these are: the sampling and detection assembly, the reference cell, the laser system, the electronic components used to detect and count photons, and finally the computer program that controls the instrument and logs data. Each of these are described in the following sections.

3.1.1 Sampling and detection assembly

The sampling and detection assembly, shown in Figure 3.2, is a ~ 1 m long black anodised aluminium tube with an inner diameter of 50 mm. A conical cap is screwed into one end of the tube with a 1 mm diameter pinhole drilled through its apex, whilst the other end is connected to a rotary backed roots blower pump system (Leybold Trivac D40B and Ruvac WAU 251) *via* a 50 mm ID flexible tube. The pinhole serves as the sample inlet, and the conical profile minimises the reactive metal surface area in proximity to the sample. The pump set and pinhole combination mean the interior of the instrument is maintained at ~2.5 Torr with gas being drawn in from atmospheric pressure at a rate of ~5 SLM. The pressure in the instrument is monitored by a capacitance manometer (MKS Baratron, 10 Torr) connected just prior to the pump line. A ball shut-off valve is the final component before the pump line and allows the instrument to be isolated from the vacuum system.

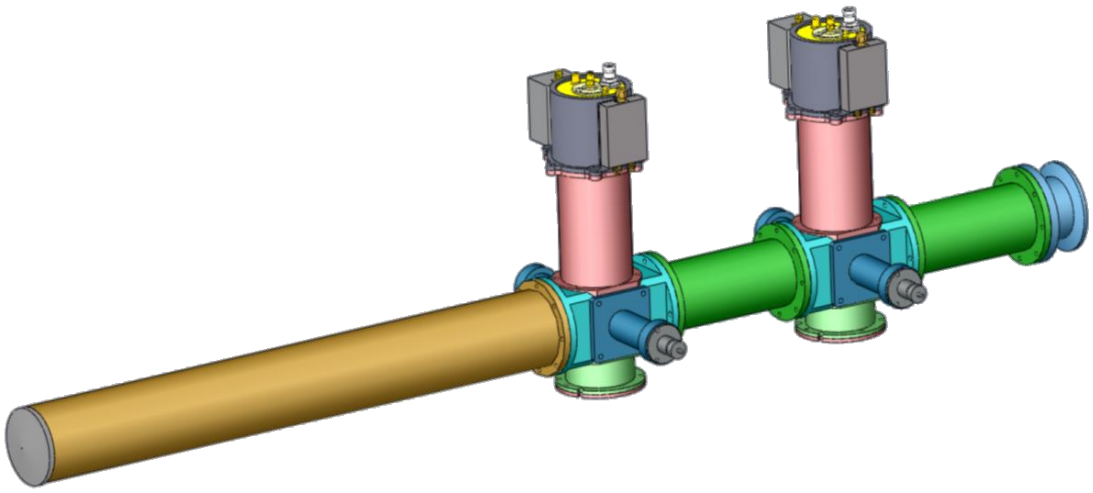

Figure 3.2 SolidWorks representation of the FAGE sampling assembly. Gas is drawn in through the pinhole drilled through the conical cap (grey, left-most side), moves through the fluorescence cells (blue) and exits towards the pumps (right most side). The long inlet is a feature that allows the instrument to work with HIRAC, as it allows the sampling point to be placed near the centre of the chamber, well away from the walls where heterogeneous chemistry may interfere with measurements.

Two fluorescence cells are integrated into the tube, the centre of the first cell is ~380 mm from the pinhole, and the centre of the second cell is a further ~390 mm downstream. The large distance between the pinhole and fluorescence cells (~380 mm) is normally something to be avoided as it provides a large surface area for radicals to be lost upon. However, this long inlet is a necessary compromise to enable the FAGE instrument to work with HIRAC (section 2.4), as it enables the instrument to sample from near the centre of the chamber and away from the interior walls where heterogeneous chemistry may interfere with measurements.

A cross sectional view of the fluorescence cells is shown in Figure 3.3, they are both identical in construction. The probe laser beam is delivered to the cell by fibre-optic cable (Elliot Scientific, QMMJ-55-UVVIS-200/240-3-1) that is attached to the input arm. A lens collimates the divergent light exiting the fibre into a ~10 mm diameter beam, which then passes through the centre of the cell perpendicular to the gas flow. The beam exits the other side of the cell through a quartz window at the end of the output arm and impinges upon a photodiode (UDT-555UV, Laser Components, UK) which is used to monitor any changes in the laser power. The input and output arms contain a series of baffles which

serve to prevent non-collimated laser light and ambient light from entering the cell.

A microchannel plate (MCP) photomultiplier is mounted directly above the laser axis, perpendicular to the gas flow and the laser beam. A set of two plano-convex lenses (CVI PLCX-50.8-50.0-308, fused silica 50.8 mm diameter, 49.97 mm radius of curvature, 100 mm focal length) collimates the fluorescent photons and directs them through a bandpass interference filter (Barr Associates, 308.75 ± 2.5 nm, 50 % transmission). Another set of two identical plano-convex lenses focuses the filtered photons onto the MCP photocathode. The pairing of the plano-convex lenses helps to correct for any astigmatism or other optical aberrations that may occur with only a single lens. The solid angle (field of view) of the photocathode is approximately doubled by a concave spherical mirror (CVI) that is mounted on the opposite side of the cell to reflect photons that are emitted away from the detector. The optical components are protected from the gas flow by quartz windows, and all optical components are anti-reflection coated for 308 nm light. The MCP detectors are discussed in more detail in section 3.1.4.

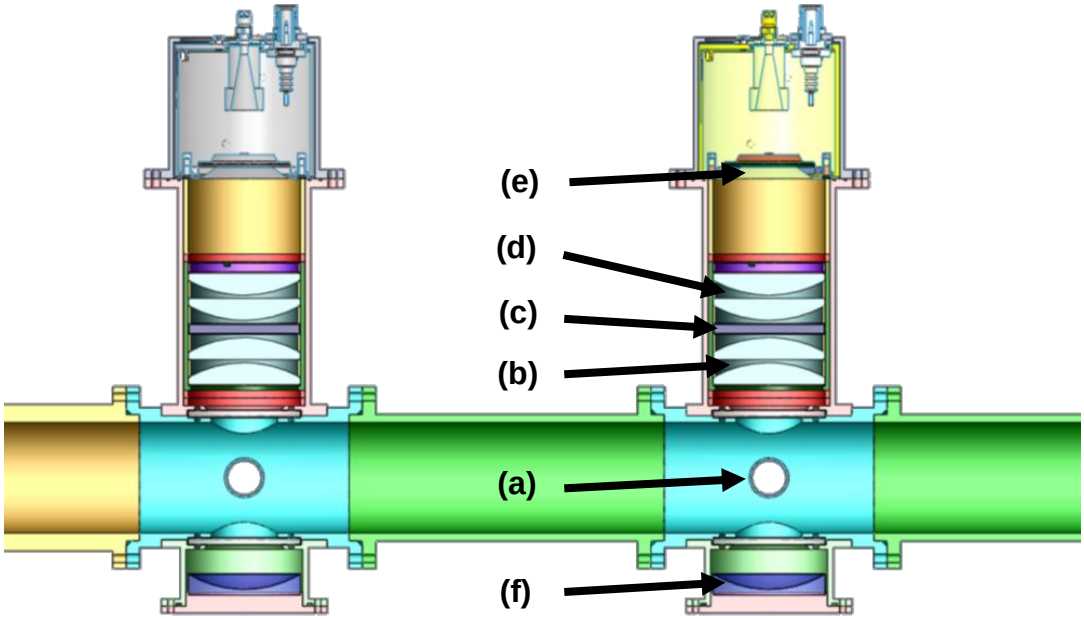

Figure 3.3 SolidWorks sectional view of the fluorescence cells in pale blue, with gas flow from left to right, the laser axis (a) is perpendicular to the image. The cells are identical, but arrows point only to the right cell for clarity. The lower pair of plano-convex lenses (b) direct photons through the interference filter (c), and the second pair of lenses focus (d) them onto the MCP photocathode (e). A retro-reflector (f) is mounted below the cell, opposite the detector, to re-direct photons back up towards the detector, effectively doubling its field of view.

The serial cell arrangement allows for simultaneous measurement of OH and HO_2 radicals in the front and rear cells respectively, however direct LIF measurement of the HO_2 radicals is not possible, requiring the radical to be reduced to OH first. This is performed by injecting NO (BOC, N2.5 Nitric Oxide) into the centre of the gas flow *via* 1/8th inch OD, 0.07-inch ID, stainless steel tubing. The injection point is ~25 mm prior to the laser axis of each cell, and the flow rate is controlled by a mass flow controller (Brooks 5850S, 0-10 sccm), typically at a rate of ~1-2 sccm. The NO injection can be turned on/off using solenoid valves (Parker, 24 V DC) to switch between measurement of different radical species, and the spacing of the two cells ensures that the NO injected into the rear cell is unable to diffuse back into the first and interfere with measurements there.

3.1.2 Reference cell

As fluorescence excitation lines tend to be very narrow (on the order of a few picometres), the laser's internal wavelength calibration cannot be relied upon to acquire the maximum point of fluorescence. Instead, a so called 'reference cell' is needed that can generate a large and stable quantity of radicals that can be used to guide the laser onto the wavelength of maximum fluorescence *via* a feedback loop. Like a FAGE cell, the reference cell is held at a low pressure (around 4 Torr) and slowly draws water vapour in through a bubbler. The water vapour is pyrolysed by a hot (orange glow, ~900 ˚C) 80:20 Ni:Cr wire filament positioned just off the laser axis and on the opposite side to a CPM detector. The pyrolysis process generates OH radicals *in situ*, producing strong fluorescence signals when the wavelength is appropriate. The reference cell is much simpler in design and operation than a standard FAGE cell as the quantification of radicals is unimportant and it doesn't need to be as sensitive. As such, the laser power through the cell is very low, <1 mW, the detector is ungated and there are no collection optics present, except for a 308 nm notch filter (Barr Associates, 308.75 ± 2.5 nm, 50 % transmission) that removes the red/orange filament glow and prevents blinding of the detector.

3.1.3 Laser system

The UV laser light used in these experiments was generated using a dye laser (Sirah Credo-Dye-N) pumped by a Nd:YAG laser (JDSU Q201-HD-1000R), and a schematic diagram of the laser system and light distribution is shown in Figure 3.4. The dye used is DCM special dissolved in ethanol which when pumped by the 532 nm YAG laser emits between ~600-650 nm. A diffraction grating is used to select individual wavelengths, in this case ~616 nm, and a barium borate (BBO) frequency doubling crystal is used to convert this to 308 nm. Frequency doubling is a very inefficient process, only ~20 % of the fundamental beam is doubled, meaning the resulting beam is not monochromatic and is instead a mixture of 308 nm UV photons and the fundamental 616 nm beam. The fundamental photons are separated out of the beam by diffraction through four Pellin-Broca prisms, and the resulting UV light is distributed into the reference cell (section 3.1.2) or into fibre optic cables which transfer the light to instruments.

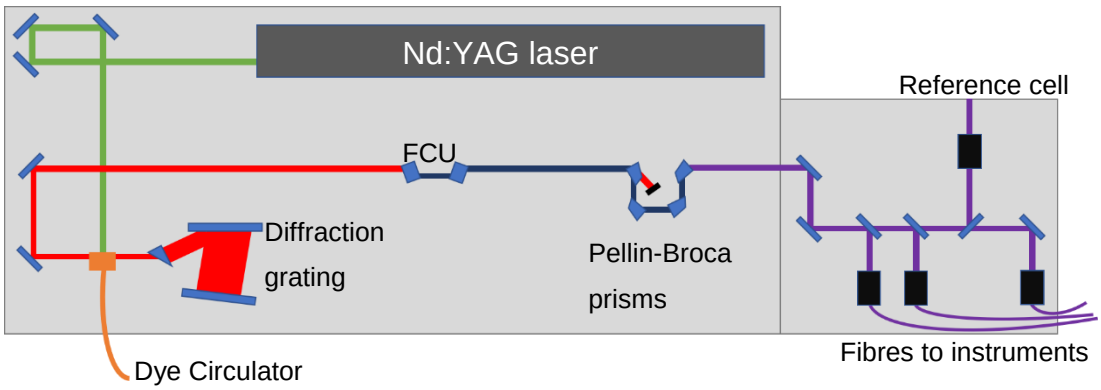

Figure 3.4 Schematic diagram of the laser system to show the beam path from the 532 nm Nd:YAG light through to the 308/298 nm UV light delivered to the instruments. Telescoping and focusing optical components have been omitted for clarity. 532 nm light from the Nd:YAG laser is directed onto the dye cell and optical resonator (orange). The resonator and diffraction grating allow specific wavelength selection. The beam is then passed through the frequency conversion unit (FCU) that doubles the frequency to UV light. The UV and fundamental red beams are separated by four Pelin-Broca prisms, and the UV light is passed through beamsplitters into the reference cell or fibre launchers. The fibre optics deliver the light to various instruments.

The Nd:YAG pump laser is Q-switched and triggered at a rate of 5 kHz, equating to one pulse every 200 µs. With a typical pump power between 7 – 9 W the UV power delivered to the fluorescence cells was around 5 – 10 mW, which was measured prior to each experiment using a thermopile power meter (Maestro,

Gentec-EO). The use of dye laser also enabled the generation of ~595 nm light, doubled by the BBO crystal to ~298 nm, which was used for LIF detection of CH_3O in the following chapters.

3.1.4 Fluorescence detection and photon counting

The intensity of fluorescent light generated by LIF is very weak, especially compared to the excitation laser light. Take, for example, a typical OH measurement signal in the range of ~100 counts s^{-1} generated using the 5 kHz laser system described above. This means that of the 5000 laser pulses impinging on the sampled gas, only 1 in 50 pulses caused LIF to occur. Therefore, LIF measurements require the use of photomultipliers, highly sensitive detectors that can respond to individual photons and generate detectable electronic signals.

Photomultipliers take the general form of a vacuum tube with an electrode at either end and a gain stage in between. The end of the tube exposed to incident light is constructed of a window, e.g quartz, with a photemissive conductor deposited on its interior surface. Photons that impinge the photocathode cause it to emit an electron as per the photoelectric effect, which is accelerated towards the anode by a -3900 V potential difference generated by a high voltage power supply (SRS PS350, ±5 kV). These photoelectrons are too few to generate any significant current, so a gain stage is incorporated into the tube to provide amplification. There a few types of gain stage, for example channel photomultipliers or dynode chains, but in this work microchannel plate (MCP) photomultipliers were used (Photek PMT325/Q/BI/G) where the electron multiplier is a set 3 of microchannel plates. Each plate has an array of tubes passing through them (microchannels) at an angle, and the three plates stacked together make a Z-shaped path for electrons to travel along. As the electrons pass, the non-linear path ensures that they strike the tube walls multiple times and generate secondary electrons, turning one photoelectron into millions of secondary electrons by the time they reach the anode. These electron pulses are amplified from ~10 mV by a factor of 10 (Photek PA200-10) then counted by a multichannel scaler (MCS, Becker & Hickl PMS 400 A). The MCS pulses are recorded temporally in 30 bins each of which is 1 µs wide giving a total collection

time of 30 µs. The counts measured in the first bin, termed as the 'A counts', contain a combination of laser scattered light, fluorescence photons and detector noise. The rest of the bins are beyond the fluorescence lifetime and so only comprise detector noise, which may originate from the detector itself, light leaking into the cells or even cosmic radiation. An average of the final 10 bins, termed 'B counts' are subtracted from the A counts to leave the *signal* that is due only to laser light and LIF:

$$signal = A - {}^{B}/_{10} \qquad \textbf{Eq. 3.1}$$

This process is shown in Figure 3.5.

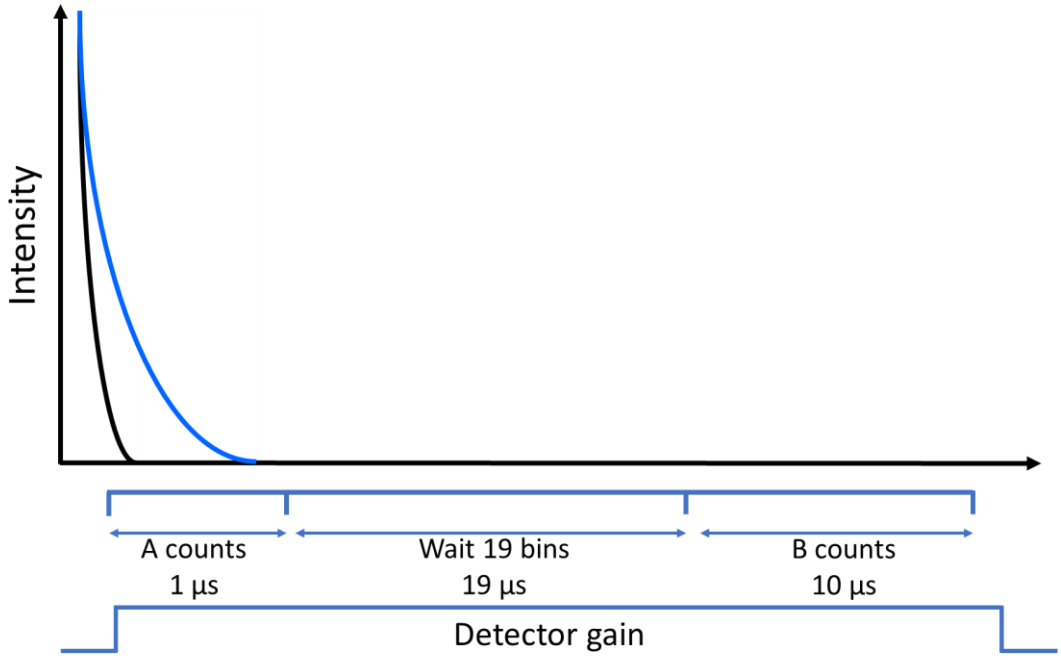

Figure 3.5 Schematic to show the fluorescence detection and counting process. The laser pulse (black) and fluorescence signal (blue) are temporally distinct. The detector gain is switched on near to the end of the laser scatter lifetime.

To protect the detectors from high intensity laser scatter they are switched off during each laser pulse by a gating unit (Photek GM10-50), which switches the potential on the photocathode between -200 V (detector on, full gain) and +50 V (detector off, no gain). When positively charged the photocathode essentially draws photoelectrons back into itself and prevents them from reaching the gain stage, whereas when negatively charged it repels the photoelectrons towards the

gain stage and generates signal. Rapid switching is required as fluorescence begins instantaneously upon excitation, and the pairing of these MCP detectors and gating units offers switching times around 50 ns. This allows the gate on/off trigger to be moved close to the laser pulse and captures more of the fluorescence photons. Figure 3.6 shows the raw signal measured on the MCS both with and without OH present in the FAGE cell. To acquire Figure 3.6 the timing of the detector gating relative to the laser pulse was advanced by ~10 ns (the detector was switched on 10 ns earlier) to allow more laser light than usual to be detected. The long lived OH fluorescence signal (blue) is easily differentiated from the short-lived laser scatter (black).

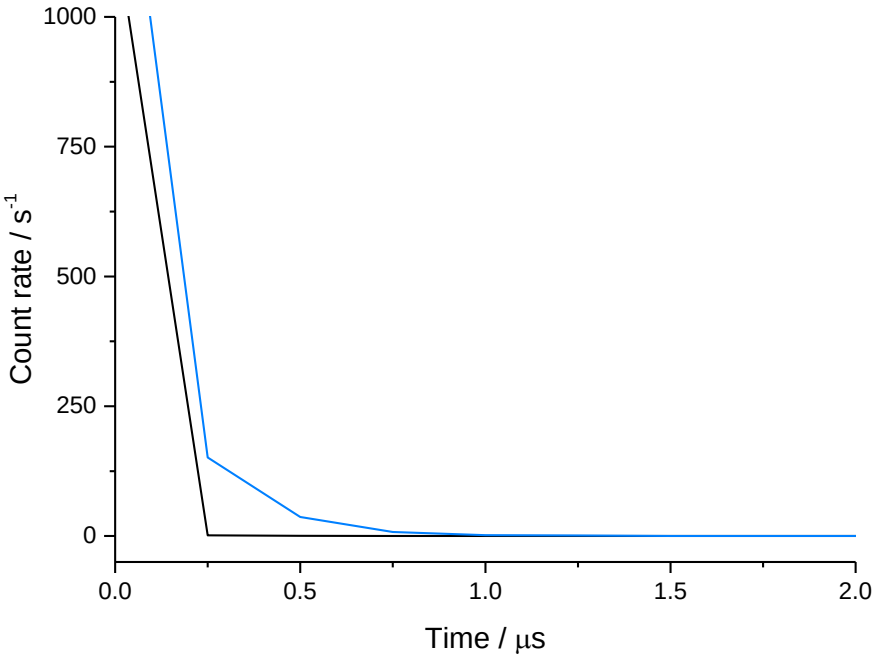

Figure 3.6 Signal measured by the MCS cards in the absence (black) and presence (blue) of OH in the FAGE cell. The high energy laser pulse generates a large amount of scattered light in the cell, and if ungated will saturate the detector. In normal experiments the gate would be switched on (no detector gain) before Time = 0 and switched off (high detector gain) at approximately Time = 250 ns to capture the longer lived OH fluorescence, which lives for approximately 750 ns.

3.1.5 Control and data collection

The laser pulses, gating units and MCS cards are kept in synchronisation by a digital delay generator (Quantum Composers 9520) which triggers the laser, gate units and counting cards using 5 V pulses, and the frequency and length of these pulses dictates how the components behave. All experiments here were run at 5 kHz pulse repetition frequency, meaning the processes described in the sections above are repeating every 200 µs, once for each laser pulse. As the LIF events generated from each laser pulse are very low, the result of Eq. 3.1 is summed over a set number of laser pulses to increase the signal and reduce noise at the cost of time resolution. In typical experiments this was 5000 pulses and equates to one data point every second, giving the signal in the units of *counts* s^{-1}. For kinetic experiments this number was reduced to increase the time resolution of the experiments at the cost of signal quality. For example, during many of the experiments in the following chapters each point was integrated for $1/10^{th}$ of a second, reducing the amount of signal acquired by a factor of 10 in return for a higher rate of data acquisition to help capture the fast changes in signal during kinetic experiments.

The experiment is controlled and recorded by a custom made LabView program that, as well as the signal, logs the pressure and laser power through each cell. Each FAGE measurement is a three-step cycle, shown in Figure 3.7 and is as follows:

1. Finding line (blue area) – The laser steps incrementally between two wavelengths inside which the $A^2\Sigma^+(v'=0)\leftarrow X^2\Pi_i(v''=0)$ transition is known to reside. The two peaks that are observed correspond to the $Q_1(2)$ and $Q_{21}(2)$ rotational lines. The strongest line, $Q_1(2)$, is the target. Whilst the laser wavelength scans the signal in the reference cell is monitored and the maximum count rate is stored. The laser then repeats the scan, and if the signal gets within ~5% of the stored maximum the scan stops, and the laser remains at this wavelength. The line has been found.
2. On-line (green area) – The laser remains at the same wavelength for a predetermined time and the signal is logged. During this time, NO injectors may be switched on or off to alternate between OH/HO_2 measurements.

3. Off-line (pink area) – The laser wavelength is stepped off the fluorescence transition, returning the signal to the baseline. This baseline is then logged for a predetermined time, usually 1 minute.

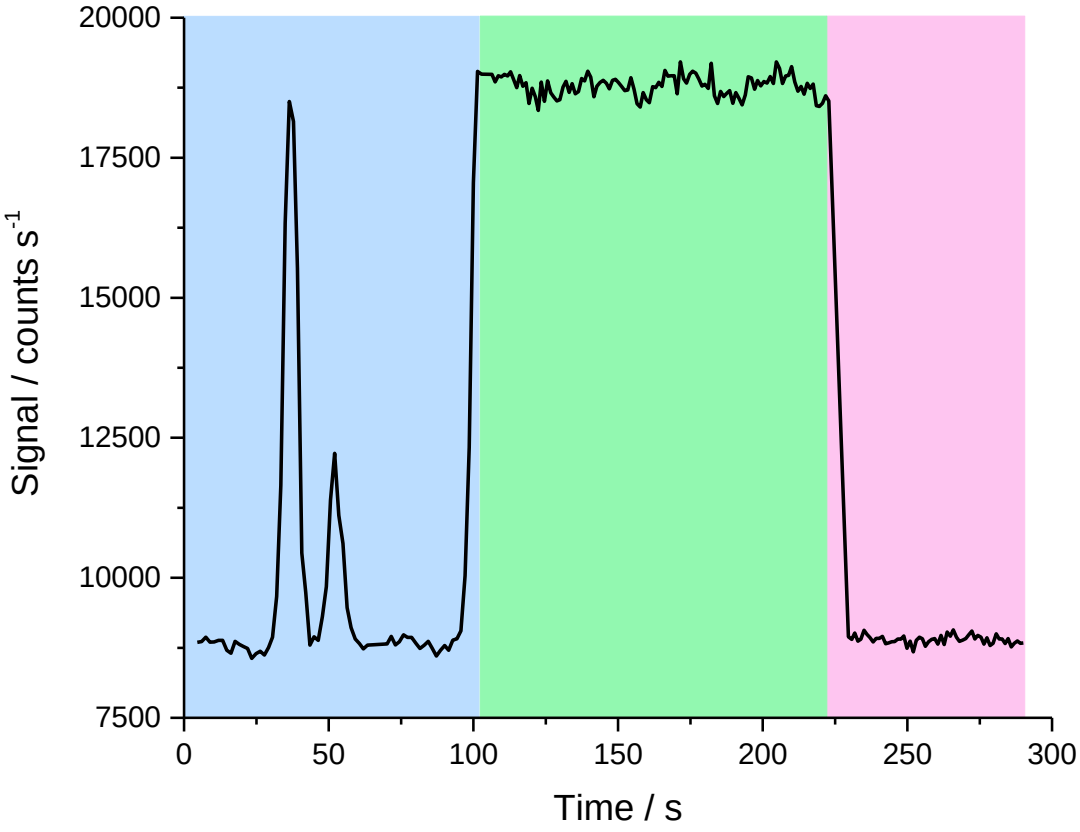

Figure 3.7 A typical reference cell signal during the three stages of each FAGE measurement, with signal plotted against measurement time. The first stage (blue) is the finding line stage and during this time the laser wavelength is scanning over the region the $A^2\Sigma^+(v'=0) \leftarrow X^2\Pi_i(v''=0)$ OH transition is known to reside. The scan then restarts at around 70 s and the line is found at 100 s. The second stage (green) is a period of constant wavelength, as is where the measurement is made. The final stage (pink) is the off-line measurement, where the laser wavelength has stepped 0.02 nm off the transition.

The amount of time that can be spent in the on-line stage is limited by the stability of the laser wavelength, which would vary from day to day. The laser could typically maintain a set wavelength for at least 10 minutes before drift was observed, but much longer times of 20 or 30 minutes were not uncommon. The likely cause of this drifting was slowly changing ambient temperatures that

caused the laser diffraction grating to move. This drifting wavelength was easily detected with the aid of the reference cell for HO_x measurements, and the line could be found again by re-scanning the laser.

The signal generated in the On-Line phase of measurements is comprised of fluorescence photon counts and additional counts from laser scatter or detector noise, which must be removed. When moving to the Off-Line phase only the latter sources of signal remain, so by subtracting the Off-Line signal from the On-Line signal, the signal due only to fluorescence photons is obtained. The result is then divided by the laser power to return the LIF signal in the units of *counts* s^{-1} mW^{-1}.

3.2 Calibration

The magnitude of the LIF signal is not an absolute measurement of radical concentration as it depends as much on the instrument as it does on the number of radicals present. For example, the cell pressure, the quantum efficiency of the detector and the cleanliness of the optical components all impact the magnitude of the signal, and these factors may vary over time. It is therefore necessary to regularly calibrate the instrument to find the sensitivity factor, *C*, that describes the amount of fluorescence signal measured per radical and is unique to that radical species and instrument configuration. When FAGE is coupled to HIRAC, the pressure in the chamber has a direct impact on the pressure in the FAGE cells, so the instrument must be calibrated at these pressures too and is an important detail for the inter-comparison experiments in Chapter 5.

Two calibration methods are discussed here. The first uses water vapour photolysis to generate radicals (section 3.2.1) and has been used extensively in work at many research institutions (Fuchs et al., 2011, Ren et al., 2012, Winiberg et al., 2015), however it can currently only be performed at atmospheric pressure. The water vapour photolysis method also requires further steps to characterise the calibration source through N_2O actinometry (section 3.2.2). The second calibration method uses the kinetics of the HO_2 self-reaction inside the HIRAC chamber to elucidate C_{HO2}, as the second order decay rate of these reactions is dependent upon the initial concentration of the radicals (section 3.2.3). This

kinetic calibration method can be performed at any pressure in HIRAC. The results of these calibrations are summarised here, and the details on their determination is in the flowing sections.

The HO_2 calibration factor at 1000 mbar was found using both the water vapour photolysis method and using the second order decay method in HIRAC at 1000 mbar. The average calibration factor using the water vapour photolysis method was C_{HO_2} = (2.6 ± 0.4) × 10^{-7} counts s^{-1} mW^{-1} cm^3 $molecule^{-1}$, where the error represents the systematic and statistical uncertainty at 1 σ (section 4.5). This value is in very good agreement with the calibration factor determined through the second order decay method, C_{HO_2} = (2.4 ± 0.5) × 10^{-7} counts s^{-1} mW^{-1} cm^3 $molecule^{-1}$, and previous work (Winiberg et al., 2015). The average calibration factor at 1000 mbar was therefore $C_{HO_2 1000mbar}$ = (2.5 ± 0.5) × 10^{-7} counts s^{-1} mW^{-1} cm^3 $molecule^{-1}$.

The HO_2 calibration factor at 150 mbar was found using the second-order decay method in HIRAC, with an average value of $C_{HO_2 150mbar}$ = (2.5 ± 0.5) × 10^{-7} counts s^{-1} mW^{-1} cm^3 $molecule^{-1}$. This shows that the reduced FAGE cell pressured (i.e ~2.5 Torr *vs* ~0.7 Torr when sampling from HIRAC at a pressure of 1000 mbar *vs* 100 mbar) does not significantly affect the HO_2 calibration, which is in accordance with previous findings (Winiberg et al., 2015).

Once calibrated, FAGE signals are converted into radical concentration using:

$$[X] = \frac{S_X}{C_X} \qquad \textbf{Eq. 3.2}$$

where *[X]* is the radical concentration, S_X is the signal for radical *X* and C_x is the sensitivity factor for radical *X*.

3.2.1 Water vapour photolysis calibration

Water vapour is photolysed in air at 184.9 nm to produce OH and H radicals, the H radical reacts rapidly with oxygen to produce HO_2 in equal measure to OH (Fuchs et al., 2011):

$$H_2O + h\nu\ (184.9\ \text{nm}) \rightarrow OH + H \qquad \textbf{R 3.4}$$

$$H + O_2 + M \rightarrow HO_2 + M \qquad \textbf{R 3.5}$$

The radical generation occurs just before the outlet of a ~300 mm long black anodised aluminium square section tube with internal dimensions of 12.8 × 12.4 mm, where a UV mercury pen-ray lamp (LOT-Oriel, Hg(Ar) Pen-Ray) is mounted under the tube and shines through a quartz window into its interior. An array of small tubes assembled in a honeycomb pattern is mounted between the lamp and the quartz window, which acts to collimate the UV light and allows the illuminated volume of the wand to be calculated. As the quartz window is 38.1 mm long the illuminated area, or photolysis volume, is ~605 mm^3. The square section tubing, as opposed to round, helps to generate a turbulent gas flow in the tube, meaning the air, water and radicals are well mixed during the photolysis stage, and when exiting the wand. The lamp housing is flushed with a small flow of nitrogen to cool the lamp and remove oxygen, which would otherwise attenuate the light and produce ozone. From this point, the radical source described here will be referred to as a 'wand' and is shown in Figure 3.8.

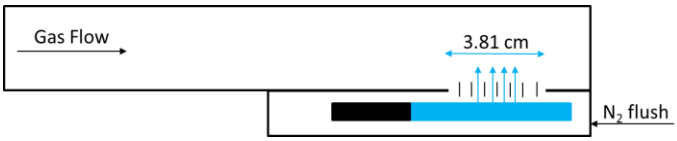

Figure 3.8 Schematic diagram of the calibration wand. Gas flows from left to right in the top section and passes over a window behind which is the UV lamp housed in the lower section. An array of steel tubes collimate the light to create a well-defined cuboid volume of irradiation. The lamp is flushed with nitrogen to prevent overheating and ozone generation.

Dry air (BOC, BTCA 178) is delivered to the wand by a thermal mass flow controller (Brooks Instruments GF40, 0-100 SLMP), typically at a flow rate of 40 SLM. Prior to the wand, the air is humidified by passing through a water bubbler. A fraction of the flow is syphoned into a dew-point hygrometer (CR4, Buck Research Instruments) to monitor the water concentration, typically ~3000 ppm, whilst the bulk flow is directed towards the wand. A catch pot is mounted in-line with the hygrometer to prevent any large water droplets from reaching the hygrometer and contaminating the internal mirror. The outlet of the wand is placed against the FAGE inlet pinhole and overfills it, preventing any ambient air from entering the instrument. The radical concentration can then be calculated using:

$$[\mathrm{OH}] = [\mathrm{HO_2}] = [\mathrm{H_2O}] \times \sigma_{\mathrm{H_2O,185\,nm}} \times \Phi_{\mathrm{OH}} \times F_{185nm} \times t \qquad \textbf{Eq. 3.3}$$

where $\sigma_{\mathrm{H_2O,\,185nm}}$ is the photolysis cross-section of water vapour at 185 nm, Φ_{OH} is the quantum yield for OH formation, $F_{185\ nm}$ is the photon flux and t is the photolysis time. The photolysis cross-section and quantum yield are well known, and $F_{185\ nm}$ is determined through N_2O actinometry (0 below). The photon flux is modulated by changing the current supplied to the lamp, which in turn generates a range of radical concentrations and the resulting change in FAGE signal is logged. Eq. 3.4 shows a typical calibration for HO_2 radicals that gave a sensitivity factor C_{HO2} = (2.64 ± 0.05) × 10^{-7} counts s^{-1} mW^{-1} cm^3 $molecule^{-1}$.

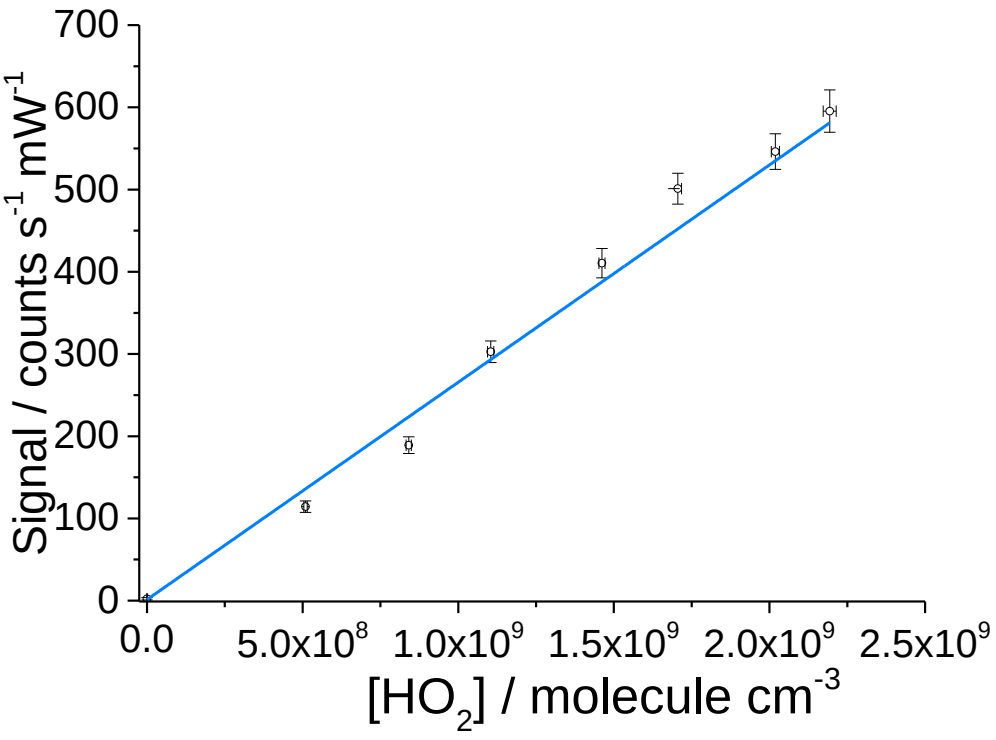

Figure 3.9 FAGE calibration plot for HO_2, with internal cell pressure of 2.5 Torr and water concentration of approximately 3000 ppm. Radicals were generated using the wand at 40 SLM. The gradient of the line gives the sensitivity factor C_{HO2} = (2.64 ± 0.05) × 10^{-7} counts s^{-1} mW^{-1} cm^3 $molecule^{-1}$, where the errors represent the statistical error at 1 σ.

3.2.2 N_2O actinometry

The water photolysis calibration method (0 above) relies upon a UV lamp to generate a known quantity of radicals, but before this is possible the flux output of the mercury lamp must be measured. Photolysis of N_2O at 184.9 nm produces $O(^1D)$ radicals that react with other N_2O molecules to produce NO, which is then measured by a chemiluminescence NO_x analyser (Thermo Electron Corporation 42C, LOD = 50 ppt). The number of NO radicals produced is directly proportional to the lamp flux. However, $O(^1D)$ can be lost or quenched to $O(^3P)$ in several competing reactions:

$$N_2O + h\nu\ (184.9\ \text{nm}) \rightarrow N_2 + O(^1D) \qquad \textbf{R 3.6}$$

$$N_2 + O(^1D) \rightarrow N_2 + O(^3P) \qquad \textbf{R 3.7}$$

$$O_2 + O(^1D) \rightarrow O_2 + O(^3P) \qquad \textbf{R 3.8}$$

$$N_2O + O(^1D) \rightarrow N_2 + O_2 \qquad \textbf{R 3.9}$$

$$N_2O + O(^1D) + M \rightarrow 2NO + M \qquad \textbf{R 3.10}$$

where M is N_2 or O_2. The fraction of NO produced is determined using the literature rate constants for R 3.6-R 3.9, and the product of *F* and *t* can be calculated using:

$$Ft = \frac{(k_{3.7}[N_2] + k_{R3.8}[O_2] + [N_2O](k_{R3.9} + k_{R3.10}))\ [NO]}{2(k_{R3.10}\ \sigma_{N2O}\ [N_2O]^2)} \qquad \textbf{Eq. 3.4}$$

where σ_{N2O} is 1.43×10^{-19} cm^{-2}, $k_{R3.7} = 2.15 \times 10^{-11}$ molecule^{-1} cm^3 s^{-1}, $k_{R3.8} = 3.3 \times 10^{-11}$ molecule^{-1} cm^3 s^{-1}, $k_{R3.9} = 4.63 \times 10^{-11}$ molecule^{-1} cm^3 s^{-1} $k_{R3.10} = 7.25 \times 10^{-11}$ molecule^{-1} cm^3 s^{-1} at 298 K (Creasey et al., 2000). The rate coefficients are taken from the JPL recommendations (Burkholder et al., 2015). The flux can then be isolated by division of the residence time, *t*, which is ~8.3 ms at a 40 SLM flow rate. Figure 3.10 shows an actinometry plot of the lamp flux against the supplied lamp current. The gradient $(6.45 \pm 0.01) \times 10^{12}$ photons cm^{-2} s^{-1} mA^{-1} is then used to calculate the flux at each lamp current used in the wand calibrations (0 above).

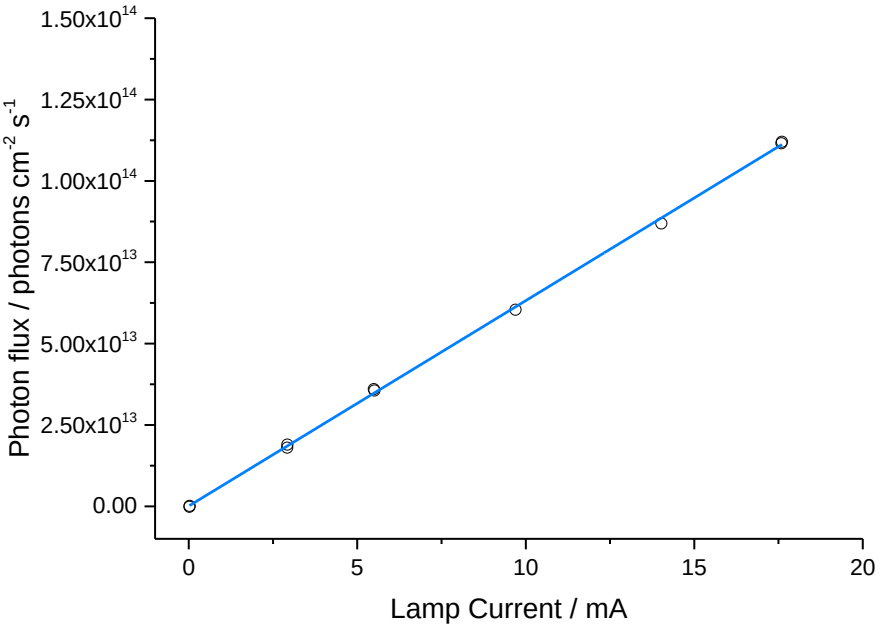

Figure 3.10 Actinometry plot of lamp flux against supplied current. The gradient of the line is (6.45 ± 0.01) × 10^{12} photons cm^{-2} s^{-1} mA^{-1} can be used to calculate F_{185nm} for any given lamp current.

Figure 3.11 shows the experimental setup. N_2O (BOC, 98.0 %, Medical grade) was added at ~2 SLM to a 40 SLM flow of high purity synthetic air (BOC, synthetic BTCA 178) to give a ~5 % N_2O mixture, which was flowed through the calibration 'wand'. The output from the wand was directed towards a ¼ inch OD PTFE tube connected to a commercial NO_x analyser (Thermo Electron Corporation 42C, LOD = 50 ppt). The analyser was connected to a pump that drew the sample through the instrument at around 1 SLM. The NO signal produced is proportional to the NO concentration in the sample and is usually around 1 ppb. The lamp current was varied between 0-20 mA to generate a range of NO concentrations, which the NO_x analyser measured with a 60 second moving average.

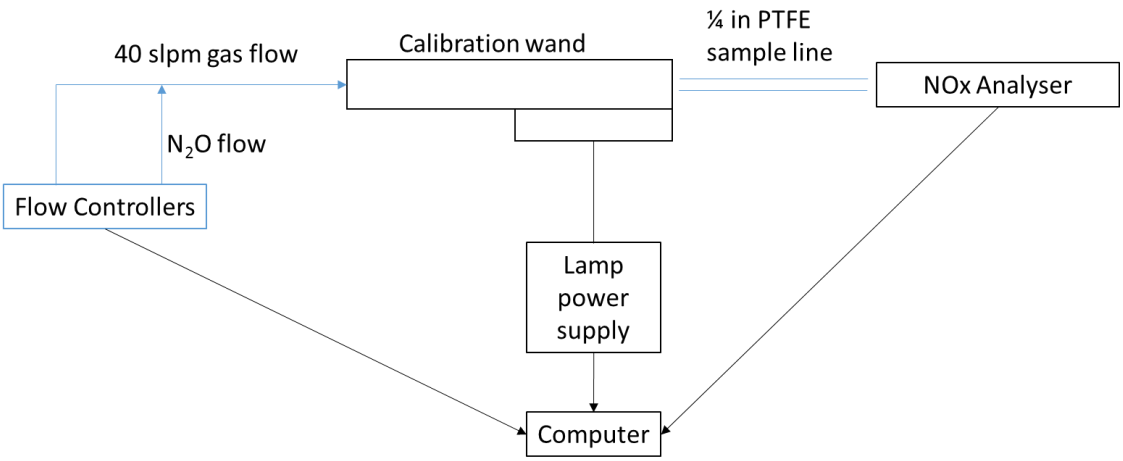

Figure 3.11 Diagram of the actinometry setup. 40 SLM of air or nitrogen was flowed through the wand, with the addition of ~2 SLM of N_2O. The lamp current is varied between 0-20 mA to photolyse N_2O and form NO. A ¼ inch PTFE tube is placed in front of the wand outlet and is over filled. The tube is connected to the NO_x analyser, which detects NO and reports the concentration to the calibration computer.

Further steps are required, however, as the NO_x analyser is a non-absolute photon counting technique like FAGE, it requires calibrating. The calibration method involved flowing a known concentration of NO into the analyser and comparing that to its measured output. The analyser measures NO by titrating it with excess O_3, which produces excited NO_2 molecules that undergo radiative decay and release a photon. However, this chemiluminescence is quenched by N_2O molecules that are used in the actinometry experiments and lowers the instruments sensitivity (Dusanter et al., 2008). Repeating the calibration experiments whilst introducing a known N_2O fraction allows the quenching effect to be accounted for. Figure 3.12 shows a typical set of calibrations for the NO_x analyser, the quenching effect is small, with approximately 1 % sensitivity drop for each percentage of N_2O added. With a typical actinometry experiment will utilise around 5 % N_2O the effect is almost negligible.

The NO_x analyser was calibrated by adding dilute NO (BOC, 465 ± 23 ppb in N_2) to a 2 SLM flow of synthetic air (BOC, synthetic BTCA 178), which was then sampled by the NO_x analyser. The flow rate of NO was varied between 0 and 0.3 SLM, and the resulting signal was correlated to the actual concentration in the sample. The N_2O interference was measured by repeating the calibration with an additional flow of N_2O, to give a 2, 5 and 10 % N_2O sample composition.

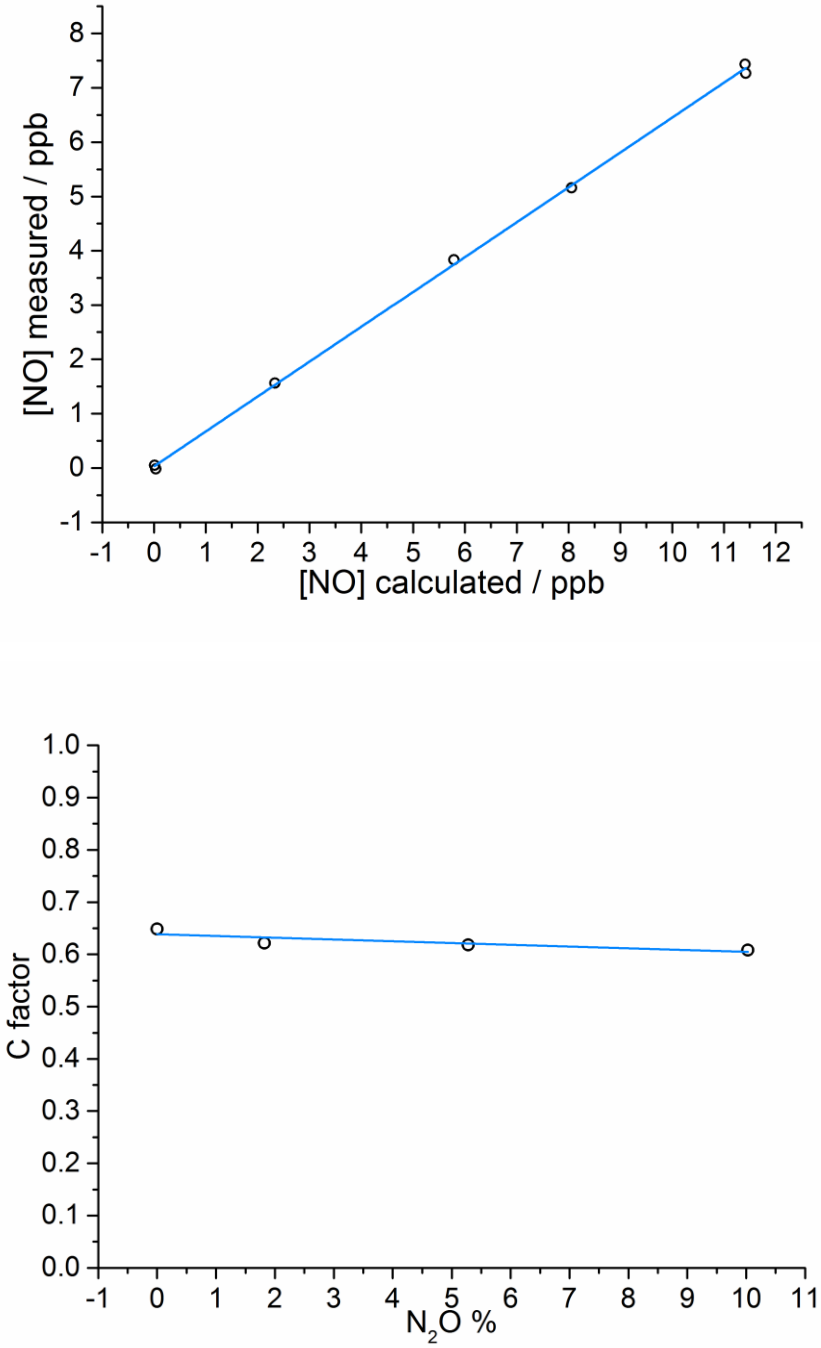

Figure 3.12 The upper panel shows a set of NOx analyser calibrations with the measured NO concentration on the y-axis plotted against the actual concentration delivered. The gradient of the line is the sensitivity factor. The calibration was repeated using different levels of N_2O to measure the quenching effect. The lower panel shows the change in sensitivity factor (gradient) with added N_2O. The effect is small but detectable, typical actinometry measurements are performed around 2-5% N_2O.

3.2.3 Kinetic calibration in HIRAC

The second order decay rate of HO_2 is dependent upon the initial radical concentration, and by knowing the overall rate coefficient of this reaction the sensitivity of FAGE can be calculated. HO_2 is consumed through both a bimolecular and a termolecular reaction:

$$HO_2 + HO_2 \rightarrow H_2O_2 + O_2 \qquad \textbf{R 3.11}$$

$$HO_2 + HO_2 + M \rightarrow H_2O_2 + O_2 + M \qquad \textbf{R 3.12}$$

where M is a bath gas such as N_2 or O_2. Additionally, there is a third HO_2 loss mechanism through reactions with the walls of the HIRAC chamber. Combining these factors together gives the total removal rate of HO_2:

$$\frac{d[HO_2]}{dt} = -\left(2 \times k_{self\text{-}r.}[HO_2]^2 + k_{loss}[HO_2]\right) \qquad \textbf{Eq. 3.5}$$

where $k_{self\text{-}r}$ is the overall HO_2 self-reaction rate constant, and k_{loss} is the rate constant for the wall loss of HO_2. Integrating Eq. 3.5 for $[HO_2]_t$ yields:

$$\frac{1}{[HO_2]_t} = \left(\frac{1}{[HO_2]_0} + \frac{2\times k_{self\text{-}r.}}{k_{loss}}\right) \times \exp(k_{loss}(t - t_0)) - \left(\frac{2\times k_{self\text{-}r.}}{k_{loss}}\right) \qquad \textbf{Eq. 3.6}$$

where $[HO_2]_t$ is the HO_2 concentration at time t of the decay, and $[HO_2]_0$ is the concentration at the start of the decay, t_0. Substituting Eq. 3.2 for HO_2 into Eq. 3.6 gives:

$$(S_{HO_2})_t = \left(\left(\frac{1}{(S_{HO_2})_0} + \frac{2\times k_{self\text{-}r.}}{k_{loss}\times C_{HO_2}}\right) \times \exp(k_{loss}(t - t_0)) - \left(\frac{2\times k_{self\text{-}r.}}{k_{loss}\times C_{HO_2}}\right)\right)^{-1} \qquad \textbf{Eq. 3.7}$$

where $(S_{HO_2})_0$ is the FAGE signal at the start of the decay and $(S_{HO_2})_t$ is the signal at time t. Fitting an exponential curve that is described by equation 2.4 to a decay measurement allows the C_{HO2} factor to be extracted. With the current experimental setup, the position of t_0 is not precisely known and instead had to be estimated. At typical data acquisition rates of 10 Hz t_0 could be approximated to within two or three data points, fitting to these points only affected the values of C by around 5 %. Improvements to the methodology are underway to mark t_0

programmatically, however the effects are negligible. Figure 3.13 shows the FAGE signal during an example HO_2 decay measured by FAGE whilst sampling from HIRAC, which was at a pressure of 150 mbar. Fitting Eq. 3.7 to the data, with $k_{self\text{-}r.}$ fixed to 1.79×10^{-12} cm^{-3} molecule^{-1} s^{-1} according to the IUPAC recommendation, and with C_{HO2} and k_{loss} allowed to float. An average of 10 such decays gave an average sensitivity factor of $C_{HO2} = (2.6 \pm 0.5) \times 10^{-7}$ counts cm^3 molecule^{-1} s^{-1} mW^{-1}.

The fitting also yielded the wall-loss rate coefficient, $k_{loss} = (0.09 \pm 0.02)$ s^{-1}, which has overlapping error limits with the range of values reported previously for HO_2 in HIRAC, 0.03–0.07 s^{-1} (Winiberg et al., 2015). The wall loss rate is dependent on the chamber conditions during the experiment and may change from day to day. Also, the loss rate increases with decreasing pressure as the mean free path of each molecule becomes longer, making collision with the chamber walls more likely than collision with other molecules. As such, a value of $k_{loss} = (0.04 \pm 0.01)$ s^{-1}, has been obtained by the kinetic analysis of the FAGE signal decays measured at 1000 mbar in HIRAC in this work.

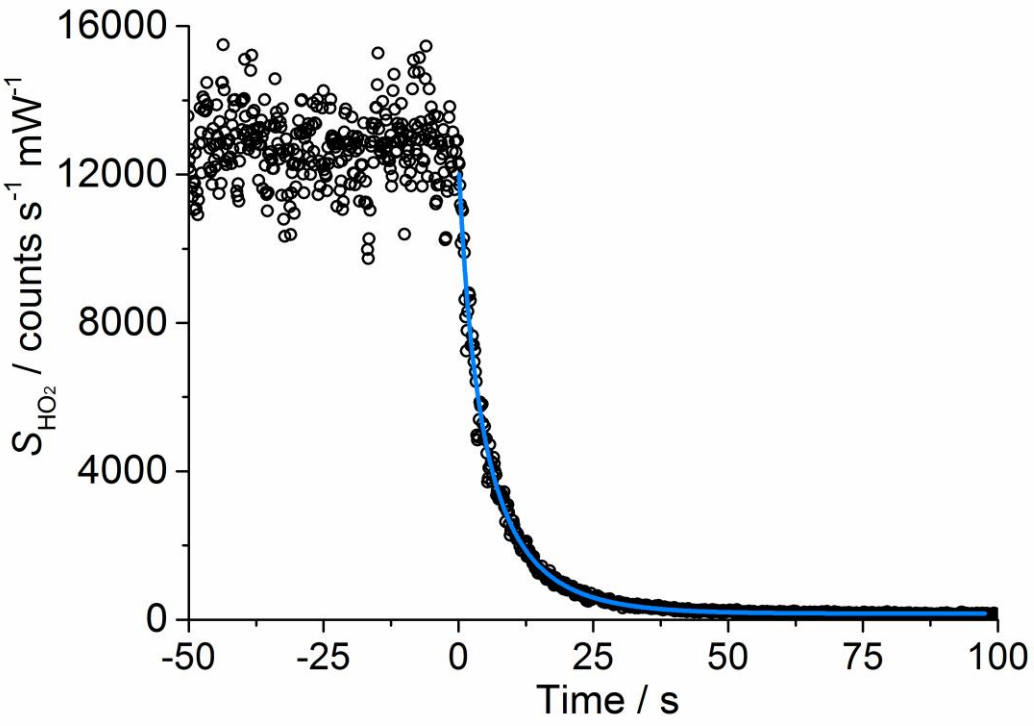

Figure 3.13 An example of a second-order decay of the normalized FAGE HO_2 signal with 0.1 second time resolution (black) recorded at 298 K and a 150 mbar air mixture. HO_2 was generated using $[Cl_2]$ ~3 × 10^{13} and $[CH_3OH]$ ~5 × 10^{13} molecule cm^{-3}. At time zero the photolysis lamps were turned off to allow the radicals to decay. Fitting Eq. 3.7 to this example trace (blue) gave C_{HO2} = (2.45 ± 0.12) × 10^{-7} counts cm^3 molecule^{-1} s^{-1} mW^{-1}.

3.3 Summary

The design and operation of a FAGE instrument for the detection of OH and HO_2 radicals has been shown. Two independent methods of calibrating the instrument for HO_2 radicals have also been shown, with each method yielding very similar sensitivity factors. Additionally, calibrating the instrument at reduced pressure (150 mbar in HIRAC, 0.9 mbar in the FAGE cells) showed no significant pressure dependence.

In the next chapter, the FAGE instrument and its calibration procedures will be modified and adapted to develop a novel method that can detect CH_3O and CH_3O_2 radicals in a manner analogous to the OH and HO_2 detection described here. The operating principles of the FAGE instrument and the two calibration procedures described here are almost directly applicable to this new method.

3.4 References

Commane, R., Floquet, C. F. A., Ingham, T., Stone, D., Evans, M. J. & Heard, D. E. 2010. Observations of OH and HO_2 radicals over West Africa. *Atmospheric Chemistry and Physics,* 10**,** 8783-8801.

Creasey, D. J., Heard, D. E. & Lee, J. D. 2000. Absorption cross-section measurements of water vapour and oxygen at 185 nm. Implications for the calibration of field instruments to measure OH, HO_2 and RO_2 radicals. *Geophysical Research Letters,* 27**,** 1651-1654.

Dusanter, S., Vimal, D. & Stevens, P. S. 2008. Technical note: Measuring tropospheric OH and HO_2 by laser-induced fluorescence at low pressure. A comparison of calibration techniques. *Atmospheric Chemistry and Physics,* 8**,** 321-340.

Dusanter, S., Vimal, D., Stevens, P. S., Volkamer, R. & Molina, L. T. 2009. Measurements of OH and HO_2 concentrations during the MCMA-2006 field campaign - Part 1: Deployment of the Indiana University laser-induced fluorescence instrument. *Atmospheric Chemistry and Physics,* 9**,** 1665-1685.

Faloona, I. C., Tan, D., Lesher, R. L., Hazen, N. L., Frame, C. L., Simpas, J. B., Harder, H., Martinez, M., Di Carlo, P., Ren, X. R. & Brune, W. H. 2004. A laser-induced fluorescence instrument for detecting tropospheric OH and HO_2: Characteristics and calibration. *Journal of Atmospheric Chemistry,* 47**,** 139-167.

Fuchs, H., Bohn, B., Hofzumahaus, A., Holland, F., Lu, K. D., Nehr, S., Rohrer, F. & Wahner, A. 2011. Detection of HO_2 by laser-induced fluorescence: calibration and interferences from RO_2 radicals. *Atmospheric Measurement Techniques,* 4**,** 1209-1225.

German, K. R. 1975. Radiative and predissociative lifetimes of v'=0, 1 and 2 levels of $A^2\Sigma^+$ state of OH and OD. *Journal of Chemical Physics,* 63**,** 5252-5255.

Hard, T. M., Obrien, R. J., Chan, C. Y. & Mehrabzadeh, A. A. 1984. Tropospheric free-radical determination by FAGE. *Environmental Science & Technology,* 18**,** 768-777.

Heard, D. E. 2006. Atmospheric field measurements of the hydroxylradical using laser-induced fluorescence spectroscopy. *Annual Review of Physical Chemistry.* Palo Alto: Annual Reviews.

Hofzumahaus, A., Aschmutat, U., Hessling, M., Holland, F. & Ehhalt, D. H. 1996. The measurement of tropospheric OH radicals by laser-induced fluorescence spectroscopy during the POPCORN field campaign. *Geophysical Research Letters,* 23**,** 2541-2544.

Novelli, A., Hens, K., Ernest, C. T., Kubistin, D., Regelin, E., Elste, T., Plass-Dulmer, C., Martinez, M., Lelieveld, J. & Harder, H. 2014. Characterisation of an inlet pre-injector laser-induced fluorescence instrument for the measurement of atmospheric hydroxyl radicals. *Atmospheric Measurement Techniques,* 7**,** 3413-3430.

Ren, X., Mao, J., Brune, W. H., Cantrell, C. A., Mauldin, R. L., Hornbrook, R. S., Kosciuch, E., Olson, J. R., Crawford, J. H., Chen, G. & Singh, H. B. 2012. Airborne intercomparison of HO_x measurements using laser-induced fluorescence and chemical ionization mass spectrometry during ARCTAS. *Atmospheric Measurement Techniques,* 5**,** 2025-2037.

Sander, S. P., R. R. Friedl, J. P. D. Abbatt, J. Barker, D. M. Golden, C. E. Kolb, M. J. Kurylo, G. K. Moortgat, P. H. Wine, Huie, R. E. & Orkin, V. L. 2011. Chemical kinetics and photochemical data for use in atmospheric studies - Evaluation 17. *Jet Propulsion Laboratory, Pasadena*.

Stevens, P. S., Mather, J. H. & Brune, W. H. 1994. Measurement of tropospheric OH and HO_2 by laser-induced fluorescence at low-pressure. *Journal of Geophysical Research-Atmospheres,* 99**,** 3543-3557.

Wang, C. C., Davis, L. I., Wu, C. H. & Japar, S. 1976. Laser-induced dissociation of ozone and resonance fluorescence of OH in ambient air. *Applied Physics Letters,* 28**,** 14-16.

Wang, C. C., Davis, L. I., Wu, C. H., Japar, S., Niki, H. & Weinstock, B. 1975. Hydroxyl Radical Concentrations Measured in Ambient Air. *Science,* 189**,** 797-800.

Wennberg, P. O., Cohen, R. C., Hazen, N. L., Lapson, L. B., Allen, N. T., Hanisco, T. F., Oliver, J. F., Lanham, N. W., Demusz, J. N. & Anderson, J. G. 1994. Aircraft-borne, laser-induced fluorescnece instrument for the in-situ detection of hydroxyl and hydroperoxyl radicals. *Review of Scientific Instruments,* 65**,** 1858-1876.

Whalley, L. K., Edwards, P. M., Furneaux, K. L., Goddard, A., Ingham, T., Evans, M. J., Stone, D., Hopkins, J. R., Jones, C. E., Karunaharan, A., Lee, J. D., Lewis, A. C., Monks, P. S., Moller, S. J. & Heard, D. E. 2011. Quantifying the magnitude of a missing hydroxyl radical source in a tropical rainforest. *Atmospheric Chemistry and Physics,* 11**,** 7223-7233.

Winiberg, F. A. F., Smith, S. C., Bejan, I., Brumby, C. A., Ingham, T., Malkin, T. L., Orr, S. C., Heard, D. E. & Seakins, P. W. 2015. Pressure-dependent calibration of the OH and HO_2 channels of a FAGE HO_x instrument using the Highly Instrumented Reactor for Atmospheric Chemistry (HIRAC). *Atmospheric Measurement Techniques,* 8**,** 523-540.

Chapter 4. Development of the FAGE method for CH_3O_2 detection

Chapter 1 explained why the methyl peroxy (CH_3O_2) radical is a key component of atmospheric chemical systems, and that despite its importance there are no direct, specific methods to detect it in the atmosphere, and laboratory measurements are almost exclusively absorption based. The focus of this chapter is the development of a FAGE technique to detect CH_3O_2 radicals that is sensitive enough to fill the gap in atmospheric measurements and complement the absorption-based kinetics measurements. In Chapter 3 a FAGE instrument designed to detect OH and HO_2 radicals was described in detail, showing its construction and working principles. This FAGE instrument provides the foundation that the new technique builds upon to produce a FAGE instrument that can detect OH, HO_2 and CH_3O_2 radicals.

As with HO_2 LIF, the O-O bond in CH_3O_2 is too weak to be a viable target for LIF detection and instead the radical must be converted into the methoxy radical (CH_3O) first. With five atoms, this radical has a much more complex LIF excitation and emission spectrum than OH, and the FAGE instrument had to be adapted to detect CH_3O before work could begin on detecting CH_3O_2 radicals.

To test, optimise and calibrate the instrument, methods to generate quantifiable CH_3O and CH_3O_2 radicals were developed by adapting the HO_x calibration equipment described in section 3.2.1. The calibration methods are discussed first, followed by the development of the FAGE instrument itself. The development is broken up into two parts: firstly, optimising the detection of CH_3O radicals as these are the LIF active species that will be used when detecting CH_3O_2 radicals; secondly the final setup for detecting CH_3O_2 radicals by conversion with NO, which is analogous to the detection of HO_2.

4.1 CH_3O and CH_3O_2 Radical generation – water vapour photolysis

Methods to quantitatively generate CH_3O and CH_3O_2 radicals were required to develop the FAGE instrument and calibrate it. The HO_x calibration equipment, described in section 3.2.1, was adapted to generate these radicals photolytically

at 184.9 nm. CH_3O radicals were generated directly by photolysing methanol in nitrogen, whilst CH_3O_2 radicals were generated by photolysing water vapour in the presence of methane and oxygen. The quantity of radicals generated could be varied in the range of 0.5-5 $\times 10^{10}$ molecule cm^{-3} by changing the electrical power supplied to the photolysis lamp.

4.1.1 Methoxy radicals

CH_3O radicals were generated using the same equipment described in section 3.2.1, except the air was replaced with nitrogen (BOC, 99.998 %) as a carrier gas and a methanol bubbler was used in place of a water bubbler. Nitrogen was flowed through the system at 40 SLM, with a portion of the flow directed through the methanol bubbler. The nitrogen and methanol vapour re-join the main flow and pass through the calibration wand where the methanol is photolysed at 184.9 nm. The dominant photolysis channel of CH_3OH between 165-200 nm produces CH_3O radicals (Kassab et al., 1983, Marston et al., 1993, Wen et al., 1994) *via*:

$$\mathrm{CH_3OH} + h\nu(165 - 200\ \mathrm{nm}) \rightarrow \mathrm{CH_3O} + \mathrm{H} \qquad \textbf{R 4.1}$$

Nitrogen was used as the carrier gas in this experiment, as any oxygen present will react with CH_3O to give formaldehyde and interfere with the calibration:

$$\mathrm{CH_3O} + \mathrm{O_2} \rightarrow \mathrm{HCHO} + \mathrm{HO_2} \qquad \textbf{R 4.2}$$

The radical concentration was then calculated by adapting Eq. 3.3 which was used for HO_x radical calibrations to give Eq. 4.1:

$$[\mathrm{CH_3O}] = [\mathrm{CH_3OH}] \times \sigma_{\mathrm{methanol}} \times \phi_{\mathrm{CH3O}} \times F \times t \qquad \textbf{Eq. 4.1}$$

where $\sigma_{methanol}$ is the absorption cross section of methanol at 184.9 nm, 6.35×10^{-19} cm^2 $molecule^{-1}$ taken as an average of reported values (Nee et al., 1985, Jimenez et al., 2003, Dillon et al., 2005). The product of the lamp flux, *F,* and the photolysis time, *t,* at 40 SLM was determined by N_2O actinometry (section 3.2.2). While it is known that breaking the O-H bond is a major product of methanol photolysis at 184.9 nm (Porter and Noyes, 1959, Buenker et al., 1984), the quantum yield of the CH_3O radical, $\Phi_{\mathrm{CH_3O},184.9\ \mathrm{nm}}$, is not reported. However,

the quantum yield at 193.3 nm has been reported as $\Phi_{CH_3O,193.3\ nm}$ = 0.86 ± 0.10 (Satyapal et al., 1989) and is assumed to be equal to that at 184.9 nm for this work. The methanol concentration could not be measured directly and instead the average water concentration during a typical HO_x calibration was used with the ratio of the methanol and water vapour pressures, p_{CH3OH} and p_{H2O}, to estimate [CH_3OH] using Eq. 4.2:

$$[CH_3OH] = [H_2O]\frac{p_{CH3OH}}{p_{H2O}} \qquad \textbf{Eq. 4.2}$$

Typical [H_2O] values are ~8.5 × 10^{16} molecule cm^{-3}, and the vapour pressures are corrected for the temperature of the methanol and water bubblers, 13 and 15 ˚C. This is an approximation that cannot be relied upon for accurate measurement of CH_3O radicals, however for the purposes of this thesis only the ability to generate CH_3O to optimise the instrument was required.

4.1.2 Methyl peroxy radicals

CH_3O_2 radicals were generated using the same equipment described in section 3.2.1 to generate HO_x radicals with some minor adaptations. Synthetic air (BOC, synthetic BTCA 178) was passed through the water bubbler and calibration wand at 40 SLM to produce a humidified air mixture, with a total photolysis time of ~8.3 ms. The humidity of the gas mixture was adjusted by allowing a portion of the air to bypass the water bubbler, producing water vapour concentrations in the range of 0.8-3 × 10^{17} molecule cm^{-3}. Methane (BOC, CP grade (BOC, CP grade, 99.5 %) was added in excess to the gas flow prior to the calibration wand at 82.5 sccm. The UV lamp in the wand (LOT-Oriel, Hg(Ar)) photolysed the water vapour to produce OH that reacts with methane to produce methyl radicals:

$$CH_4 + OH \rightarrow CH_3 + H_2O \qquad \textbf{R 4.3}$$

The methyl radicals then combined rapidly with oxygen to produce CH_3O_2 radicals:

$$CH_3 + O_2 + M \rightarrow CH_3O_2 + M \qquad \textbf{R 4.4}$$

where M was N_2 or O_2. At these flow rates, methane was present in ~5 × 10^{16} molecule cm^{-3}, taking the rate coefficient of R 4.3 to be $k_{R4.3}$ = 6.4 × 10^{-15} cm^3 $moleucle^{-1}$ s^{-1} (Atkinson et al., 2006) the lifetime of OH, τ_{OH}, can be calculated using the following equation:

$$\tau_{OH} = \frac{1}{k_{R4.3}[\mathrm{CH_4}]} \qquad \textbf{Eq. 4.3}$$

giving τ_{OH} = ~3 ms, which is much shorter than the ~8 ms photolysis time. Typical OH concentrations were in the range ~4 × 10^8 molecule cm^{-3}, and the fraction of OH converted to CH_3 radicals can be calculated using pseudo-first order kinetics as methane is in excess:

$$[\mathrm{OH}]_t = [\mathrm{OH}]_0 \exp(-k't) \qquad \textbf{Eq. 4.4}$$

where *k'* is the pseudo-first order rate coefficient of R 4.3, *k'* = $k_{R4.3}$ × $[CH_4]$. The total reaction time, *t*, is longer than the ~8 ms photolysis time as the gas mixture leaves the wand and travels ~0.5-1 cm to the FAGE inlet. The total reaction time is therefore estimated to be ~11 ms and using Eq. 4.7 $[OH]_{11ms}$ = ~1.3 × 10^7 molecule cm^{-3}, or 97 % loss. This was confirmed experimentally by measuring the OH signal using FAGE both with and without the presence of methane, shown in Figure 4.1, in which showed a ~96 ± 4 % loss in signal upon switching on the methane flow at 82.5 ms. Increasing the methane flow yielded no discernible increase in the CH_3O_2 detected by FAGE.

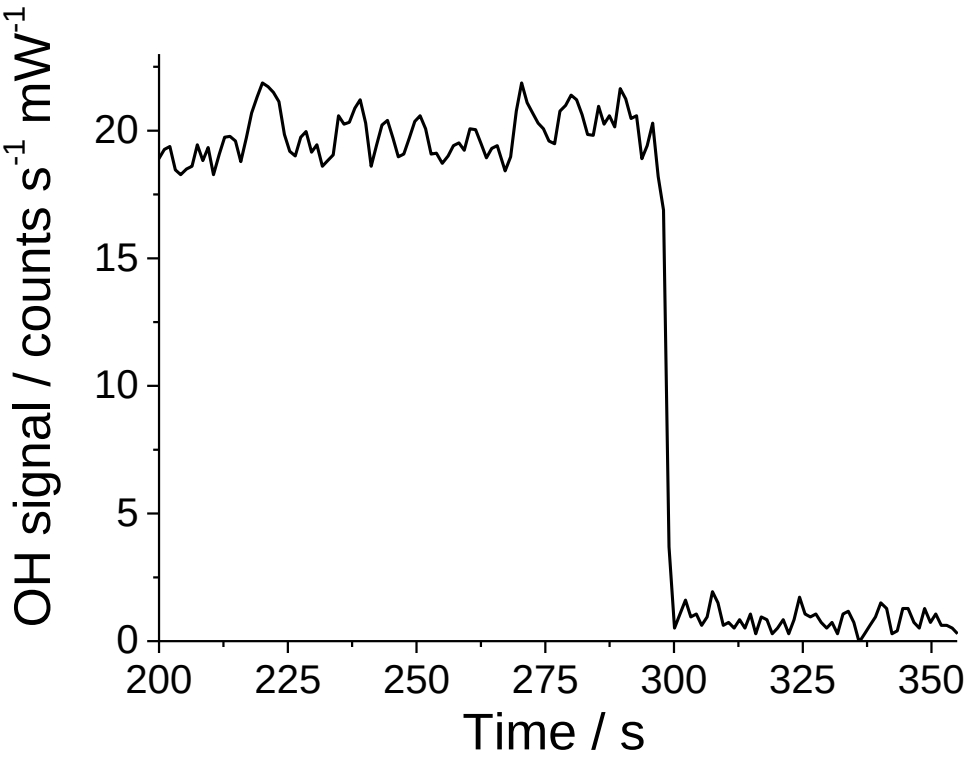

Figure 4.1 FAGE measurement of a constant level of OH being generated by the calibration wand. At 300 seconds, methane is added to the calibration gas flow and consumes the OH to produce CH_3O_2 radicals. The signal drops by ~96 % indicating near total conversion.

To calculate the CH_3O_2 concentration generated by the wand, the HO_2 calibration equation, Eq. 3.3, needs to be modified to account for the 96 % conversion of OH into CH_3O_2 and becomes:

$$[\mathrm{CH_3O_2}] = 0.96 \times [\mathrm{H_2O}] \times \sigma_{\mathrm{H_2O,185\,nm}} \times \Phi_{\mathrm{OH}} \times F \times t \qquad \textbf{Eq. 4.5}$$

The calibration procedure has been updated more recently, using a slower total flow rate of 20 SLM and higher methane flows of 114 sccm to generate higher total radical concentrations, therefore the testing outlined here needs to be repeated. It is noted however that the correction of ~4 % is very small and may be neglected.

The HO_2 co-product of the water photolysis method is a potential sink of CH_3O_2 radicals, but with a rate coefficient of 5.2×10^{-12} cm^3 $molecule^{-1}$ s^{-1} (Atkinson et al., 2006) the reaction takes place on timescales >10 seconds at the

concentrations present in the wand, whereas the photolysis and FAGE sampling occur on the millisecond timescale, and so can be ignored. By adjusting the lamp current, flow rate and the fraction of air bypassing of the bubbler, this method can generate CH_3O_2 radicals up to approximately 2×10^{10} molecule cm^{-3}.

4.2 FAGE development - CH_3O LIF excitation spectrum

LIF detection of CH_3O radicals has been used extensively in the past for a range of kinetic studies involving the radical (Biggs et al., 1993, Biggs et al., 1997, Albaladejo et al., 2002, Shannon et al., 2013, Chai and Dibble, 2014), each using the $A\ ^2A_1 \leftarrow X\ ^2E$ electronic transition which spans ~275-317 nm and produces red shifted fluorescence in the range of ~320-400 nm (Inoue et al., 1980, Kappert and Temps, 1989, Powers et al., 1997b, Powers et al., 1997a, Nagesh et al., 2014). Figure 4.2 shows the fluorescence excitation spectrum of the CH_3O radical between 277 and 322 nm (36000-31000 cm^{-1}) excitation range obtained by Inoue et al., 1980.

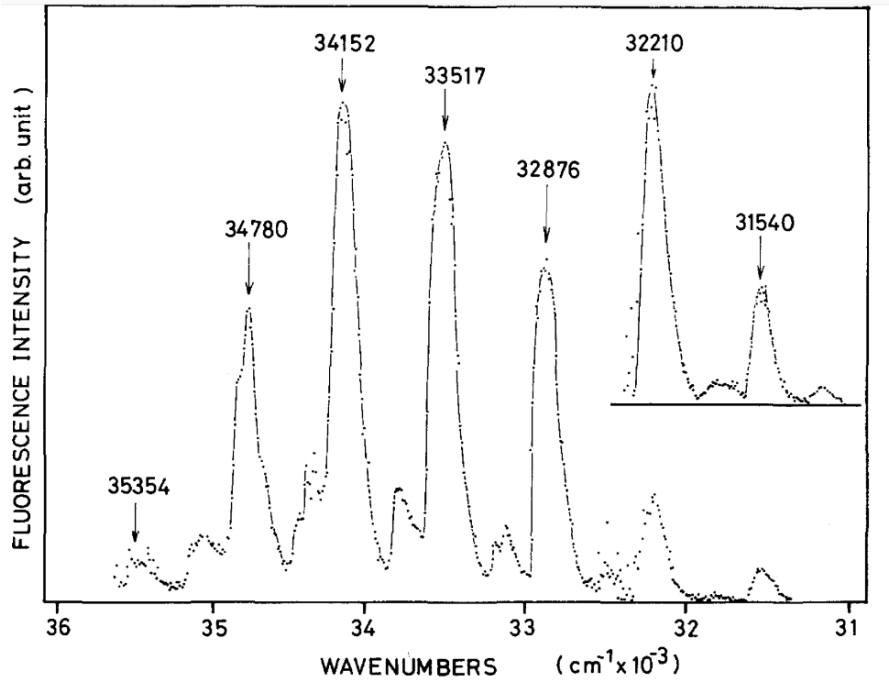

Figure 4.2 Fluorescence excitation spectrum of the methoxy radical $A\ ^2A_1 \leftarrow X\ ^2E$ electronic transition, obtained by Inoue et al., 1980. Methoxy radicals were excited with a bandwidth of 4.5 cm^{-1}, and fluorescence from 500 to 2000 cm^{-1} was monitored and normalised to laser power and relative instrument response. The large peaks represent the vibronic excitations, with the highest fluorescence intensity obtained when exciting the $v' = 4 \leftarrow v'' = 0$ transition at 34152 cm^{-1} (293 nm). Image taken from Inoue et al., 1980.

Each of the labelled peaks in Figure 4.2 correspond to the different vibronic transitions available within the electronic excitation band, with the peaks at 31540, 32210 and 32876 cm^{-1} attributed to excitation from v''=0 to v'=0, 1 and 2 respectively. The fluorescence intensity of the transitions increases successively as the overlap of the vibrational wavefunctions increases according to the Franck-Condon principle, peaking with the A^2A_1 (ν'_3 = 4) ← X^2E (ν''_3 = 0) transition at 34152 cm^{-1} (293 nm). This is shown more clearly in Figure 4.3, which shows the Morse potential energy curves of the ground and excited states.

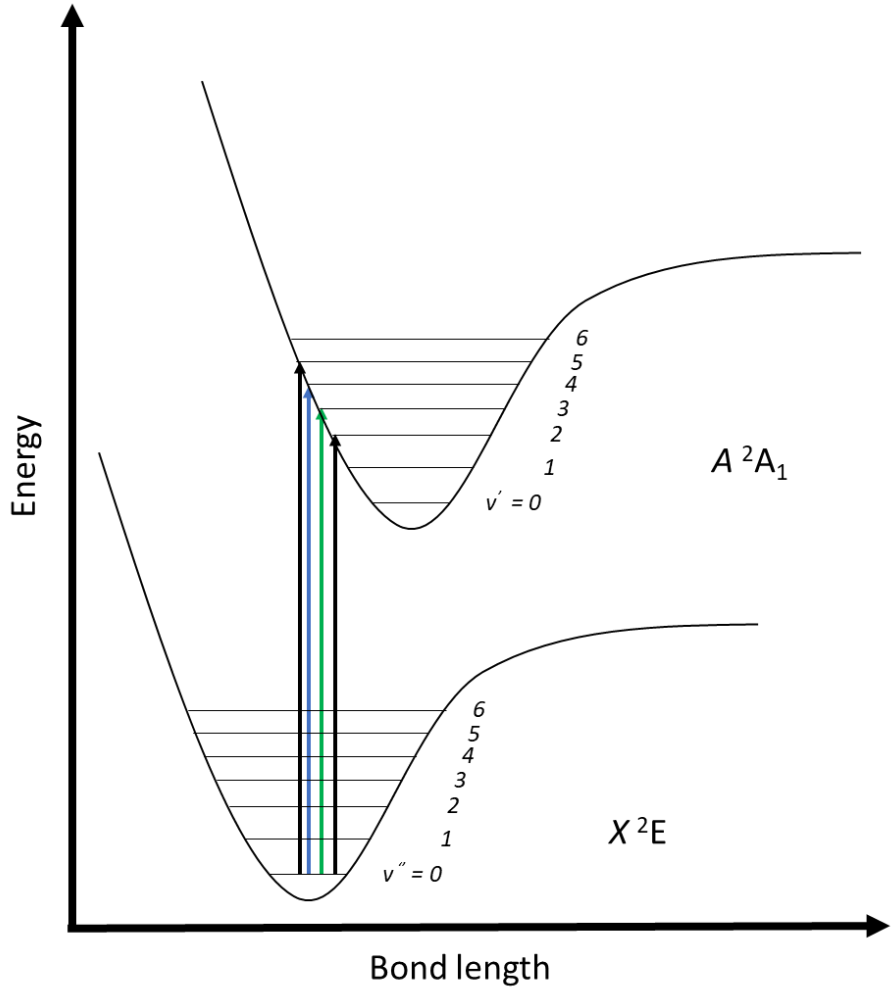

Figure 4.3 Morse potential energy diagram of the CH_3O radical $A\ ^2A_1 \leftarrow X\ ^2E$ excitation. Only the v''=0 → v'=2, 3, 4 and 5 transitions are shown for clarity, and each one requires a successively higher energy photon to occur. The excited state bond length is longer than in the ground state, causing the two curves to be offset from each other. The v''=0 → v'=4 transition (blue, 34152 cm^{-1}, 293 nm) yields the highest fluorescence signal as the Frank-Condon overlap is highest here.

The transition at ~293 nm (34152 cm^{-1}) yields the highest fluorescence signal and would therefore be the ideal wavelength to use, however it lies outside the optimum wavelength range of our laser dye mix (section 3.1.3). The transition at ~298 nm (33517 cm^{-1}) corresponds to the $v'' = 0 \rightarrow v' = 3$ transition, which is a convenient compromise as it resides within the wavelength range of the laser and the fluorescence signal is not significantly weaker. This enables the FAGE instrument to be quickly switched between HO_x and CH_3O_x (CH_3O or CH_3O_2) measurements, without needing to change laser dyes.

In contrast to OH, the abundance of possible vibrational and rotational states available to the CH_3O radical means that the fluorescence spectrum is broad and red-shifted to around 320 - 400 nm. Figure 4.4 shows the emission spectrum of the CH_3O radical after it was excited to the $^2A_1$ ($v' = 2$) rovibronic level by 304 nm light (Inoue et al., 1980), where the emitted photons are spread between ~305 and 380 nm as the excited radical relaxes into successively higher vibrational levels in the ground electronic state. The relative intensity of the emission is again dictated by the Franck-Condon principle.

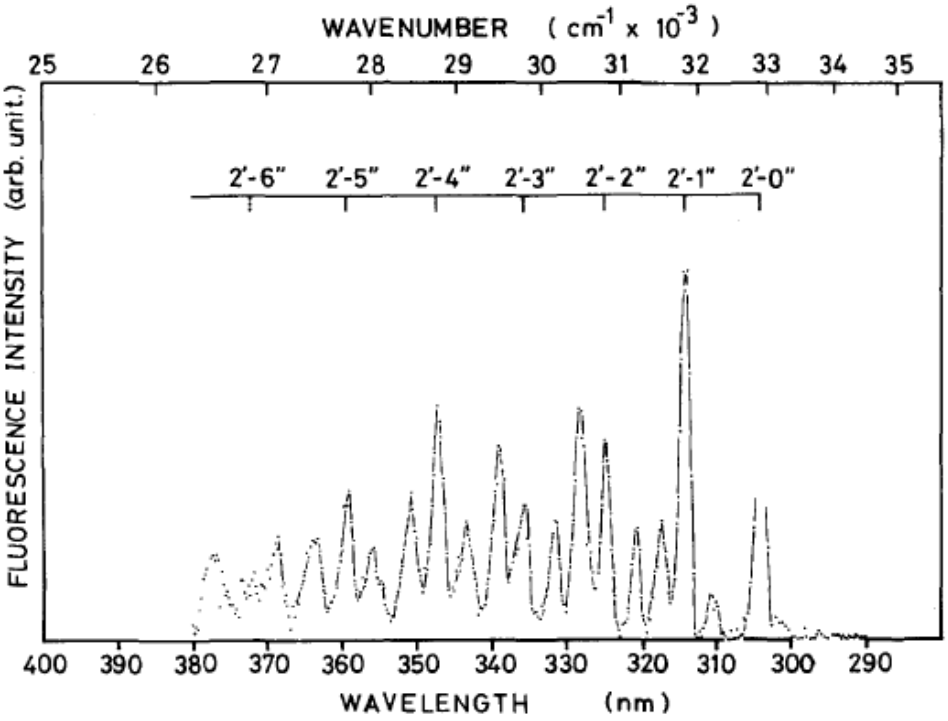

Figure 4.4 Fluorescence spectrum of the CH_3O radical after excitation to the $v' = 2$ vibration level of the $^2A_1$ electronic state. The fluorescence photons are spread over a large range, requiring a broad interference filter to collect as much light as possible. Image taken from Inoue et al., 1980.

The optical setup for collecting fluorescence photons was described in section 3.1.1, with four plano-convex lenses passing photons through an interference filter and onto the detector photocathode. The 308 ± 2.5 nm interference filter was not suitable for the broader and lower frequency fluorescence spectrum of CH_3O radicals and was replaced with a 320-430 nm bandpass filter (MagicGlass, >80 % transmission, 320-430 nm) with an average transmission of >80 % to accommodate the broad emission spectrum. The MCP detector (Photek PMT325/Q/BI/G) has a photocathode with a relatively flat quantum efficiency over 300-400 nm and therefore did not require modification.

In addition to the spectrum, the fluorescence lifetimes of OH and CH_3O are also different. At typical cell pressures of ~2.5 Torr the OH fluorescence lifetime is <1 µs, whereas the CH_3O lifetime has been measured on the order of 0.9 - 1.5 µs (Inoue et al., 1979, Wendt and Hunziker, 1979, Ebata et al., 1982). The signal integration time of the multi-channel scalar (photon counting card, section 3.1.4) was varied between 1 and 3 µs to find the point at which the entire fluorescence lifetime had been recorded after each laser pulse. The maximum signal was obtained at 2 µs and no change was observed when the time was increased to 3 µs, indicating that all fluorescent photons had been emitted within this timeframe.

4.2.1 The CH_3O A^2A_1 ($\nu'_3 = 3$) ← X^2E ($\nu''_3 = 0$) transition

The A^2A_1 ($\nu'_3 = 3$) ← X^2E ($\nu''_3 = 0$) transition is the ideal absorption feature for CH_3O LIF detection as it is a strong feature and lies within our laser dye range. The spectrum shown in Figure 4.2 is of low resolution, 4.5 cm^{-1}, compared to our 0.08 cm^{-1} bandwidth, and is therefore lacking the rotational fine structure. Figure 4.5 shows a CH_3O fluorescence excitation spectrum obtained using the FAGE instrument, and a constant radical concentration generated by methanol photolysis as described in section 4.1.1. The excitation wavelength was stepped in 1 pm increments from 297.0 nm to 299.5 nm, giving 2500 points integrated for one second each and capturing the peak of the feature reported by Inoue et al. and Kapert et al. at ~298 nm.

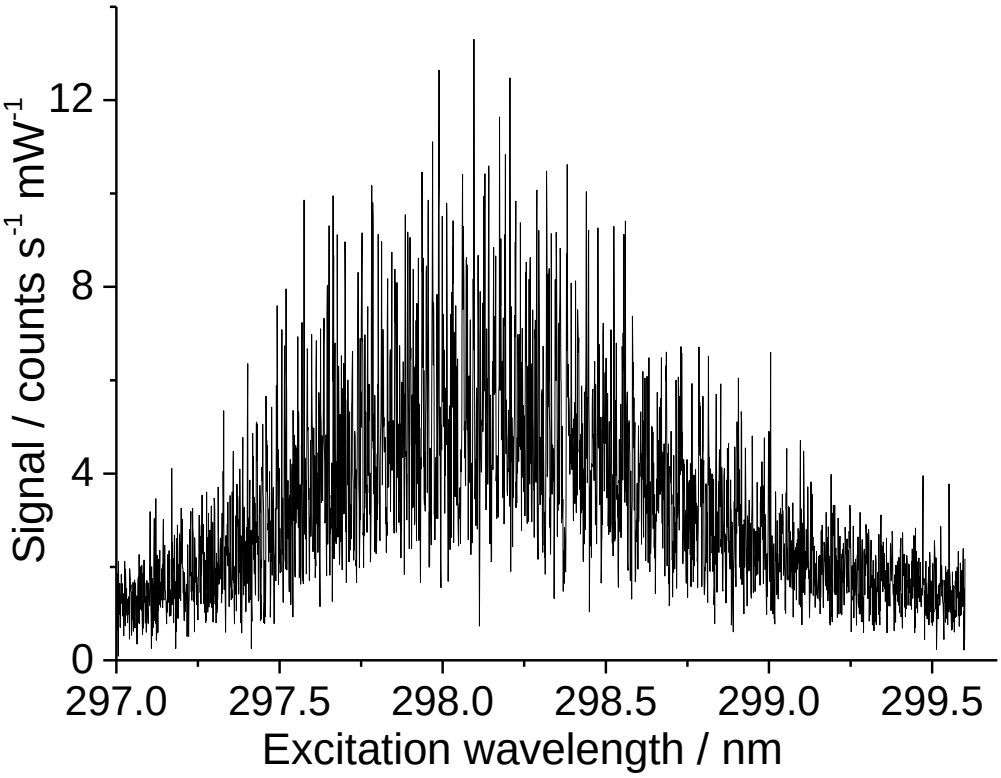

Figure 4.5 The fluorescence excitation spectrum of the CH_3O A^2A_1 ($\nu'_3 = 3$) ← X^2E ($\nu''_3 = 0$) transition, as measured using the FAGE instrument at 2.6 Torr. The scan was performed between 297.0 and 299.5 nm with incremental steps of 1 pm, and the signal at each point was integrated for 1 second.

With the higher resolution it is possible to see the curve is comprised of many sharp peaks that correspond to changes in the rotational structure of the molecule within the electronic transition, shown in Figure 4.6.

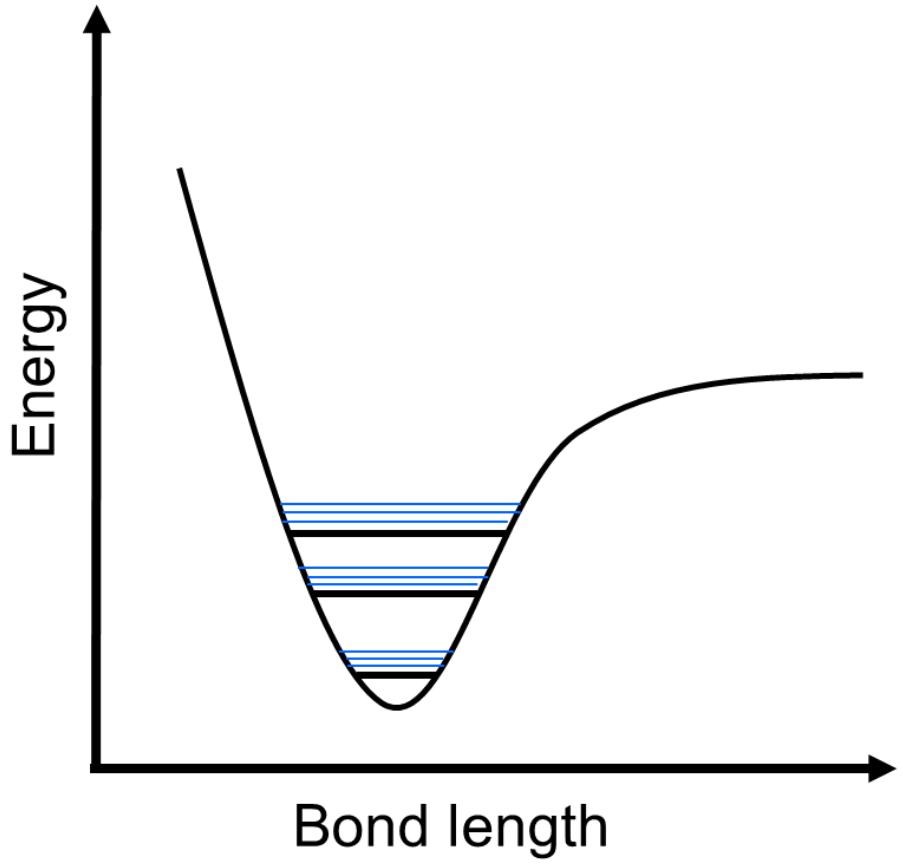

Figure 4.6 Arbitrary Morse potential of a polyatomic molecule, showing *v* = 0, 1 and 2 in black. Also represented are rotational energy levels in blue. These levels are very close together, with more complex molecules having a higher density. As they are very close together these higher rotational levels can be occupied by the molecule even at low temperature, making more discrete transitions possible but reducing the population density of any given energy level.

A simulation of the A^2A_1 ($\nu'_3 = 3$) ← X^2E ($\nu''_3 = 0$) transition at 300 K was provided by Professor Terry Miller of Ohio State University using their 'Spec View' program and is shown in Figure 4.7. The simulation is very similar in appearance to the FAGE measured spectrum, but the overlap is imperfect due to the signal noise introduced to an already crowded spectrum.

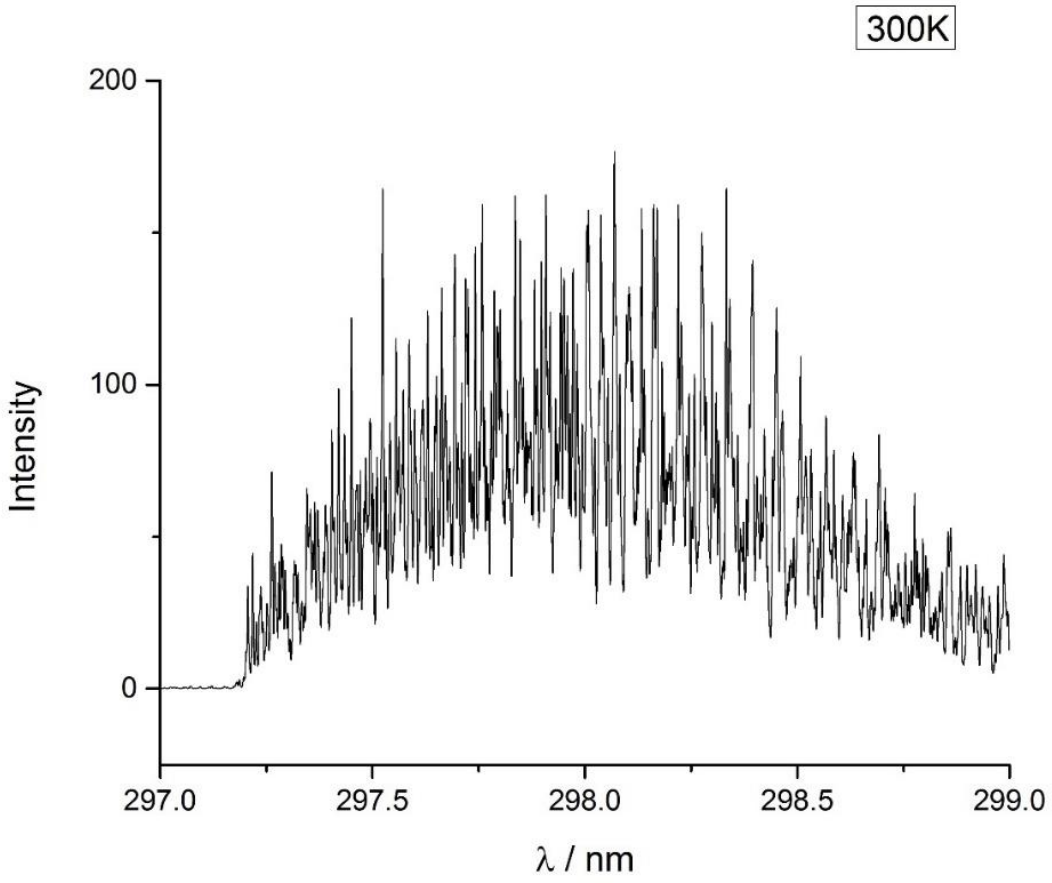

Figure 4.7 Simulated fluorescence excitation spectrum of the A^2A_1 ($\nu'_3 = 3$) ← X^2E ($\nu''_3 = 0$) provided by Professor Terry Miller of Ohio State University using their 'Spec View' simulation software. The simulation was performed at 300 K, and indicates maximum fluorescence is obtained when exciting at ~298 nm. Numerous rotational transitions are present, and the spectrum exhibits close similarity with the spectrum measured using FAGE.

Another simulation, this time at 100 K, is shown in Figure 4.8. The simulation shows the maximum LIF signal shifts to lower wavelengths and becomes narrower, which is a result of the much colder radicals having insufficient energy to occupy the higher rotational energy levels in the ground electronic state. This increases the population density in the lower rotational states and means more radicals are available for LIF excitation with higher frequency photons.

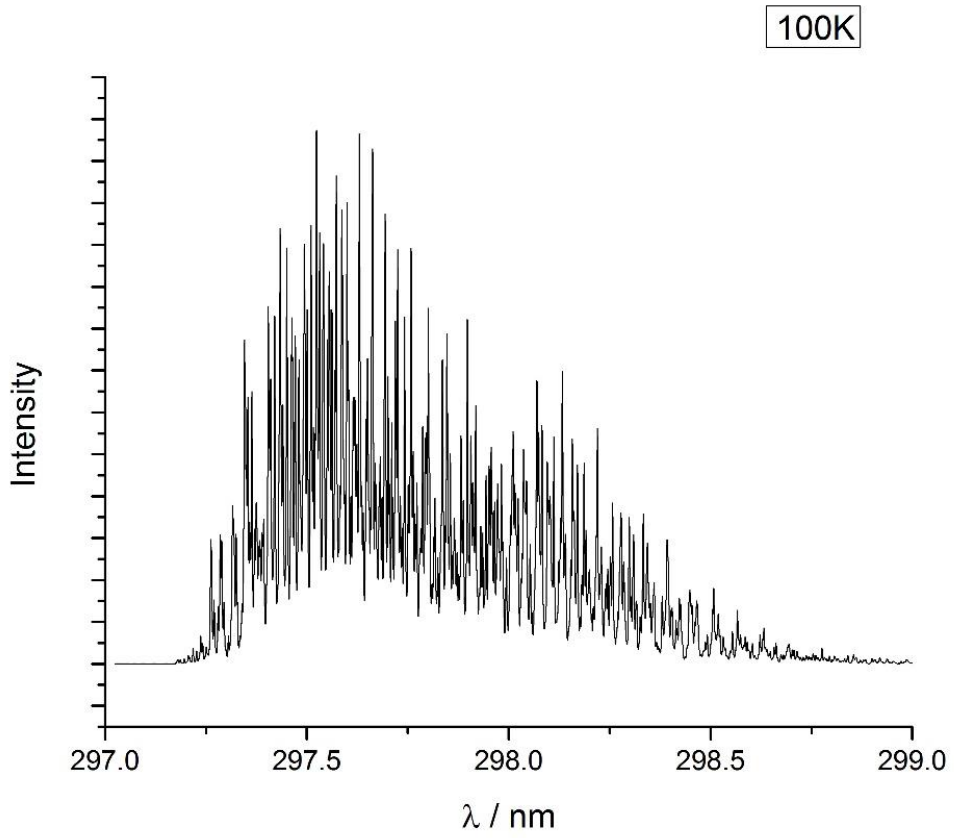

Figure 4.8 Simulated fluorescence excitation spectrum of the A^2A_1 ($\nu'_3 = 3$) ← X^2E ($\nu''_3 = 0$) provided by Professor Terry Miller of Ohio State University using their 'Spec View' simulation software. The simulation was performed at 100 K and shows the LIF spectrum begins to collapse towards shorter wavelengths as the cooling shifts the ground state population density to the lower energy levels.

The LIF excitation spectrum of the A^2A_1 ($\nu'_3 = 3$) ← X^2E ($\nu''_3 = 0$) transition at ~82 K and ~150 Torr has been measured by (Shannon et al., 2013), using a pulsed Laval nozzle system and the photolysis of methyl nitrite at 248 nm. The spectrum, shown in Figure 4.9, resembles the simulation at 100 K and shows a similar narrowing of the spectrum. From this, cooling the CH_3O radicals sampled by the FAGE instrument may be a way to increase the instrument sensitivity, and could be achieved by shortening the inlet to bring the pinhole and colder jetting region of the gas flow closer to the laser detection axis. While no determinations have been made at this time, the temperature in the FAGE cell is estimated to be close to the ambient laboratory temperature, which is maintained at approximately 292 K (19 ˚C), due to the long inlet allowing the gas inside to thermalize. This is based on previous work done with a different FAGE

instrument by Dr James Lee (Lee, 2000), who found that the rotational temperature of OH returned to ambient temperatures approximately 250 mm after the pinhole (whereas the inlet on the instrument in this work is 300 mm long). This may explain the imperfect overlap of the observed spectrum (Figure 4.5) and the simulation at 300 K (Figure 4.7).

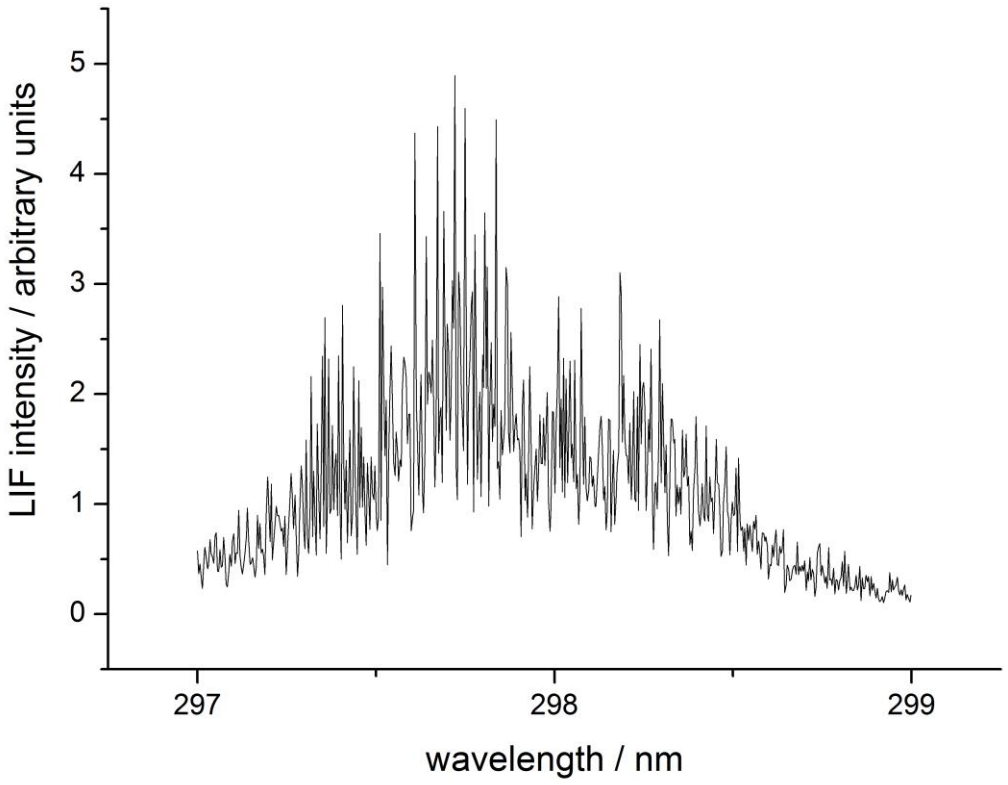

Figure 4.9 The fluorescence excitation spectrum of the CH_3O A^2A_1 ($\nu'_3 = 3$) ← X^2E ($\nu''_3 = 0$) transition at 82±4 K and ~150 Torr, measured by LIF using a pulsed Laval nozzle apparatus. Figure taken from Shannon et al., 2013.

The wavelength that produces maximum fluorescence yield is located at approximately 298 nm, and narrow scans of this portion of the spectrum were performed to locate the strongest rotational feature. Figure 4.10 shows the strongest feature that could be found and is composed of two peaks that relate to rotational transitions. The larger of the two features at 297.792 nm yields the highest fluorescence for the entire band and is the target of all CH_3O and CH_3O_2 LIF measurements reported here.

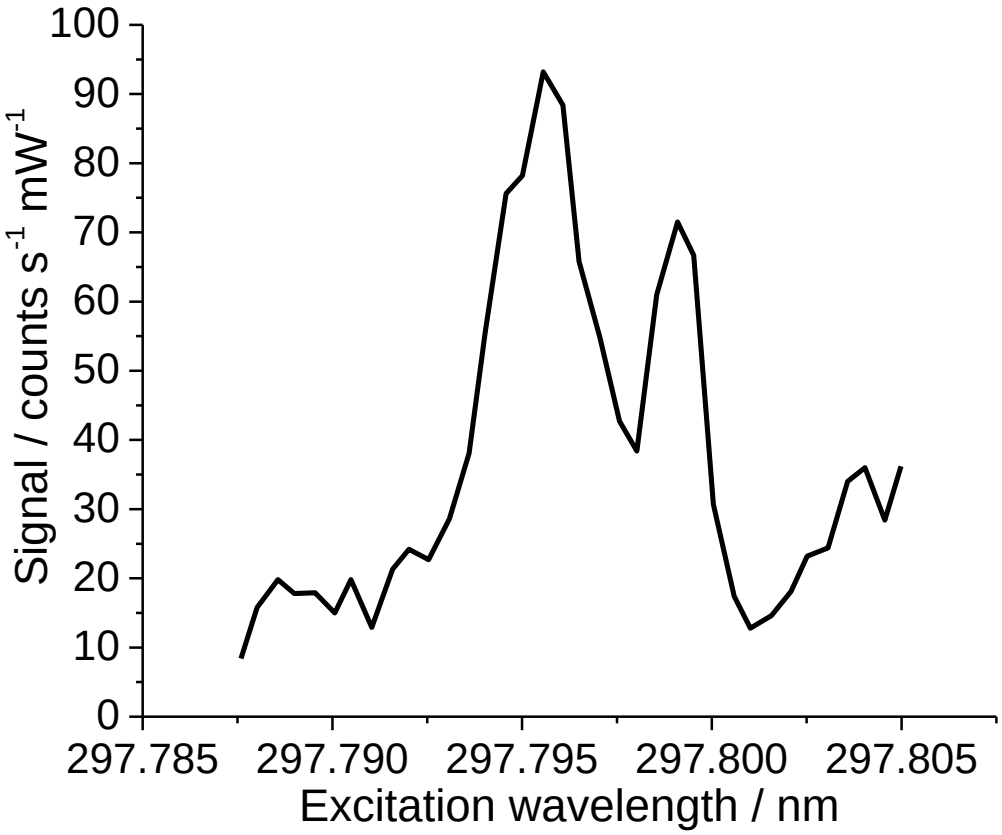

Figure 4.10 A fluorescence excitation spectrum of the CH_3O A^2A_1 ($\nu'_3 = 3$) ← X^2E ($\nu''_3 = 0$) transition between 297.780 and 297.805 nm, the region of maximum signal within the vibronic transition. Two peaks are present, one at 297.792 nm and a smaller one at 297.795 nm that are highly reproducible and represent two CH_3O rotational lines. The higher peak at 297.792 nm is used for all FAGE measurements of CH_3O radicals

The laser background is measured by moving the excitation wavelength away from any absorption features. This was described for OH LIF in section 3.1.5, where the wavelength is stepped 2 pm shorter to move off the narrow OH line. In contrast, the CH_3O absorption band is very wide and complex, a small increment like this would not move sufficiently far enough to leave only laser scatter as a signal. To get a truly offline measurement the laser was stepped +2.5 nm to move completely away from the absorption feature.

4.3 FAGE development - detection of CH_3O_2

The CH_3O_2 radical, like HO_2, must be titrated with nitric oxide to produce CH_3O radicals in the reaction:

$$CH_3O_2 + NO \rightarrow CH_3O + NO_2 \qquad \textbf{R 4.5}$$

and the CH_3O radicals are then detected by LIF. The NO is injected through the same 1/8th inch stainless steel pipe for HO_2 detection discussed in section 3.1.1, 25 mm from the laser detection axis. The rate at which the NO is injected is critical to achieving a good LIF signal; too little will lead to low conversion and low signal, whilst too much will promote further reactions that destroy CH_3O before detection:

$$CH_3O + NO + M \rightarrow CH_3ONO + M \qquad \textbf{R 4.6}$$

$$CH_3O + NO \rightarrow CH_2O + HNO \qquad \textbf{R 4.7}$$

$$CH_3O + O_2 \rightarrow CH_2O + HO_2 \qquad \textbf{R 4.8}$$

where M is N_2 or O_2. The NO injection point was approximately 25 mm prior to the laser detection axis, and with a typical instrumental sampling rate of approximately 5 SLM leaves around 3 ms of reaction time before reaching the laser axis. The optimum addition rate was determined experimentally by generating a constant CH_3O_2 concentration using the method described in section 4.1.2 and increasing the NO injection rate to see how the signal responds. Figure 4.11 shows the effect of varying the NO injection concentration between 0 and 1×10^{14} molecule cm^{-3}, which corresponds to 0 and 4 sccm injection flow rates.

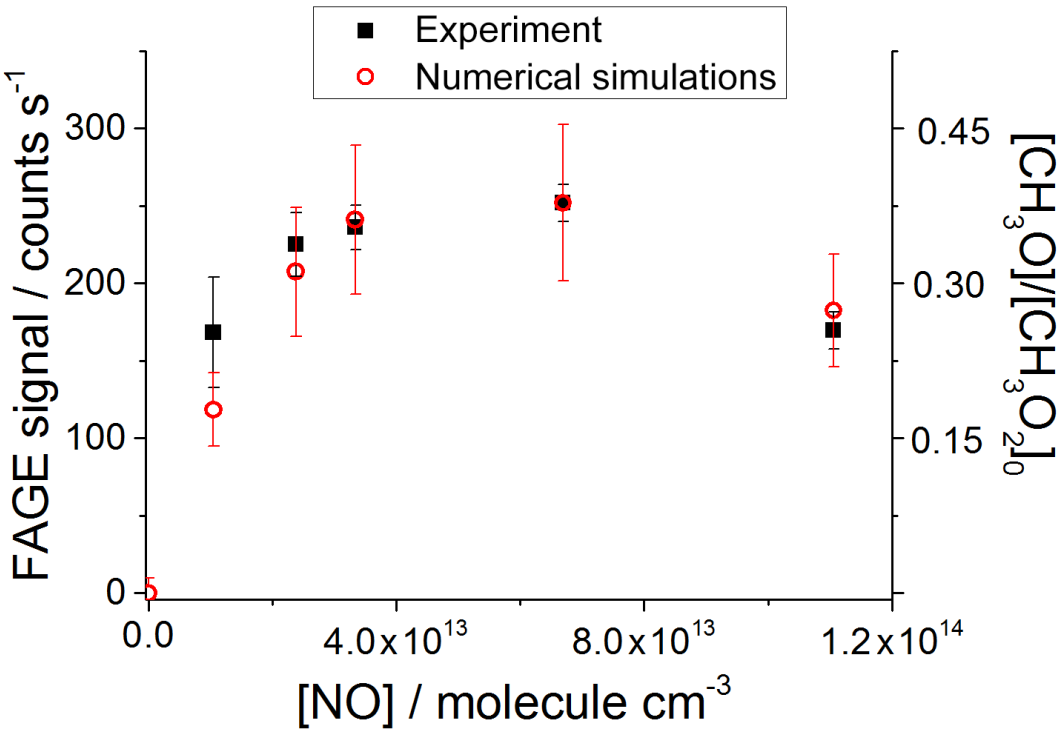

Figure 4.11 The effect of addition rate of pure NO on the FAGE signal (left axis) and fractional conversion (right axis). The experimental points (black) were obtained by generating a constant CH_3O_2 concentration whilst varying the NO addition rate between 0 and 4 sccm. The maximum fluorescence signal was obtained when adding NO in the region of 4 to 8 × 10^{13} molecule cm^{-3}, corresponding to ~1.5-3 sccm addition rate. This is confirmed by numerical simulations performed by Dr. L. Onel (red) that also reveal a maximum ~40 % $[CH_3O]/[CH_3O_2]$ ratio obtained at similar NO concentrations.

Maximum fluorescence was obtained with an injection flow rate of 2.5 sccm, which corresponds to 6.7 × 10^{13} molecule cm^{-3} of NO. Numerical simulations, performed by Dr L. Onel, using Kintecus (Ianni, 2002) indicated that maximum conversion occurs at concentrations around 4-5 × 10^{13} molecule cm^{-3} and showed that the conversion ratio $[CH_3O]/[CH_3O_2]_0$ was around 40 %. These calculations were performed using the chemical mechanism described by reactions R 4.5–R 4.8 with rate coefficient shown, in the following table:

Table 4.1 Table of rate coefficients for reactions used in Kintecus (Ianni, 2002) modelling of CH_3O_2 titration with NO to produce CH_3O radicals. Rate coefficients are the IUPAC preferred values at 298 K by Atkinson et al., 2006. The rate constant for the termolecular R4.6 was calculated for a typical cell pressure of 2.6 Torr.

Reaction	Rate coefficient / molecule^{-1} cm^3 s^{-1}
R4.5	7.7×10^{-12}
R4.6	2.2×10^{-12}
R4.7	2.3×10^{-12}
R4.8	1.9×10^{-15}

4.4 Calibration

The FAGE instrument was calibrated for CH_3O and CH_3O_2 radicals using the UV photolysis methods described in section 4.1 to generate radicals. The power delivered to the photolysis lamp was varied to generate a range of radical concentrations and the response of the FAGE signal normalised to laser power recorded. Fitting a linear regression to a plot of the normalised FAGE signal against generated radical concentration, gives the sensitivity factor for each radical, C_{CH_3O} and $C_{CH_3O_2}$ from the gradient. In a procedure similar to the HO_2 self-reaction calibration described in section 3.2.3, the instrument was also calibrated using the CH_3O_2 self-reaction by using the observed rate coefficient for the self-reaction, k_{obs}, recommended by IUPAC.

As with the HO_2 calibrations, the sensitivity factor links the FAGE signal to $[CH_3O_2]$ *via*:

$$[\mathrm{CH_3O_2}] = \frac{S_{\mathrm{CH_3O_2}}}{C_{CH_3O_2}} \qquad \textbf{Eq. 4.6}$$

where $S_{\mathrm{CH_3O_2}}$ is the normalised CH_3O_2 signal measured by FAGE, in units of counts s^{-1} mW^{-1}.

4.4.1 Wand calibration method

Figure 4.12 and Figure 4.13 show calibration plots for CH_3O and CH_3O_2 radicals respectively, from which average FAGE sensitivity factors C_{CH_3O} = (5.1 ± 2.2) × 10^{-10} counts s^{-1} mW^{-1} cm^3 $molecule^{-1}$ and $C_{CH_3O_2}$ = (8.0 ± 2.7) × 10^{-10} counts s^{-1} mW^{-1} cm^3 $molecule^{-1}$ where the error reported is the overall systematic and statistical error, 43 % and 34 %, respectively. The larger error for the CH_3O calibration is attributed to the indirect measurement of the methanol concentration and 12 % error in the photolysis yield of CH_3O. The sources of error are discussed in more detail in section 4.5 below. It should be noted that these two calibrations were performed almost two years apart, during which time the instrument has been re-built / cleaned and is the reason the sensitivity for CH_3O_2 is much higher than CH_3O.

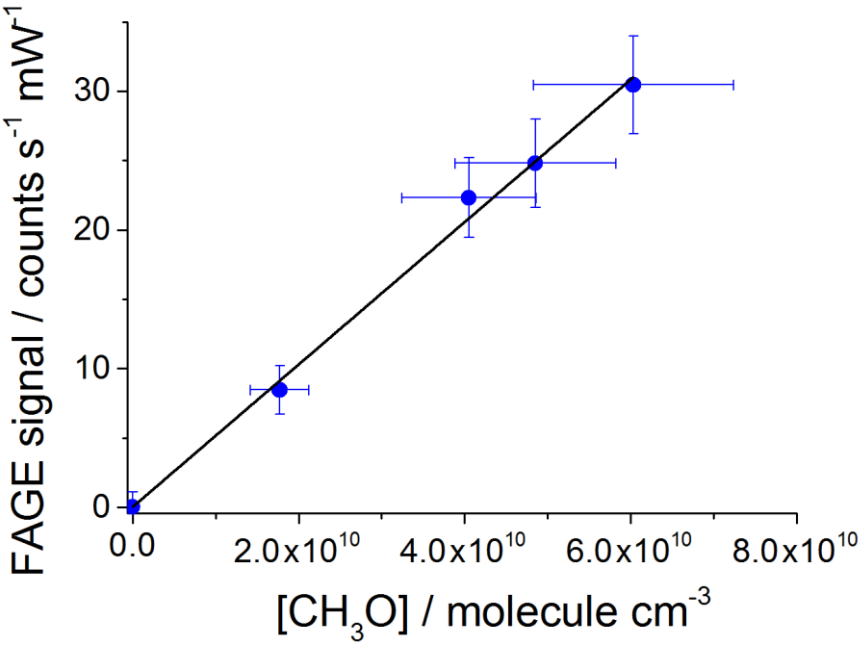

Figure 4.12 Calibration plot of the FAGE instrument for CH_3O using the methanol photolysis method to generate the radicals. The error bars on [CH_3O] and FAGE signal represent the systematic and statistical errors at 1σ detailed in the main text. The gradient of the linear fit gives the sensitivity factor C_{CH_3O} = (5.1 ± 0.6) × 10^{-10} counts s^{-1} mW^{-1} cm^3 $molecule^{-1}$, where the error reported is the standard error in the fitting process. Figure adapted from (Onel et al., 2017).

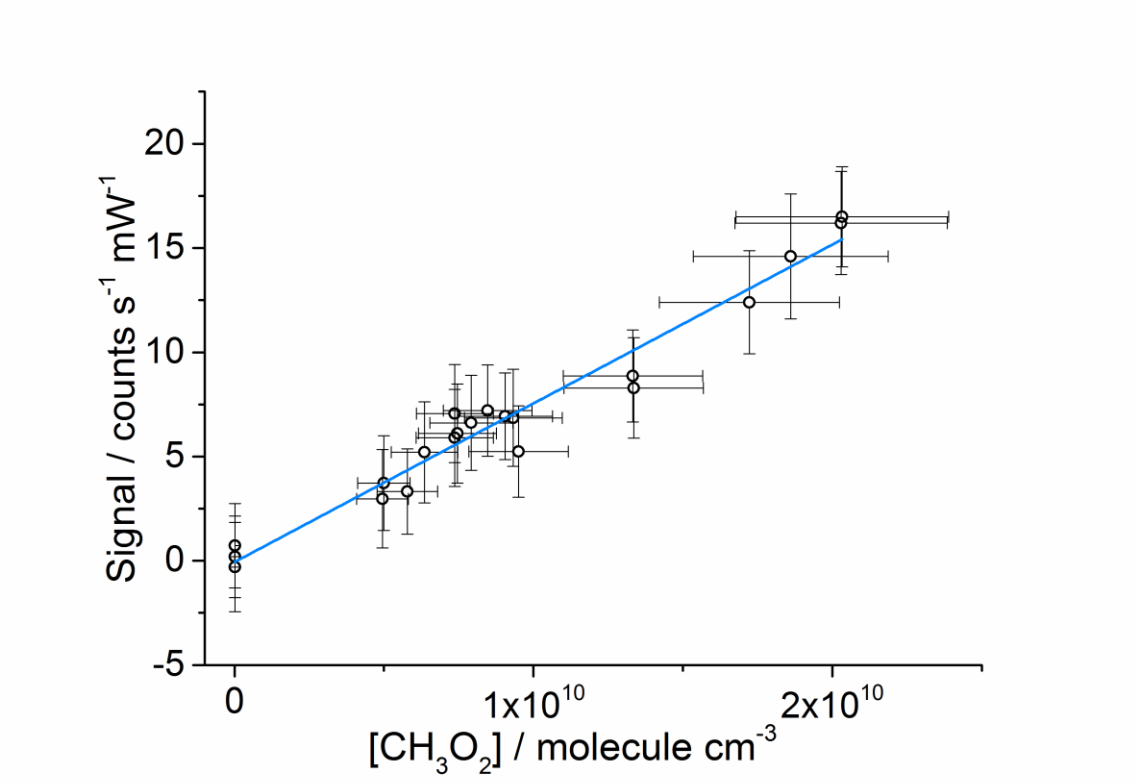

Figure 4.13 Calibration plot of the FAGE instrument for CH_3O_2 using the water vapour photolysis method to generate the radicals. The error bars on [CH_3O_2] and FAGE signal represent the systematic and statistical errors at 1σ detailed in the main text. The gradient of the linear fit gives a sensitivity factor $C_{CH_3O_2}$ = (7.6 ± 0.4) × 10^{-10} counts s^{-1} mW^{-1} $molecule^{-1}$ cm^3, where the error reported is the standard error in the fitting process.

The limits of detection (LOD) of the FAGE instrument was calculated using the following equation:

$$LOD = \frac{SNR}{C_X \times P}\sqrt{\frac{S_{Back} \times P}{t}\left(\frac{1}{m}+\frac{1}{n}\right)} \qquad \textbf{Eq. 4.7}$$

where SNR is the signal to noise ratio, C is the sensitivity factor, P is the laser power in mW, S_{back} is the normalised background (offline) signal and t is the averaging time in seconds. The values m and n are the number of measurement (online) points and the number of background points respectively. For the two radicals, LOD(CH_3O) = 3.0 × 10^8 molecule cm^{-3} and LOD(CH_3O_2) = 2.1 × 10^8 molecule cm^{-3} respectively for a 5-minute average measurement, where SNR =2, P = 15 mW, *t* = 1 s and *m* = *n* = 150.

4.4.2 Kinetic calibration method for CH_3O_2

The kinetic calibration method for HO_2 radicals detailed in section 3.2.3 can also be applied to the CH_3O_2 radical using its self-reaction, using similar chlorine photolysis at ~360 nm to initiate the reaction. These calibrations were performed in the HIRAC chamber at 298 K and 1000 mbar using a N_2 (BOC, >99.998 %) and O_2 (BOC, 99.999%) mixture in the ratio 80:20. Methane (BOC, CP grade) and molecular chlorine (Sigma Aldrich, ≥ 99.5 %) were added to the chamber in quantities of 2-3 × 10^{17} molecule cm^{-3} and 0.3-2.1 × 10^{14} molecule cm^{-3} respectively. Molecular chlorine is photolysed by ~360 nm light (Phillips, TL-D 36W/BLB), and the resulting chlorine atoms react with methane to produce methyl radicals which combine with oxygen to form CH_3O_2 radicals:

$$CH_4 + Cl_2 \rightarrow CH_3 + HCl \qquad \textbf{R 4.9}$$

$$CH_3 + O_2 + M \rightarrow CH_3O_2 + M \qquad \textbf{R 4.10}$$

The lamps are left on for 2-3 minutes to generate a steady state radical concentration, and are then switched off for a further two minutes to initiate a self-reaction decay:

$$CH_3O_2 + CH_3O_2 \rightarrow CH_3OH + CH_2O + O_2 \qquad \textbf{R 4.11}$$

$$CH_3O_2 + CH_3O_2 \rightarrow CH_3O + CH_3O + O_2 \qquad \textbf{R 4.12}$$

$$CH_3O + O_2 \rightarrow CH_2O + HO_2 \qquad \textbf{R 4.13}$$

The process of turning the lights on and off was repeated to generate a series of typically 4 decays. The loss of CH_3O_2 can be described by the integrated second order rate equation:

$$\frac{1}{[CH_3O_2]_t} = \frac{1}{[CH_3O_2]_0} + 2 \times k_{obs} \times t \qquad \textbf{Eq. 4.8}$$

where $[CH_3O_2]_t$ is the radical concentration at time *t* of the decay, $[CH_3O_2]_0$ is the initial concentration of CH_3O_2 when the lamps are switched off, and k_{obs} is the observed rate coefficient recommended by IUPAC, k_{obs} = (4.8 ± 1.1) × 10^{-13} cm^3

molecule^{-1} s^{-1} (Atkinson et al., 2006), which accounts for the additional loss caused by the generation of HO_2 radicals in R 4.13 (This is discussed more in section 6.1). Substituting Eq. 4.6 into Eq. 4.8 allows the measured signal during the temporal decay to be related to the sensitivity *via*:

$$\frac{1}{(S_{CH_3O_2})_t} = \frac{1}{(S_{CH_3O_2})_0} + \frac{2 \times k_{obs} \times (t - t_0)}{C_{CH_3O_2}} \qquad \textbf{Eq. 4.9}$$

where $(S_{CH_3O_2})_t$ and $(S_{CH_3O_2})_0$ are the FAGE signals at time t and t = 0 respectively. The reciprocal of Eq. 4.9 is then used to fit the CH_3O_2 self-reaction:

$$(S_{CH_3O_2})_t = \left(\frac{1}{(S_{CH_3O_2})_0} + \frac{2 \times k_{obs} \times (t - t_0)}{C_{CH_3O_2}} \right)^{-1} \qquad \textbf{Eq. 4.10}$$

There is also the potential for loss of CH_3O_2 radicals onto the metal walls of HIRAC, analogous to the HO_2 self-reaction kinetics. Including this first order loss process gives:

$$(S_{CH_3O_2})_t = \left(\left(\frac{1}{(S_{CH_3O_2})_0} + \frac{2 \times k_{obs}}{k_{loss} \times C_{CH_3O_2}} \right) \times \exp(k_{loss} \times (t\text{-}t_0)) - \left(\frac{2 \cdot k_{obs}}{k_{loss} \cdot C_{CH_3O_2}} \right) \right)^{-1} \qquad \textbf{Eq. 4.11}$$

where k_{loss} is the first order loss rate coefficient and could float during fitting. Figure 4.14 shows an example of this kinetic calibration where both Eq. 4.10 and Eq. 4.11 have been used to extract the CH_3O_2 sensitivity factors, $C_{CH_3O_2}$ = (1.18 ± 0.02) and $(1.15 \pm 0.03) \times 10^{-10}$ counts cm^3 molecule^{-1} s^{-1} mW^{-1}, respectively, where the error values are statistical fitting errors. The two factors are almost identical, and the k_{loss} fitting parameter returned extremely small values that were in the range of 10^{-6} - 10^{-14} s^{-1}. Compared to the HO_2 walls loss values in the range of 10^{-2} s^{-1} (section 3.2.3), this shows that there is negligible loss of CH_3O_2 to the walls, and this term is ignored from now on. Further evidence for the negligible wall loss is shown in section 5.1.3, when no significant concentration gradient could be measured across the diameter of HIRAC.

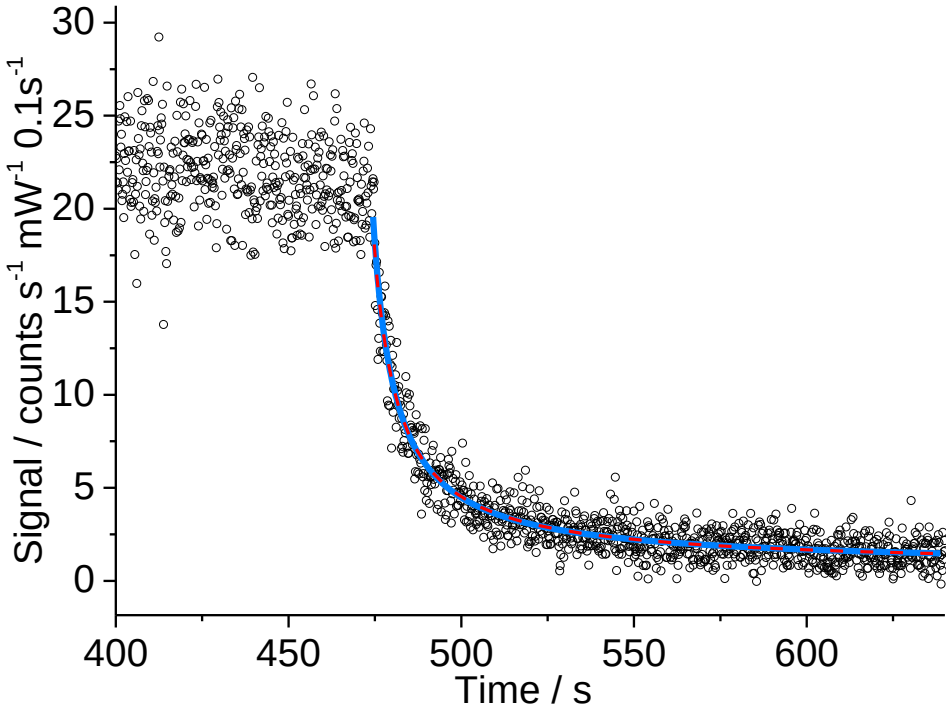

Figure 4.14 Second-order decay of the normalized CH_3O_2 signal with 0.1 s time resolution generated in HIRAC using the chlorine photolysis method described in the main text. $[CH_4] = 2.5 \times 10^{16}$ molecule cm^{-3} and $[Cl_2]_0 = 1.1 \times 10^{14}$ molecule cm^{-3} at 295K and 1 bar mixture of N_2:O_2 = 4:1. At ~475 seconds the 365 nm photolysis lamps were turned off. Fitting Eq. 4.10 to the data yielded $C_{CH3O2} = (1.18 \pm 0.02) \times 10^{-9}$ counts cm^3 molecule^{-1} s^{-1} mW^{-1} (statistical error at 1σ level). Fitting including the wall loss parameter gave $C_{CH3O2} = (1.15 \pm 0.03) \times 10^{-9}$ counts cm^3 molecule^{-1} s^{-1} mW^{-1}.

These calibrations were also performed at lower chamber pressures: 80 mbar of He:O_2 3:1, and 100 mbar of air, which are relevant conditions for the experiments detailed in Chapter 5. When sampling from HIRAC at these pressures the FAGE cell pressure is much lower, ~0.7 Torr at 100 mbar, compared to ~2.5 Torr at 1000 mbar. This caused a significant increase in sensitivity due to reduced collisional quenching of the excited CH_3O radicals, and the results are summarised in Table 4.2, where each value is an average of typically 8 decays.

Table 4.2 Average sensitivity factors for the FAGE instrument derived using the kinetic decay method (see text) under three different chamber environments. Each average is the result of typically 8 decays, the errors shown are the overall uncertainty (described in next section) of 28 % at 2σ.

Chamber Conditions	$C_{CH_3O_2}$ / counts cm^3 $molecule^{-1}$ s^{-1} mW^{-1}
80 mbar, He + O_2	$(3.83 \pm 1.1) \times 10^{-9}$
100 mbar, Air	$(2.80 \pm 0.78) \times 10^{-9}$
1000 mbar, Air	$(1.16 \pm 0.32) \times 10^{-9}$

The sensitivity obtained at 1000 mbar is approximately 31 % higher than the sensitivity obtained through the wand calibration method. This value does lie within the 2σ error limits, but the discrepancy is systematic. A similar 27 % discrepancy was observed during the first experiments performed with this instrument (Onel et al., 2017), more than a year prior to the ones listed here. The source of this discrepancy will be discussed in section 4.7.2, and will be investigated in the following chapters.

4.5 Instrument uncertainty

The error limits of the FAGE measurements for CH_3O and CH_3O_2 have been calculated as 43 % and 34 % at 2σ respectively with the wand calibration method. These error limits represent the sum in quadrature of the systematic uncertainty introduced by the calibration process and the statistical error in the fitting of the calibration plots. The error limit for CH_3O_2 when using the kinetic calibration method was calculated as 28 % at 2σ.

The sources of uncertainty in measurements made with the FAGE instrument can be split into two components: systematic and statistical uncertainty. The systematic uncertainty lies in the FAGE method and its calibration, whilst the statistical uncertainty arises through the random scatter of the FAGE signal which follows Poisson statistics and is accounted for in the fitting process.

4.5.1 Wand method

Water vapour photolysis is the most common calibration method for calibrating OH instruments, and is well established (Heard and Pilling, 2003, references therein). Previous work done using the FAGE instrument estimated similar uncertainty of 36 % when measuring HO_x radicals (Winiberg et al., 2015), compared to the 34 % estimated here for CH_3O_2 radicals. This similarity is because the two instruments rely on an almost identical calibration procedure, where most of the uncertainty lies in the same factor, the 184.9 nm photon flux of the lamp, $F_{184.9\,nm}$, at 28 %. The flux is determined by N_2O actinometry, described in section 3.2.2, where measurements are based on four chemical conversions and their associated rate coefficients, introducing ~20 % (±2σ) uncertainty (Burkholder et al., 2015), and the subsequent detection of trace levels of NO (0.2-1.5 ppb) by a commercial TEC 42C NO_x analysers, introducing another ~20 % (±2σ). The measurements also depend the volumetric flow rate of gas through the wand, defined by the error in the mass flow controllers, 2 % (±2σ). This gives a total error of ~28 % in $F_{184.9\,nm}$ at the 2σ level. A further uncertainty of 6 % in $\sigma_{H_2O,185\,nm}$ (Cantrell et al., 1997), and 10 % in $[H_2O]$ taken from the instrumental uncertainty of the hygrometer is also considered.

The uncertainties discussed so far only pertain to how well the quantity of radicals generated by the wand can be known. There are additional systematic errors that relate to how well the LIF signal generated by the instrument can be known: ~6 % uncertainty in the laser power to which all signals are normalised, and ~12 % in the on-line signal, which relates to how reliably the laser wavelength is tuned to maximum fluorescence. This was determined by repeatedly finding the line and is the average deviation of the signal each time, caused by the ±5 × 10^{-4} nm wavelength uncertainty in the laser. The sum in quadrature of these systematic uncertainties, together with the typical ~8 % statistical uncertainty in the calibration fitting process, is 34 %.

The CH_3O calibration uncertainty, 43 %, is significantly higher due to uncertainty in the $[CH_3OH]$ concentration used to generate CH_3O, which is not measured directly (see section 4.1.1), and a 12 % uncertainty in the yield of CH_3O from the photolysis of methanol (Satyapal et al., 1989).

4.5.2 Decay method

The decay calibration relies on the kinetics of the CH_3O_2 self-reaction to calculate the instrument sensitivity factor. However, the IUPAC recommended value of the observed rate coefficient, k_{obs} = (4.8 ± 1.1) × 10^{-13} cm^3 $molecule^{-1}$ s^{-1} (Atkinson et al., 2006) has a 23 % error associated with it. There is an additional 10 % uncertainty in the initial CH_3O_2 signal, $(S_{CH_3O_2})_0$, caused by signal noise and uncertainty in the precise location of t = 0. The 6 % uncertainty in the laser power and 12 % in the on-line signal that applied to the wand calibration method must also be included here to bring the total uncertainty to 28 %.

4.6 Development and calibration of RO_xLIF instrument

The concept of a RO_xLIF instrument was introduced in section 1.2.4, and two such instruments are already in circulation (Fuchs et al., 2009, Whalley et al., 2011). In this section, the design and calibration of a RO_xLIF instrument for use in HIRAC is detailed, and as a LIF technique some of the same principles and components as FAGE can be applied.

The RO_xLIF instrument is constructed from two parts. The first part is the flow reactor tube, where RO_2 radicals are converted into HO_2. The second part is the LIF cell, where the HO_2 radicals are converted into OH which is subsequently detected by LIF at 308 nm. The two sections are differentially pumped, meaning the reaction tube is held at ~30 Torr to encourage chemical reactions, and the LIF cell is at ~3 Torr to aid LIF detection. The flow reactor and LIF cell assembly are shown in Figure 4.15, labelled **(A)** and **(B)**, respectively.

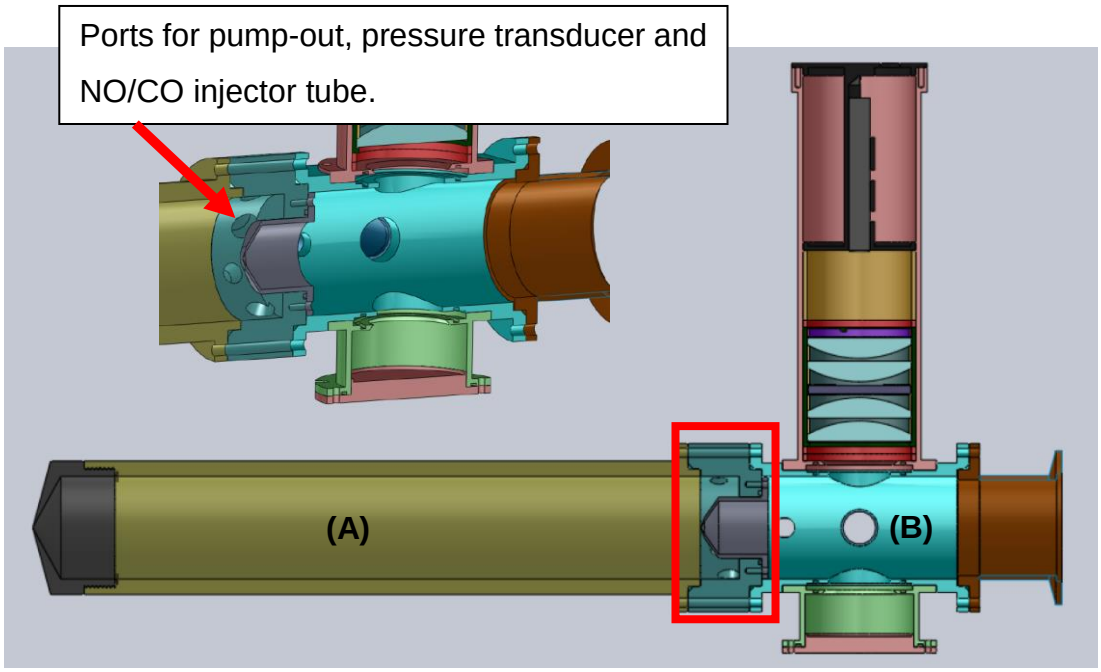

Figure 4.15 Sectional view of the RO_xLIF instrument. Gas is drawn through the pinhole (a) into the reaction tube, where the NO/CO mixture is injected. The chemical mixture is held at ~30 Torr and resides in the tube for ~0.5 s before a fraction is drawn through a 4 mm nozzle (b) into the 2.5 Torr LIF cell, the remainder of the gas mixture is pumped away. NO is injected to convert the HO_2 into OH which is detected by LIF. The OH signal is proportional to the $[RO_2]$ sampled at (a). The inset image shows the transfer nozzle and pump-out locations more clearly.

The LIF cell is almost identical to the ones used in the FAGE instrument, detailed in section 3.1.1. The only major difference is the photomultiplier, which in this case is a Channel Photo-Multiplier (CPM, Perkin Elmer C943P) as opposed to the MCP detectors used in FAGE. The principle of photo-multiplication is the same, but rather than an array of micro-channels the gain stage is a curved channel through which the photoelectrons cascade, with each impact on the sides of the channel causing emission of secondary electrons. The CPM was operated with a gain of -2900 V (SRS PS350, ±5 kV), and was gated using an in-house built high voltage gating unit. This gating method is inferior to the MCP gating used in FAGE, as it takes longer for the detector to reach maximum gain after each laser pulse. However, as the RO_xLIF method utilises the detection of OH radicals the LIF signals observed are far larger than CH_3O, compensating for the signal lost due to slow gating.

4.6.1 Principle of operation

The flow reactor tube is 300 mm long with a 50 mm internal diameter, and has a conical cap screwed into the end with a 0.5 mm pinhole drilled through the apex. Gas is drawn through the pinhole at ~2.5 SLM into the 30 Torr reactor, and a 1/8th inch stainless steel tube terminates in the centre of the gas flow just behind the pinhole. This tube delivers dilute NO (BOC, 545 ppm in N_2) which convert all radicals into OH *via* the following scheme:

$$RO_2 + NO \rightarrow NO_2 + RO \qquad \textbf{R 4.14}$$

$$RO + O_2 \rightarrow R'O + HO_2 \qquad \textbf{R 4.15}$$

$$HO_2 + NO \rightarrow OH + NO_2 \qquad \textbf{R 4.16}$$

Dilute CO (BOC, 9.88 % in N_2) is injected simultaneously through the same tube to convert the OH back into HO_2 *via*:

$$CO + OH \rightarrow CO_2 + H \qquad \textbf{R 4.17}$$

$$H + O_2 + M \rightarrow HO_2 + M \qquad \textbf{R 4.18}$$

where M is the bath gas, N_2 or O_2. This prevents the loss of sensitivity that would result from heterogeneous loss of OH to the instrument walls, as the HO_2 loss rate is approximately 10 times smaller (Fuchs et al., 2008). The ratio of $[HO_2]/[OH]$ is controlled by the concentrations of the injected NO and CO and will be discussed in the next section.

The flow reactor tube is connected to the lower pressure LIF cell by a pump out and gas transfer assembly (Figure 4.15, Red box and inset image). The assembly features 8 feedthrough ports, one of which is used for the 1/8th inch stainless steel tube that delivers the NO and CO to the top of the reaction tube. The other ports are used for a pressure transducer (MKS, 1000 Torr) and 4 pump-out lines. The pump out lines are connected to a rotary vane vacuum pump (Edwards RV 5) with a throttle valve to allow tuning of the flow tube pressure. In the centre of the assembly is the 4 mm diameter transfer nozzle through which

gas is drawn from the reaction tube into the lower pressure, ~3 Torr, LIF cell. The nozzle is raised on a turret above the ports for the pump-out lines to promote transfer of gas into the LIF cell. Just after the transfer nozzle pure NO (BOC N2.5 Nitric Oxide) is injected into the cell through another 1/8th inch stainless steel tube, converting HO_2 into OH which is then detected by LIF at 308 nm.

By switching off the dilute NO injection in the flow reactor the conversion of RO_2 to HO_2 is halted and allows measurement of OH and HO_2. Switching off the injection of neat NO into the LIF cell halts conversion of HO_2 to OH and allows measurement of only OH.

4.6.2 Optimisation

With an inlet flow rate of ~2.5 SLM, pressure of ~30 Torr and reactor length of ~300 mm the residence time inside the reactor is approximately 0.5 s. This is close to the 0.6 s residence time used successfully by Fuchs et al., 2008, which uses a longer tube (830 mm), higher flow rate (7 SLM) and lower pressure (~20 Torr). The maximum signal was attained by adding dilute NO into the flow reactor at a rate of 5 sccm, corresponding to ~1 × 10^{12} molecule cm^{-3}, and dilute CO at a rate of 50 sccm, corresponding to ~2 × 10^{15} molecule cm^{-3}. The $[HO_2]/[OH]$ ratio is controlled by the competition between R 4.16 and R 4.17, and can be calculated using the following equation:

$$\frac{[\mathrm{HO_2}]}{[\mathrm{OH}]} = \frac{k_{R4.17}[\mathrm{CO}]}{k_{R4.16}[\mathrm{NO}]} \qquad \textbf{Eq. 4.12}$$

where $k_{R4.16}$ = 8.1 × 10^{-12} cm^3 molecule^{-1} s^{-1} and $k_{R4.17}$ = 1.5 × 10^{-13} cm^3 molecule^{-1} s^{-1} (Sander et al., 2003). Using Eq. 4.12 with these rate coefficients, and the NO and CO concentration calculated above, the $[HO_2]/[OH]$ ratio in the tube is ~34. This is significantly lower than the ratio of 50 reported by Fuchs et al., 2008, but the instrument was relatively unresponsive to changes in the ratio. Despite this, good signal was obtained for both HO_2 and CH_3O_2 radicals, and the instrument was calibrated by generating HO_2 and CH_3O_2 radicals simultaneously using the same water vapour photolysis method described in section 4.1.2. From the calibration, shown in Figure 4.16, sensitivity factors of C_{HO2} = (2.48 ± 0.16) × 10^{-9} counts mW^{-1} s^{-1} molecule^{-1} cm^3 and C_{CH3O2} = (2.58 ± 0.31) × 10^{-9} counts mW^{-1} s^{-1} molecule^{-1} cm^3 were obtained. The fact

that these two sensitivity factors are very similar is a good indication that the instrument is working well as both CH_3O_2 and HO_2 are generated in equal quantity, and then all converted ultimately into OH before detection by LIF.

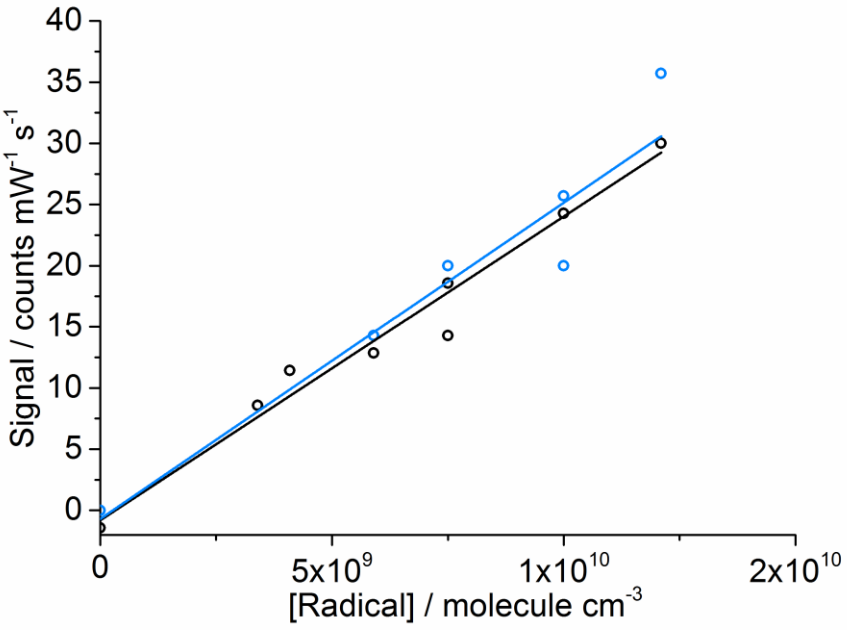

Figure 4.16 Calibration of the RO_xLIF instrument for HO_2 (black) and CH_3O_2 (blue) using the water vapour photolysis calibration method in the presence of methane to generate both radicals simultaneously. The gradient of the linear fits gives the sensitivity factors C_{HO2} = (2.48 ± 0.16) × 10^{-9} counts mW^{-1} s^{-1} $molecule^{-1}$ cm^3 and C_{CH3O2} = (2.58 ± 0.31) × 10^{-9} counts mW^{-1} s^{-1} $molecule^{-1}$ cm^3. The close agreement between the two lines is expected, as both radicals are detected by conversion to OH and subsequent detection by LIF.

4.7 Summary

4.7.1 Final FAGE instrument configuration

Figure 4.17 shows the FAGE instrument in its current form, where the front cell is used to detect OH and HO_2 radicals, and the rear cell is used to detect CH_3O_2 radicals. This configuration ensures the more reactive HO_x radicals have the shortest possible travel time before reaching the detection axis, whereas the less reactive CH_3O_2 radicals can reach the rear detection cell with no significant wall reactions. This configuration also keeps the broad bandpass filter required for CH_3O_2 detection further from the inlet pinhole, where UV lamp light enters from the HIRAC chamber and is otherwise detected and increases the background

signal and noise. The narrow 308 nm filter in the front cell is not affected by scatter of UV light from the lamps.

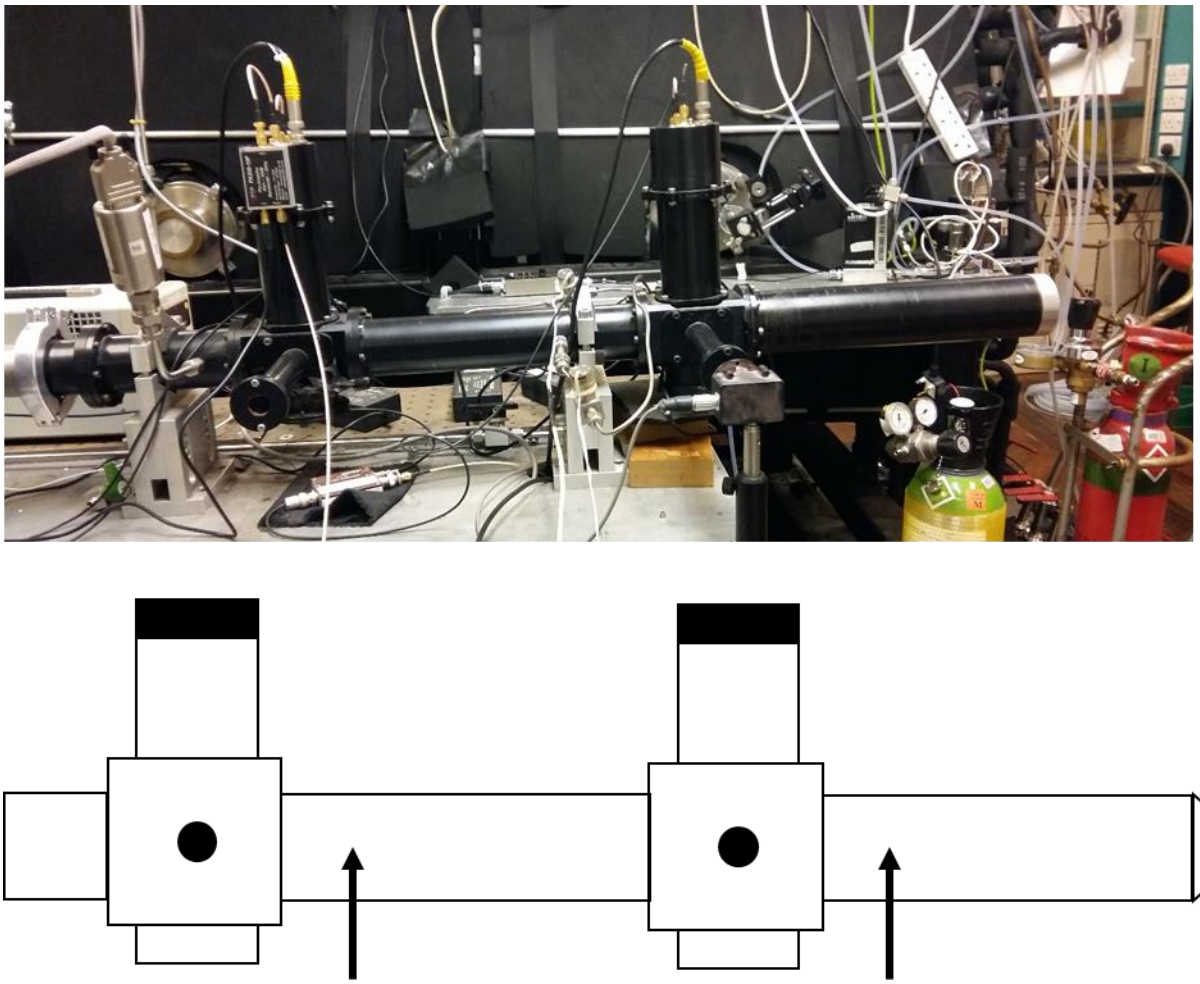

Figure 4.17 Photograph and schematic drawing of the FAGE instrument. Gas is drawn through the conical pinhole (right hand side of images). The black arrows represent the terminal position of 1/8th stainless steel lines that inject NO in front of the cells, to measure HO_2 and CH_3O_2 in the front (right) and back (left) cells.

The key modifications lie in the new optical components in the rear cell that are more suited to the CH_3O LIF spectrum, and a 1/8th inch stainless steel tube that injects NO into the front cell to facilitate HO_2 detection there. This tube enters the instrument downstream of the first cell and passes along the wall of the cell, between the laser axis and fluorescence collection axis, and ends ~10 cm upstream.

4.7.2 Calibration methods

The FAGE instrument has been calibrated for CH_3O_2 radicals using two independent methods: the wand calibration method that relies on water vapour photolysis and N_2O actinometry, and the kinetic calibration method that relies on the CH_3O_2 self-reaction kinetics. A reasonable agreement was found between the two methods within their 2σ error limits (34 % and 28 %, respectively), reporting $C_{CH_3O_2}$ = (7.8 ± 2.66) × 10^{-10} counts s^{-1} mW^{-1} cm^3 $molecule^{-1}$ and $C_{CH_3O_2}$ = (1.16 ± 0.32) × 10^{-9} counts s^{-1} mW^{-1} cm^3 $molecule^{-1}$ respectively. However, the wand calibration method consistently reports sensitivity factors that are approximately 30 % lower than the kinetic determination which indicates a systematic problem with one of the two methods that is not being accounted for, or there may be smaller errors in both systems. The wand calibration method is well established for OH and HO_2 calibrations (Heard and Pilling, 2003) and has been validated for OH by comparison with hydrocarbon decay kinetics in the HIRAC chamber (Winiberg et al., 2015). Furthermore, good agreement was found in section 3.2 when comparing the HO_2 wand calibration factor to the calibration factor obtained from the kinetics of the HO_2 self-reaction in HIRAC.

The discrepancy between the two calibration methods will be examined further in section 5.4 where FAGE measurements are compared to simultaneous CRDS measurements of HO_2 and CH_3O_2 radicals in the HIRAC chamber, and in Chapter 6 where the kinetics of the CH_3O_2 self-reaction and cross-reaction with HO_2 are investigated.

4.7.3 Sensitivity and Limit of Detection

The FAGE instrument is relatively insensitive when detecting CH_3O and CH_3O_2 radicals, with sensitivity factors in the range of 10^{-10} counts s^{-1} mW^{-1} cm^3 $molecule^{-1}$ it is at least two orders of magnitude less sensitive than OH and HO_2 FAGE detection. This is caused by the relative complexity of the CH_3O radical, which can exist in many more vibronic states at ambient temperatures than OH can – in other words, for any given pressure it has a higher partition function than OH. This distributes the radicals over a large range of energy levels, reducing the population density in any given state that is excited by the laser pulse and thus lowering fluorescence yields.

Despite the relative insensitivity compared to OH, the new FAGE method is a useful tool, particularly in a laboratory setting. With a LOD in the region of 10^8 molecule cm^{-3} for FAGE instrument is not viable for atmospheric measurements of CH_3O radicals, as their atmospheric concentrations are very low, with modelling predictions in the region of 10^3-10^4 molecule cm^{-3} in clean environments. This method is more suitable for laboratory measurements where radical concentrations of CH_3O and CH_3O_2 may be much higher.

The new FAGE method does show potential in a field measurement setting, as modelling of CH_3O_2 radicals shows the concentration to be highly dependent on atmospheric loading of VOCs and NO_x, with levels in the region of 2-6 × 10^8 molecule cm^{-3} in remote environments where NO_x levels are low (Whalley et al., 2010, Whalley et al., 2013). With the CH_3O_2 LOD of 2.05 × 10^8 molecule cm^{-3} for a 5-minute average, the FAGE technique could be a viable measurement in this scenario.

This instrument is designed for laboratory use, there are several changes that could be made to make it more appropriate for field measurements, such as:

1. Reducing cell pressure – The calibrations at reduced pressure shown in section 4.4.2 showed that the instrument gains significant sensitivity as the FAGE cell pressure is reduced. This is caused by reduced collisional quenching of the excited CH_3O radicals, and a purpose-built field instrument could use higher capacity pumps or a smaller inlet pinhole to reach lower cell pressures and increase sensitivity and reduce the LOD.
2. Shorter inlet length – The CH_3O_2 radicals travel ~580 mm from the pinhole before reaching the NO injection point, this is a combination of a 300 mm long inlet to keep the pinhole far away from the inner walls of the HIRAC chamber and a result of measuring CH_3O_2 in the rear cell. This is not necessary in a field instrument and can only hinder sensitivity due to heterogeneous loss of the radicals to the interior of the instrument. If the pinhole can me moved close enough to the laser axis, jet-cooling of the radicals may improve instrument sensitivity by condensing the population density into fewer rotational levels.

3. Selecting a more appropriate laser dye would enable excitation of CH_3O at 293 nm where the fluorescence yield is higher and may increase sensitivity.
4. It may be possible to increase the amount of fluorescent light that is collected. The fluorescence spectrum of CH_3O shown in Figure 4.4 indicates there is fluorescence from the v' = 2 level that is below 320 nm, which lies outside the range of the interference filter used here. There would likely be even more fluorescence below 320 nm from the v'=3 level that is pumped in this work, so an interference filter that can accommodate this range may improve sensitivity.
5. A reference cell is required to perform atmospheric measurements, this is discussed in the next section.

4.7.4 Reference cell

A reference cell for OH radicals was described in section 3.1.2, where water is pyrolysed by a hot wire filament to generate large quantities of OH radicals that can be used to guide the laser wavelength onto the wavelength of maximum fluorescence yield. Attempts were made to modify the reference cell by replacing the water vapour with methanol, with the assumption that the weak O-H bond would be pyrolysed to produce CH_3O radicals. This proved to be unsuccessful as the pyrolysis was more likely to break the C-H and C-OH bonds instead (Aronowitz et al., 1977). The photolysis of CH_3OH at 185 nm, as used in the calibration in section 4.1.1, would be a viable method of producing radicals but could not be implemented without designing a new reference cell. Alternatively, a wave meter could be used to guide the laser wavelength, although this would be an expensive upgrade.

For the work detailed in this thesis a reference cell, whilst helpful, was not mandatory as radicals are produced in large enough quantities inside the HIRAC chamber to find the line reliably at the cost of a few minutes' reaction time at the start of each experiment.

4.7.5 RO_xLIF instrument

The design and calibration of a RO_xLIF instrument was shown in section 4.6. As it relies on converting all RO_2 species ultimately into OH, which is a better target for LIF than CH_3O (as explained in section 4.2), and converts more than 40 % (unlike FAGE, section 4.3) the RO_xLIF instrument is ~3.2 times more sensitive for CH_3O_2 radicals than FAGE from the ratio of their respective calibration factors, however it is non-specific. The heightened sensitivity, and hence better signal to noise, will makes this instrument a complementary addition to FAGE, and will be useful in resolving the ~30 % discrepancy between the two FAGE calibration methods (section 4.4). The instrument is very much in its infancy, however preliminary measurements of the CH_3O_2 self-reaction in HIRAC are shown in section 6.4.1.

4.8 References

Albaladejo, J., Jimenez, E., Notario, A., Cabanas, B. & Martinez, E. 2002. CH_3O yield in the CH_3+O_3 reaction using the LP/LIF technique at room temperature. *Journal of Physical Chemistry A,* 106**,** 2512-2519.

Aronowitz, D., Naegeli, D. W. & Glassman, I. 1977. Kinetics of the pyrolysis of methanol. *Abstracts of Papers of the American Chemical Society,* 173**,** 241-241.

Atkinson, R., Baulch, D. L., Cox, R. A., Crowley, J. N., Hampson, R. F., Hynes, R. G., Jenkin, M. E., Rossi, M. J. & Troe, J. 2006. Evaluated kinetic and photochemical data for atmospheric chemistry: Volume II - gas phase reactions of organic species. *Atmospheric Chemistry and Physics,* 6**,** 3625-4055.

Biggs, P., Canosamas, C. E., Fracheboud, J. M., Parr, A. D., Shallcross, D. E., Wayne, R. P. & Caralp, F. 1993. Investigation into the pressure-dependence between 1 and 10 Torr of the reactions of NO_2 with CH_3 and CH_3O. *Journal of the Chemical Society-Faraday Transactions,* 89**,** 4163-4169.

Biggs, P., Canosamas, C. E., Fracheboud, J. M., Shallcross, D. E. & Wayne, R. P. 1997. Kinetics of the reaction of F atoms with CH_3ONO and CH_3O, and the reaction of CH_3O with a number of hydrocarbons. *Journal of the Chemical Society-Faraday Transactions,* 93**,** 2481-2486.

Buenker, R. J., Olbrich, G., Schuchmann, H. P., Schurmann, B. L. & Vonsonntag, C. 1984. Photolysis of methanol at 185 nm - Quantum-mechanical calculations and product study. *Journal of the American Chemical Society,* 106**,** 4362-4368.

Burkholder, J. B., Sander, S. P., Abbatt, J. P. D., Barker, J. R., Huie, R. E., Kolb, C. E., Kurylo, M. J., Orkin, V. L., Wilmouth, D. M. & Wine, P. H. 2015. Chemical kinetics and photochemical data for use in atmospheric studies – Evaluation 18. *JPL Publication 15-10, Jet Propulsion Laboratory, Pasadena*.

Cantrell, C. A., Zimmer, A. & Tyndall, G. S. 1997. Absorption cross sections for water vapor from 183 to 193 nm. *Geophysical Research Letters,* 24**,** 2195-2198.

Chai, J. J. & Dibble, T. S. 2014. Pressure Dependence and Kinetic Isotope Effects in the Absolute Rate Constant for Methoxy Radical Reacting with NO_2. *International Journal of Chemical Kinetics,* 46**,** 501-511.

Dillon, T. J., Holscher, D., Sivakumaran, V., Horowitz, A. & Crowley, J. N. 2005. Kinetics of the reactions of HO with methanol (210-351 K) and with ethanol (216-368 K). *Physical Chemistry Chemical Physics,* 7**,** 349-355.

Ebata, T., Yanagishita, H., Obi, K. & Tanaka, I. 1982. *A-X* fluorescence spectra of CH_3O and C_2H_5O generated by the ArF laser photolysis of alkyl nitrites. *Chemical Physics,* 69**,** 27-33.

Fuchs, H., Brauers, T., Haseler, R., Holland, F., Mihelcic, D., Musgen, P., Rohrer, F., Wegener, R. & Hofzumahaus, A. 2009. Intercomparison of peroxy radical measurements obtained at atmospheric conditions by laser-induced fluorescence and electron spin resonance spectroscopy. *Atmospheric Measurement Techniques,* 2**,** 55-64.

Fuchs, H., Holland, F. & Hofzumahaus, A. 2008. Measurement of tropospheric RO_2 and HO_2 radicals by a laser-induced fluorescence instrument. *Review of Scientific Instruments,* 79**,** 12.

Heard, D. E. & Pilling, M. J. 2003. Measurement of OH and HO_2 in the troposphere. *Chemical Reviews,* 103**,** 5163-5198.

Inoue, G., Akimoto, H. & Okuda, M. 1979. Laser-induced fluorescence spectra of CH_3O. *Chemical Physics Letters,* 63**,** 213-216.

Inoue, G., Akimoto, H. & Okuda, M. 1980. Spectroscopy of the CH_3O $A^2A_1 \leftarrow X^2E$ system by laser-excited fluorescence method. *Journal of Chemical Physics,* 72**,** 1769-1775.

Jimenez, E., Gilles, M. K. & Ravishankara, A. R. 2003. Kinetics of the reactions of the hydroxyl radical with CH_3OH and C_2H_5OH between 235 and 360 K. *Journal of Photochemistry and Photobiology a-Chemistry,* 157**,** 237-245.

Kappert, J. & Temps, F. 1989. Rotationally resolved laser-induced fluorescence excitation studies of CH_3O. *Chemical Physics,* 132**,** 197-208.

Kassab, E., Gleghorn, J. T. & Evleth, E. M. 1983. Theoretical aspects of the photochemistry of methanol, methylene, and related materials. *Journal of the American Chemical Society,* 105**,** 1746-1753.

Lee, J. D. 2000. Development and deployment of the FAGE instrument for measurement of HO_x radicals in the troposphere. *PhD Thesis, University of Leeds.*

Marston, C. C., Weide, K., Schinke, R. & Suter, H. U. 1993. Product selectivity of vibrationall mediated photofracmentation of methanol. *Journal of Chemical Physics,* 98**,** 4718-4727.

Nagesh, J., Sibert, E. L. & Stanton, J. F. 2014. Simulation of $A^2A_1 \leftarrow X^2E$ laser excitation spectrum of CH_3O and CD_3O. *Spectrochimica Acta Part a-Molecular and Biomolecular Spectroscopy,* 119**,** 90-99.

Nee, J. B., Suto, M. & Lee, L. C. 1985. Photoexcitation processes of CH_3OH - Rydberg states and photofragment fluorescence. *Chemical Physics,* 98**,** 147-155.

Onel, L., Brennan, A., Seakins, P. W., Whalley, L. & Heard, D. E. 2017. A new method for atmospheric detection of the CH_3O_2 radical. *Atmospheric Measurement Techniques,* 10**,** 3985-4000.

Porter, R. P. & Noyes, W. A. 1959. Photochemical studies .54. methanol vapor. *Journal of the American Chemical Society,* 81**,** 2307-2311.

Powers, D. E., Pushkarsky, M. B. & Miller, T. A. 1997a. Rovibronic analysis of the laser induced fluorescence excitation spectrum of the jet-cooled methoxy radical. *Journal of Chemical Physics,* 106**,** 6863-6877.

Powers, D. E., Pushkarsky, M. B. & Miller, T. A. 1997b. Vibrational mode and frequency dependence of the photofragmentation of the methoxy radical. *Journal of Chemical Physics,* 106**,** 6878-6884.

Sander, S. P., R. R. Friedl, D. M. Golden, M. J. Kurylo, R. E. Huie, V. L. Orkin, G. K. Moortgat, A. R. Ravishankara, C. E. Kolb, M. J. Molina, P. H. Wine & Finlayson-Pitts, B. J. 2003. Chemical kinetics and photochemical data for use in atmospheric studies - Evaluation 14. *NASA-JPL Publication No. 02-25,*.

Satyapal, S., Park, J., Bersohn, R. & Katz, B. 1989. Dissociation of methanol and ethanol activated by a chemical-reaction or by light. *Journal of Chemical Physics,* 91**,** 6873-6879.

Shannon, R. J., Blitz, M. A., Goddard, A. & Heard, D. E. 2013. Accelerated chemistry in the reaction between the hydroxyl radical and methanol at interstellar temperatures facilitated by tunnelling. *Nature Chemistry,* 5**,** 745-749.

Wen, Y., Segall, J., Dulligan, M. & Wittig, C. 1994. Photodissociation of methanol at 193.3 nm - translational energy-release spectra. *Journal of Chemical Physics,* 101**,** 5665-5671.

Wendt, H. R. & Hunziker, H. E. 1979. Electronic absorption spectrum of CH_3O. *Journal of Chemical Physics,* 71**,** 5202-5205.

Whalley, L. K., Blitz, M. A., Desservettaz, M., Seakins, P. W. & Heard, D. E. 2013. Reporting the sensitivity of laser-induced fluorescence instruments used for HO_2 detection to an interference from RO_2 radicals and introducing a novel approach that enables HO_2 and certain RO_2 types to be selectively measured. *Atmospheric Measurement Techniques,* 6**,** 3425-3440.

Whalley, L. K., Edwards, P. M., Furneaux, K. L., Goddard, A., Ingham, T., Evans, M. J., Stone, D., Hopkins, J. R., Jones, C. E., Karunaharan, A., Lee, J. D., Lewis, A. C., Monks, P. S., Moller, S. J. & Heard, D. E. 2011. Quantifying the magnitude of a missing hydroxyl radical source in a tropical rainforest. *Atmospheric Chemistry and Physics,* 11**,** 7223-7233.

Whalley, L. K., Furneaux, K. L., Goddard, A., Lee, J. D., Mahajan, A., Oetjen, H., Read, K. A., Kaaden, N., Carpenter, L. J., Lewis, A. C., Plane, J. M. C., Saltzman, E. S., Wiedensohler, A. & Heard, D. E. 2010. The chemistry of OH and HO_2 radicals in the boundary layer over the tropical Atlantic Ocean. *Atmospheric Chemistry and Physics,* 10**,** 1555-1576.

Winiberg, F. A. F., Smith, S. C., Bejan, I., Brumby, C. A., Ingham, T., Malkin, T. L., Orr, S. C., Heard, D. E. & Seakins, P. W. 2015. Pressure-dependent calibration of the OH and HO_2 channels of a FAGE HO_x instrument using the Highly Instrumented Reactor for Atmospheric Chemistry (HIRAC). *Atmospheric Measurement Techniques,* 8**,** 523-540.

Chapter 5. FAGE and CRDS intercomparison experiments

This chapter presents results from inter-comparison experiments between the FAGE and Cavity Ringdown Spectroscopy (CRDS) instrumental techniques performed in the HIRAC chamber for HO_2 and CH_3O_2 radicals to help validate the FAGE calibration methods discussed in chapters 3 and 4. The CRDS system was also used to examine the room temperature spectroscopic characteristics of HO_2 and CH_3O_2 radicals, centred around 1506.43 nm and 1335.47 nm respectively, at pressures between 80 and 1000 mbar.

Chapter 3 presented a FAGE instrument designed to detect OH and HO_2 radicals and study their kinetic behaviour, and in Chapter 4 the same instrument was modified to add CH_3O_2 to its measurement capabilities. These modifications showed that the instrument could potentially be an effective tool both in determining the atmospheric abundance of CH_3O_2 and in kinetic measurements. However, these FAGE measurements are non-absolute, meaning the signal produced is not dependent only upon the quantity of radicals present and is a function of the instrument itself. Therefore, the accuracy of these measurements is entirely dependent upon the quality of the instrument calibration. Two independent methods for calibrating the FAGE instrument have been described so far, one using chemical kinetics and the other generating known radical concentrations *via* photolysis of water vapour. For HO_2 both methods were shown to agree well in section 3.2, whereas for CH_3O_2, the photolysis method reports ~30 % lower *C*-factor values in section 4.4.

Inter-comparison experiments between instruments that utilise different detection principles are an excellent way to check the accuracy of instrumental techniques, as interferences or systematic errors in one are unlikely to affect the other. They also help to validate instruments when they are operating very close to their limits of detection. A Cavity Ringdown Spectroscopy (CRDS) instrument was described in section 2.5 and, as an absorption technique, it is an absolute measurement of radicals where the magnitude of the signal depends only on the concentration of the species present. However, there is large scope for the absorption band of the target molecule to overlap with other species, especially

at higher pressures where absorption bands may become broader and lose structure that could otherwise allow two species to be distinguished.

5.1 Experimental

All experiments were conducted inside the HIRAC chamber at 298 K and at pressures of 80, 100, 150 or 1000 mbar. The pressure, lamps and reagents used for HO_2 and CH_3O_2 radical generation are detailed in the following sections. All gaseous reagents were admitted to the chamber using the vacuum system and liquids were injected through a rubber septum opposite the FAGE instrument, both were described in section 2.3. Once admitted to the chamber the reagents were allowed to mix for ~1 minute before experiments began, whereupon the photolysis lamps were switched on to initiate photochemistry. Depending on the type of experiment the lamps were either left on for several minutes to generate steady state radical concentrations, or they were switched off and on several times at one to two-minute intervals to measure kinetic decays and monitor the absorption background. The HIRAC chamber and CRDS instrument were described in detail in Chapter 2, the FAGE instrument for HO_2 detection was described in Chapter 3, and it's conversion to CH_3O_2 detection was described in Chapter 4. The instrumental setup inside HIRAC is shown in Figure 5.1. The CRDS system measures across the width of the chamber, whilst FAGE samples from a fixed point near to the centre of the reactor volume. The chamber mixing fans ensure a homogeneous radical concentration throughout the chamber, meaning the spatial separation of the two instruments, and the fact that the cavity effectively averages the concentration along its length, did not affect the comparison experiments as detailed in section 5.1.3.

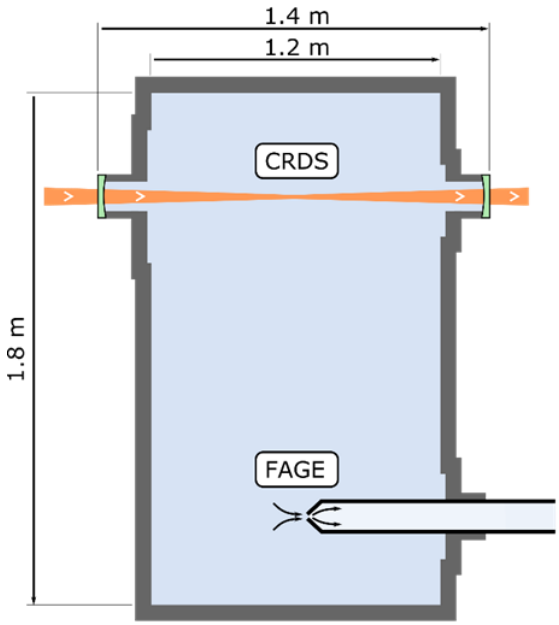

Figure 5.1. The instrumental layout inside the HIRAC chamber. The FAGE instrument samples from near the centre of the chamber, whereas the CRDS system measures across the width of the chamber. The spatial separation of the instrument detection regions does not affect comparison measurements as mixing fans ensure a homogeneous radical concentration. Figure created by Dr. Michele Gianella of the University of Oxford.

When performing experiments using absorption measurement techniques such as CRDS, it is important to avoid reagents and reaction products that absorb light in the same region as the target molecule, or at least be able to quantify their absorption and how this may change during an experiment. Consumption of reagents during the experiments would decrease the absorption baseline, causing the measured radical concentration to appear to decrease during an experiment (see section 5.2). This caused problems when scanning the wavelength of the laser over the absorption peaks, as the scans could take several minutes, during which time the baseline would change significantly and be difficult to subtract accurately. However, the changing baseline was more easily accounted for in the fixed wavelength comparison experiments as it could be measured regularly by switching off the photolysis lamps and remove the radicals, leaving only the reagents and photolysis products that make up the background absorption. These difficulties required a balance between enough reagents to generate a detectable quantity of radicals for a suitable length of time, whilst not using so much that the reagents interfere with the CRDS system or

take part in secondary chemical reactions to produce species that in turn interfere with the measurements.

5.1.1 HO_2 chemical systems

The HO_2 inter-comparison experiments were conducted at pressures of 150 and 1000 mbar in synthetic air composed of nitrogen (BOC, > 99.998 %) and oxygen (BOC, > 99.999 %) in an 80:20 ratio. HO_2 radicals were generated by photolysing molecular chlorine (Sigma Aldrich, ≥ 99.5 %) at ~365 nm (Phillips, TL-D36W/BLB, λ = 350–400 nm) in the presence of methanol (Sigma Aldrich, HPLC grade, ≥ 99.9 %,):

$$Cl_2 + h\nu\ (365\ nm) \rightarrow 2Cl \qquad \textbf{R 5.1}$$

$$CH_3OH + Cl \rightarrow CH_3O + HCl \qquad \textbf{R 5.2}$$

$$CH_3O + O_2 \rightarrow HCHO + HO_2 \qquad \textbf{R 5.3}$$

The concentration of HO_2 produced was controlled primarily by varying the amount of Cl_2 present in the chamber. Changing the amount of methanol had limited effect on the radical concentration as it was always in excess to ensure that the Cl atoms preferentially reacted with methanol, rather than taking part in secondary chemistry with reaction products or the chamber walls. This system was chosen as it is a relatively clean chemical process in that, aside from HO_2, only HCl and HCHO are formed as potential absorbing species. HCl was found to have no significant absorption cross-section at these wavelengths, and HCHO only began to interfere after long reaction times. Being a homonuclear diatomic, Cl_2 did not pose a risk of absorptive interference for the near-IR wavelengths used in these measurements, whereas the methanol did. Injection of methanol *via* syringe into the HIRAC chamber caused the overall ringdown time of the CRDS system to decrease significantly (5 - 10 %). The strong methanol absorption was found to be relatively flat across the whole wavelength range relevant to this work (1506.39 – 1506.48 nm), meaning there was no optimal wavelength away from the maximum on the HO_2 line to perform these measurements without interference.

5.1.2 CH_3O_2 chemical systems

The experiments were conducted inside the HIRAC using three different pressure / gas mixtures. The first used 80 mbar total pressure of helium (BOC, >99.99 %) and oxygen (BOC, >99.999 %) in the ratio of He:O_2 = 3:1, which are similar conditions to those used in previous work done by done by Farago et al. (Faragó et al., 2013). The second and third systems both used synthetic air, but at 100 and 1000 mbar total pressure. CH_3O_2 was generated in the chamber by photolysing one of two precursor gas mixtures. The first was a mixture of Cl_2 (Sigma Aldrich, ≥ 99.5 %) and CH_4 (BOC, CP grade, 99.5 %), where the Cl_2 was photolysed at ~365 nm (Phillips, TL-D36W/BLB, λ = 350–400 nm, R 1.15) to initiate CH_3O_2 formation *via* the reactions:

$$CH_4 + Cl \rightarrow CH_3 + HCl \qquad \textbf{R 5.4}$$

$$CH_3 + O_2 + M \rightarrow CH_3O_2 + M \qquad \textbf{R 5.5}$$

where M is the bath gas He, N_2 or O_2. Typical reagent concentrations for this system were [CH_4] = 1.2–2.5 × 10^{16} molecule cm^{-3} and [Cl_2] = 1.1–5.5 × 10^{15} molecule cm^{-3}. At 1000 mbar pressure, the overlap of the methane absorption lines due to the pressure broadening (see section 5.2.1) resulted in a significant CH_4 absorption over the range from 1334.9 - 1335.8 nm in the background of the CH_3O_2 measurements, making it an unsuitable system for the higher pressure measurements. Instead, a second method using the photolysis of acetone (Sigma Aldrich, HPLC grade, ≥ 99.9 %) was used, typically [$(CH_3)_2CO$] = 8.8 × 10^{14} molecule cm^{-3}, at 254 nm (Lamps: GE G55T8/OH 7G) to produce CH_3O_2 *via*:

$$(CH_3)_2CO \xrightarrow{h\nu} 2CH_3 + CO \qquad \textbf{R 5.6}$$

$$(CH_3)_2CO \xrightarrow{h\nu} CH_3 + CH_3CO \qquad \textbf{R 5.7}$$

The methyl radicals then form CH_3O_2 *via* R 5.5 as before. While this system alleviated the interference from methane it was not perfect as the 254 nm light required for photolysis was able to pass through the interference filter placed over the InGaAs photodiode (section 2.5.2) and generate heightened signal noise.

5.1.3 Radical gradient measurements and chamber wall losses

As the CRDS system averages the absorption across the ~1.2 m diameter HIRAC chamber, whereas FAGE samples from a single point near the centre, it was necessary to establish whether there was a significant radical concentration gradient across the width of the chamber. An extended FAGE inlet of ~520 mm length was used to measure the radical concentration, translating the inlet position between 0 and ~500 mm from the reactor walls and observing the change in signal. Radicals were generated by photolysing ozone at 254 nm to produce $O(^1D)$ in the presence of either water or methane to generate HO_2 or CH_3O_2 respectively *via* reactions:

$$O_3 + h\nu\ (254\ nm) \rightarrow O(^1D) + O_2 \qquad \textbf{R 5.8}$$

$$O(^1D) + H_2O \rightarrow 2OH \qquad \textbf{R 5.9}$$

$$OH + O_3 \rightarrow HO_2 + O_2 \qquad \textbf{R 5.10}$$

$$OH + CH_4 \rightarrow H_2O + CH_3 \qquad \textbf{R 5.11}$$

CH_3O_2 is then formed by R 5.5. The HO_2 concentration was constant between 100 and 500 mm from the walls and decreased by ~16 % when the pinhole was flush with the reactor wall. CH_3O_2 radicals were found to be less sensitive to the chamber walls as the FAGE inlet was translated across the width of the chamber the signal showed no decrease within the ~10% 1σ statistical error of each measurement, up until the point at which the pinhole was level with the chamber wall. Moving the instrument further backwards positioned the pinhole inside the ISO-K160 coupling flange and effectively ~4 cm behind the chamber walls where there is likely to be little air movement. This position is analogous to that of the CRDS mirrors, which are recessed into the chamber walls as they mount to the outside of the chamber. In this position a signal drop of ~14 % was observed, within the statistical error margins of the measurements.

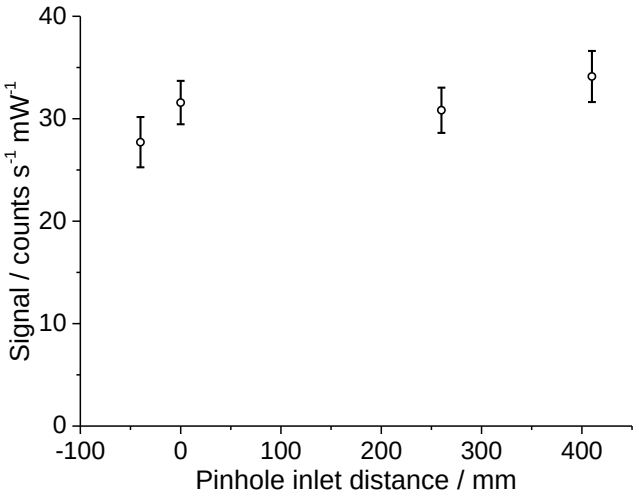

Figure 5.2 Measurement of the CH_3O_2 radical concentration with the FAGE inlet at different distances from the inside wall of HIRAC. The signal did not change within the statistical error of the measurement until the FAGE inlet was behind the chamber wall, inside the coupling flange analogous to the CRDS mirror. Figure produced by Dr Lavinia Onel.

These results suggest that the CRDS system measurements will be unaffected by any radical gradients, and the comparison with FAGE will be valid. Furthermore, the lack of any measurable CH_3O_2 gradient up to the walls of the chamber suggests the wall loss rate can be ignored completely for this radical.

5.1.4 Absorption spectra of HO_2 and CH_3O_2 radicals

To measure the HO_2 spectrum, the laser wavelength was scanned over the absorption region (1506.382 – 1506.462 nm) in steps of ~ 1 pm, first with the UV lamps off to establish a background measurement. The eight UV lamps were then switched on to produce HO_2 radicals and the laser wavelength was scanned again. As the laser moved to each wavelength, data acquisition was paused for 10 seconds to allow the temperature controlled wavelength to stabilise. The following ringdown events, 50 at 150 mbar and 25 at 1000 mbar, were then averaged together into one data point and the laser moved on to the next position. The averaging process included two filters that discarded spurious ringdown events. One filter eliminated events that lay outside of a pre-set ringdown time window, which may be caused by dust particles passing through the cavity, and the other removed points that exceeded 3 standard deviations of the average

ringdown time. This led to a typical ~0.2 % standard deviation on each point measured.

The CH_3O_2 absorption feature is a band associated with v_{12} vibronic band within the $A^2A' \leftarrow X^2A''$ electronic transition, centred around 1335 nm. This transition has been documented in previous work (Pushkarsky et al., 2000, Atkinson and Spillman, 2002, Faragó et al., 2013) and more detail is given in section 5.3. Unfortunately, there are interfering methane and water lines in this region, and these, together with the change in [CH_3O_2] during longer ($\gtrsim$ 5 min) scanning times, made it impossible to perform a single, high resolution scan across the CH_3O_2 transition like was done for the HO_2 spectrum. Therefore the spectrum was mapped out as a series of point measurements at fixed wavelengths, normalised by the absorption at the optimum measurement point, 1335.47 nm, where the absorption feature is sufficiently strong and furthest in wavelength from interfering methane absorption lines and where the CH_3O_2 cross section was determined in section 5.3.3. Each data point was obtained by measuring the absorption coefficient, $\alpha_{CH_3O_2}$, (photolysis lamps on) and the baseline (photolysis lamps off) at 1335.47 nm followed by measuring $\alpha_{CH_3O_2}$ and the baseline at another wavelength on the absorption feature and then reverting to measuring at 1335.47 nm again. This pattern was repeated multiple times for different wavelengths to build up an absorption feature, with all points normalised to $\alpha_{CH_3O_2}$ at 1335.47 nm. This method was used to measure the CH_3O_2 absorption spectrum under each of the three experimental conditions detailed in section 5.1.2: 80 mbar (He + O_2) and 100 mbar and 1000 mbar of synthetic air.

5.1.5 FAGE / CRDS Inter-comparison experiments

For HO_2 the CRDS laser was fixed to the wavelength of maximum absorption, 1506.43 nm. For CH_3O_2 the wavelength was fixed to 1335.47 nm which was a compromise between high absorption and minimal interference from methane, and the radical concentration was measured with both FAGE and CRDS simultaneously. The lamps were either left on for ~10 - 20 minutes to acquire a near steady state comparison measurement, or they were periodically switched off and on again (~2-3 minutes intervals) to allow the radicals to decay away and have both instruments measure the range of concentrations throughout the

decay, and to monitor the changeable background signal. These temporal decays and associated self-reaction kinetics were also used to calculate the absorption cross section of each radical at each chamber pressure.

5.2 CRDS data analysis

The ringdown time, τ, as measured by the CRDS system is proportional to the absorbance of the species inside the cavity, and therefore to the concentration of the absorbing species. To extract the radical concentration from τ, the absorption coefficient, α, must first be calculated:

$$\alpha = \frac{1}{c} \times \left(\frac{1}{\tau} - \frac{1}{\tau_0}\right) \qquad \textbf{Eq. 5.1}$$

where c is the speed of light in centimetres per second, τ is the ringdown time with radicals present, and τ_0 is the ringdown time in the absence of radicals. As the absorption coefficient denotes the total amount of light absorbed, it can be converted to a concentration by dividing through the absorption cross section, σ, which relates to the probability of an absorption event occurring and is proportional to the cross-sectional area of the molecule presented to the photon:

$$[X] = \frac{\alpha}{\sigma} \qquad \textbf{Eq. 5.2}$$

where [X] is the concentration of HO_2 or CH_3O_2. The value of the absorption cross section is unique to each radical and is discussed in more detail in section 5.2.1. The values used for the absorption cross section are discussed in section 5.3. Figure 5.3 shows an example of a raw data set from a CRDS measurement of HO_2, where the measured ringdown time is plotted over time and the lamps were switched on (low τ values) and off (high τ values) periodically. Figure 5.3 shows the effect of the changing absorption baseline over time described in section 5.1. To correct for this baseline shift a linear fit was applied to the lamps off sections that correspond to the baseline, which was then used as τ_0 in Eq. 5.1 to produce the absorption coefficient, α, as a function of time in Figure 5.1. Using Eq. 5.2 converts α into $[HO_2]$.

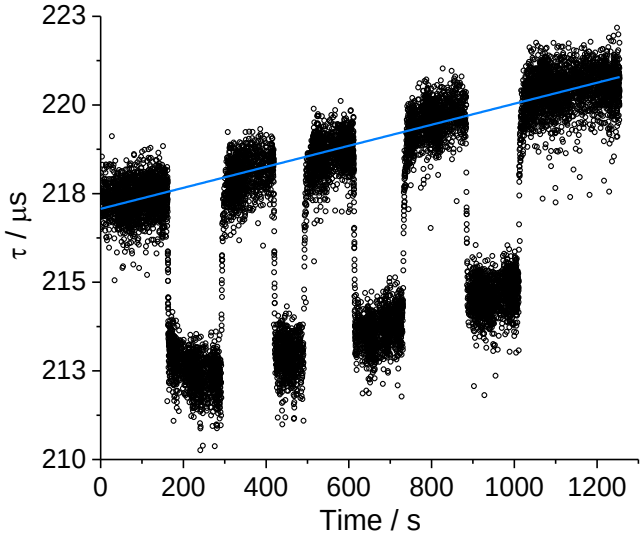

Figure 5.3. A series of lamps on / off measurement of HO_2 made at 1000 mbar using CRDS at 1506.43 nm. The increasing baseline from 218 µs to 221 µs was caused by depletion of methanol and was accounted for by fitting a line (blue) to the periods where the lamps were switched off. Also visible are the numerous signal drops attributed to dust particles crossing the cavity beam, these would be filtered out by the program mentioned in the main text.

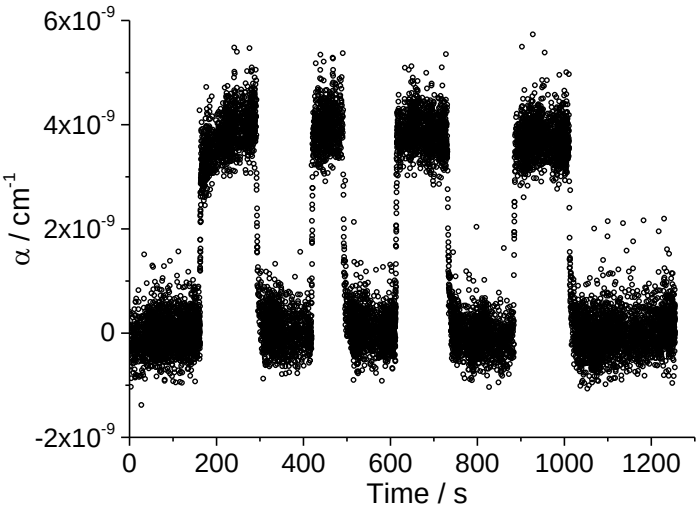

Figure 5.4. The same measurement with the fitted baseline subtracted and τ converted into absorption coefficient, α, using Eq. 5.1. Using the absorption cross section and Eq. 5.2 converts α into the HO_2 concentration.

5.2.1 The absorption cross section and pressure broadening

In section 4.2 the LIF excitation spectrum of CH_3O radicals was discussed and compared to the much simpler OH spectrum, and the same principles that control which photon energies can be absorbed by the radicals are applicable here, albeit with lower photon energies. The absorption cross section, σ, is a measure of the probability of an absorption event occurring and with units of cm^2 it can be likened to the surface area that a molecule presents to the photon, with larger cross sections equating to higher absorption chance and thus higher absorption signal. Pressure broadening is the phenomenon where absorption features become wider and weaker as pressure increases, directly affecting the absorption cross section. The effect is illustrated in Figure 5.5 which shows a pair of arbitrary energy levels that a molecule may occupy. At low pressure the energy levels are well defined and only a small frequency bandwidth will excite the ground state molecules. As the pressure is increased the molecule is distorted by collisions with neighbouring species causing the energy levels to lose definition, effectively creating a continuum of slightly different energy levels that the molecule can occupy. This broadens the frequency range that can be absorbed and simultaneously distributes the molecules over more energy levels, reducing the amount of absorption that can occur at any specific wavelength – the absorption cross section has been reduced.

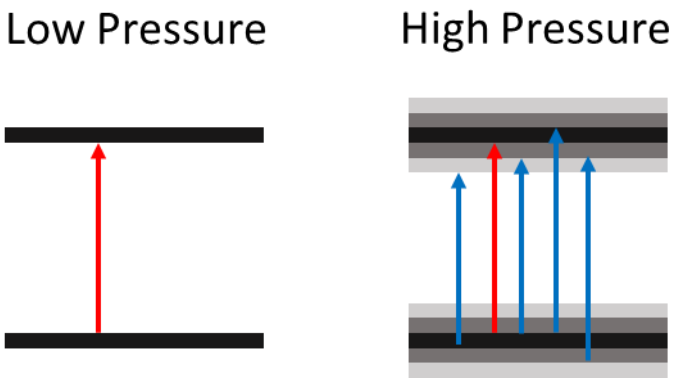

Figure 5.5 Diagram to show the effect of pressure broadening on molecular energy levels. At low pressure the upper and lower state levels are well defined and only a narrow range of frequencies can excite the molecule. At high pressure the upper and lower states become less well defined and the molecule may be excited by a wider frequency range. Additionally, the ground state population density is distributed over a wider range meaning less molecules can be excited by any given frequency, lowering the absorption cross section.

The experiments in this chapter occur at a range of pressures, so the cross section must be calculated at each of these pressures in order to convert the absorption signal into radical concentration.

5.3 HO_2 and CH_3O_2 absorption lines

The HO_2 absorption feature used in the HO_2 intercomparison measurements is centred around ~1506.43 nm, corresponding to the $2\nu_1$ vibrational overtone band of the H-O stretch, based on previous studies (Taatjes and Oh, 1997, DeSain et al., 2003, Thiebaud et al., 2007). Figure 5.6 shows the absorption spectrum of the $2\nu_1$ band measured by Thiebaud et al. which lies between 6604.5 and 6696 cm^{-1} (~1493 – 1514 nm) and consists of many discrete absorptions linked to rotational transitions within the vibrational overtone. The strongest absorption lies at 6638.2 cm^{-1} = 1506.43 nm at 50 Torr, and as such is the wavelength used in all HO_2 inter-comparison experiments reported in this chapter. However, the measurement in Figure 5.6 was performed in helium at ~66 mbar, and all other studies of this transition are at similarly low pressure. The effect of pressure broadening means that the absorption cross sections reported in these papers are not directly applicable to the work presented in this chapter, which was performed at 150 and 1000 mbar. The determination of the HO_2 cross section used in this work is shown in sections 5.3.2 and 5.3.3.

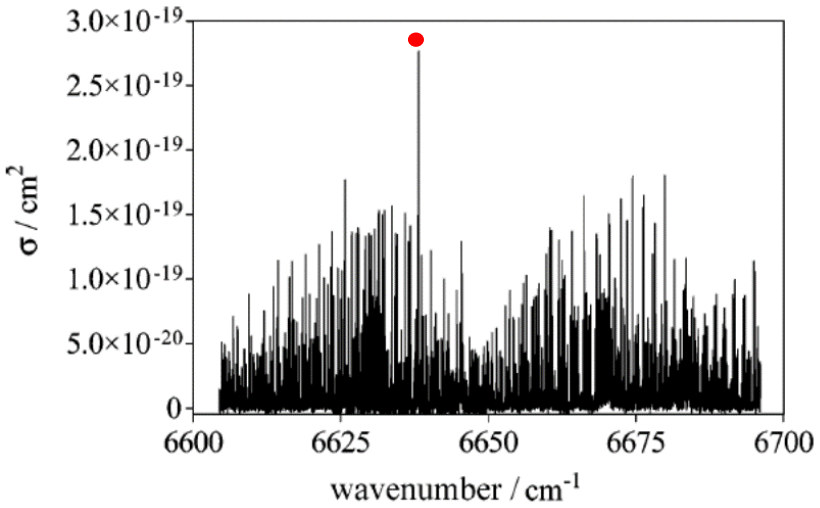

Figure 5.6 High resolution HO_2 absorption spectrum at 50 Torr helium (~66 mbar) in the range of 6604.5 – 6696 cm-1 (1514-1493 nm) as measured by Thiebaud et al. The strongest absorption at 6638.2 cm-1 (1506.43 nm, red dot) is the focus of this work.

The CH_3O_2 absorption feature used in the CH_3O_2 inter-comparison experiments is associated with the $A\ ^2A \leftarrow X\ ^2A''$ electronic transition that has been studied in the past (Pushkarsky et al., 2000). The spectrum obtained at ~250 Torr (~330 mbar) Ne:O_2 by Pushkarsky et al. is shown in Figure 5.7, where the strong transition located at 7382.8 cm^{-1} (1354.50 nm) is the $v'=0 \leftarrow v''=0$ origin. It was not possible to use the origin in this work as there were water absorption features located in the same region that would interfere with the measurements at higher pressures made here. Instead, the weaker transition around 7488 cm^{-1} (1335.47 nm) attributed to the vibronic $v'=1 \leftarrow v''=2$ transition was used and has been the focus of more recent work (Atkinson and Spillman, 2002, Faragó et al., 2013). A spectrum of this transition reported by Atkinson and Spillman at 20 Torr (~26 mbar) nitrogen is shown in Figure 5.8. As with the HO_2 transition above, these measurements were performed at reduced pressure, while some of the measurements in this work were at 1000 mbar. The effects of pressure broadening on this transition were investigated in the following section.

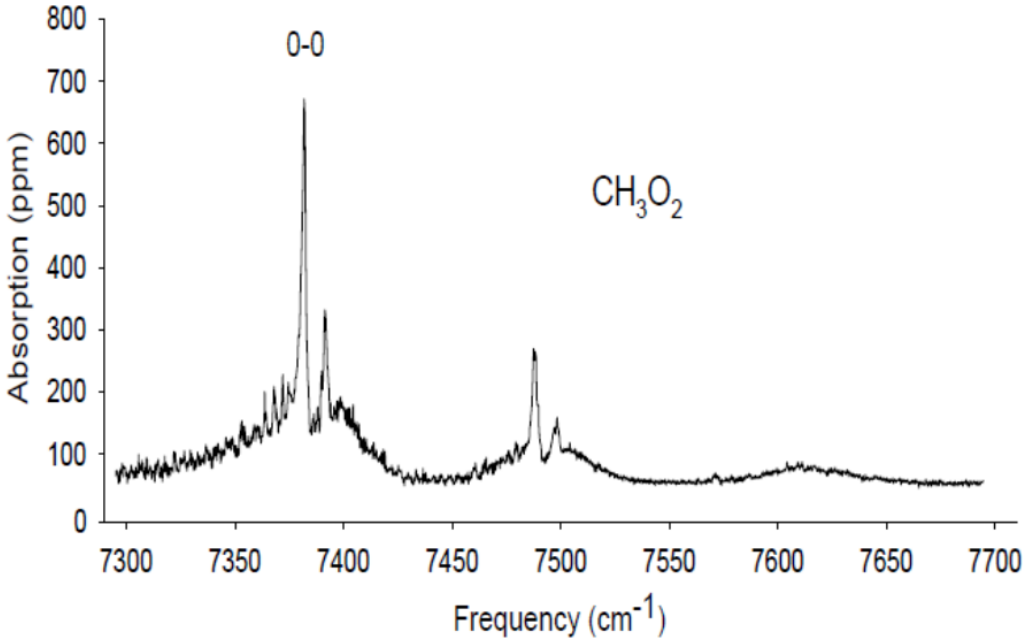

Figure 5.7 CH_3O_2 $A\ ^2A \leftarrow X\ ^2A''$ electronic transition measured by Pushkarsky et al., 2000. In 250 Torr Ne:O_2. The origin of the transition is at 7382.8 cm^{-1} (1354.50 nm).

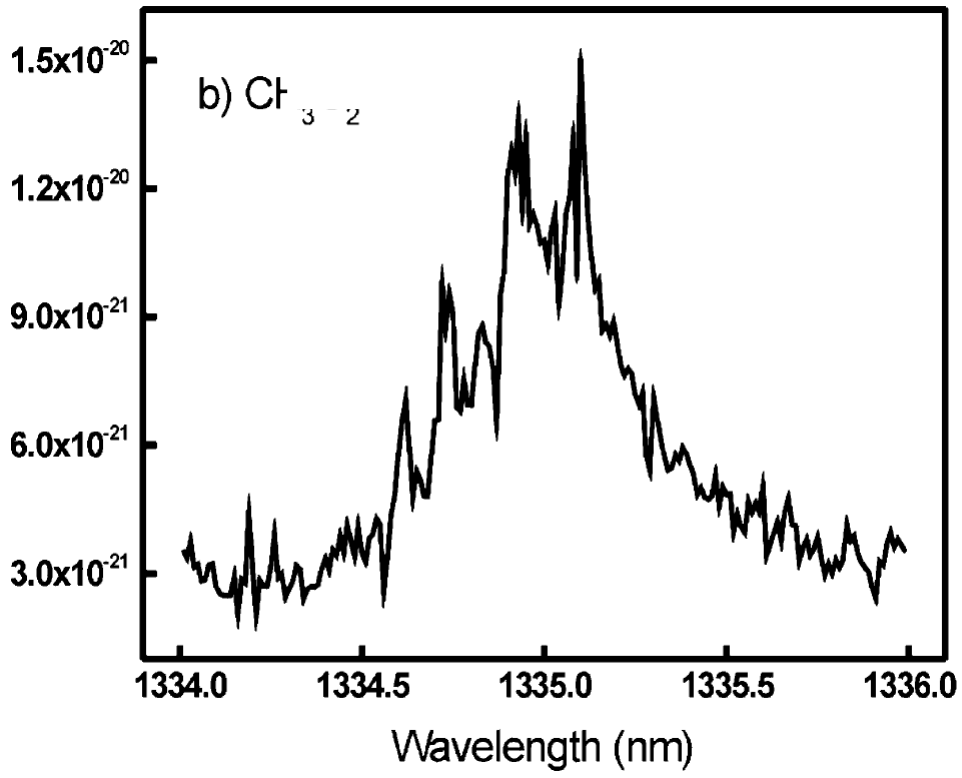

Figure 5.8 CH_3O_2 *A* ^{2}A← *X* ^{2}A'' v_{12} absorption feature measured by Atkinson and Spillman, 2002 in 20 Torr Nitrogen.

5.3.1 Spectroscopic measurement of HO_2 and CH_3O_2

Figure 5.9 is a plot of the CRDS ringdown time, τ, as the laser wavelength was scanned over the HO_2 absorption line at 150 and 1000 mbar at 298 K in the HIRAC chamber. The scan at 150 mbar shows stronger absorption and more structure than the scan at 1000 mbar, where the two lines at 1506.43 and 1506.45 nm have merged in accordance with the pressure broadening effects described in section 5.2.1. For this reason, the 1000 mbar scan was made with 25 event averages per point and 2 pm increments, whilst a higher resolution scan with 50 event averages per point and 0.8 pm increments was used at 150 mbar to capture the structure. The maximum absorption of both scans lies at 1506.43 nm, corresponding to the strongest HO_2 absorption in the ~1493 – 1514 nm wavelength range, and agrees well with previous work (Taatjes and Oh, 1997, DeSain et al., 2003). The CRDS laser wavelength was therefore fixed at 1506.43 nm during all HO_2 inter-comparison experiments to maximise signal.

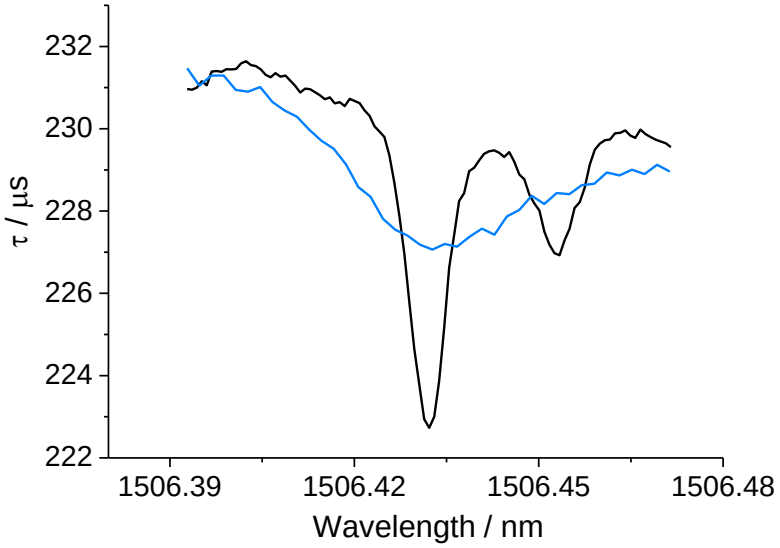

Figure 5.9. Typical laser scans of the CRDS ringdown time (τ) as a function of wavelength in an air mixture at 150 mbar (black) and 1000 mbar (blue) at 298 K. The measurement at 150 mbar averaged 50 ringdown events per point, with an increment of 0.8 pm between points. The measurement at 1000 mbar averaged 25 ringdown events per point, with an increment of 2 pm between points, and has been offset by +18 µs to overlap the baseline with that of 150 mbar. HO_2 radicals were generated using $[CH_3OH] = 7 \times 10^{13}$ molecule cm^{-3} and $[Cl_2] = 4 \times 10^{13}$ molecule cm^{-3} in the experiment at 150 mbar and $[CH_3OH] = 2 \times 10^{14}$ molecule cm^{-3} and $[Cl_2] = 2 \times 10^{14}$ molecule cm^{-3} in the experiment at 1000 mbar.

Figure 5.10 shows the comparatively broad CH_3O_2 absorption feature located in the range of ~1334.93 to 1335.83 nm. The spectrum is almost the same at 80 mbar $He:O_2$ = 3:1 and at 100 and 1000 mbar of synthetic air, showing that CH_3O_2 is unaffected by pressure broadening. This is because the absorption feature is already very wide, owing to the larger partition function and increased density of states available to the more complex radical. This is the same reasoning behind the complexity of the CH_3O LIF spectrum, explained further in section 4.2.1, and it causes the absorption cross section to be significantly lower than for HO_2. Also shown in Figure 5.10 is the CH_3O_2 spectrum measured by Faragó et al., at 67 mbar $He:O_2$ ~ 1:1 scaled to match the updated absorption cross section, $\sigma_{1335.29\text{nm}}$ = 2.2 × 10^{-20} cm^2 $molecule^{-1}$ (Fittschen, 2019). The general shape agrees well with the data measured here, however the two sharp features at 1335.47 and 1335.29 nm in the spectrum obtained by Faragó et al. could not be reproduced here. The spectrum measured by Pushkarsky et al. at 250 Torr

Ne:O_2 over a larger wavelength range, 1298.70 to 1369.89 nm (Figure 5.7), shows these sharp features, as does the spectrum reported by Atkinson and Spillman at 27 mbar N_2:O_2 (Figure 5.8), but there is a ~0.5 nm offset in the spectrum reported there. It may be that the sharp features are more significantly affected by pressure broadening and are lost in the measurements made here, or the inability to perform a single high-resolution scan with this equipment. Nevertheless, the similarity of the results at 80 mbar He:O_2 = 3:1 and at 100 and 1000 mbar of air reported in this work, and their agreement with the previous measurements (Pushkarsky et al., 2000, Atkinson and Spillman, 2002, Faragó et al., 2013, Fittschen, 2019) suggests that the absorption cross section at the optimum measurement wavelength, 1335.47 nm, is unaffected by pressure broadening and can be assumed constant under all of the conditions used in this work, i.e. at 80 mbar of He and O_2 and at 100 and 1000 mbar of air.

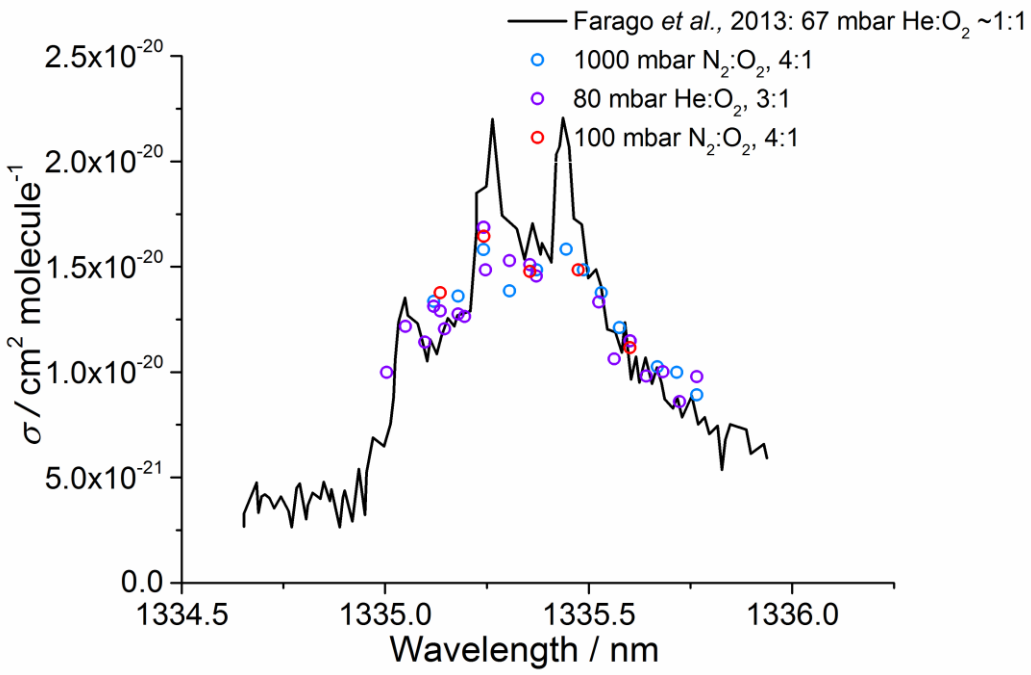

Figure 5.10 The measured absorption spectra were scaled to the cross section determined at 1335.47 nm using the kinetics of the CH_3O_2 decay monitored using CRDS (section 5.3.3). The black line represents the CH_3O_2 spectrum measured by Faragó et al. 2013 at 67 mbar He:O_2 ~ 1:1 but scaled to reflect updated cross section released by Fittschen, 2019. There is good agreement between the previous measurement of the spectrum and the measurements made here at all pressures, indicating there is no significant effect of pressure broadening. The only exception is the two sharp features at 1335.47 and 1335.29 nm which could not be detected. These smaller features may be susceptible to pressure broadening and lost in the measurements made here.

5.3.2 Modelling the HO_2 absorption cross section between 50 and 1100 mbar

Pressure broadening effects cause the absorption wavelength band to become wider and the cross section to decrease as pressure increases, meaning discrete cross section values exist for the 1506.43 nm HO_2 absorption at 100 mbar and the same absorption at 1000 mbar. By taking the line centres and line strengths of the HO_2 transition at 1506.43 nm and its neighbours from spectra reported by Thiebaud et al. in 66 mbar (50 Torr) of helium (shown in Figure 5.6), the absorption cross section of HO_2 at 1506.43 nm was modelled as a function of pressure by Dr. Michele Gianella of the University of Oxford. The line strengths were assumed to be the same in air as those reported in helium, and a broadening coefficient, γ_{air}, was taken from an average of 34 HO_2 transitions between 1508 – 1499 nm to be 1.14×10^{-4} $cm^{-1}mbar^{-1}$ in previous work (Ibrahim et al., 2007) and was assumed constant for all transitions in the model. Figure 5.11 is the result of the modelling, showing the simulated cross section as a function of pressure. The error bars arise from repeating the calculation at each pressure using the maximum and minimum values of γ_{air} reported by Ibrahim *et al*.

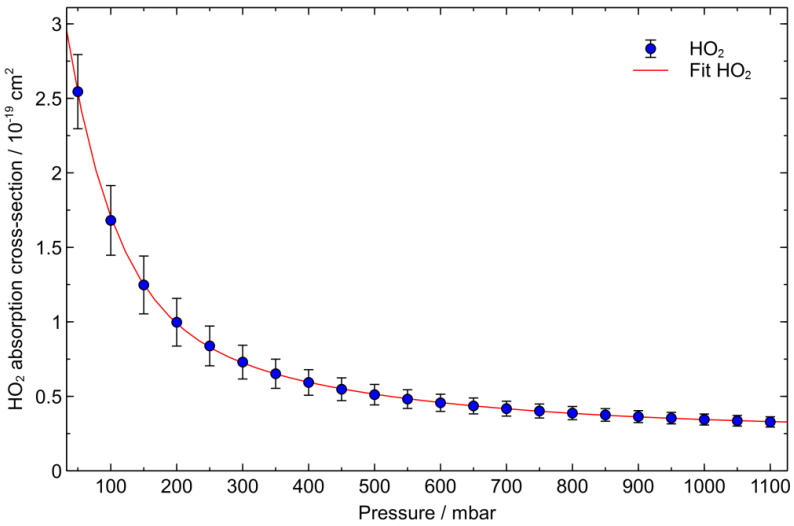

Figure 5.11. Absorption cross section of HO_2 at 1506.43 nm vs. pressure of air. The σ_{HO2} values (blue circles) were computed using the line strengths of the HO_2 transitions contributing to the absorption at 1506.43 nm (Taken from Thiebaud et al) and the pressure broadening coefficients assumed to be the same for all transitions and equal to the average of the values reported for the spectral region between 1499 and 1508 nm ($0.115\ cm^{-1}\ atm^{-1} = 1.14 \times 10^{-4}\ cm^{-1}\ mbar^{-1}$, Ibrahim et al.) Modelling performed by Dr. Michele Gianella of the University of Oxford.

This modelling work yields the HO_2 cross section at 150 mbar of σ_{HO_2150}= (1.25 ± 0.19) × 10^{-19} cm^2 $molecule^{-1}$, which agrees well with an equation developed through experimental determinations of the cross section between 27 – 133 mbar (Tang et al., 2010), which calculates σ_{HO_2150}= (1.29 ± 0.23) × 10^{-19} cm^2 $molecule^{-1}$. At 1000 mbar the model computes a cross section of σ_{HO_21000} = (3.44 ± 0.37) × 10^{-20} cm^2 $molecule^{-1}$, but there is currently no experimental work to compare this value to. Both cross sectional values were also determined using kinetic decays of HO_2, which is shown in the following section.

5.3.3 Measuring the absorption cross section through temporal decays of the radical self-reaction

The absorption cross section of can be determined through analysis of the second order decay kinetics of the HO_2 or CH_3O_2 radicals, in a similar manner to that described in the calibration of FAGE through decay measurements (sections 3.2.3 and 4.4.2). This is possible as the sensitivity factor of FAGE, *C*, is analogous to the absorption cross section as they both describe the amount of 'signal' observed per molecule. For FAGE, this signal is fluorescence, whereas for CRDS the signal is absorbance. This gives an equation very similar to the ones use calibrate the FAGE instrument in 3.2.3:

$$\alpha_t = \left(\left(\frac{1}{(\alpha)_0} + \frac{2 \times k_{\text{self-r.}}}{k_{\text{loss}} \times \sigma}\right) \times \exp(k_{\text{loss}} t) - \left(\frac{2 \times k_{\text{self-r.}}}{k_{\text{loss}} \times \sigma}\right)\right)^{-1} \qquad \textbf{Eq. 5.3}$$

where α_t is the absorption coefficient at time *t* in the decay and α_0 is the absorption coefficient at time *t* = 0, and σ is the absorption cross section. Figure 5.12 shows an HO_2 decay measurement made by CRDS at 150 mbar, and Eq. 5.3 was fitted to the data to extract σ_{HO2}. Fitting to eight decay traces gave an average value of σ_{HO_2150} = (1.02 ± 0.18) × 10^{-19} cm^2 $molecule^{-1}$, which agrees very well with the (1.25 ± 0.19) × 10^{-19} cm^2 $molecule^{-1}$ predicted by the modelling procedure described in section 5.3.2.

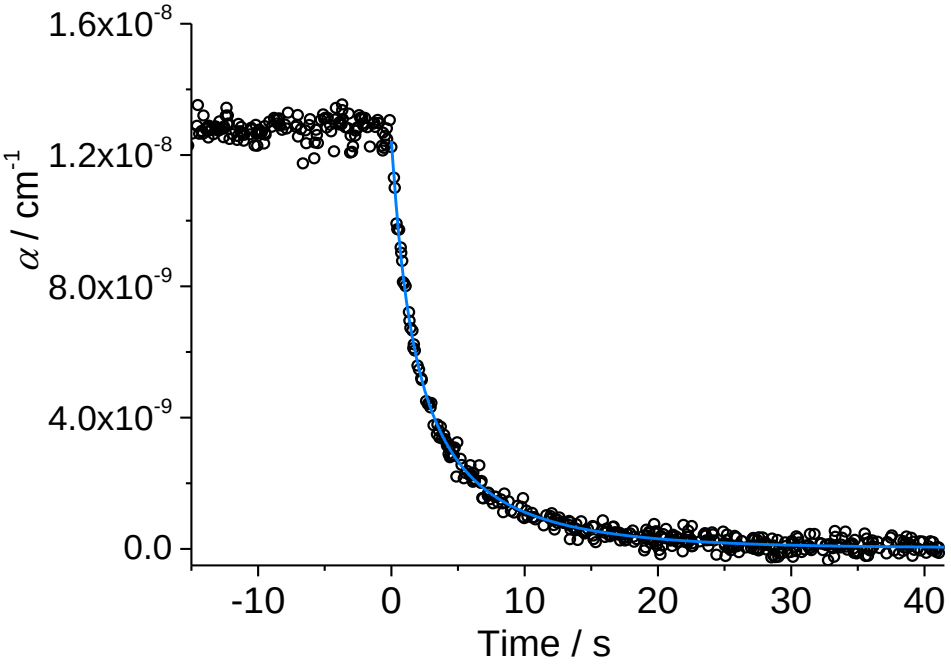

Figure 5.12. A second order HO_2 decay as measured by CRDS at 150 mbar and 298 K in an air mixture (black). HO_2 was generated using $[Cl_2]$ ~1.5 × 10^{14} molecule cm^{-1} and $[CH_3OH]$ ~ 1.0 × 10^{14} molecule cm^{-3}. The UV photolysis lamps were turned off at time = 0, and the resulting decay was fitted using Eq. 5.3 (blue).

The modelling shown in section 5.3.2 predicts that an increase in pressure to 1000 mbar causes the cross section to decrease by a factor of ~3.6, which in turn causes the absorption signal for an equal concentration to be lower by the same factor. This leads to a reduced signal to noise ratio and is evidenced in the decay shown in Figure 5.13. Fitting Eq. 5.3 to these decays therefore yields higher uncertainties of ~14 % on average, compared to ~3 % at 150 mbar. A more reliable determination of the cross section could be made by using the FAGE decay traces that were scaled to match the profile of the CRDS trace. The FAGE data was scaled by taking the average of the signal from each instrument at times prior to t = 0 and using the ratio of these numbers to scale down all the FAGE data points. This is also shown in Figure 5.13, where the FAGE signal has been scaled to match the absorption coefficient measured by the CRDS system. Fitting Eq. 5.3 to these scaled FAGE decays yields an average $\sigma_{HO_2 1000}$= (3.91 ± 0.74) × 10^{-20} cm^2 $molecule^{-1}$, which agrees very well with the model predicted cross section of (3.44 ± 0.37) × 10^{-20} cm^2 $molecule^{-1}$ in section 5.3.2.

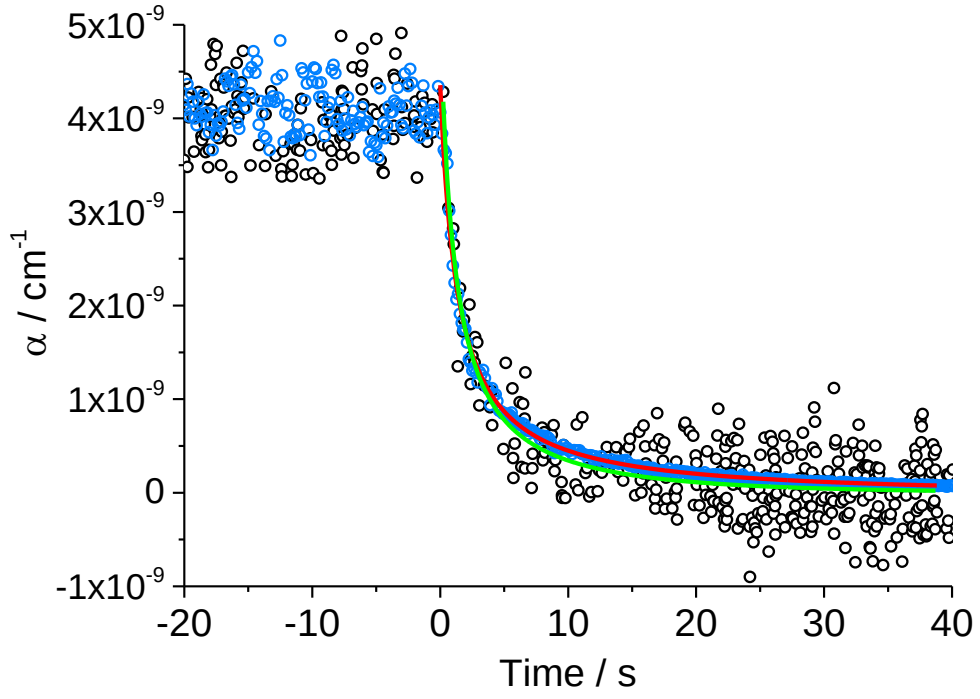

Figure 5.13. An HO_2 decay measured by CRDS (black) and FAGE (blue) at 1000 mbar and 298 K, where the FAGE signal has been scaled down (see text) to overlap that of the CRDS absorption coefficient. HO_2 was generated using $[Cl_2]$ ~1.7 × 10^{14} molecule cm^{-3} and $[CH_3OH]$ ~2.0 × 10^{14} molecule cm^{-3}. Fitting Eq. 5.3 to the CRDS data (green) gave $\sigma_{HO_2 1000}$ = (3.59 ± 0.52) × 10^{-20} cm^2 $molecule^{-1}$, whereas fitting to the much less scattered FAGE data (blue) gave the more precise $\sigma_{HO_2 1000}$ = (3.54 ± 0.05) × 10^{-20} cm^2 $molecule^{-1}$.

Additionally, the good overlap of the two decay profiles is evidence that both instruments were measuring almost the same HO_2 radical concentrations, with no interfering effects.

The CH_3O_2 cross section was determined in the same way using k_{obs} = (4.8 ± 1.1) × 10^{-13} cm^3 $molecule^{-1}$ s^{-1} (Atkinson et al., 2006) for the self-reaction rate constant. However, in section 4.4.2 the wall loss was found to be negligible for CH_3O_2 radicals, and this is further evidenced by the lack of a concentration gradient in the HIRAC chamber (section 5.1.3), meaning that k_{loss} can be ignored and Eq. 5.3 simplified to give the following expression:

$$\alpha_t = \left(\frac{1}{\alpha_0} + \frac{2 \cdot k_{obs.}(t\text{-}t_0)}{\sigma(1335.47\text{nm})}\right)^{-1} \qquad \textbf{Eq. 5.4}$$

Fitting Eq. 5.4 to CH_3O_2 decays measured by CRDS at 100 mbar air gave an average value for the cross section of $\sigma(1335.47\text{nm})$ = (1.51 ± 0.19) × 10^{-20} cm^2 $molecule^{-1}$, which is in very good agreement with the determination by Atkinson and Spillman who report (1.5 ± 0.8) × 10^{-20} cm^2 $molecule^{-1}$ in ~26 mbar of nitrogen. Although not directly measured by Pushkarsky et al., the cross section at 1335.47 nm was estimated using their reported value for the v_{00} transition, 2.7 × 10^{-20} cm^2 $molecule^{-1}$ (error estimated <50 %), and scaling it by the relative peak heights in their reported spectrum, Figure 5.7, giving approximately 1 × 10^{-20} cm^2 $molecule^{-1}$. Fitting Eq. 5.4 to decays measured by CRDS at 80 mbar He:O_2 was more difficult due to poor signal quality, and is shown in Figure 5.14. Despite the poor signal the fit to the CRDS data gave a cross section of (1.71 ± 0.15) × 10^{-20} cm^2 $molecule^{-1}$, which is in reasonable agreement with the determination at 100 mbar but relatively imprecise. However, by employing the same FAGE signal scaling technique described during the determination of the HO_2 cross section and re-fitting Eq. 5.4 to the scaled FAGE data, also shown in Figure 5.14, gave a more precise value of (1.55 ± 0.02) × 10^{-20} cm^2 $molecule^{-1}$. The average value obtained from these fits at 80 mbar He:O_2 was (1.46 ± 0.17) × 10^{-20} cm^2 $molecule^{-1}$ which is in very good agreement with the value determined at 100 mbar. The cross section at 1000 mbar could not be measured adequately as it required the use of the acetone photolysis method to generate radicals (see section 5.1.2), giving signal quality too poor to measure meaningful kinetics. However, as no significant pressure broadening was observed in section 5.3.1 it is assumed that an average of the cross section determined at 80 and 100 mbar, $\sigma(1335.47\text{nm})$ = (1.49 ± 0.19) × 10^{-20} cm^2 $molecule^{-1}$, can be used for all CH_3O_2 inter-comparison measurements here.

The cross section determined here can also be compared to the very recent determination at 1335.26 nm, $\sigma(1335.26\text{nm})$ = 2.2 × 10^{-20} cm^2 $molecule^{-1}$ (no error reported, Fittschen, 2019), by scaling the value measured in this work with the ratio of the cross sections at these wavelengths obtained in the high resolution scan by Faragó et al., giving 1.9 × 10^{-20} cm^2 $molecule^{-1}$, which is in good agreement.

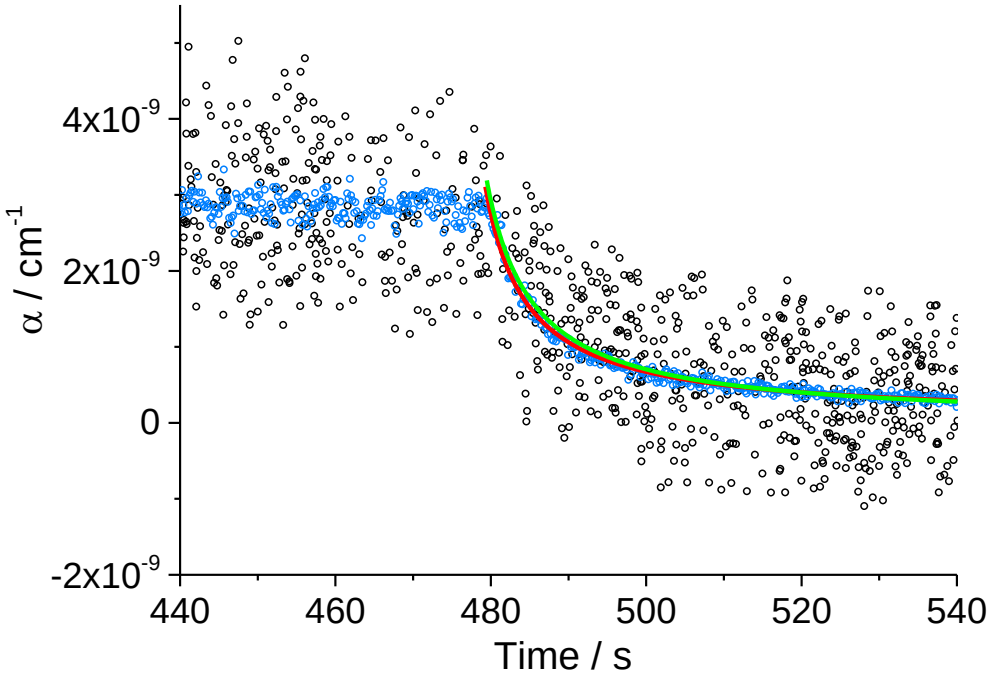

Figure 5.14 Second order decay of the CH_3O_2 absorption coefficient at 1335.47 nm from CRDS data (black) obtained in HIRAC at 295 K under 80 mbar He:O_2 3:1 conditions. The signal quality is very poor, but fitting Eq. 5.4 to the CRDS data gave an absorption cross section of (1.71 ± 0.15) × 10^{-20} cm^2 $molecule^{-1}$, where the error limit is the statistical fitting error at 1σ. A FAGE measurement (blue) that was made simultaneously with the CRDS measurement and is of much higher quality was scaled down (see text) to overlap with the CRDS data. Fitting Eq. 5.4 to this scaled data (green) gave an absorption cross section of (1.55 ± 0.02) × 10^{-20} cm^2 $molecule^{-1}$, which is in reasonable agreement with the fit to the CRDS data but more precise. $[Cl_2]_0$ = 1.1 × 10^{14} molecule cm^{-3} and $[CH_4]_0$ = 2.5 × 10^{16} molecule cm^{-3}.

5.4 Inter-comparison results

The inter-comparison experiments were performed using the chemical systems detailed in sections 5.1.1 and 5.1.2 for HO_2 and CH_3O_2 respectively. The CRDS measurements of HO_2 and CH_3O_2 were performed at 1506.43 nm and 1335.47 nm respectively, as determined in section 5.3, and data were analysed using the absorption cross section values determined experimentally in section 5.3, the HO_2 data were also re-calculated using the modelled cross section values from section 5.3.2 to compare with the measured values. For the measurements at pressures below 1000 mbar the FAGE data have been analysed using calibration factors derived from the kinetics of the radical self-reaction, which was explained in sections 3.2.3 and 4.4.2 for HO_2 and CH_3O_2 respectively. At 1000 mbar the wand calibration method is also applicable for both radicals, and so these data sets were analysed using the average calibration factor of the two methods.

5.4.1 HO_2 Inter-Comparison results

Figure 5.15 shows a comparison measurement between FAGE and CRDS made over ~10 minutes at 150 mbar, where the CRDS data have been analysed using the measured cross section (blue) and the modelled cross section (black). The plot shows excellent agreement with the CRDS data using the modelled cross section σ_{HO_2150} = (1.25 ± 0.19) × 10^{-19} cm^2 $molecule^{-1}$. Using the kinetically determined cross section σ_{HO_2150} = (1.02 ± 0.18) × 10^{-19} cm^2 $molecule^{-1}$ (blue) gave a less good agreement (FAGE ~80 % of CRDS), suggesting the modelled cross section is more accurate. The data also exhibits the gradual decrease in [HO_2] caused by reagent consumption.

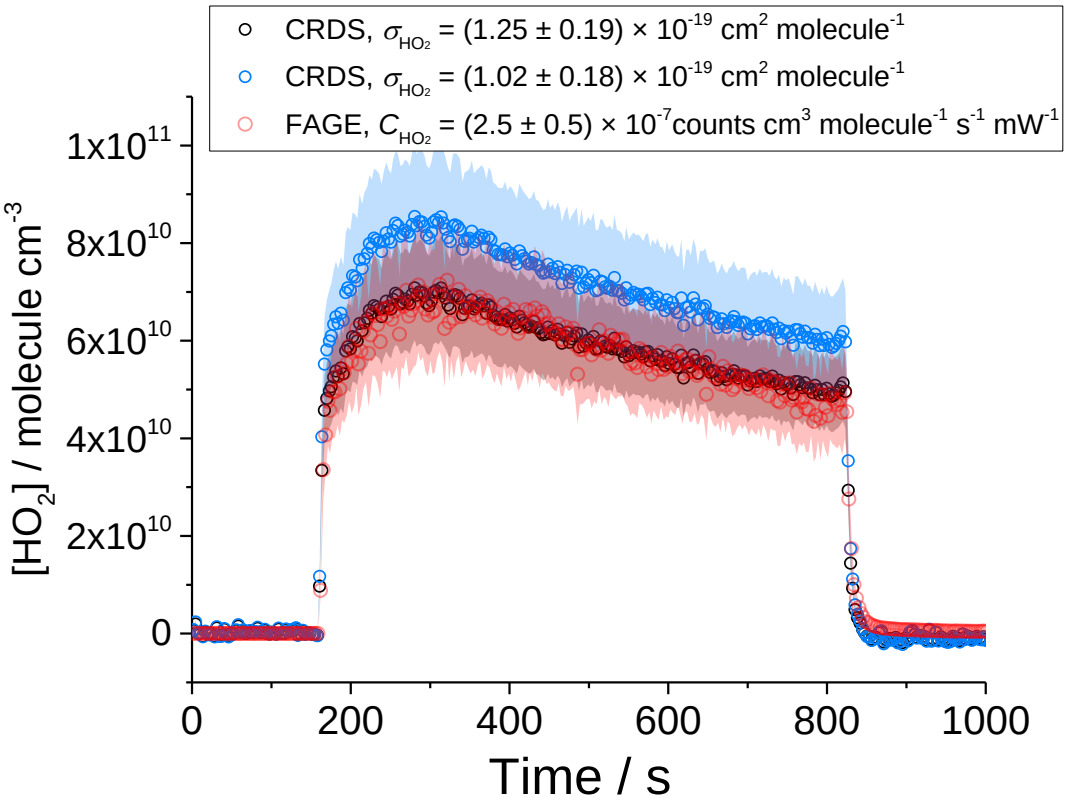

Figure 5.15. Comparison measurement at 150 mbar air and 298 K where the lamps were switched on at t = ~150 seconds for ~10 minutes. HO_2 measured by FAGE (red) is plotted with HO_2 measured by CRDS using the modelled cross-section, σ_{HO_2150} = 1.25 × 10^{-19} cm^2 molecule^{-1} (black), and the cross-section determined using the kinetic method σ_{HO_2150} = 1.02 × 10^{-19} cm^2 molecule^{-1} (blue). Each data point is an average of 3 seconds. HO_2 was generated using [CH_3OH] = 6.6 × 10^{13} molecule cm^{-3}, [Cl_2] = 4.4 × 10^{13} molecule cm^{-3}.

Figure 5.16 is another example of the simultaneous measurements made by the CRDS and FAGE at 150 mbar where the UV photolysis lamps have been switched on and off periodically to produce a sequence of high and low HO_2 concentrations. The FAGE data (red) are plotted against the CRDS data (black) that have been analysed using the modelled cross section, σ_{HO_2150} = 1.25 × 10^{-19} cm^2 molecule^{-1}, for clarity. The two signal traces overlap very well, even in the periods of rapid [HO_2] change when the lamps are switched off, further suggesting there are no interfering species present in either measurement.

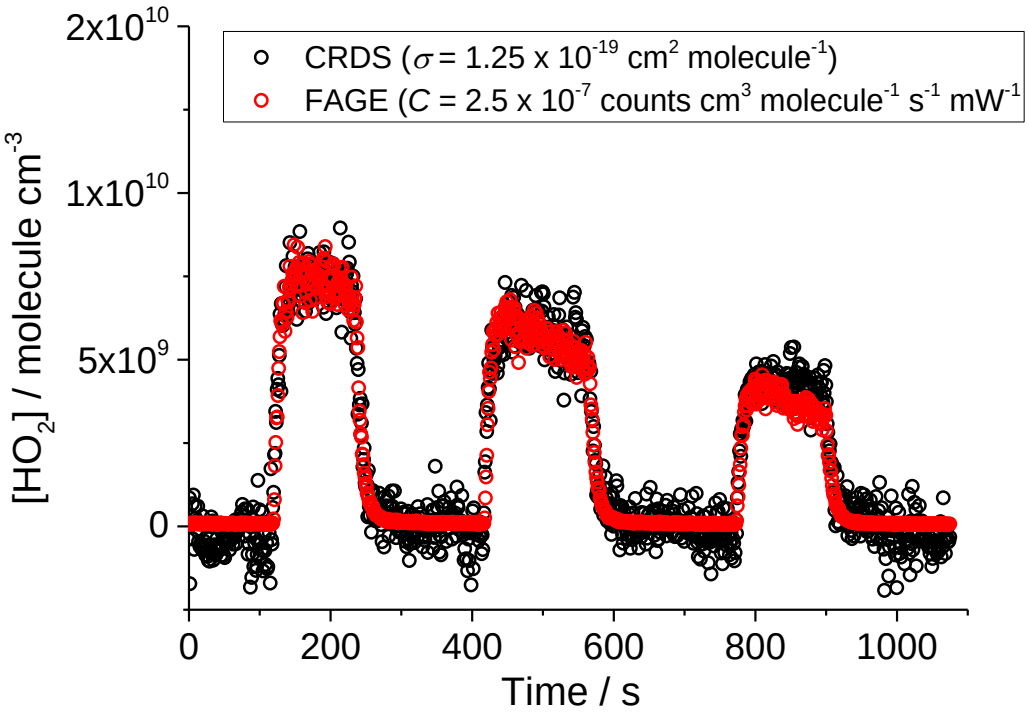

Figure 5.16. An overlay of FAGE (red) and CRDS (black), using the modelled cross section σ_{HO_2150} = 1.25 × 10^{-19} cm^2 molecule^{-1}, measurements of HO_2 at 150 mbar air and 298 K, where the lamps were turned on and off every ~200 seconds. HO_2 was generated using [CH_3OH] = 6.6 × 10^{13} molecule cm^{-3}, [Cl_2] = 7.1 × 10^{12} molecule cm^{-3}. Both instrument data sets have been averaged into 1 second groups.

By plotting the HO_2 concentration measured by FAGE against those measured by CRDS, the correlation plot in Figure 5.17 was produced. Both instrument data sets were averaged into 3 second groups, and the CRDS data were analysed using both the modelled and kinetically measured absorption cross sections to produce two linear data sets. The comparison includes data from both steady state and decay measurements.

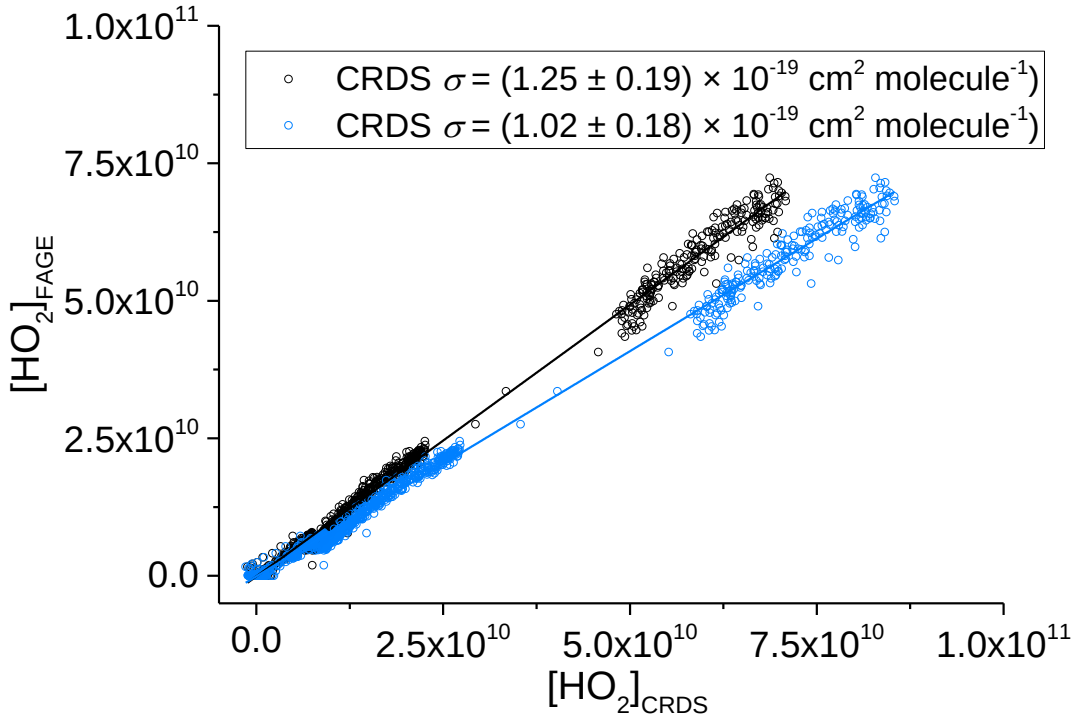

Figure 5.17. Overall correlation plot at 150 mbar and 298 K. $[HO_2]_{CRDS}$ was calculated using the modelled cross-section, σ_{HO_2150} = 1.25 × 10^{-19} cm^2 molecule^{-1}, (black) and the cross-section derived through kinetics, σ_{HO_2150} = 1.02 × 10^{-19} cm^2 molecule^{-1}, (blue). Linear fits of the data gave gradients of 0.987 ± 0.002 and 0.819 ± 0.002 respectively.

Linear regression fits of the data yield a gradient of 0.987 ± 0.002 and 0.819 ± 0.002 for the σ_{HO_2150} = 1.25 × 10^{-19} cm^2 molecule^{-1} and σ_{HO_2150} = 1.02 × 10^{-19} cm^2 molecule^{-1} respectively, and both lines have a negligible intercept at y = (-1.0 ± 0.5) × 10^8 molecule cm^{-3}. The agreement between the two instruments at 150 mbar is very good, within 2 % for the modelled cross-section and within 18 % using the cross-section derived from the kinetics.

Figure 5.18 shows an experiment performed at 1000 mbar over ~5 minutes, and as with the 150 mbar experiments the FAGE method agrees very well with the CRDS data that has been analysed using the modelled absorption cross-section, $\sigma_{HO_2 1000}$ = (3.44 ± 0.37) × 10^{-20} cm^2 $molecule^{-1}$ (blue), however the kinetically determined cross section $\sigma_{HO_2 1000}$ = (3.87 ± 0.74) × 10^{-20} cm^2 $molecule^{-1}$ (black) gives an even closer match between the two instruments. The model is still in remarkably good agreement considering it has extrapolated data from ~66 mbar up to 1000 mbar.

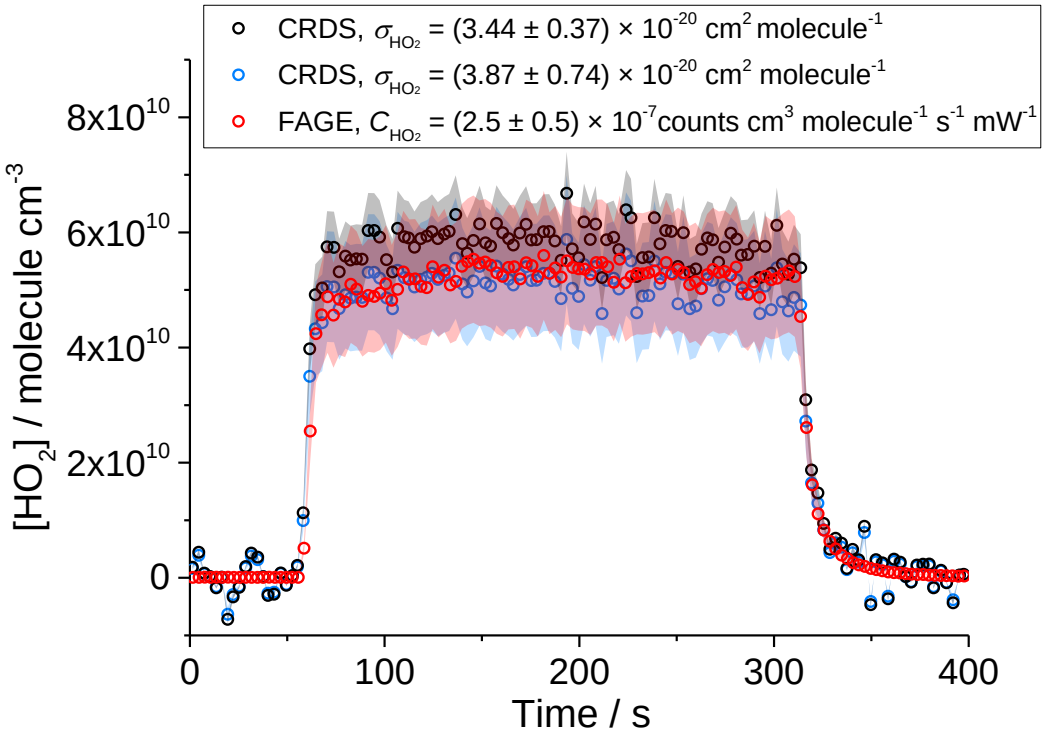

Figure 5.18. Comparison measurement at 1000 mbar air where the lamps were left on for ~4 minutes. The HO_2 concentration measured by FAGE (red) is plotted with HO_2 measured by CRDS using the modelled cross-section, $\sigma_{HO_2 1000}$ = 3.44 × 10^{-20} cm^2 $molecule^{-1}$ (blue), and the cross section determined through kinetic decays, $\sigma_{HO_2 1000}$ = 3.87 × 10^{-20} cm^2 $molecule^{-1}$ (black). Each data point is an average of 3 seconds. HO_2 was generated using [CH_3OH] = ~1.65 × 10^{15} molecule cm^{-3}, and [Cl_2] = ~1.10 × 10^{14} molecule cm^{-3}.

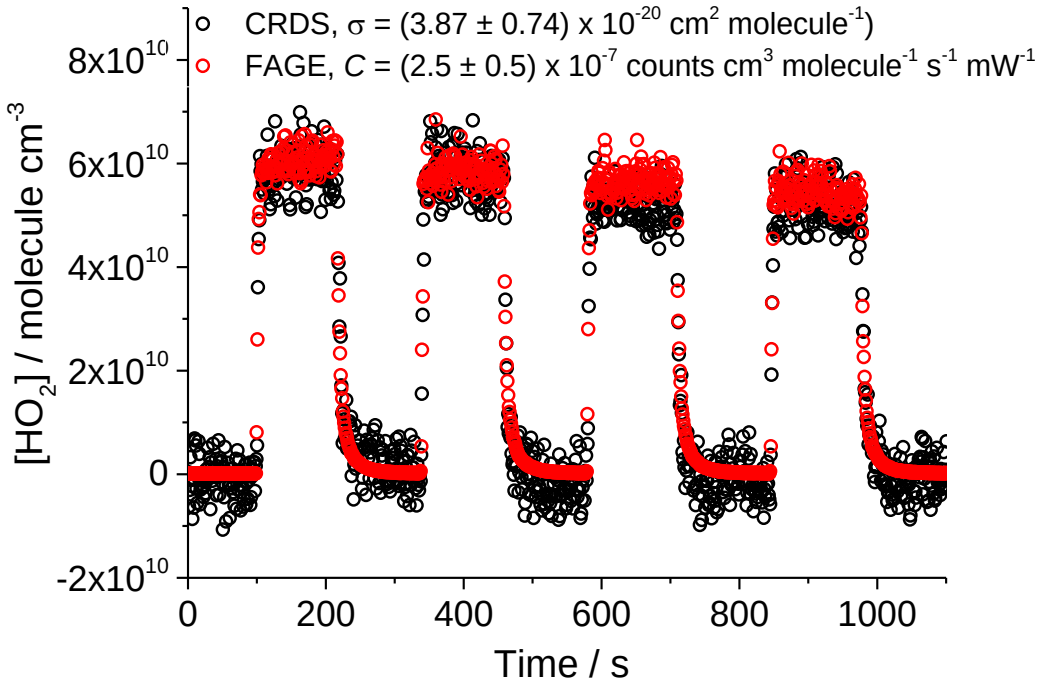

Figure 5.19. An overlay of FAGE (red) and CRDS (black), using the cross section derived from kinetic decays, $\sigma_{HO_2 1000}$ = 3.87 × 10^{-20} cm^2 molecule^{-1}, measurements of HO_2 at 1000 mbar air and 298 K. The UV photolysis lamps were switched on and off in ~100 second intervals. HO_2 was generated using [CH_3OH] = ~8.27 × 10^{13} molecule cm^{-3}, [Cl_2] = ~3.8 × 10^{13} molecule cm^{-3}.

Figure 5.20 shows an overall correlation plot between FAGE and CRDS at 1000 mbar, where the CRDS data have been analysed using both the modelled cross section (blue) and kinetically determined cross section (black).

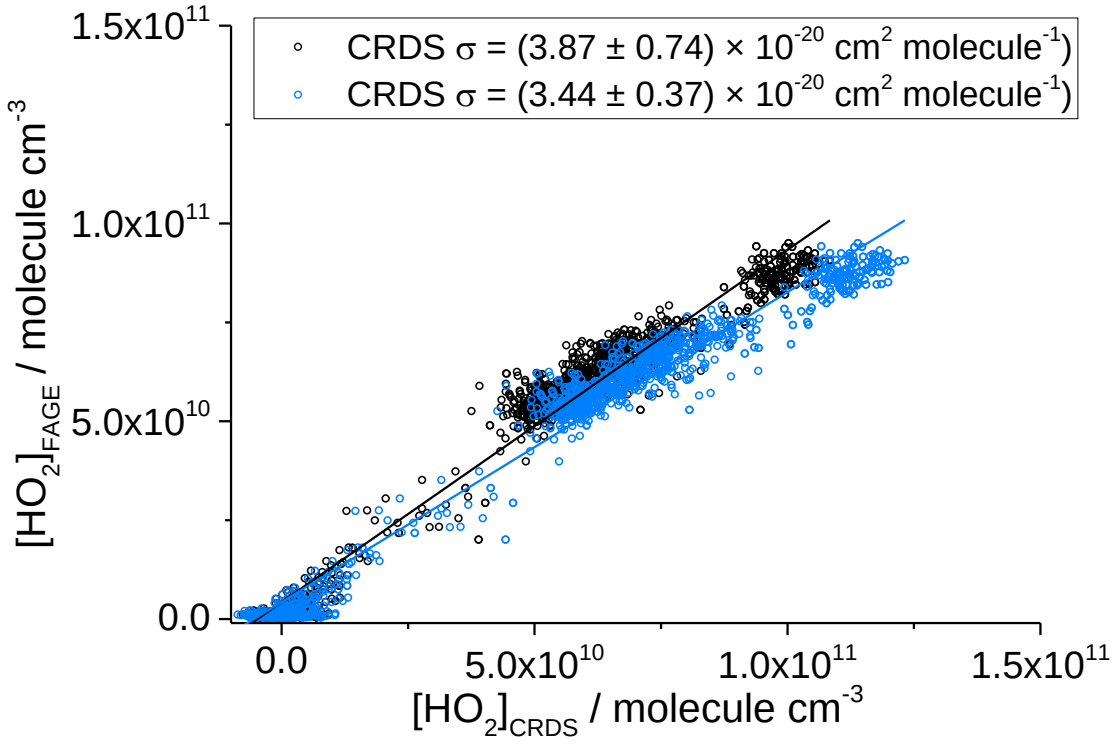

Figure 5.20. Overall correlation plot at 1000 mbar air. $[HO_2]_{CRDS}$ was calculated using the modelled $\sigma_{HO_2 1000}$= 3.44 × 10^{-20} cm^2 (blue) and the experimentally determined through kinetic decay $\sigma_{HO_2 1000}$ = 3.87 × 10^{-20} cm^2 (black). Linear fits of the data gave gradients of 0.890 ± 0.004 and 0.783 ± 0.004 respectively. $[HO_2]_{FAGE}$ was calculated using a sensitivity factor of 2.5 × 10^{-7} counts cm^3 $molecule^{-1}$ s^{-1} mW^{-1}.

Performing a linear regression yields a gradient of 0.890 ± 0.004 and 0.783 ± 0.004 for the data sets analysed using the cross sections $\sigma_{HO_2 1000}$ = 3.44 × 10^{-19} cm^2 $molecule^{-1}$ (Modelled) and $\sigma_{HO_2 1000}$ = 3.91 × 10^{-20} cm^2 $molecule^{-1}$ (Kinetic) respectively. As with the 150 mbar experiments, both lines have a negligible intercept of (-4.3 ± 0.3) × 10^9 molecule cm^{-3} and (-1.0 ± 0.5) × 10^8 molecule cm^{-3} respectively. The agreement between the two instruments is not as good as the 150 mbar data, but the overlap is still good. The higher gradient error and overall signal variability than the 150 mbar measurements is due to the reduced signal to noise ratio resulting from the effects of pressure broadening lowering the absorption signal (section 5.2.1).

5.4.2 CH_3O_2 Inter-comparison results

Figure 5.21 shows a typical inter-comparison measurement of CH_3O_2 radicals in a helium:oxygen atmosphere at 80 mbar, where the radicals were generated using the photolysis of acetone using 254 nm lamps that were switched on at ~250 seconds, and switched off again at ~550 seconds. There is good overlap between the FAGE (blue) and CRDS (black) measurements, but there is a stark contrast in the signal to noise ratio of the two techniques. The CRDS data are of inferior quality as they are subject to interference from the 254 nm photolysis lamps (section 5.1.2). This is evidenced by the distinct difference in CRDS signal variation between the lamps on and lamps off sections, whereas the FAGE instrument is less affected as the detector is isolated from the light by the inlet pinhole and lower proximity to the lamps. There is also an imperfect overlap of the data during the radical decay after the lamps were switched off, with the CRDS instrument measuring a slower decay that is likely caused by interference species generated during photolysis of acetone.

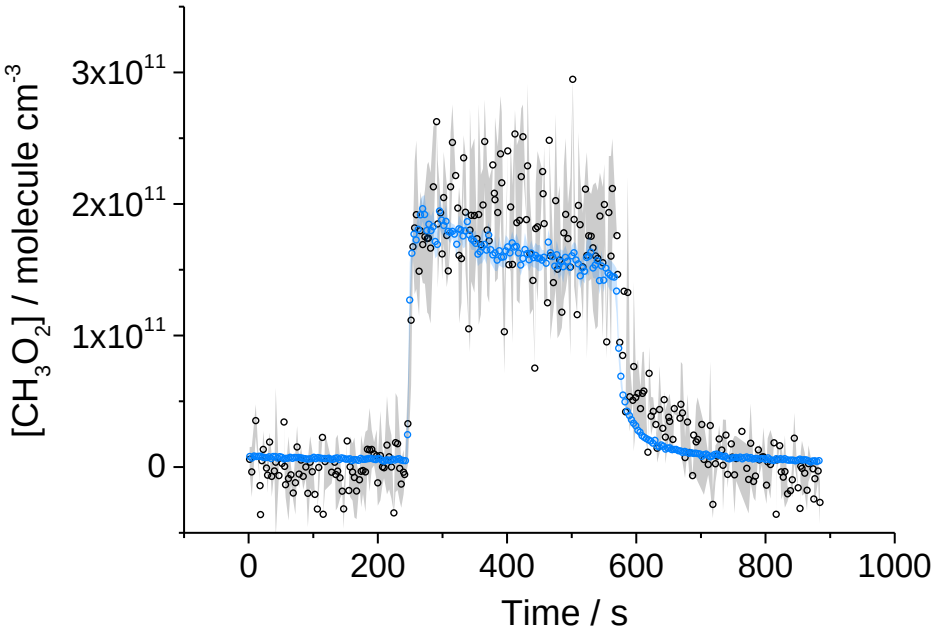

Figure 5.21 Comparison of CH_3O_2 measurement at 80 mbar He:O_2 (3:1) where the lamps were turned on at t ~ 250 s for ~ 5 min to generate CH_3O_2 and then turned off again. The measurement by FAGE is shown in blue and the measurement by CRDS is plotted in black. CH_3O_2 radicals were generated using the 254 nm photolysis of $(CH_3)_2CO$ (8.8 × 10^{14} molecule cm^{-3}). The 1σ statistical errors generated by the data averaging are shown as grey (CRDS) and blue (FAGE) shadows.

Figure 5.22 is a correlation plot of five experiments under these conditions where the radicals were generated using both the acetone photolysis method and the chlorine/methane method. The linear fit to the data gives a gradient of 0.91 ± 0.02, showing a very good agreement, within 9 %, between the two instruments. Figure 5.22 also shows the difference in the signal to noise ratio between the two instruments, with most of the data spread being in the CRDS axis.

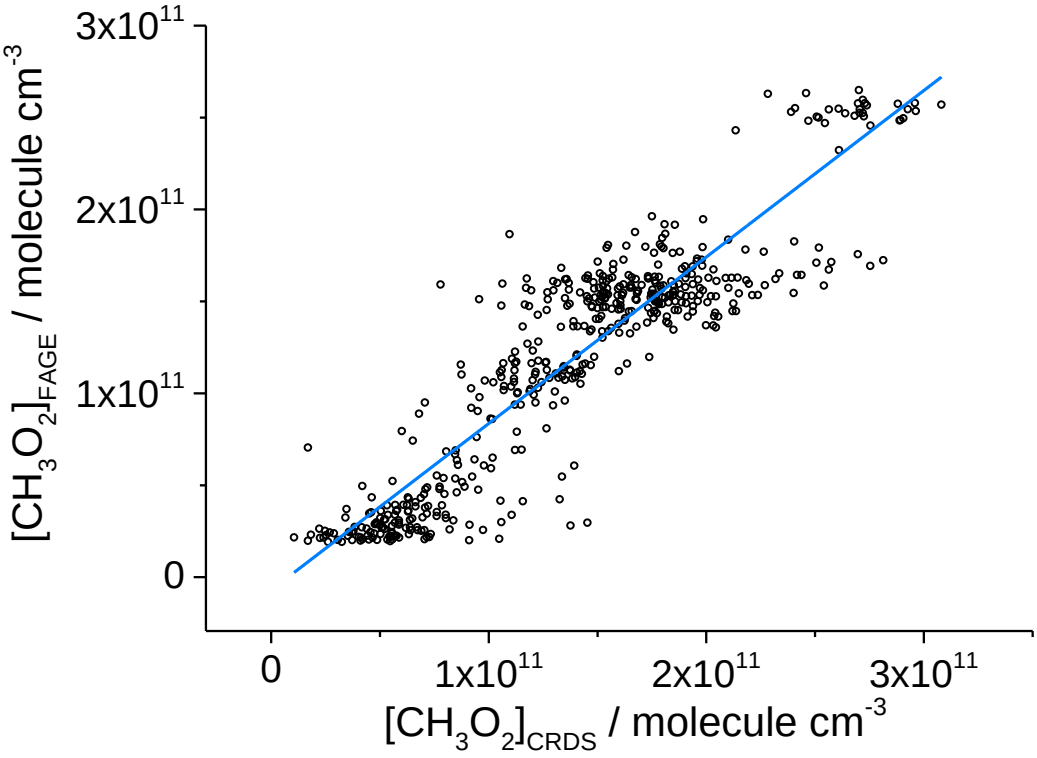

Figure 5.22 Correlation plot at 80 mbar He:O_2 (3:1) combining the data obtained using acetone/O_2/254 nm lamps with the data generated using Cl_2/CH_4/O_2/UV black lamps. [CH_3O_2] measured by FAGE is plotted against [CH_3O_2] measured by CRDS. The linear fit to the data generates a gradient of 0.91 ± 0.02. $[CH_3O_2]_{FAGE}$ was determined using a calibration factor of 3.83×10^{-9} counts cm^3 $molecule^{-1}$ s^{-1} mW^{-1} and $[CH_3O_2]_{CRDS}$ was calculated using a cross section of 1.49×10^{-20} cm^2 $molecule^{-1}$. Each point is an averaged value over 3 s.

Figure 5.23 shows a similar inter-comparison measurement, this time performed in synthetic air at a pressure of 100 mbar and using the chlorine/methane system to generate the CH_3O_2 radicals. Again, the overlap between the FAGE (blue) and CRDS (black) data is very good. The deviation of the FAGE instrument around ~450 seconds is caused by the laser wavelength drifting off the maximum

fluorescence position and is only a minor error in the measurement. The two instruments overlap well during the radical decays where the concentration is changing rapidly, and the signal to noise ratio on the CRDS measurement is significantly better. These are both the result of using the chlorine/methane system to generate radicals, which does not require 254 nm light that interferes with the CRDS photodiode or generate secondary chemicals that may interfere with the CRDS measurement.

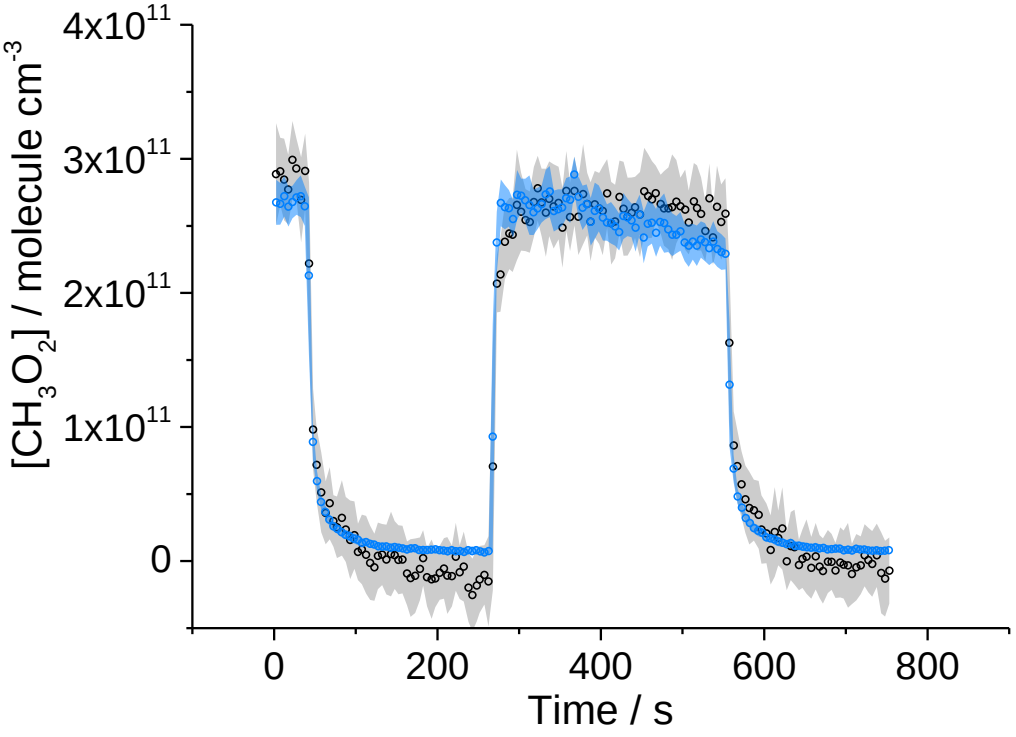

Figure 5.23 Comparison of CH_3O_2 measurement at 100 mbar N_2:O_2 (4:1), with the measurement by FAGE (blue) and the measurement by CRDS (black). CH_3O_2 radicals were generated by the photolysis of Cl_2 (2.5×10^{15} molecule cm^{-3}) in the presence of CH_4 (2.4×10^{16} molecule cm^{-3}) and O_2. The 1σ statistical errors generated by the data averaging are shown as grey (CRDS) and blue (FAGE) shadows.

Figure 5.24 is a correlation plot of 8 experiments under these conditions. The linear fit to the data gives a gradient of 1.06 ± 0.01 and shows an excellent agreement between the two methods. The plot also shows the better quality of data that can be obtained using the chlorine/methane system.

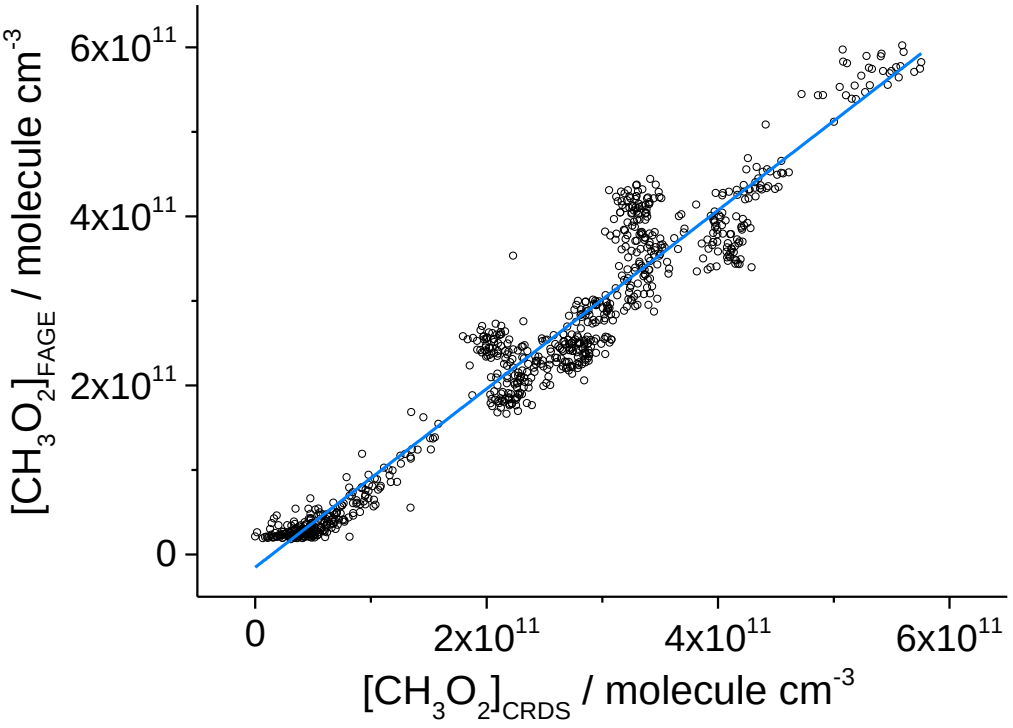

Figure 5.24 Combined data obtained using acetone/O_2/254 nm lamps with the data generated using Cl_2/CH_4/O_2/UV black lamps, all in 100 mbar air. [CH_3O_2] measured by FAGE is plotted versus [CH_3O_2] measured by CRDS. The linear fit to the data results in a gradient of 1.06 ± 0.01.

Figure 5.25 shows an inter-comparison measurement in air at a pressure of 1000 mbar, where radicals have been generated using the acetone photolysis method. Here, the relatively poor CRDS (black) signal to noise ratio returns as the photolysis lamps interfere with the photodiode, again evidenced by the reduction in noise when the lamps are off (between times 25-200 and 300-400 seconds). Despite this, the overlap with the FAGE data (blue) is good even during the kinetic decays when the lamps are switched off.

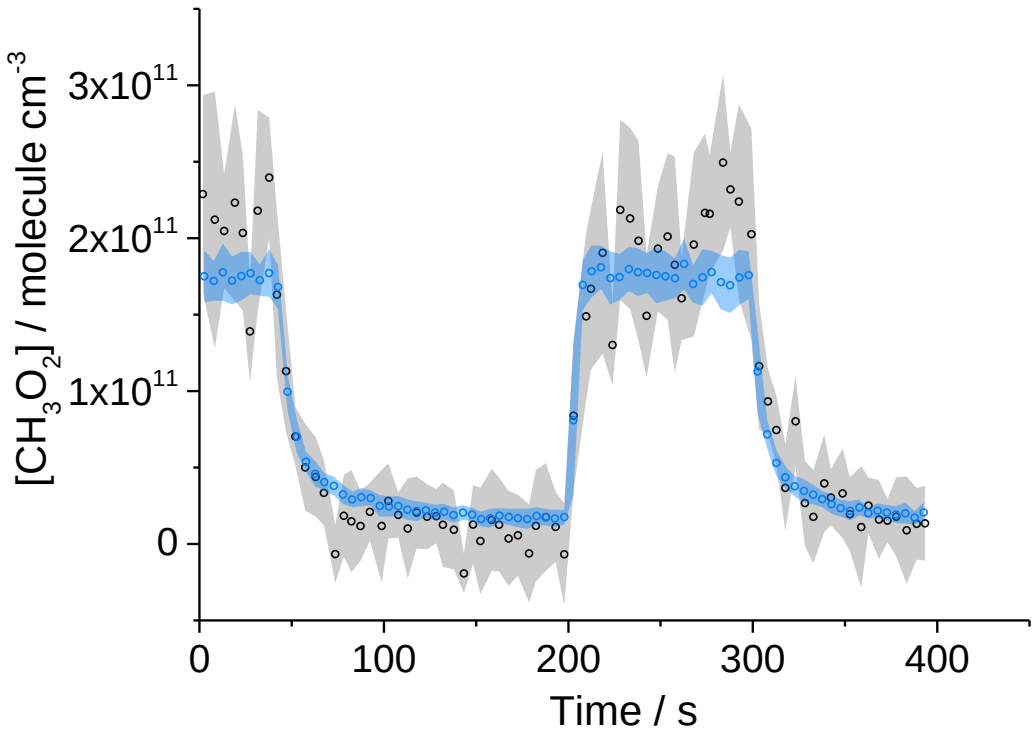

Figure 5.25 Comparison of CH_3O_2 measurement at 1000 mbar of synthetic air where the lamps were turned off at *t* ~ 40 s and then on at *t* ~ 200 s for ~ 2 min before being switched off again. The measurement by FAGE is shown in blue and the measurement by CRDS is plotted in black. CH_3O_2 radicals were generated using the 254 nm photolysis of $(CH_3)_2CO$ (8.8×10^{14} molecule cm^{-3}). The 1σ statistical errors generated by the data averaging are shown as grey (CRDS) and blue (FAGE) shadows

Figure 5.26 is a correlation plot of 4 data sets obtained under these conditions, where radicals were generated only using the acetone photolysis method. The linear fit to the data gives a gradient of 0.91 ± 0.02, which again indicates a good agreement between the two methods.

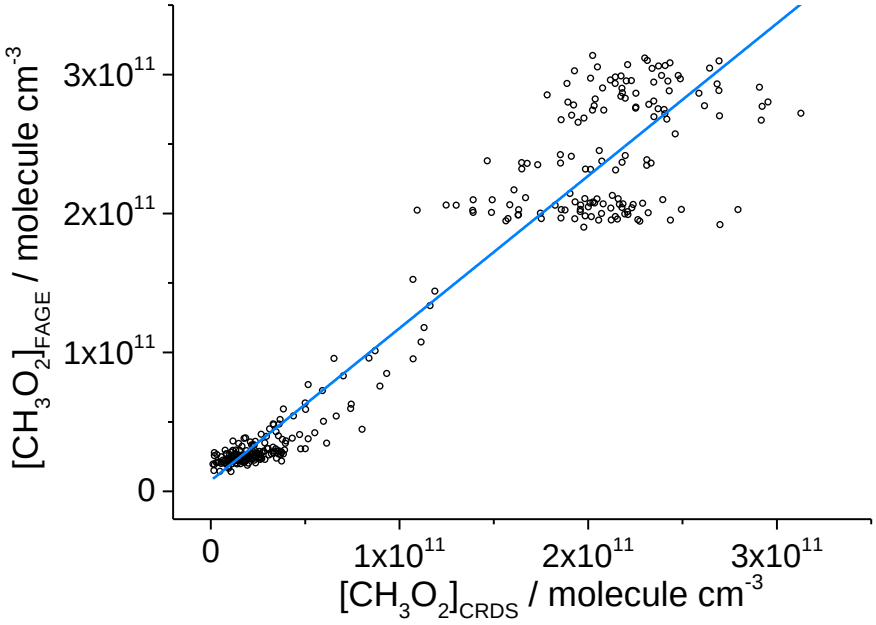

Figure 5.26 Correlation plot of all the data generated at 1000 mbar of air. [CH_3O_2] measured by FAGE is plotted against [CH_3O_2] measured by CRDS. The linear fit to the data generates a gradient of 1.10 ± 0.02, however this uncertainty does not accurately represent the scatter in the data as it is weighted to the dense data around the origin. Each point is an averaged value over 5 s.

As with the HO_2 intercomparison results in the previous section, the agreement between FAGE and CRDS measurements if CH_3O_2 is good, within 10 % in all cases, however the large amount of scatter in the CRDS data at 80 and 1000 mbar makes this an unreliable indicator. Furthermore, the FAGE calibration factor at 1000 mbar can be determined using either the kinetics of the self-reaction or the wand calibration method (sections 4.4.1 and 4.4.2, respectively), between which there is a ~30 % discrepancy. When the FAGE data are analysed using the sensitivity factor obtained from the wand calibration the linear fit has a gradient of 1.32 ± 0.02 to reflect this. The cause of the discrepancy may lie in the wand calibration method, or it may lie in the kinetics of the CH_3O_2 self-reaction upon which both the kinetic calibration and absorption cross section rely. This will be discussed in more detail in Chapter 6. It is also noted that the FAGE data never reaches the baseline in these measurements, this was due to insufficient time being allowed for the decays proceed below the lower limit of detection of the FAGE instrument compared to CRDS.

5.5 CRDS detection limit – Allan Deviation

The Allan deviation, $\sigma_A(n)$, is an estimation of the stability of a system to noise over time, and indicates the optimum number of data points, *n*, that should be averaged together to achieve the highest signal to noise ratio and therefore the lowest limit of detection. Longer averaging times increase the signal to noise ratio at the cost of temporal resolution by smoothing out high frequency noise sources, such as electrical and vibration noise. However, if averaging time is continually increased the signal to noise ratio may begin to decrease again as lower frequency signal variations, such as slow changes in cavity length, are captured in the averaging interval.

The Allan deviation measurements were performed by allowing the CRDS system to acquire ringdown events for around an hour whilst the chamber was under experimental conditions, meaning it was at pressure and filled with reagents but the lamps were not switched on. The Allan deviation, is $(1/\sqrt{2})$ multiplied by the root-mean-square value of the difference between adjacent points and gives an estimate of the error, *δα*, between successively measured absorption coefficients for a given averaging size *n.* All Allan deviation data shown here was analysed using software written by Dr Michele Gianella of the University of Oxford.

Figure 5.27 shows two Allan deviation plots, one at 150 mbar and another at 1000 mbar, of the absorption coefficient (calculated using Eq. 4.2) at 1506.43 nm against averaging group size, *n*. At 150 mbar, the plot shows that the standard deviation for one single data point (*n* = 1) is 1.9×10^{-10} cm^{-1}, but after averaging 250 events (~25 seconds at typical 10 Hz acquisition rate) this is reduced to 1.5×10^{-11} cm^{-1}. To be detectable, a quantity of HO_2 must generate a signal that exceeds this value, allowing the HO_2 detection limit to be calculated by dividing through the absorption cross section. This was repeated for the measurement at 1000 mbar, and also by using the modelled and kinetically determined cross section values to produce Table 5.1, which shows the detection limit for each pressure and cross section at 0.1, 1 and 30 second averaging intervals.

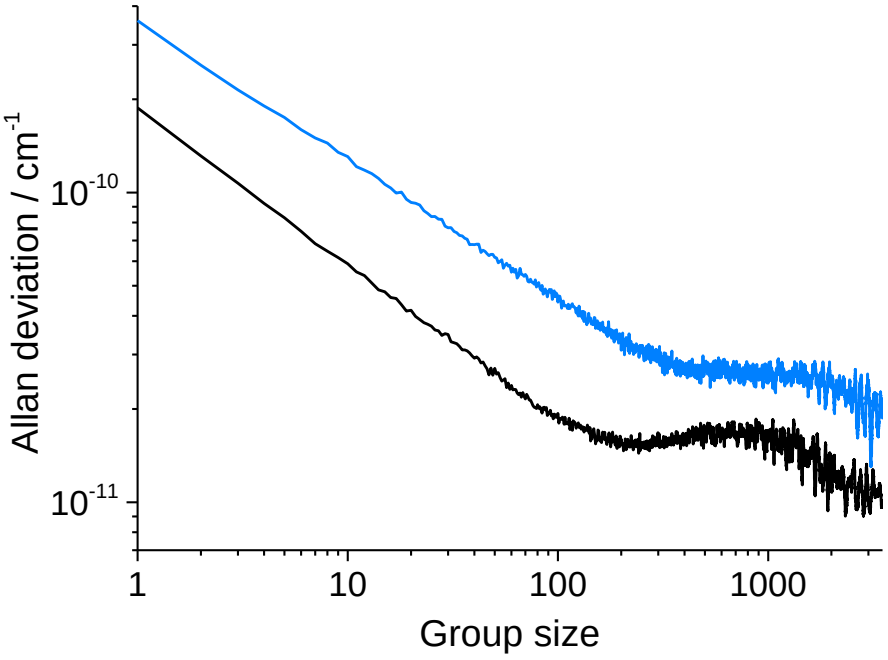

Figure 5.27. Allan deviation plots of the absorption coefficient at the HO_2 absorption wavelength, 1506.43 nm, at 150 mbar air (black) and 1000 mbar air (blue) against the averaging group size, n.

Table 5.1. The CRDS detection limit for HO_2 calculated at 150 and 1000 mbar air with both the modelled and kinetically measured cross sections. Also shown is the effect of averaging time, Δt, on the limit of detection, between 0.1 and 30 seconds. Table produced by Dr. Lavinia Onel.

Pressure / mbar	$\sigma_{HO2} \times 10^{20}$ / cm^2 molecule^{-1}	$LOD_{HO2} \times 10^8$ / molecule cm^{-3}		
		Δt = 0.1 s[c]	Δt = 1 s	Δt = 30 s
150	12.5 ± 1.9[a]	30.4	9.6	2.7
	10.2 ± 1.8[b]	37.3	11.7	3.3
1000	3.4 ± 0.4[a]	208	75.5	16.4
	3.9 ± 0.7[b]	185	67.0	14.6

[a] determined using the line strengths of the HO_2 transitions contributing to the absorption at 1506.43 nm (Thiebaud et al.) and the pressure broadening coefficients (Ibrahim et al.) (Section 5.3.2)

[b] determined using the kinetics of the HO_2 second-order decays (Section 5.3.3)

[c] the average time required for a single ring-down measurement

The same process was followed to find the CH_3O_2 LOD at 1335.47 nm, where the optimum CRDS sensitivity under all conditions is achieved averaging ~500 ring-down events, requiring ~77 s at an acquisition rate of 6.5 Hz on average, with an example shown in Figure 5.28.

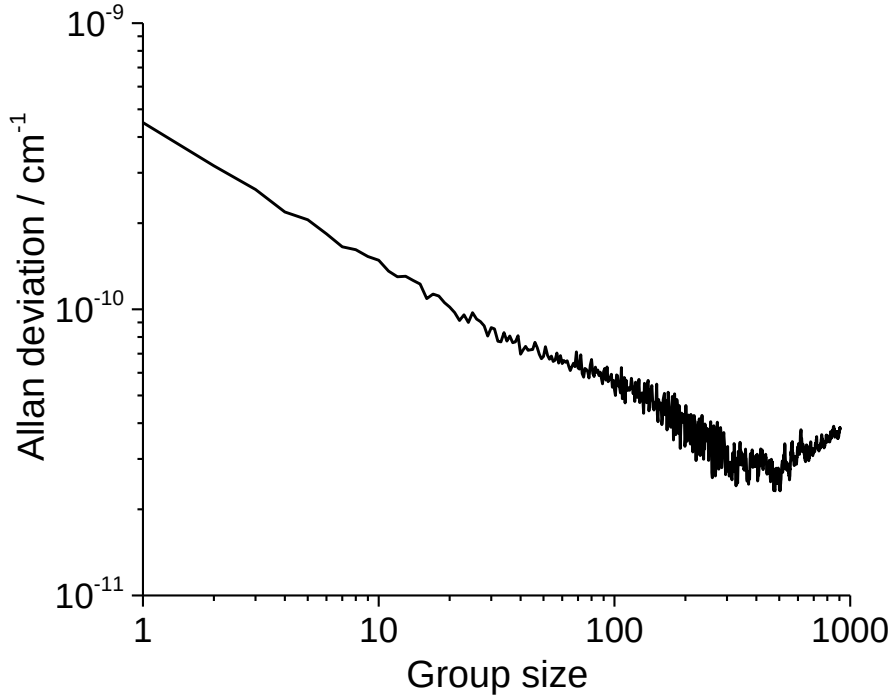

Figure 5.28 Allan deviation plot of the absorption coefficient at the CH_3O_2 absorption wavelength, 1335.47 nm, in the absence of CH_3O_2 and the presence of a typical acetone concentration of 8.8×10^{14} molecule cm^{-3} at 1000 mbar air against the number of ring-down events averaged, n. For S/N = 2 the minimum detectable absorption coefficient for a single ring-down measurement is 4.5×10^{-10} cm^{-1}, which decreases to a minimum of 2.89×10^{-11} cm^{-1} after n = 500 (requiring 77 s at an acquisition rate of 6.5 Hz).

The 254 nm lamps used to photolyse acetone in some of the CH_3O_2 inter-comparison experiments caused additional signal noise (section 5.1.2) and reduced the instrument sensitivity compared to using the ~365 nm lamps with chlorine and methane. It was not possible to perform the Allan deviation measurements with both the acetone and 254 nm light present as this would initiate chemical changes in the system. Instead, separate Allan deviation plots were generated where the chamber was filled with only the bath gas and the 254 nm were switched on, the sum in quadrature of Allan deviation obtained in

the presence of acetone and in the absence of acetone but keeping the 254 nm lamps turned on was used to determine the LOD under the acetone/O_2/254 nm experimental conditions, as shown in Table 5.2. The composite LOD of acetone + 254 nm lamps was on average ~55% greater than the LOD with only the bath gas present, and the LOD with methane and 365 nm light present was ~40% higher.

Table 5.2 CRDS detection limits for CH_3O_2 calculated at 80 mbar He:O_2 = 3:1 and 100 mbar and 1000 mbar of synthetic air for single ring-down measurements (Δt = 0.15 s), the optimum averaging time, $\Delta t_{opt.}$ (77 s under all experimental conditions) and Δt = 60 s. Table produced by Dr, Lavinia Onel.

Bath gas	p_{HIRAC} / mbar	Reagent delivered to HIRAC	LOD_{CH3O2} / 10^9 molecule cm^{-3}		
			Δt = 0.15 s	Δt = 60 s	Δt_{opt} = 77 s.
He:O_2 = 3:1	80	acetone[a]	120	7.5	6.4
Air	100	acetone[a]	133	8.6	6.8
Air	100	methane[b]	78	6.0	5.4
Air	1000	acetone[a]	147	7.3	6.1

[a] using the composite error calculated as the sum in quadrature of $\delta\alpha$ obtained using a typical concentration of acetone, 8.8 × 10^{14} molecule cm^{-3}, and $\delta\alpha$ determined in the absence of acetone but keeping the 254 nm lamps turned on during all measurement.

[b] [CH_4] = 2.4 × 10^{16} molecule cm^{-3}.

5.6 CRDS signal variability and noise

The quality of the CRDS signal would vary slightly from day to day as the cavity mirrors slowly shifted with small changes in temperature, pressure and vibrations. These changes were often minor and did not warrant spending time re-aligning the cavity. Two important sources of noise were vibrations induced by the chamber mixing fans, and noise that manifested in the form of random yet frequent signal drops, often on the order of ~ 50% of the initial signal. The fan induced vibrational noise was relatively minor and was constant throughout the measurements. The fan motors are mounted on cork padding and are connected to the fan blades themselves through a flexible drive shaft to limit the transmittance of vibrations to the chamber walls. However, the cavity mirrors

need only move a few microns to change the overall path length and shift the resonant frequency to introduce variability on the ringdown time. This effect is somewhat negated by deliberately moving the input mirror back and forth by a few microns using the piezoelectric crystals so that the resonant frequency of the cavity regularly overlaps with the laser frequency (section 2.5.1).

The larger signal drops were more problematic and difficult to diagnose and are shown in Figure 5.29. The large signal deviations were always down to lower values, rather than a statistical mix of higher and lower ringdown times, indicating that this was not typical instrument noise. Figure 5.30 shows an 8 second segment of how the ringdown time varied with the HIRAC fans spinning, showing that these spurious signals were always single data points. On switching the fans off, this single point noise signature changed to that shown in Figure 5.31. Here, the signal drops extend in time and are more gradual decreases followed by gradual increases back to the original level. This evidence suggested that particles within HIRAC were crossing the cavity beam path and interrupting the light, causing the measured ringdown time to decrease drastically. With the fans on, dust particles cross the beam rapidly, yielding only one or two points of reduced signal, whereas with the fans off the particles pass through the beam much more slowly to produce a slower change in signal.

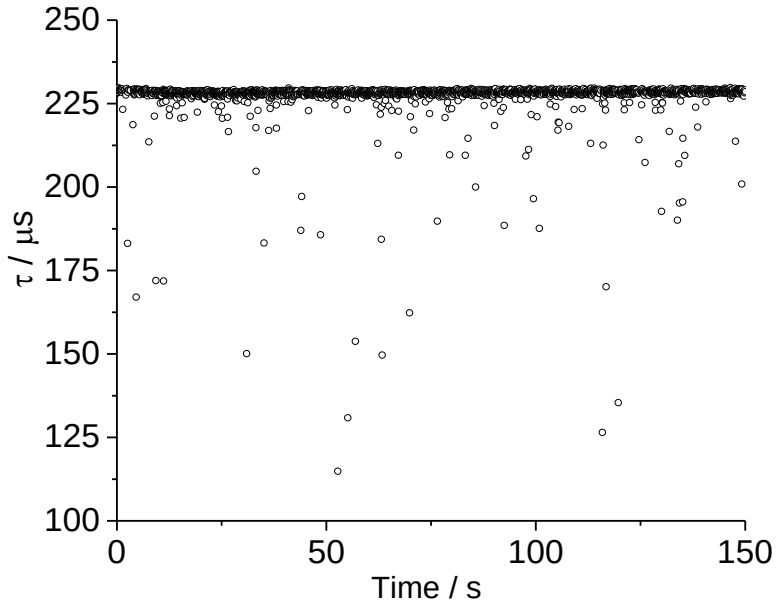

Figure 5.29. A series of ringdown events recorded at 150 mbar in air with the fans switched on. Numerous and random signal drops from the ~230 μs baseline correspond to dust particles passing through the cavity beam and scattering the light.

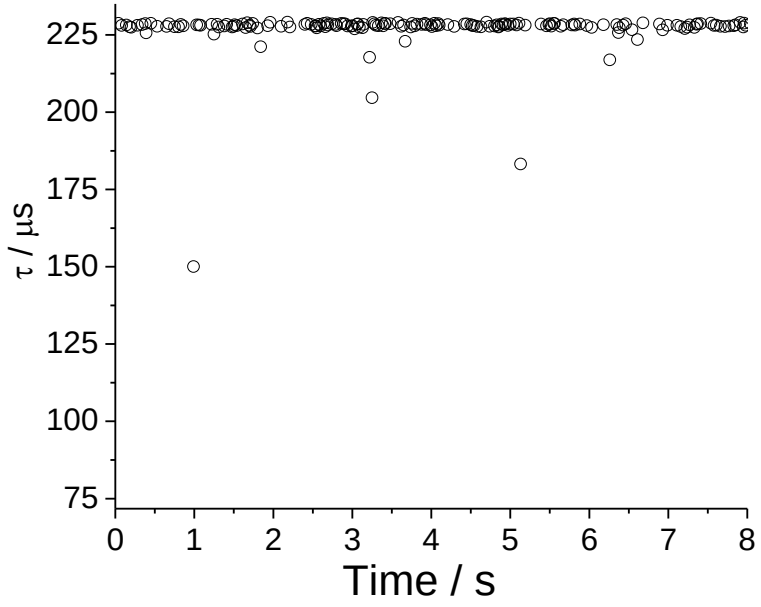

Figure 5.30. An 8 second segment of the same CRDS measurement with the HIRAC fans switched on. All 'dust events' consist of single data points due to the rapid movement of air.

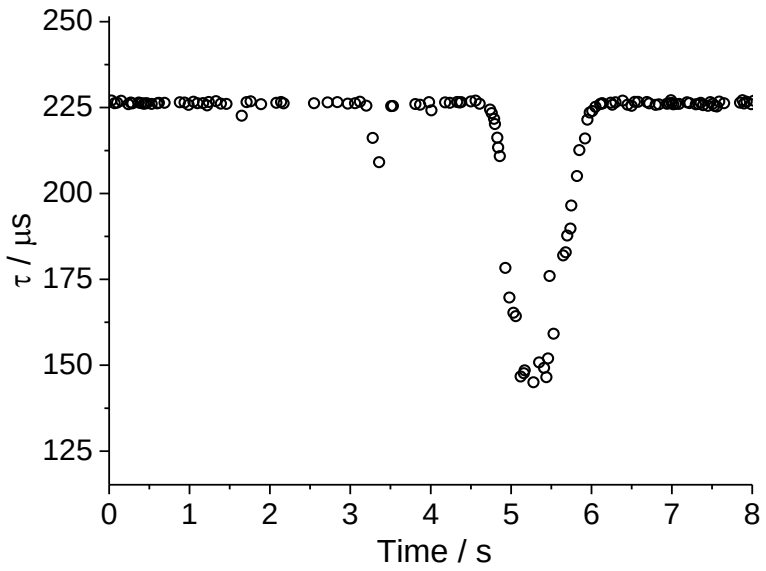

Figure 5.31. An 8 second segment of a CRDS measurement under the same conditions with the HIRAC fans switched off. The 'dust events' are less frequent but incorporate many data points as the particles are moving more slowly through the cavity beam.

The frequency and magnitude of these 'dust events' was greatly reduced by introducing gases to the HIRAC chamber slowly and operating the fans a slightly reduced speed.

5.7 Conclusion

The work done in this chapter reports the CRDS near infra-red absorption spectra of HO_2 and CH_3O_2 radicals in the ranges of 1506.39 to 1506.48 nm and 1334.93 to 1335.83 respectively, and the values of absorption cross section were calculated at various pressures for each radical. Using these cross section values the CRDS measurements of HO_2 and CH_3O_2 were compared to the independent FAGE measurements made simultaneously to help validate the FAGE method and its calibration.

5.7.1 Absorption spectra and cross section

The HO_2 absorption spectrum between 1506.39-1506.48 nm and at 150 mbar that agrees very well with previous work in this wavelength range and similarly low pressures. In section 5.3.2, modelling the effects of pressure broadening on

the HO_2 absorption cross sections found in previous studies at 50 mbar allowed the cross section at 150 mbar to be calculated as σ_{150} = (1.25 ± 0.19) cm^2 $molecule^{-1}$ and an independent calculation by Tang et al. reinforced this by giving σ_{150} = (1.29 ± 0.23) × 10^{-19} cm^2 $molecule^{-1}$. These calculated values overlap within their error limits with the cross section determined through measurement of the HO_2 decay kinetics in section 5.3.3: σ_{150} = (1.02 ± 0.18) × 10^{-19} cm^2 $molecule^{-1}$. This agreement lends confidence to the calculated absorption cross section at 1000 mbar, σ_{1000} = (3.44 ± 0.37) × 10^{-20} cm^2 $molecule^{-1}$, using the same model. The effect of pressure broadening significantly reduced cross section at 1000 mbar and hence reduced signal to noise ratio, making the accurate kinetic determination of the cross section at this pressure more difficult. However, comparing the profiles of the HO_2 decays measured by FAGE and CRDS showed excellent agreement, allowing the cross section to be calculated using the higher quality FAGE data: (3.87 ± 0.74) × 10^{-20} cm^2 $molecule^{-1}$, which agrees well with the modelled value.

The CH_3O_2 spectrum measured between 1334.93 and 1335.83 was significantly wider and less structured than the HO_2 absorption, even at low pressures of 80 mbar, due to the relative complexity of the molecule. The general shape of the spectrum agrees well with previous studies of the transition (Pushkarsky et al., 2000, Atkinson and Spillman, 2002, Faragó et al., 2013, Fittschen, 2019), with the exception of two narrow features that could not be reproduced here. The absorption cross section, $\sigma_{CH_3O_2}$ = (1.49 ± 0.19) × 10^{-20} cm^2 $molecule^{-1}$, measured at 1335.47 nm using similar techniques as described for the HO_2 radical, is also in good agreement with the previous studies and was found to be unaffected by pressure.

5.7.2 Inter-comparison experiments

The HO_2 inter-comparison experiments revealed a very good agreement between the two instruments, within ~98 % at 150 mbar and ~89 % at 1000 mbar. This correlation between the absolute CRDS technique and non-absolute FAGE technique provides a validation for both instruments, and for the calibration methods employed in section 3.2. Of particular importance is that these experiments lend confidence to the H_2O vapour photolysis calibration method that

is employed in many FAGE based field measurements (Faloona et al., 2004, Dusanter et al., 2008, Fuchs et al., 2011, Whalley et al., 2018), as well as other works using this FAGE instrument (Winiberg et al., 2015, Winiberg et al., 2016, Bejan et al., 2018).

The CH_3O_2 inter-comparison experiments were in general of poorer quality than the HO_2 measurements, resulting from a combination of the significantly lower absorption cross section that CH_3O_2 has and from the necessity to use the photolysis of acetone to generate radicals which interfered with the CRDS detector and produced secondary absorbing species. Despite this, useful information could be extracted from the data, which shows a good correlation between the instruments across the three conditions: He:O_2 at 80 mbar, air at 100 mbar and air at 1000 mbar. In section 4.4 the kinetic and water vapour photolysis FAGE calibration methods were described, including a ~30 % discrepancy between the two methods. This discrepancy is reflected in the inter-comparison experiment at 1000 mbar, where both methods are applicable, using the calibration factor derived from the self-reaction kinetics gives a gradient of 0.93 ± 0.02, indicating good agreement, whereas using the wand derived calibration factor gives a gradient of 1.32 ± 0.02. This result is expected as both the CRDS absorption cross section and the kinetic FAGE calibration factor rely upon the rate coefficient recommended by IUPAC for the self-reaction. An error in the recommended rate coefficient is a possible explanation for the ~30 % lower sensitivity factor derived from the wand calibration. An alternative explanation is a fault in the wand calibration method for CH_3O_2, but this seems unlikely as the water vapour photolysis component of the calibration has been shown to be reliable by the near 1:1 correlations found in the HO_2 inter-comparison experiments (section 5.4.1), and by the good agreement with the kinetically derived calibration factor for HO_2, and in previous work where the FAGE instrument was calibrated for OH through the kinetics of the loss of hydrocarbons through reaction with OH (Winiberg, 2015). The kinetics of the CH_3O_2 self-reaction and the source of the discrepancy are discussed in more detail in the next chapter.

5.7.3 CRDS instrument limitations and improvements

The Allan deviation measurements and LOD calculations suggest that the CRDS system is not sensitive enough for field deployment, where HO_2 and CH_3O_2 radical concentrations are in the range of 10^7 - 10^8 molecule cm^{-3} depending on the environment (Whalley et al., 2018, Lie and Zhang, 2014). In addition, whilst the typical concentrations of CH_4 and acetone in ambient air are orders of magnitude lower than [CH_4] and [$(CH_3)_2CO$] used in the HIRAC experiments, atmospheric water vapour is present in much larger concentrations (typically ~10^{17} molecule cm^{-3}) than in the relatively dry HIRAC chamber (~ 10^{14} – 10^{15} molecule cm^{-3}), and will contribute significant background absorption in the measurements. It was found that the broad absorption lines of water vapour with ambient concentrations of ~10^{17} molecule cm^{-3} in the chamber caused near total attenuation of the laser light. Whilst absorption was certainly a factor, the attenuation appears to have been mostly due to water vapour condensing onto the mirror surface itself and scattering the light. Therefore, protection of the mirrors with a gas purge should alleviate this problem, possibly allowing measurements to be performed under atmospherically relevant conditions and may make field measurements viable.

Increasing the path length or the laser power circulating within the cavity could improve the absorption signal and therefore the LOD, but perhaps the most practical improvement pathway would be to increase the rate at which ringdown events are acquired to allow for more averaging without losing temporal resolution. Currently, a ringdown event is triggered at ~10 Hz (though this is variable and could be much slower) and depends upon the cavity mirror mounted on 3 piezoelectric crystals moving back and forth through a cavity resonant frequency that matches the laser. An alternative control program was being developed at the time of this work that allows the piezoelectric crystals and thus the mirror to lock on the resonant cavity mode and track it as the cavity length changes due to thermal and mechanical drift, greatly increasing the acquisition rate by at least a factor of 10. This would improve the CRDS instruments ability to follow temporal with lower statistical errors, and may equate to an ultimately lower LOD, but this program was not finished in time for this work. This would improve the effectiveness of the CRDS instrument for kinetic measurements in

the chamber but would not alleviate the absorption due to water in atmospheric measurements.

The CRDS instrument is a useful addition to HIRAC for measuring HO_2 radicals, as it operated well at all pressures are produced data of good enough quality to extract kinetic data. However, it is not a viable technique for measuring the kinetics of CH_3O_2 radicals, and probably all other RO_2 species, due to relatively poor sensitivity and interference from the reagents used to generate alkyl-RO_2 radicals.

5.8 References

Atkinson, D. B. & Spillman, J. L. 2002. Alkyl peroxy radical kinetics measured using near-infrared CW-cavity ring-down spectroscopy. *Journal of Physical Chemistry A,* 106**,** 8891-8902.

Atkinson, R., Baulch, D. L., Cox, R. A., Crowley, J. N., Hampson, R. F., Hynes, R. G., Jenkin, M. E., Rossi, M. J. & Troe, J. 2006. Evaluated kinetic and photochemical data for atmospheric chemistry: Volume II - gas phase reactions of organic species. *Atmospheric Chemistry and Physics,* 6**,** 3625-4055.

Bejan, I. G., Winiberg, F. A. F., Mortimer, N., Medeiros, D. J., Brumby, C. A., Orr, S. C., Kelly, J. & Seakins, P. W. 2018. Gas-phase rate coefficients for a series of alkyl cyclohexanes with OH radicals and Cl atoms. *International Journal of Chemical Kinetics,* 50**,** 544-555.

Desain, J. D., Ho, A. D. & Taatjes, C. A. 2003. High-resolution diode laser absorption spectroscopy of the O-H stretch overtone band (2,0,0)<-(0,0,0) of the HO_2 radical. *Journal of Molecular Spectroscopy,* 219**,** 163-169.

Dusanter, S., Vimal, D. & Stevens, P. S. 2008. Technical note: Measuring tropospheric OH and HO_2 by laser-induced fluorescence at low pressure. A comparison of calibration techniques. *Atmospheric Chemistry and Physics,* 8**,** 321-340.

Faloona, I. C., Tan, D., Lesher, R. L., Hazen, N. L., Frame, C. L., Simpas, J. B., Harder, H., Martinez, M., Di Carlo, P., Ren, X. R. & Brune, W. H. 2004. A laser-induced fluorescence instrument for detecting tropospheric OH and HO_2: Characteristics and calibration. *Journal of Atmospheric Chemistry,* 47**,** 139-167.

Faragó, E. P., Viskolcz, B., Schoemaecker, C. & Fittschen, C. 2013. Absorption Spectrum and Absolute Absorption Cross Sections of CH_3O_2 Radicals and CH_3I Molecules in the Wavelength Range 7473-7497 cm^{-1}. *Journal of Physical Chemistry A,* 117**,** 12802-12811.

Fittschen, C. 2019. The reaction of peroxy radicals with OH radicals. *Chemical Physics Letters,* 725**,** 102-108.

Fuchs, H., Bohn, B., Hofzumahaus, A., Holland, F., Lu, K. D., Nehr, S., Rohrer, F. & Wahner, A. 2011. Detection of HO_2 by laser-induced fluorescence: calibration and interferences from RO_2 radicals. *Atmospheric Measurement Techniques,* 4**,** 1209-1225.

Ibrahim, N., Thiebaud, J., Orphal, J. & Fittschen, C. 2007. Air-broadening coefficients of the HO_2 radical in the 2v(1) band measured using cw-CRDS. *Journal of Molecular Spectroscopy,* 242**,** 64-69.

Pushkarsky, M. B., Zalyubovsky, S. J. & Miller, T. A. 2000. Detection and characterization of alkyl peroxy radicals using cavity ringdown spectroscopy. *Journal of Chemical Physics,* 112**,** 10695-10698.

Taatjes, C. A. & Oh, D. B. 1997. Time-resolved wavelength modulation spectroscopy measurements of HO_2 kinetics. *Applied Optics,* 36**,** 5817-5821.

Tang, Y. X., Tyndall, G. S. & Orlando, J. J. 2010. Spectroscopic and Kinetic Properties of HO_2 Radicals and the Enhancement of the HO_2 Self Reaction by CH_3OH and H_2O. *Journal of Physical Chemistry A,* 114**,** 369-378.

Thiebaud, J., Crunaire, S. & Fittschen, C. 2007. Measurements of line strengths in the $2\nu_1$ band of the HO_2 radical using laser photolysis/continuous wave

cavity ring-down spectroscopy (cw-CRDS). *Journal of Physical Chemistry A,* 111**,** 6959-6966.

Whalley, L. K., Stone, D., Dunmore, R., Hamilton, J., Hopkins, J. R., Lee, J. D., Lewis, A. C., Williams, P., Kleffmann, J., Laufs, S., Woodward-Massey, R. & Heard, D. E. 2018. Understanding in situ ozone production in the summertime through radical observations and modelling studies during the Clean air for London project (ClearfLo). *Atmospheric Chemistry and Physics,* 18**,** 2547-2571.

Winiberg, F. A. F. 2015. *Characterisation of FAGE apparatus for HOx detection and application in an environmental chamber.* University of Leeds.

Winiberg, F. A. F., Dillon, T. J., Orr, S. C., Gross, C. B. M., Bejan, I., Brumby, C. A., Evans, M. J., Smith, S. C., Heard, D. E. & Seakins, P. W. 2016. Direct measurements of OH and other product yields from the HO_2 + $CH_3C(O)O_2$ reaction. *Atmospheric Chemistry and Physics,* 16**,** 4023-4042.

Winiberg, F. A. F., Smith, S. C., Bejan, I., Brumby, C. A., Ingham, T., Malkin, T. L., Orr, S. C., Heard, D. E. & Seakins, P. W. 2015. Pressure-dependent calibration of the OH and HO_2 channels of a FAGE HO_x instrument using the Highly Instrumented Reactor for Atmospheric Chemistry (HIRAC). *Atmospheric Measurement Techniques,* 8**,** 523-540.

Chapter 6. Kinetics study of CH_3O_2

6.1 Introduction

In Chapter 1 the importance of peroxy radical chemistry was described. The HO_x reaction cycle that is responsible for most of the oxidation chemistry of VOCs that occurs in the troposphere was introduced, and a key component of the cycle were RO_2 radicals. As methane is the most abundant VOC in the troposphere, the CH_3O_2 radical is the most abundant individual RO_2 radical alongside HO_2. In polluted environments, such as urban areas, the CH_3O_2 radical has a short lifetime and is rapidly consumed by NO to continue the HO_x cycle and produce ozone – a respiratory irritant, greenhouse gas and smog precursor. In cleaner environments the CH_3O_2 radical survives in the atmosphere long enough for other processes to occur, such as the self-reaction and cross-reaction with HO_2 radicals. The ability to measure CH_3O_2 and understand its kinetic behaviour in these environments is therefore of critical importance.

The CH_3O_2 self-reaction can proceed through three channels:

$$CH_3O_2 + CH_3O_2 \rightarrow CH_3OH + HCHO + O_2 \qquad \textbf{R 6.1a}$$

$$CH_3O_2 + CH_3O_2 \rightarrow 2CH_3O + O_2 \qquad \textbf{R 6.1b}$$

$$CH_3O_2 + CH_3O_2 \rightarrow CH_3OOCH_3 + O_2 \qquad \textbf{R 6.1c}$$

where under most conditions the CH_3O produced in R 6.1b is entirely converted to HO_2 *via*:

$$CH_3O + O_2 \rightarrow HCHO + HO_2 \qquad \textbf{R 6.2}$$

This production of HO_2 complicates the kinetic measurements of the CH_3O_2 self-reaction as it provides an additional loss pathway for the CH_3O_2 radicals through the cross-reaction:

$$CH_3O_2 + HO_2 \rightarrow CH_3OOH + O_2$$ **R 6.3a**

$$CH_3O_2 + HO_2 \rightarrow HCHO + H_2O + O_2$$ **R 6.3b**

and the observed self-reaction rate coefficient, k_{obs}, is therefore higher than the absolute rate coefficient of the self-reaction. Knowledge of the self-reaction branching ratio, r, allows this additional loss rate to be accounted for (this is discussed more in section 6.3.1). Several product studies of the self-reaction to establish the branching have shown that the contribution of channel R 6.1c is negligible and should be ignored (Kan et al., 1980, Tyndall et al., 1998), but the branching ratio between channels R 6.1a and R 6.1b is less certain with values at 298 K in the range of $r_{6.1b}$ = 0.30 – 0.45 (Kan et al, 1980, Niki et al., 1981, Horie et al., 1990, Tyndall et al., 1998). The IUPAC recommendation is taken as the average, $r_{6.1b}$ = 0.37 at 298 K. Only two studies of the temperature dependence of the branching ratio exist, each finding a strong temperature dependence with higher temperatures favouring R 6.1b (Horie at al., 1990, Lightfoot et al., 1990a), however they do not reproduce the IUPAC recommendation at 298 K. In a comprehensive review of the chemistry of small organic peroxy radicals, Tyndall et al (2001). provided a revised temperature dependent rate coefficient, $r_{6.1b}$ = (26.2 ± 6.6) × exp[-(1130 ± 240)/T], based upon the work of Horie et al. and Lightfoot et al (1990a). that does reproduce the data at 298 K, however they note that there is considerable uncertainty in values above 298 K and more work is required to refine the branching ratio at lower temperatures relevant to the atmosphere, such as 220 to 280 K (Tyndall et al., 2001). It was also shown that there was no pressure dependence of the branching ratio over the range of 280 to 1000 mbar (Lightfoot et al., 1990a).

To date, all laboratory studies of the CH_3O_2 self-reaction kinetics have employed molecular modulation or flash photolysis to generate CH_3O_2 radicals, and then followed the CH_3O_2 temporal decay using UV absorption spectroscopy. As an absorption technique, UV spectroscopy is relatively unselective and may be susceptible to interferences, particularly from HO_2 and CH_3OOH which are produced during the self-reaction and absorb strongly below ~240 nm and overlap with the broad and featureless CH_3O_2 spectrum. This effect is minimised

by measuring CH_3O_2 at 250 nm, where the HO_2 absorption cross section is approximately 10 times lower than CH_3O_2 (Tyndall et al., 2001). The quantity measured in these UV absorption experiments is the ratio of the observed rate coefficient to the absorption cross section of CH_3O_2 radicals at the absorption wavelength used, i.e. k_{obs}/σ. It is therefore vital that the absorption cross section is accurately known to extract a reliable rate coefficient. Currently there have only been four laboratory studies of the temperature dependence of the self-reaction (Sander and Watson, 1981, Kurylo and Wallington, 1987, Lightfoot at al., 1990a, Jenkin and Cox, 1991), and their details are summarised in Table 6.1.

Table 6.1 Summary of previous laboratory studies of the temperature dependence of the CH_3O_2 + CH_3O_2 self-reaction kinetics. FP = Flash Photolysis, MM = Molecular Modulation. Values for σ have been scaled to 250 nm for comparison. Note that all studies except Lightfoot et al. report the Arrhenius equation for the observed rate coefficient, k_{obs}.

Reference	Methodology	Arrhenius equation / cm^3 $molecule^{-1}$ s^{-1}	σ at 250 nm / cm^2 $molecule^{-1}$
Sander and Watson, 1981	FP-UVAS using Cl_2-CH_4-O_2 reagents and detecting CH_3O_2 at 250 nm	$k_{obs} = (1.4\pm0.2)\times10^{-13} \exp[(223\pm41)/T]$ Between 250 - 420 K	2.45×10^{-18}
Kurylo and Wallington, 1987	FP-UVAS using Cl_2-CH_4-O_2 reagents and detecting CH_3O_2 at 250 nm	$k_{obs} = (1.7\pm0.4)\times10^{-13} \exp[(220\pm70)/T]$ Between 228 – 380 K	3.3×10^{-18}
Lightfoot et al., 1990a	FP-UVAS using Cl_2-CH_4-O_2 reagents and detecting CH_3O_2 at 210, 240 and 260 nm	$k_{6.1} = (1.27\pm0.14)\times10^{-13}$ $\exp[(365\pm41)/T)]$ Between 248 – 573 K	4.8×10^{-18}
Jenkin and Cox, 1991	MM-UVAS using CH_3I-O_2 reagents and detecting CH_3O_2 at 230 nm	$k_{obs} = 2.39\times10^{-13} \exp[(220\pm72)/T]$ Between 268 – 350 K	4.25×10^{-18}

As noted earlier, all four studies utilise UV absorption techniques to monitor CH_3O_2 radicals, and as can be seen from Table 6.1, each study used a different value for the CH_3O_2 absorption cross section. Furthermore, there is considerable spread in laboratory measurements of the rate coefficient at 298 K, spanning 2.7 - 5.2 × 10^{-13} cm^3 $molecule^{-1}$ s^{-1} reported by eight studies between 1980-1990. This discrepancy originates from the value of the absorption cross section used,

as the k_{obs}/σ ratios reported are generally in good agreement (Tyndall et al., 2001). In their review, Tyndall et al (2001). examined 21 existing CH_3O_2 cross section studies between 1977 to 1996, and arrived at a revised absorption spectrum for CH_3O_2 and a cross section of 3.78×10^{-18} cm^2 molecule^{-1} at 250 nm. Using this value with the existing self-reaction kinetic studies at room temperature gives a rate coefficient of $k_{obs} = (4.72 \pm 0.78) \times 10^{-13}$ cm^3 molecule^{-1} s^{-1} (Tyndall et al., 2001). Combining this with the recommended branching ratio $r_{6.1b} = 0.37$ gives the absolute rate coefficient $k_{6.1} = (3.5 \pm 1.3) \times 10^{-13}$ cm^3 molecule^{-1} s^{-1}, which is the IUPAC recommendation at 298 K.

The experiments to determine the absorption cross section of CH_3O_2 are themselves susceptible to interference. For example, experiments to determine the CH_3O_2 cross-section at 250 nm involved the use of very high Cl_2 concentrations, such as ~7×10^{16} molecule cm^{-3}, compared to CH_3O_2 which was only ~10^{13} molecule cm^{-3} (Dagaut and Kurylo, 1990). Even though the Cl_2 absorption spectrum is well defined and the cross section at 250 nm is small at ~0.5-1 $\times 10^{-21}$ cm^2 molecule^{-1} (Keller-Rudek et al., 2013) it is ~1000 times more abundant, meaning the absorption due to Cl_2 may be non-negligible. If the Cl_2 concentration changes during the CH_3O_2 self-reaction this will significantly affect the measurements, especially considering that the self-reaction rate is relatively slow (Tyndall et al., 2001). Additionally, high CH_3O_2 concentrations in the range of 10^{13} - 10^{15} molecule cm^{-3} were used for the self-reaction experiments, which invites the possibility of secondary chemical processes occurring and providing additional CH_3O_2 loss pathways.

The $CH_3O_2 + HO_2$ cross-reaction is better understood, with several studies of the kinetics at 298 K. The average of these studies, $k_{6.3} = 5.2 \times 10^{-12}$ cm^3 molecule^{-1} s^{-1}, is the IUPAC recommendation at 298 K. Four temperature dependence studies of the reaction exist and are summarised in Table 6.2.

Table 6.2 Summary of laboratory studies of the temperature dependence of the CH_3O_2 + HO_2 cross reaction kinetics. FP = Flash Photolysis, MM = Molecular Modulation, DF = Discharge Flow, CIMS = Chemical Ionisation Mass Spectrometry

Reference	Methodology	Arrhenius equation / cm^3 $molecule^{-1}$ s^{-1}
Cox and Tyndall, 1980	MM-UVAS using Cl_2-CH_4-H_2-O_2 reagents	$k_{6.3}$ = (7.7)×10^{-14} exp[(1296±364)/T] Between 274 – 338 K
Dagaut et al., 1988	FP-UVAS using Cl_2-CH_4-CH_3OH-O_2 reagents	$k_{6.3}$ = (3.0±1.2)×10^{-13} exp[(720±100)/T] Between 228 – 380 K
Lightfoot et al., 1990b	FP-UVAS using Cl_2-CH_4-CH_3OH-O_2 reagents	$k_{6.3}$ = (4.4±0.7)×10^{-13} exp[(780±55)/T)] Between 248 – 573 K
Raventos-Duran et al., 2007	DF-CIMS using F_2-CH_4-H_2-O_2 reagents	$k_{6.3}$ = 3.82×10^{-13} exp[(-781±127)/T] Between 205 – 298 K

Most of the studies again rely on UV absorption techniques, which gives rise to the same problems mentioned above for the self-reaction, however the most recent determination used CIMS to monitor CH_3O_2 and HO_2 radicals, which is independent of the absorption cross section, and agrees well with the previous work (Raventos-Duran et al., 2007). IUPAC recommend $k_{6.3}$ = 3.8 ×10^{-13} exp[(780±200)/T)] as the temperature dependent cross-reaction rate coefficient, based on the work by Lightfoot et al. (1990b) and Raventos-Duran et al.

To summarise, the current understanding of the CH_3O_2 self-reaction kinetics rests on only one measurement technique that is susceptible to interferences, particularly as the self-reaction is slow. Additionally, the method relies on an absorption cross section that is itself uncertain. These factors in conjunction with the discrepancy found in sections 4.4 and 5.4.2 between the FAGE calibration methods (self-reaction kinetics and the water photolysis method), and with the importance of CH_3O_2 in tropospheric chemistry, suggest that verification using a different measurement technique is required (Tyndall et al., 2001, Orlando and Tyndall, 2012). The FAGE instrument offers an independent measurement of the kinetics that is free from interference effects that UV-absorption is susceptible to.

Coupled with the HIRAC chamber it is also capable of working at much lower radical concentrations, in the range of 10^{10} - 10^{11} molecule cm^{-3}, which limits secondary chemistry.

Also shown here are preliminary measurements of the CH_3O_2 self-reaction using the RO_xLIF instrument, which was detailed in section 4.6. The instrument was used to measure the CH_3O_2 self-reaction kinetics in experiments that are under identical conditions to the FAGE measurements of the self-reaction.

6.2 Experimental

The experiments were performed in the HIRAC chamber using the same techniques and chemical systems described in previous chapters, and only the important details will be reproduced here. Radicals were generated in the HIRAC chamber using the following chemical systems:

$$Cl_2 + h\nu\ (365\ nm) \rightarrow 2Cl \qquad \textbf{R 6.4}$$

$$CH_4 + Cl \rightarrow CH_3 + HCl \qquad \textbf{R 6.5}$$

$$CH_3 + O_2 + M \rightarrow CH_3O_2 + M \qquad \textbf{R 6.6}$$

$$CH_3OH + Cl \rightarrow CH_3O + HCl \qquad \textbf{R 6.7}$$

$$CH_3O + O_2 \rightarrow HCHO + HO_2 \qquad \textbf{R 6.8}$$

The experiments were conducted at temperatures between 268 and 344 K to probe any temperature dependence in the CH_3O_2 self-reaction and cross-reaction with HO_2. The chamber heating/cooling system was described in section 2.1 and temperatures were stable throughout the experiments within approximately 2 K, with the most noticeable fluctuations occurring during the low temperature experiments as the heat generated by the photolysis lamps caused localised heating of the gas mixture that was quickly dissipated by the mixing fans.

6.2.1 Self-reaction experiments and branching ratio

For the CH_3O_2 self-reaction experiments only chlorine and methane were present in an air mixture inside HIRAC to generate CH_3O_2 *via* reactions R 6.4 - R 6.6. The amount of chlorine added was altered for each experiment to generate a range of CH_3O_2 radical concentrations in the chamber, between 10^{11} and 10^{12} molecule cm^{-3}. One experiment was performed where the FAGE instrument was replaced with the newly constructed RO_xLIF instrument, described in section 4.6.

The branching ratio was measured by switching the photolysis lamps on and monitoring the evolution of CH_3OH and HCHO for 20-30 minutes using the multi-pass FTIR system inside HIRAC, which was described in section 2.4. The two species were monitored using features at ~1050 cm^{-1} (CH stretch) and ~1750 cm^{-1} (Carbonyl stretch), respectively. A FAGE instrument to detect HCHO by LIF at ~353 nm was used to confirm the accuracy of the FTIR measurements (Cryer, 2016).

6.2.2 Cross-reaction experiments

The addition of methanol generated HO_2 radicals *via* reactions R 6.7 and R 6.8 for the cross-reaction experiments. The reagent composition had to be balanced in such a way that the radicals favoured the cross-reaction rather than their respective self-reactions, too much of one radical will favour its self-reaction, too little will favour the other. Typically, the $[CH_3O_2]/[HO_2]$ ratio was approximately 5 but ranged between 3 and 14 for different experimental runs.

The cross-reaction kinetics experiments were complex to perform as the FAGE instrument was unable to measure both CH_3O_2 and HO_2 simultaneously, meaning that at t_0 only the concentration of one of the radicals was known and the concentration of the corresponding radical had to be estimated instead, precluding deriving the rate constant from the rate equation of the cross reaction which requires both concentrations to be known simultaneously. Additionally, the cross-reaction could never occur in isolation and would always take place alongside the self-reaction of each radical, which had to be accounted for.

One method to do this was to alternate the FAGE measurement between CH_3O_2 and HO_2, measuring one of the radicals for one lamp on/off cycle and then

switching to the other for the next cycle to build up a series of alternating temporal decays. When analysing each radical decay, the concentration of the corresponding radical was estimated by interpolating a line of best fit between the decays on either side. However, due to limitations in the experimental setup switching between radical measurements was slow and could take up to 5 minutes, all the while the conditions in the chamber were changing. This was particularly prevalent when switching to CH_3O_2 measurement as the lack of a reference cell meant that the lamps had to be switched on whilst the instrument scanned for the line, expending time, reagents and the build-up of products that could begin to interfere with the measurements.

To address these issues the method was modified to focus on HO_2 measurements and reduce the number of times the instrument had to be reconfigured for each radical. Additionally, the signal quality of the HO_2 decays was superior to that of CH_3O_2 due to the significantly higher instrument sensitivity, making HO_2 decays the most valuable kinetic data to acquire. A typical FAGE measurement is shown in Figure 6.1, and the procedure to obtain it was as follows:

1) CH_3O_2 was measured for approximately 1 minute to establish the initial concentration of the radical before the lamps were switched off.
2) Alternating measurements of HO_2 (blue) and CH_3O_2 (black) were made, each consisting of four kinetic decays.
3) One final measurement of CH_3O_2 to establish the final concentration of the radical.

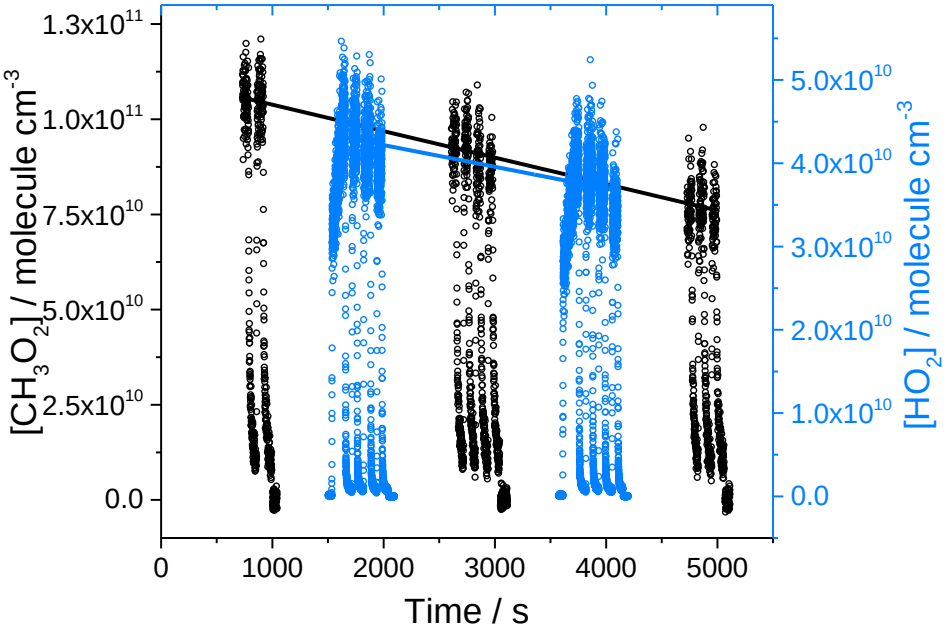

Figure 6.1 Typical FAGE measurement during the study of the CH_3O_2 + HO_2 reaction in the HIRAC chamber at 284 K, where CH_3O_2 and HO_2 measurements are shown in black and blue, respectively. Linear fits of the HO_2 initial concentration (blue line) and CH_3O_2 initial concentration (black line) were used to interpolate the radical concentration. The experimental procedure to collect these data was described in the text.

A linear fit of each data set during the lamps on periods is shown by blue and black lines for HO_2 and CH_3O_2, respectively, and was used to interpolate the concentration of each radical in the time periods they were not being measured.

6.3 Analysis methods

As these experiments are a test of the CH_3O_2 FAGE method developed throughout this thesis, all data has been analysed using the sensitivity factors derived through the water vapour photolysis method (sections 3.2.1 and 4.4.1).

6.3.1 CH_3O_2 self-reaction and branching ratio

The self-reaction cannot occur in isolation when oxygen is present because channel R 6.1b produces CH_3O radicals and subsequently HO_2 through R 6.2 which rapidly removes an additional CH_3O_2 radical as this reaction is approximately an order of magnitude faster than the self-reaction itself (Atkinson et al., 2006). This means that all measurements reported here are the observed

rate coefficient, k_{obs}, which can be extracted from FAGE measurements of the temporal decay by integrating the rate equation for the self-reaction, shown by Eq. 6.1 and Eq. 6.2, and Eq. 6.3 is the reciprocal equation used to fit the data:

$$-\frac{d[\mathrm{CH_3O_2}]}{dt} = 2 \times k_{obs}[\mathrm{CH_3O_2}]^2 \qquad \textbf{Eq. 6.1}$$

$$\frac{1}{[\mathrm{CH_3O_2}]_t} = \frac{1}{[\mathrm{CH_3O_2}]_0} + 2{\times}k_{obs}{\times}t \qquad \textbf{Eq. 6.2}$$

$$[\mathrm{CH_3O_2}]_t = [\mathrm{CH_3O_2}]_0 + \frac{1}{2{\times}k_{obs}{\times}t} \qquad \textbf{Eq. 6.3}$$

The self-reaction experiments were performed over the course of four years, generating a large amount of data. For each temperature, the data were analysed by global fitting of the data gathered each year, and the average of the global fits was taken. For example, room temperature measurements were made in 2016, 2017, 2018 and 2019. A global fit of Eq. 6.3 to the data gathered each year yielded rate coefficients of (3.22 ± 0.03, 16 decays), (4.56 ± 0.04, 3 decays), (2.38 ± 0.01, 19 decays) and (3.49 ± 0.04, 9 decays) × 10^{-13} cm^3 $molecule^{-1}$ s^{-1}, respectively, where the error is the standard deviation of the fitting process. The average of these values was then taken, giving k_{obs} (295 K) = $(3.41^{+1.77}_{-0.85})$ × 10^{-13} cm^3 $molecule^{-1}$ s^{-1}. The error margin was estimated by re-analysing the data with the 34 % uncertainty in the calibration factor (section 4.5.1) included, i.e. the data was analysed with $C_{\mathrm{CH_3O_2}} + 34\,\%$ and with $C_{\mathrm{CH_3O_2}} - 34\,\%$. Re-fitting Eq. 6.3 to each gives the asymmetric uncertainty of +52 % and -25 %. It is notable that the data from 2017 is high compared to the other values, this may be an anomaly as it is the result of only three temporal decays (one experiment) but does fit within the wide error margin.

To calculate the second-order rate coefficient the self-reaction branching ratio between the two channels, R 6.1a and R 6., must be known. It can be determined by monitoring the production of CH_3OH and HCHO from each channel respectively as shown by:

$$r_{6.1a} = \frac{k_{6.1a}}{k_{6.1b}} = \frac{[CH_3OH]}{[CH_3OH] + \frac{[HCHO]_{R6.1b}}{2}}$$ **Eq. 6.4**

where $r_{6.1a}$ is the branching ratio with respect to channel R 6.1a, $k_{6.1a}$ and $k_{6.1b}$ are the rate coefficients of reaction channels R 6.1a and R 6. respectively, and $[HCHO]_{R6.1b}$ is the HCHO concentration produced only by channel R 6.. CH_3OH is produced exclusively by channel R 6.1a, but HCHO is also produced as a co-product in a 1:1 ratio. Therefore $[HCHO]_{R6.1b}$ can be calculated by subtracting $[CH_3OH]$ from the total measured [HCHO] using Eq. 6.5.

$$[HCHO]_{R6.1b} = [HCHO]_{total} - [CH_3OH]$$ **Eq. 6.5**

The branching ratio with respect to channel R 6., $r_{6.1b} = 1 - r_{6.1a}$, can then be used to correct k_{obs} for the additional HO_2 loss and calculate the second-order rate coefficient using Eq. 6.6.

$$k_{obs} = k(1 + r_{R6.1b})$$ **Eq. 6.6**

6.3.2 CH_3O_2 + HO_2 cross-reaction

It was not possible to measure both CH_3O_2 and HO_2 simultaneously and the rate coefficient of the cross-reaction could not be calculated analytically, instead the Kintecus® (Ianni, 2017) chemical simulation software was used. Each temporal decay measured by FAGE is composed of three main reactions that take place simultaneously in the chamber, these are the cross-reaction itself as well as the self-reactions of HO_2 and CH_3O_2. There is also an additional HO_2 wall loss component to account for, whereas the CH_3O_2 wall-loss was found to be insignificant (section 4.4.2). The model uses the initial concentration of HO_2 and CH_3O_2 determined in section 6.2 and the rate coefficients of the three reactions to simulate the radical concentration at regular time intervals. The self-reaction rate coefficients are known and fixed in the model (see below), but the cross-reaction rate coefficient is unknown and can float. The model repeatedly adjusts this rate coefficient to get the predicted curve as close as possible to the measured data, at which point the cross-reaction rate coefficient has been 'found'.

These experiments were performed over a range of temperatures, so temperature dependent rate coefficients were taken from IUPAC. For HO_2 there are three loss channels, one bimolecular, one termolecular and finally the unimolecular wall loss:

$$HO_2 + HO_2 \rightarrow H_2O_2 + O_2 \qquad \textbf{R 6.9a}$$

$$HO_2 + HO_2 + M \rightarrow H_2O_2 + O_2 + M \qquad \textbf{R 6.9b}$$

$$HO_2 \rightarrow loss \qquad \textbf{R 6.10}$$

and the respective rate coefficients are calculated using:

$$k_{6.9a} = 2.2 \times 10^{-13} \exp(^{600}/_{T}) \qquad \textbf{Eq. 6.7}$$

$$k_{6.9b} = 1.9 \times 10^{-33} [N_2] \exp(^{980}/_{T}) \qquad \textbf{Eq. 6.8}$$

The wall loss rate is unique to the HIRAC chamber and was determined by studying the self-reaction as described in Chapter 3 when calibrating the FAGE instrument (section 3.2.3), and typically $k_{6.11} \approx 0.07$ s^{-1} during this work.

For CH_3O_2 there are also two reaction channels, shown in R 6.1a and R 6., the latter of which goes on to produce HO_2 in reaction R 6.2. As the CH_3O_2 wall loss rate was found to be insignificant it is ignored here. Using the IUPAC recommendations of both k_{obs} and the branching ratio produced poor quality fits to the measured data, whereas using the value of k_{obs} determined in this work produced good quality fits. This is not because the IUPAC value is 'wrong' per se, but it cannot describe the decay of [CH_3O_2] that has been calculated using the sensitivity factor derived from the water vapour photolysis method due to the ~30 % discrepancy between them. Therefore, all cross-reaction data shown here is the result of fitting with the k_{obs} values determined in this work and the IUPAC recommended branching ratio. The data will be re-analysed using the branching ratio determined as part of this work in the future. The temperature dependent rate coefficient for R 6.2 was taken from the latest JPL evaluation (Burkholder et al., 2015):

$$k_{6.2} = 3.9 \times 10^{-14} \exp(^{900}/_{T}) \qquad \textbf{Eq. 6.9}$$

6.4 CH_3O_2 Self-Reaction and branching ratio results

Figure 6.2 shows the FTIR measurements of formaldehyde and methanol inside HIRAC at 295 K over the course of ~30 minutes whilst the photolysis lamps were switched on. Formaldehyde is produced by both reaction channels, R 6.1a and R 6.1b, so its concentration rises much faster than methanol which is produced only by channel R 6.1a. The rate of production of both radicals begins to slow after ~400 seconds as reagents in the chamber are consumed and the reaction of the growing HCHO and CH_3OH concentration with Cl atoms becomes more significant.

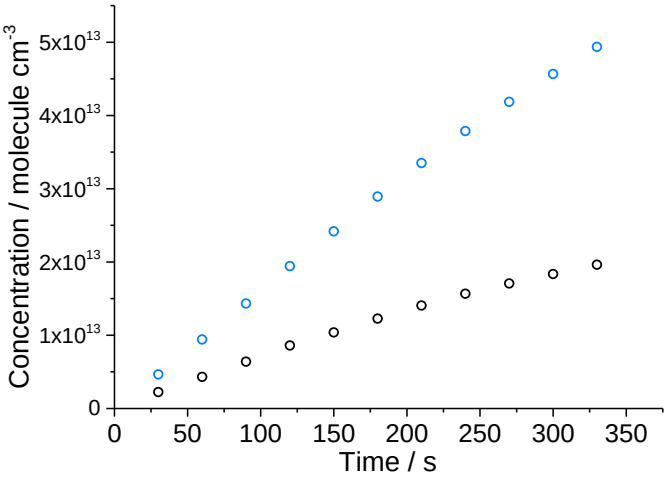

Figure 6.2 The evolution of formaldehyde and methanol during the CH_3O_2 self-reaction at 295 K inside HIRAC. Methanol and formaldehyde were measured by FTIR using features at ~1050 cm^{-1} (CH stretch) and ~1750 cm^{-1} (Carbonyl stretch) respectively. The rate of production becomes non-linear beyond ~400 seconds, so only data acquired before this point were used to calculate the branching ratio.

A FAGE instrument that detects HCHO by LIF at ~353 nm (Details of the instrument can be found in Cryer, 2016) was used to check the accuracy of the FTIR measurements of HCHO. Figure 6.3 shows the evolution of HCHO during the CH_3O_2 self-reaction at 295 K, with a good agreement found between the two instruments.

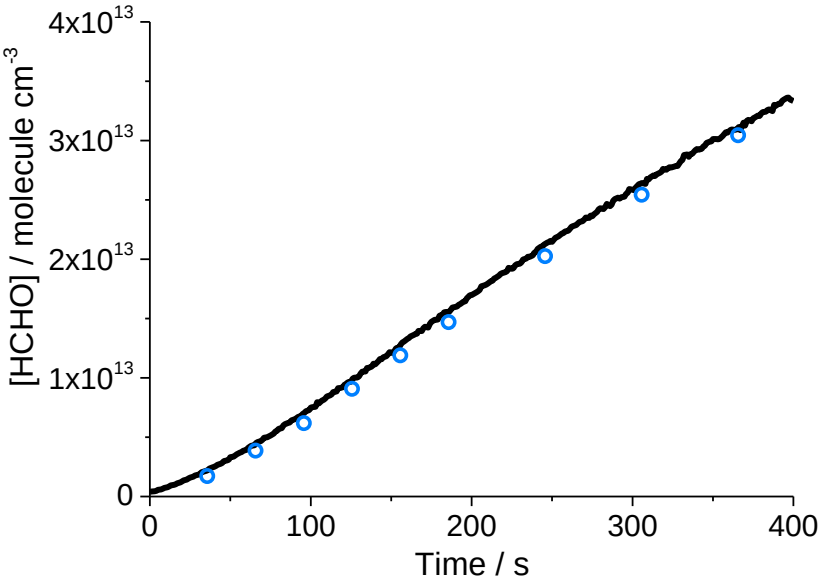

Figure 6.3 Measurement of the evolution of HCHO in HIRAC at 295 K during the CH_3O_2 self-reaction, using FTIR (blue circles) to monitor the carbonyl stretch at 1750 cm^{-1}, and a FAGE instrument that detects HCHO by LIF at ~353 nm. A good agreement was found between the two methods, lending credence to the branching ratios determined here through the FTIR measurement of HCHO. More information about the HCHO FAGE instrument can be found in Cryer, 2016.

The branching ratio was determined at five temperatures between 265 and 340 K, shown in Figure 6.4. Also shown in the figure is a previous determination of the temperature dependent branching (black line, Horie et al., 1990). The blue line shows the same data after modification by Tyndall et al. to reproduce the IUPAC recommended value at 298 K. A good agreement is found between this work and the two other data sets.

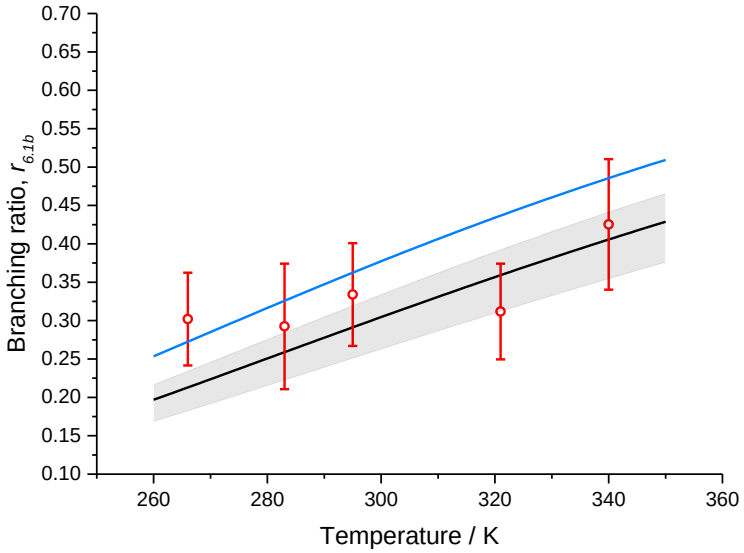

Figure 6.4 Temperature dependence of the CH_3O_2 branching ratio of the channel that ultimately produces HO_2, $r_{6.1b}$ The data measured here (red circles) is in good agreement with previous determinations by Horie et al., 1990 (black line) and the recommendation by Tyndall et al., 2001 (blue line), showing a similar temperature dependence.

A typical CH_3O_2 temporal decay at 295 K measured by FAGE and the inverse plot is shown in Figure 6.5, and the fit to extract k_{obs} using Eq. 6.3 is shown by the blue curve. The linearity of the inverse plot shows the temporal decay is second order, meaning there are no additional processes besides the self-reaction contributing to the decay.

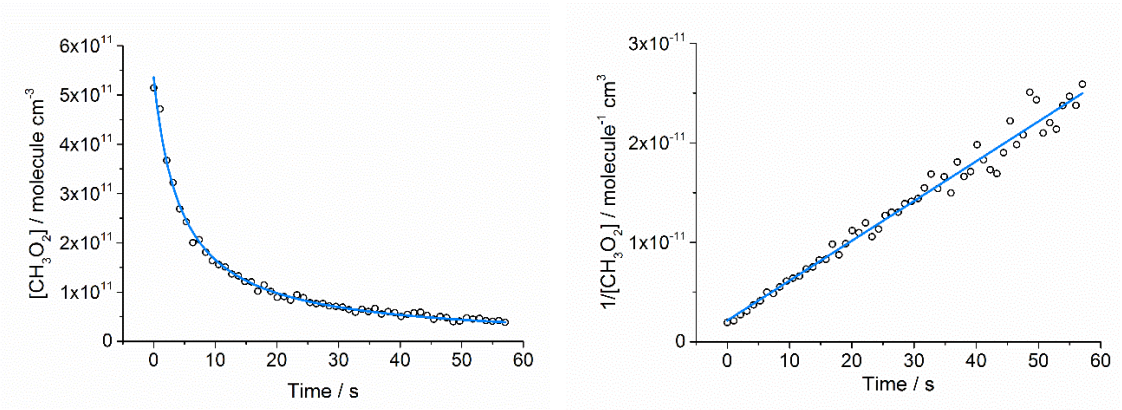

Figure 6.5 An example CH_3O_2 temporal decay measured by FAGE in HIRAC at 295 K (left) and its inverse plot (right). The linearity of the inverse plot indicates that the reaction is second-order, meaning the CH_3O_2 self-reaction has been captured with no additional effects such as wall loss.

The observed rate coefficients, k_{obs}, obtained in this work at each temperature are shown in Table 6.3, along with the absolute rate coefficient for the self-reaction, $k_{6.1}$, that was obtained using the revised temperature dependent branching ratio obtained by Tyndall et al. (see section 6.1 for details on revised ratio, see 6.3.1 for conversion of k_{obs} to $k_{6.1}$)

Table 6.3 CH_3O_2 self-reaction rate coefficients obtained in this work. k_{obs} was converted to the absolute rate coefficient $k_{6.1}$ using the revised temperature dependent branching ratio obtained by Tyndall et al. (detailed in section 6.1). 2σ errors are shown.

Temperature / K	k_{obs} / 10^{-13} cm^3 molecule^{-1} s^{-1}	$k_{6.1}$ / 10^{-13} cm^3 molecule^{-1} s^{-1}
268	$4.15^{+2.26}_{-1.14}$	$3.24^{+1.76}_{-0.89}$
284	$2.85^{+1.51}_{-0.74}$	$2.14^{+1.13}_{-0.55}$
295	$3.41^{+1.84}_{-0.92}$	$2.50^{+1.35}_{-0.67}$
323	$3.73^{+1.99}_{-0.98}$	$2.59^{+1.38}_{-0.68}$
344	$2.57^{+1.36}_{-0.67}$	$1.72^{+0.91}_{-0.45}$

The change in $k_{6.1}$ for the CH_3O_2 self-reaction as a function of temperature is plotted in Figure 6.6a, with the data from this work shown as red triangles. Each data point is the result of the global fitting and averaging process described in 6.3.1. The Arrhenius equation for the temperature dependent rate coefficient recommended by IUPAC is shown by the blue line, and the data from previous works that contributed to the IUPAC recommendation are also plotted. Figure 6.6b shows the Arrhenius plots of the same data sets. The data from this work agrees well with the work by Sander and Watson, and with Kurylo and Wallington. The works of Lightfoot et al. (1990a) and Jenkin and Cox show similar temperature dependence but are offset as they used different absorption cross section data (see section 6.1 and Table 6.1). The IUPAC recommendation lies between the two groups of data, and while it is within the error margins, the data gathered here is relatively imprecise and lies on average 30 % lower. Fitting a line to the data obtained in this work gives the Arrhenius equation $k_{6.1} = (4.2 \pm 3.8) \times 10^{-14} \exp[(516 \pm 284)/T]$ cm^3 molecule^{-1} s^{-1} and an activation energy of 4.29 ± 2.36 kJ mol^{-1}. Using this equation to evaluate the rate coefficient

at 298 K, a value of $k_{6.1}$ = (2.37 ± 1.09) × 10^{-13} cm^3 $molecule^{-1}$ s^{-1} is obtained, which is approximately 33 % lower than the IUPAC value at 298 K of (3.5 ± 1.3) × 10^{-13} cm^3 $molecule^{-1}$ s^{-1} but within the error margin. The E_a/R value of 516 lies within the error margin of the IUPAC recommendation of 365 ± 200 K, based on Lightfoot et al. (1990a), however the *A* factor is significantly lower and outside the error margin. The relative imprecision of the data from this work makes it difficult to recommend revised Arrhenius parameters, however the good agreement between the values of $k_{6.1}$ found here with the work of Sander and Watson and Kurylo and Wallington lends credence to their determinations of the rate coefficient, and by extension their CH_3O_2 cross-section values which are lower than those of Jenkin and Cox, and Lightfoot et al. (1990a).

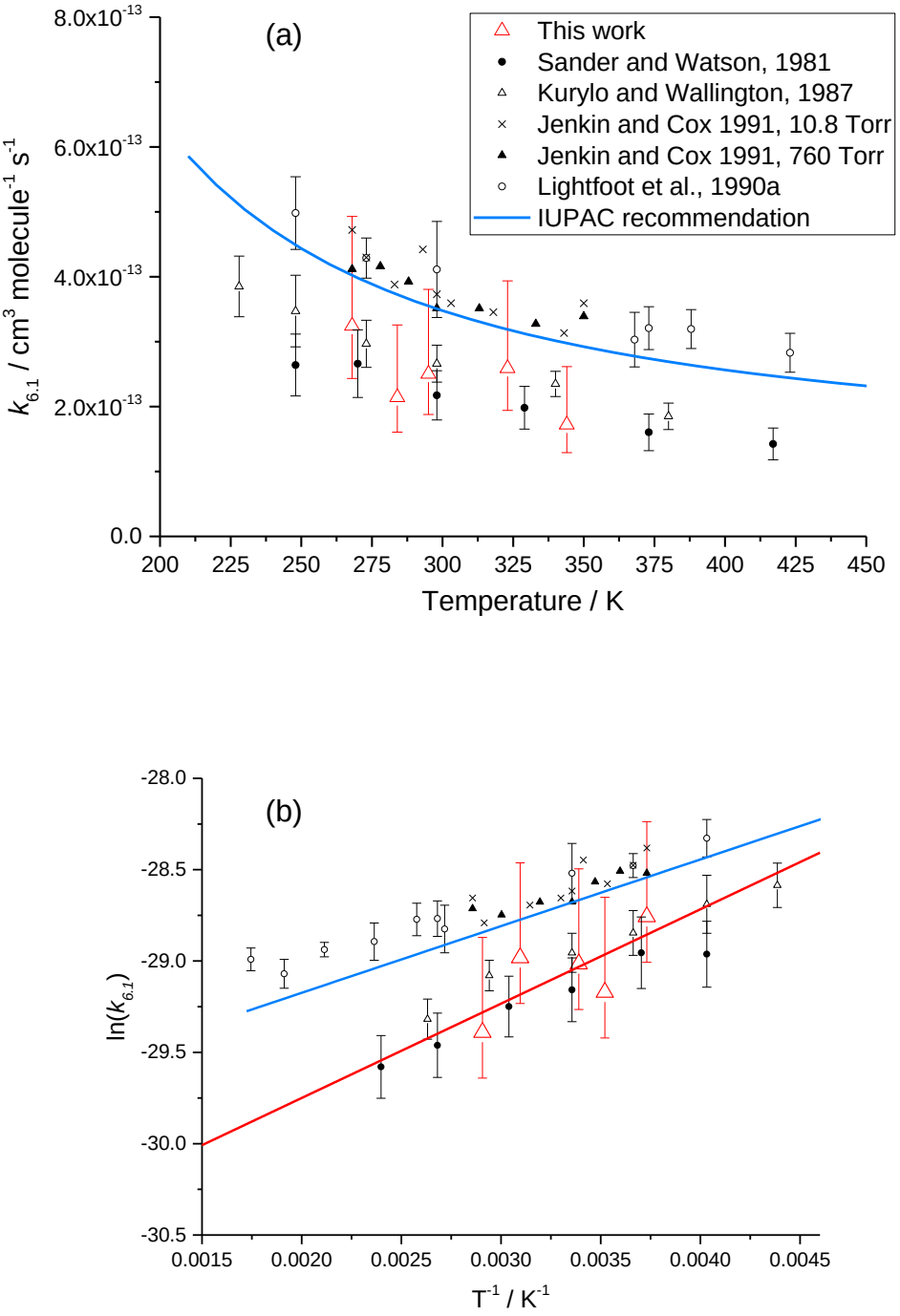

Figure 6.6 a) The effect of temperature on the CH_3O_2 self-reaction rate coefficient, $k_{6.1}$, between 268 and 344 K (-5 – 71 °C) and b) an Arrhenius plot of the same data sets. The data gathered in this work is shown by the red triangles, where each data point is the result of global fitting analysis method described in section 6.3.1. The linear regression to extract the Arrhenius parameters is shown by the red line, see text for detail. The previous studies are shown for comparison, with the works of Sander and Watson and Kurylo and Wallington agreeing well with this work. The studies of Lightfoot et al. (1990a) and Jenkin and Cox are offset due to the use of different CH_3O_2 absorption cross sections. Note that all data has been analysed using the IUPAC recommended branching ratio.

The discrepancy between the measurements in this work and the IUPAC value was not unexpected as the FAGE calibration experiments discussed earlier in this thesis indicated a ~30 % discrepancy in calibration factors derived from the kinetics of the self-reaction and the wand calibration method. The cause of this discrepancy is still being investigated, but there are possible sources of error both in the IUPAC measurements, discussed above in section 6.1, and in the FAGE measurements made here, which are discussed below.

Figure 6.7 shows of the observed rate coefficient derived from each individual temporal decay and shows how the measured k_{obs} of the self-reaction changed as a function of the initial concentration of CH_3O_2 generated in HIRAC. The average observed rate coefficient, $k_{obs} = 3.21 \times 10^{-13}$ cm^3 molecule^{-1} s^{-1}, is shown by the blue line. The plot indicates that there is an effect of the initial concentration on the observed rate coefficient, with higher concentrations yielding slower self-reaction rates. This trend is difficult to explain, as higher radical concentrations would be expected to promote losses through secondary chemistry, and hence show higher k_{obs} values, however the opposite is seen in the plot. The data where $[CH_3O_2]_0 > 5 \times 10^{11}$ molecule cm^{-3} were all obtained in 2018, it is possible that there was a systematic problem with the FAGE instrument or calibration this year, however none have been detected thus far. The ~34 % uncertainty in the FAGE calibration may go some way to account for the scatter in these results which were acquired over the space of four years.

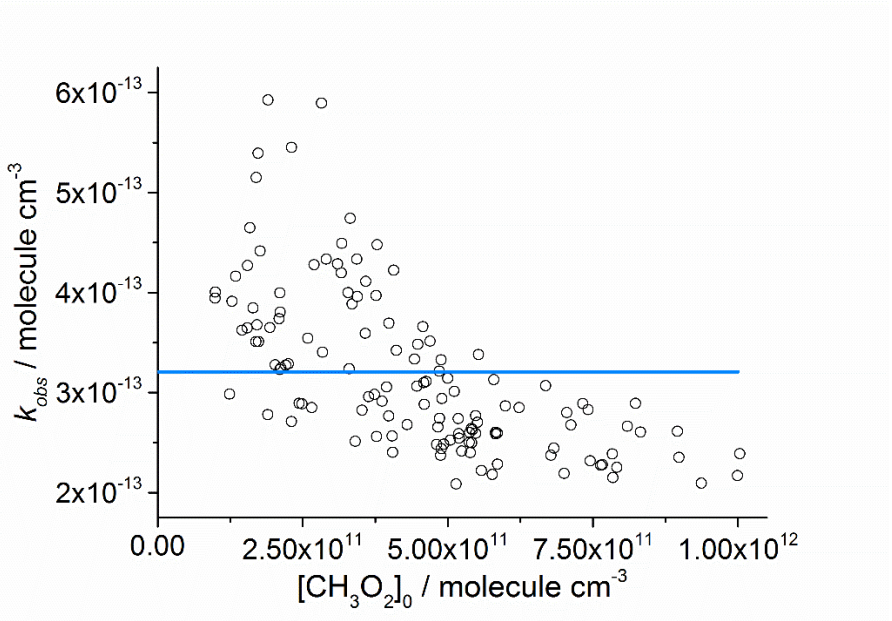

Figure 6.7 A plot of the k_{obs} determined from each temporal decay taken at all temperatures, to show how it varied as a function of initial CH_3O_2 concentration. The average, k_{obs} = 3.21 × 10^{-13} cm^3 $molecule^{-1}$ s^{-1}, is shown by the blue line. The plot shows a negative correlation between the rate coefficient and initial concentration; however, the spread of data could reflect the ~34% error margin in the FAGE calibration.

Another possible explanation for the ~30 % lower measured k_{obs} values is a systematic problem with the wand calibration method for CH_3O_2 radicals. The issue cannot lie with the actinometry measurements as the HO_2 wand calibrations, which use the same actinometric data, agree well with the kinetic calibrations using the HO_2 self-reaction (section 3.2), and a good agreement was observed between FAGE and CRDS when measuring HO_2 (section 5.4.1). This leaves the conversion of OH into CH_3O_2 by reaction with methane, which was assumed to be complete (±4 %) based on the loss of OH when adding methane to the calibration gas flow (section 4.1.2). However, it is possible that impurities present in the methane gas, such as ethane, consumed a portion of the OH radicals meaning less CH_3O_2 radicals were generated than calculated. The sensitivity factor represents the amount of signal generated per molecule of CH_3O_2:

$$C_{CH_3O_2} = \frac{S_{CH_3O_2}}{[CH_3O_2]} \qquad \textbf{Eq. 6.10}$$

where [CH_3O_2] is generated through the water vapour photolysis method, assuming all OH is converted to CH_3O_2. If this assumption was incorrect this would in turn mean the instrument sensitivity was higher than expected. By looking at Eq. 6.11, which was used for the kinetic calibrations in section 4.4.2, this would cause the measured k_{obs} value to increase by the same proportion, which would begin to reconcile the difference between the two calibration methods.

$$\frac{1}{(S_{\mathrm{CH_3O_2}})_t} = \frac{1}{(S_{\mathrm{CH_3O_2}})_0} + \frac{2 \times k_{obs} \times (t - t_0)}{C_{\mathrm{CH_3O_2}}} \qquad \textbf{Eq. 6.11}$$

For example, the IUPAC recommended rate coefficients for the reaction of OH with ethane is approximately 37 times faster than with methane (2.4×10^{-13} and 6.4×10^{-15} cm^3 $molecue^{-1}$ s^{-1} respectively). With a methane purity of 99.9 % and assuming the remaining 0.1 % is ethane, this could only explain approximately 4 % of the difference between the two calibration methods.

6.4.1 RO_xLIF measurements of CH_3O_2 self-reaction

A preliminary measurement of the CH_3O_2 self-reaction with the newly built RO_xLIF instrument is shown here. The RO_xLIF instrument was described and calibrated for CH_3O_2 in section 4.6 using the same water vapour photolysis in the presence of methane methodology as FAGE. As the RO_xLIF instrument converts all RO_2 species into HO_2 and then OH for detection by LIF it is unlikely to be influenced by impurities in the methane used for calibration – i.e. both methane and any higher order hydrocarbon impurities will both react with OH to form RO_2, all of which will be detected.

Figure 6.8 shows a trace of the signal measured by the RO_xLIF instrument during a CH_3O_2 self-reaction experiment at 295 K. When NO is injected into the pre-reactor the observed signal represents the sum of HO_2 and CH_3O_2 present in the chamber, switching off the NO injection (blue shaded area) shows only the HO_2.

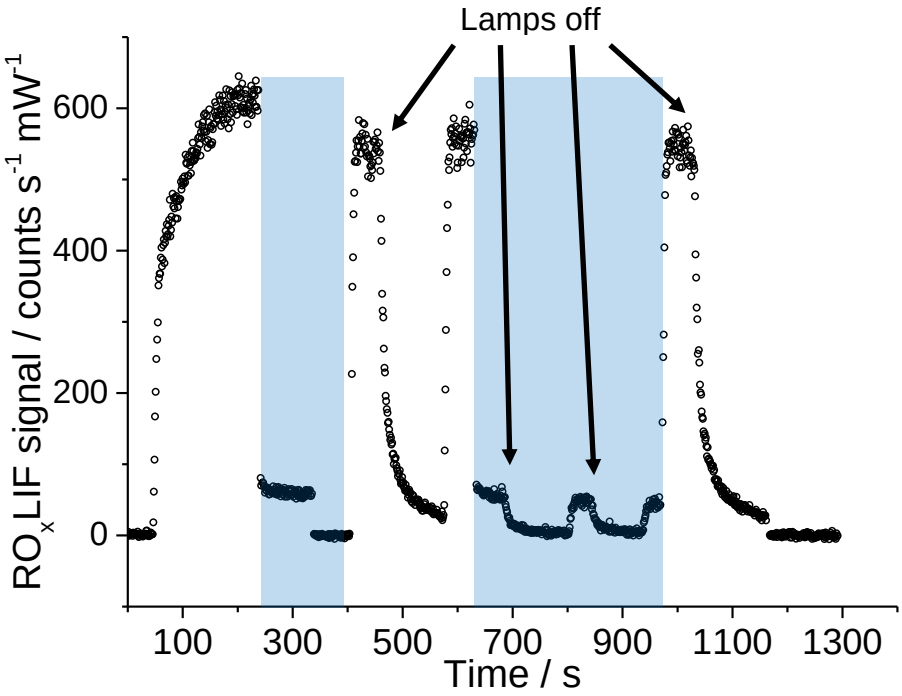

Figure 6.8 Trace of the RO_xLIF signal during a CH_3O_2 self-reaction experiment at 295 K, where the photolysis lamps were switched on and off (labelled) to measure the temporal decay, analogous to the FAGE measurements. The RO_xLIF instrument can measure either the HO_2 concentration (blue shaded area), or the sum of all RO_2 radicals by injecting NO into the pre-reactor. The drop in signal from ~80 to 0 counts s^{-1} mW^{-1} at around 350 seconds was caused by switching off the NO injection into the LIF cell, stopping conversion on HO_2 into OH. This was switched back on at ~ 400 seconds.

Figure 6.9 shows an example temporal decay measured using the RO_xLIF instrument at 295 K, and the blue line is the result of fitting Eq. 6.3. Fitting of the two decays gave an average k_{obs} = (3.7 ± 0.1) × 10^{-13} cm^3 $molecule^{-1}$ s^{-1}, where the error is the standard deviation of the average. This is in good agreement with FAGE derived value of the observed rate coefficient at 295 K, k_{obs} = $(3.41^{+1.77}_{-0.85})$ × 10^{-13} cm^3 $molecule^{-1}$ s^{-1} (see section 6.3.1), which is within 10 %. This result also suggests that the ~0.5 second residence time of the sampled gas in the pre-reactor tube does not affect temporal measurements. This shows the RO_xLIF instrument has potential for use as a complementary method to measure radicals in HIRAC and will be useful in probing the earlier discrepancy in k_{obs} further. It is noted, however, that these results are from a single experiment and the RO_xLIF instrument is not fully understood, for example it is largely insensitive

to the addition of CO. Further testing and characterisation of the instrument is required before the results may be relied upon.

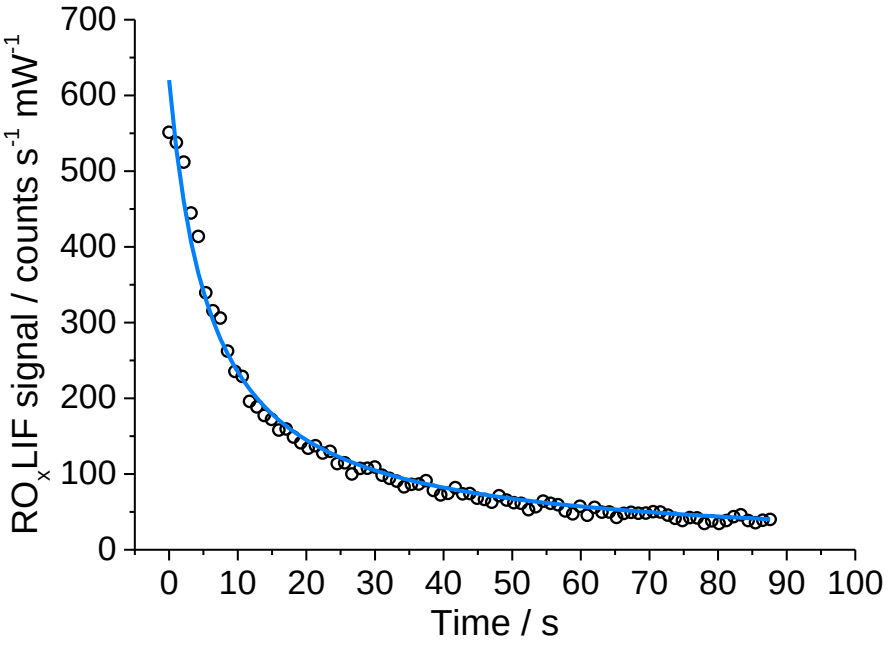

Figure 6.9 An example CH_3O_2 decay measured by the RO_xLIF instrument at 1000 mbar and 295 K, and the line produced by fitting Eq. 6.3 to the data, giving k_{obs} = (3.66 ± 0.01) × 10^{-13} cm^3 $molecule^{-1}$ s^{-1}, where the error is the statistical error in the fitting process.

6.5 CH_3O_2 + HO_2 Cross-Reaction results

Figure 6.10 shows example temporal decays of the HO_2 and CH_3O_2 radicals measured during a cross-reaction experiment performed at 295 K, and the resulting Kintecus® (Ianni, 2017) fit to the data using the methodology described in section 6.3.2. The reactions and rate coefficients for the fits in Figure 6.10 are shown in Table 6.4.

Table 6.4 The reactions are rate coefficients used in the Kintecus® model to fit data at 295 K to extract the CH_3O_2 + HO_2 cross-reaction rate coefficient, $k_{6.3}$.

Reaction	Rate Coefficient
R 6.1a	1.61×10^{-13} cm^3 molecule^{-1} s^{-1}
R 6.1b	0.89×10^{-13} cm^3 molecule^{-1} s^{-1}
R 6.2	1.85×10^{-15} cm^3 molecule^{-1} s^{-1}
R 6.9	2.99×10^{-12} cm^3 molecule^{-1} s^{-1}
R 6.10	0.0745 s^{-1}
R 6.3	Float

The rate coefficient calculated from each fit was $k_{6.3}$ = 5.61 and 5.37×10^{-12} cm^3 molecule^{-1} s^{-1} respectively, however the Kintecus® does not report error values in the fitting process. The agreement in the rate coefficient derived from HO_2 decays and CH_3O_2 decays was generally very good, usually within 10%. This is especially important as it offers further evidence that the CH_3O_2 wand calibration method is reliable. Otherwise, a similar 30 % discrepancy between the two measurements would be expected.

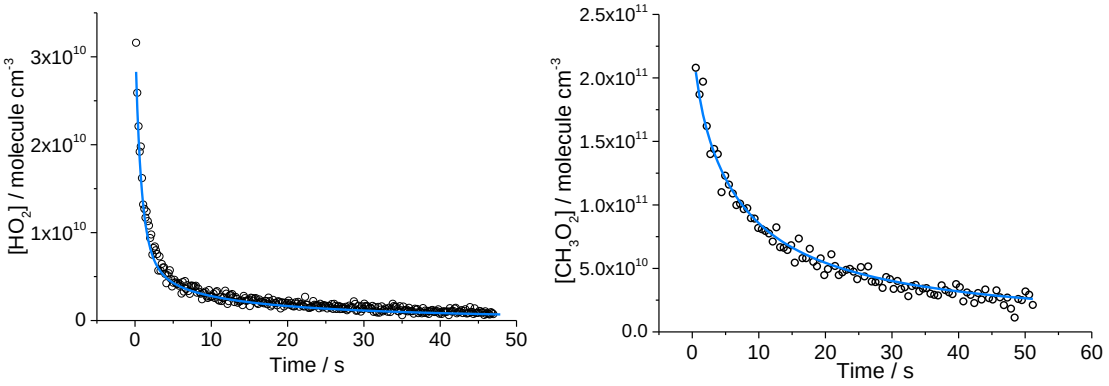

Figure 6.10 An example Kintecus® (Ianni, 2017) fit of the HO_2 decay (left) and CH_3O_2 decay (right) during a CH_3O_2 + HO_2 cross-reaction experiment. The fitting methodology was described in section 6.3.2. The HO_2 decay is the sum of cross-reaction loss, self-reaction loss and wall loss, making it appear much faster than the CH_3O_2 decay that has comparatively negligible self-reaction and wall loss rates. However, the inferior sensitivity of the FAGE instrument for the CH_3O_2 radical results in the lower quality data.

The CH_3O_2 + HO_2 rate coefficients obtained at each temperature in this work are shown in Table 6.5.

Table 6.5 CH_3O_2 + HO_2 cross-reaction rate coefficients obtained in this work. 2σ errors are shown and do not include systematic calibration uncertainty.

Temperature / K	$k_{6.3}$ / 10^{-12} cm^3 molecule^{-1} s^{-1}
268	8.3 ± 5.4
284	6.3 ± 1.6
295	5.0 ± 1.2
323	3.8 ± 1.0
344	3.2 ± 1.1

The change in the CH_3O_2 + HO_2 cross-reaction rate coefficient as a function of temperature is shown in Figure 6.11a, with the average rate coefficient at each temperature from this work represented by the red triangles. The error bars represent the 2σ statistical error in the average, and while the rate coefficient measured at 268 K is consistent with the trend of the other points it has an

exceptionally large statistical error of ~60 %. This reason for this is unknown but may be related to the cold chamber walls offering increased heterogeneous radical or reagent loss pathways or condensation of reagents onto the chamber walls, although this would likely cause a systematic offset rather than scatter. The radical gradient measurements discussed in 5.1.3 could be repeated at these lower temperatures to see if this is the case. A more likely cause was that the photolysis lamps in HIRAC were also very cold. As shown in section 2.2 this makes their output intensity very low when first switched on, or may cause delayed ignition, and their output intensity continually changes over the course of at least 10 minutes. This may mean the interpolation method described in section 6.3.2 is flawed as the lamp intensity was not constant throughout the experiment. Figure 6.11b shows the Arrhenius plot for the data gathered here, and the linear regression is shown by the red line to give the Arrhenius equation $k_{6.3} = (1.26 \pm 0.38) \times 10^{-13} \exp[(1119 \pm 89)/T]$ cm^3 molecule^{-1} s^{-1} and an activation energy of 9.30 ± 0.74 kJ mol^{-1}. Using this equation to evaluate the rate coefficient at 298 K, a value of $k_{6.3} = (5.38 \pm 0.18) \times 10^{-12}$ cm^3 molecule^{-1} s^{-1}, which agrees well with the IUPAC recommendation of $(5.2 \pm 1.6) \times 10^{-12}$ cm^3 molecule^{-1} s^{-1}. The *Ea/R* value of 1119 ± 89 K lies outside the IUPAC recommendation of 780 ± 200 K (based on Lightfoot et al., 1990b), but is similar to the determination by Cox and Tyndall with a value of 1296 ± 364 K.

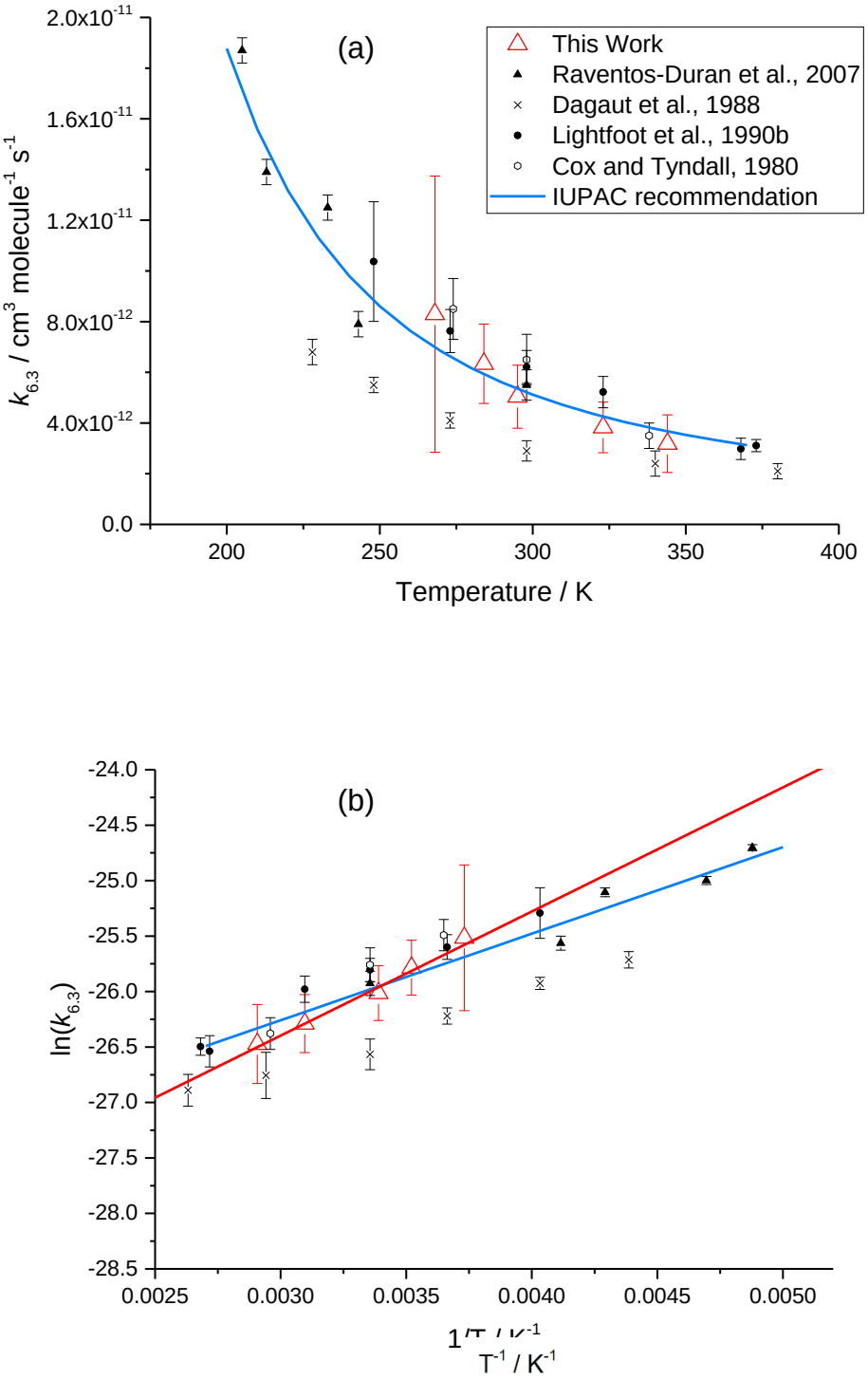

Figure 6.11 a) The effect of temperature on the rate coefficient of the CH_3O_2 + HO_2 cross-reaction rate coefficient, $k_{6.3}$, between 268 and 344 K (-5 – 71 °C) and b) an Arrhenius plot of the same data sets. The data gathered in this work is shown by the red triagnles, where each data point is the average value of $k_{6.3}$ from at least 10 decay fits at each temperature, the error bars represent the standard deviation of the average at 2σ. The linear regression to extract the Arrhenius parameters from this work is shown by the red line, see main text for details. Data from previous studies is shown for comparison.

The fact that the cross-reaction exhibits a negative temperature dependence is interesting, as typically reactions become faster as the available energy to break bonds is increased. The negative dependence suggests that an intermediate complex must form as part of the reaction process, turning R 6.3 into:

$$CH_3O_2 + HO_2 \rightleftharpoons CH_3O_4H \rightarrow \text{products} \qquad \textbf{R 6.11}$$

where raising the temperature of the system will break the weak bonds holding the complex together before the reaction can proceed, i.e. the rate coefficient for the reverse reaction increases with temperature more than the forwards reaction. A similar effect is seen with the HO_2 self-reaction (Cox and Burrows, 1979, Cox and Tyndall, 1980), though the dependency is less, as it is thought to proceed through a similar intermediate, while the CH_3O_2 self-reaction shows only a very weak negative dependence.

6.6 Summary

The rate of the CH_3O_2 self-reaction has been measured using the FAGE instrument between 268 K and 344 K. Compared to the IUPAC recommendation for the observed rate coefficient, these measurements are on average ~30 % lower at all temperatures. The reason for the discrepancy has not yet been resolved, but suggestions were made above as to where errors may lie, both in the FAGE measurements and its calibration, and in the IUPAC recommendation. The FAGE measurements of $k_{6.1}$ are relatively imprecise, with estimated error margins of (+52 %, - 25 %) that overlap with the uncertainty in the IUPCA values. Most of the uncertainty in the FAGE measurements can be attributed to the ~34 % error associated with the calibration factor, which was estimated in section 4.5.1, however there appeared to be a negative correlation between k_{obs} and the initial CH_3O_2 concentration that is difficult to explain. Further experiments at higher initial concentrations should be conducted to see if the trend continues. The measurements reported here were made sporadically over a very long period, which may have introduced errors if any changes in the FAGE instrument sensitivity were unaccounted for, however this can only explain the spread in measured values and does not explain the systematically lower average values of the observed rate coefficient.

The observed rate coefficient at 295 K was also measured using the newly developed RO_xLIF instrument, described and calibrated in section 4.6, and the value obtained agreed with the FAGE determination within 10 %. However, this value was obtained from a single experiment and cannot be relied upon, further measurements are required. The RO_xLIF instrument could be a key tool to solve the mystery behind the discrepancy in k_{obs}, as it is more sensitive to CH_3O_2 (though non-specific), meaning lower initial CH_3O_2 concentrations could be used without sacrificing signal quality.

The CH_3O_2 self-reaction branching ratio was measured between 260 K and 340 K by monitoring the evolution of methanol and formaldehyde using FTIR. A good agreement was found with a previous determination by Horie et al. The FTIR measurements of formaldehyde were validated by comparison against a FAGE instrument that detects formaldehyde by LIF at 353 nm.

The CH_3O_2 + HO_2 cross-reaction kinetics have also been measured between 268 K and 344 K and agree within 10 % of the IUPAC recommended values. This is remarkable given how difficult these experiments were to perform, that it was not possible to perform simultaneous measurements of both radicals, and the down time caused by having to switch between the detection of HO_2 at 308 nm and CH_3O_2 at 298 nm, particularly with no reference cell for CH_3O_2. The measurement at 268 K has a very large error margin of ~60 %. Note that this is just the statistical error, calibration uncertainty has still not been included. The source of this scatter could be due to the photolysis lamps being too cold and outputting non-uniform intensity over the course of the experiments, which may have caused problems with the interpolation process in the analysis. The cross-reaction experiments would be greatly improved by performing simultaneous measurements of HO_2 and CH_3O_2 in the front and rear FAGE cells, respectively. This requires two lasers though, one for 308 nm and the other for 298 nm excitation. These simultaneous experiments were attempted, but problems quickly arose with the second laser system and time did not permit finding a remedy.

Both the self-reaction and cross-reaction experiments would be improved with a working CH_3O_2 reference cell, which should be the primary focus of future work. Especially since a reference cell is mandatory for field measurements.

6.7 References

Atkinson, R., Baulch, D. L., Cox, R. A., Crowley, J. N., Hampson, R. F., Hynes, R. G., Jenkin, M. E., Rossi, M. J. & Troe, J. 2006. Evaluated kinetic and photochemical data for atmospheric chemistry: Volume II - gas phase reactions of organic species. *Atmospheric Chemistry and Physics,* 6**,** 3625-4055.

Burkholder, J. B., Sander, S. P., Abbatt, J., Barker, J. R., Huie, R. E., Kolb, C. E., Kurylo, M. J., Orkin, V. L., Wilmouth, D. M. & Wine, P. H. 2015. Chemical Kinetics and Photochemical Data for Use in Atmospheric Studies, Evaluation No. 18, *JPL Publication 15-10, Jet Propulsion Laboratory, Pasadena*.

Cox, R. A. & Burrows, J. P. 1979. Kinetics and Mechanism of the Disproportionation of HO_2 in the Gas Phase. *Journal of Physical Chemistry,* 83, 2560-2568.

Cox, R. A. & Tyndall, G. S. 1980. Rate Constants for the Reactions of CH_3O_2 with HO_2, NO and NO_2 using Molecular Modulation Spectrometry. *Journal of the Chemical Society,* 76, 153-163.

Cryer, D. R. 2016. Measurement of hydroxyl radical activity and formaldehyde in the atmopshere*. PhD Thesis, University of Leeds*.

Dagaut, P. & Kurylo, M. J. 1990. The gas phase UV absorption spectrum of CH_3O_2 radicals - a reinvestigation. *Journal of Photochemistry and Photobiology a-Chemistry,* 51**,** 133-140.

Dagaut, P., Wallington, T. J. and Kurylo, M. J. 1988. Temperature Dependence of the Rate Constant for the HO_2 + CH_3O_2 Gas-Phase Reaction. *Journal of Physical Chemistry,* 92, 3833-3836.

Horie, O., Crowley, J. N. & Moortgat, G. K. 1990. Methylperoxy self-reaction - products and branching ratio between 223 K and 333 K. *Journal of Physical Chemistry,* 94**,** 8198-8203.

Ianni, J. C. 2017. Kintecus. *Windows Version 6.01*.

Jenkin, M. E. and Cox, R. A. 1991. Kinetics of Reactions of CH_3O_2 and $HOCH_2CH_2O_2$ Radicals Produced by the Photolysis of Iodomethane and 2-Iodoethanol. *Journal of Physical Chemistry,* 95, 3229-3237.

Kan, C. S, Calvert, J. G. & Shaw, J. H. 1980. Reactive Channels of the CH_3O_2 – CH_3O_2 Reaction. *Journal of Physical Chemistry,* 84, 3411-3417.

Keller-Rudek, H., Moortgat, G. K., Sander, R. & Sorensen, R. 2013. The MPI-Mainz UV/VIS Spectral Atlas of Gaseous Molecules of Atmospheric Interest. *Earth System Science Data,* 5**,** 365-373.

Kurylo, M. J. & Wallington, T. J. 1987. The temperature dependence of the rate constant for the gas phase disproportionation reaction of CH_3O_2 radicals. *Chemical Physics Letters,* 138, 543-547.

Lightfoot, P. D., Lesclaux, R. & Veyret, B. 1990a. Flash Photolysis Study of the CH_3O_2 + CH_3O_2 Reaction: Rate Constants and Branching Ratios from 248 to 573 K. *Journal of Physical Chemistry,* 94, 700-707.

Lightfoot, P. D., Lesclaux, R. & Veyret, B. 1990b. Flash Photolysis Study of the CH_3O_2 + HO_2 Reaction between 248 and 573 K. *Journal of Physical Chemistry,* 94, 708-714.

Niki, H., Maker, P. D., Savage, C. M. & Breitenbach, L. P. 1981. Fourier Transform Infrared Studies of the Self-Reaction of CH_3O_2 Radicals. *Journal of Physical Chemistry*, 85, 877-881.

Orlando, J. J. & Tyndall, G. S. 2012. Laboratory studies of organic peroxy radical chemistry: an overview with emphasis on recent issues of atmospheric significance. *Chemical Society Reviews,* 41**,** 6294-6317.

Raventos-Duran, M. T., McGillen, M., Percival, C. J., Hamer, P. D. and Shallcross, D. E. 2007. Kinetics of the CH_3O_2 + HO_2 Reaction: A Temperature and Pressure Dependence Study Using Chemical Ionization Mass Spectrometry. *International Journal of Chemical Kinetics,* 39, 571-579.

Sander, S. P. & Watson, R. T. 1981. Temperature Dependence of the Self-Reaction of CH_3O_2 Radicals. *Journal of Physical Chemistry,* 85, 2960-2964.

Tyndall, G. S., Cox, R. A., Granier, C., Lesclaux, R., Moortgat, G. K., Pilling, M. J., Ravishankara, A. R. & Wallington, T. J. 2001. Atmospheric chemistry of small organic peroxy radicals. *Journal of Geophysical Research-Atmospheres,* 106**,** 12157-12182.

Tyndall, G. S., Wallington, T. J. & Ball, J. C. 1988. FTIR Product Study of the Reactions CH_3O_2 + CH_3O_2 and CH_3O_2 + O_3. *Journal of Physical Chemistry A,* 102, 2547-2554.

Chapter 7. Conclusions and outlook

This thesis has detailed the development of a new method to detect CH_3O_2 radicals, based on the well-established FAGE technique described in Chapter 3. The aim was to develop a technique that could specifically detect CH_3O_2 radicals with enough sensitivity to be applicable in field measurements, which at the time of writing this is not otherwise possible, as detailed in section 1.2. This aim was achieved in Chapter 4, where the FAGE technique was developed and used to successfully measure CH_3O_2 radicals. Calibration of the instrument showed it to be capable of reaching detection limits in the region of 10^8 molecule cm^{-3} for a 5-minute averaging time, which is approaching the expected CH_3O_2 levels present in clean, rural environments. The sensitivity is, however, likely to be insufficient for polluted urban environments where CH_3O_2 is rapidly destroyed by NO.

The atmospheric simulation chamber HIRAC, detailed in Chapter 2, was used in combination with the FAGE instrument to probe the kinetic behaviour of the CH_3O_2 radical, specifically its self-reaction and its cross-reaction with HO_2, pertinent to its role in the HO_x cycle that dominates tropospheric oxidation of VOCs. The rate coefficient of the self-reaction was measured between 268 K and 344 K, finding an almost negligible negative temperature dependence which is in-line with previous studies. However, the absolute value of the rate coefficient was on average 30 % lower than the IUPAC recommended value at all temperatures, but within the error margins.

Inter-comparison experiments between the FAGE instrument and the absorption based CRDS instrument were described in Chapter 5 and showed very good agreement between the instruments when targeting HO_2 radicals. This validates the reliability of the widely used water photolysis method to generate known quantities of OH and HO_2 radicals to calibrate the FAGE instrument, however this did not translate to inter-comparison measurements of CH_3O_2 where the FAGE instrument over-estimated radical concentrations by ~32 %. This over-estimation is a symptom of the 30 % discrepancy in the CH_3O_2 self-reaction rate coefficient mentioned above, as the CRDS instrument relies upon the rate coefficient whereas the FAGE calibration method is independent.

Suggestions were made in Chapter 6 as to possible sources of the ~30 % discrepancy in the value of the CH_3O_2 self-reaction rate coefficient, both with the FAGE method developed here and with the IUPAC recommended value of the rate coefficient but could not fully account for the difference. Further work is still needed to resolve the discrepancy before the FAGE method can be deployed for atmospheric measurements as it will rely on the accuracy of the water vapour photolysis calibration method. Even so, the difference between the rate coefficients measured here and the IUPAC recommended values is relatively small and within the error margins of both. Additionally, the fate of CH_3O_2 in the troposphere is typically dominated by the much faster reactions with HO_2 and NO, meaning the discrepancy will likely have limited effect on the current understanding of atmospheric chemistry.

The rate coefficient of the CH_3O_2 + HO_2 cross-reaction was also measured between 268 K and 344 K and is on average within 10 % of the values calculated using the IUPAC recommended temperature dependent rate coefficient. This agreement is evidence that the FAGE calibration technique is reliable for both HO_2 and CH_3O_2 radicals, as accurate knowledge of both radical concentrations and accurate knowledge of their respective competing self-reactions is required.

Also shown in this thesis was the initial development and testing of the RO_xLIF instrument that, while not a novel technique, was designed to augment the capabilities of HIRAC. The design and calibration of the instrument were shown in section 4.6, and preliminary measurements of the CH_3O_2 self-reaction kinetics using this instrument were shown in section 6.4.1, agreeing within 10 % of the analogous FAGE measurements. However, this was the result of only one experiment, the RO_xLIF instrument described in this thesis is in its infancy and further work is needed in characterising and testing the RO_xLIF instrument before measurements can be relied upon.

7.1 Outlook

The kinetic measurements made using the FAGE instrument are in reasonable agreement with previous work, even with the ~30 % discrepancy in the CH_3O_2 self-reaction rate coefficient. However, this discrepancy still needs to be investigated as any future use of the method in the field will rely upon the water vapour photolysis calibration. While the instrument is currently not sensitive enough to measure the kinetics at significantly lower radical concentrations, experiments in HIRAC could be performed at even higher radical concentrations to see if the rate coefficient continues to decrease. Given that the data on the self-reaction presented here was collected over the space of ~4 years, some of the variability in the self-reaction measurements could be attributed to changes in instrument sensitivity that were not accounted for. A small number of experiments at each temperature should be conducted in a short period of time, one month should be feasible, to see if the precision of the rate coefficient measurements can be improved.

The RO_xLIF instrument would be very useful in probing the as it is more sensitive to RO_2 radicals by virtue of converting them all to OH which has a smaller partition function than CH_3O and therefore yields higher fluorescence signals. The higher sensitivity offered would enable lower CH_3O_2 concentrations to be used in HIRAC, whilst still measuring temporal decays with a high signal to noise ratio.

One of the aims of this work was to fill the gap in tropospheric measurements of CH_3O_2 radicals, and with the work done here we will hopefully see such instruments deployed in the field. The FAGE instrument detailed in this thesis was modified from an existing instrument that was designed to measure radical kinetics and to work with the HIRAC chamber. Now that the method to detect CH_3O_2 radicals has been developed, work to build an instrument for field-based measurements can begin, which offers an opportunity to improve the design. For example, the long 30 cm inlet would be unnecessary, larger displacement pumps and a smaller inlet pinhole would allow lower cell-pressures to be reached. The low-pressure calibration experiments in section 4.4.2 showed that the sensitivity increased by a factor of ~2.4 when the cell pressure dropped from ~2.5 Torr (Sampling from HIRAC at 1000 mbar) down to ~0.7 Torr (Sampling from HIRAC

at 100 mbar). This in turn would decrease the LOD by a similar amount. Taking the LOD calculated in section 4.4.1, 2.1×10^8 molecule cm^{-3}, this may bring the LOD into the ~10^7 molecule cm^{-3} range. With detection limits 5-10 times lower than expected CH_3O_2 levels in clean environments this FAGE method would be a viable tropospheric measurement technique. However, field measurements would also require the work started on building a reference cell in chapter 4 to be completed.

In preliminary work by Dr. Lavinia Onel, the FAGE method has also been used to detect the ethyl peroxy radical, $C_2H_5O_2$, by exciting at ~323 nm in the HIRAC chamber. The sensitivity is lower as the radical is larger with a broad and strongly congested absorption spectrum but preliminary measurements of the $C_2H_5O_2$ self-reaction have been performed.